Effect of Ionic Liquid on Transition Metal-N_2 Complexes and Its Application to Electrochemical Ammonia Synthesis

イオン液体中での窒素錯体の評価と電気化学的アンモニア合成への応用

Thesis by

Akira Katayama

In Partial Fulfillment of the Requirements

for the Degree of Doctor of Philosophy

Nagoya Institute of Technology

Nagoya, Japan

January 2018

Acknowledgements

First and foremost, I would like to express my sincere gratitude to Professor Hideki Masuda for the continuous support of my Ph.D. study for his patience, motivation, enthusiasm, and immense knowledge. I am deeply indebted to him for the thinking of chemistry and life.

Beside my advisor, I would like to express my gratitude to Associate Professors Tomohiro Ozawa and Tomohiko Inomata for their encouragement, hard questions and insightful comments, and Assistant Professor Yuko Wasada-Tsutsui who taught me how to carry out DFT and TD-DFT calculations. I would like to show my appreciation to Professor Hideki Mori in Nagoya Institute of Technology who taught me chemical engineering process, helped design of the electrolysis cell, and gave me valuable advice and to Dr. Yoshiyuki Watanabe and Dr. Mitsuo Morita in JGC CORPORATION who performed feasibility studies for the electrochemical ammonia synthesis toward the industrial application. I would like to thank Professor Yoshitsugu Kojima in Hiroshima University, who gave me variable comments regarding with the electrochemical ammonia synthesis. I would like to thank the late Professor Takashi Ogura and Associate Professor Takehiro Ohta in University of Hyogo, who taught me how to measure resonance Raman spectroscopy and discussed on the results and provided incisive comments.

I would like to offer my thanks to Associate Professor Yuji Kajita in Aichi Institute of Technology, Associate Professor Takuma Yano and Assistant Professor Kenta Motobayashi in Nagoya Institute of Technology, and Dr. Jun Matsumoto, Dr. Takahiko Ogawa, Dr. Tatsuya Suzuki and Dr. Tatsuya Kitagawa who taught me how to do experiments and gave me helpful advices for all things. I am also grateful to Masuda

laboratory's members who helped my experiment and discussed my work. Especially, I would sincerely like to thank to Mrs. Hiroko Amano who is a secretary and Mrs. Yachiyo Taniyama who is a technical officer helping me various things in this laboratory.

I acknowledge the Equipment Development Center in Institute for Molecular Science for helping the development of the electrolysis cell. My Ph.D. study was supported by the New Energy and Industrial Technology Development Organization (NEDO) through the "Advanced Research Program for Energy and Environmental Technologies," and the Japan Society for the Promotion of Science (JSPS) through the research fellowship for young scientists (DC2) with "Grant-in-Aid for JSPS Fellows (No. 15J09325)".

Finally and importantly, my deepest appreciation goes to my parents Ryuji and Rika Katayama raising me and giving me this opportunity to pursue this career path.

Abstract

So far, small molecule activation reactions such as the reduction of CO_2 by using transition metal complexes in ionic liquids (ILs) have been studied. Transition metal complexes in ILs are affected by the electrostatic interaction of ILs and the reactivity in ILs are different from those in conventional organic solvents. However, the N_2 reduction by transition metal complex has never been reported before. In this thesis, therefore I focused on understanding the N_2 coordination to transition metal complexes in ILs and its activation, and applying the combination to the electrochemical NH_3 synthesis.

The main subjects are summarized as follows; (1) the construction of the electrochemical conversion system for N_2 and proton derived from H_2O to NH_3 by using transition metal complexes in ILs under mild conditions is described in Chapter 2, and (2) the evaluation of the effect of ILs toward transition metal-N_2 complexes is discussed in Chapters 3 and 4. These details containing the introduction are described in Chapter 1.

In Chapter 2, the electrochemical NH_3 synthesis by using titanocene dichloride, [Cp_2TiCl_2], in the ILs in solid polymer electrolyte (SPE) cell is described based on the results of the electrochemical redox reaction of [Cp_2TiCl_2] in ILs. To carry out the electrochemical reaction, a SPE cell having a proton exchange membrane and a gas diffusion electrode coated with 1−butyl−1−methylpyrrolidinium tris(pentafluoroethyl)trifluorophosphate (Pyr_4FAP) and 1-butyl-1-methyl-pyrrolidinium triflate (Pyr_4OTf) containing [Cp_2TiCl_2] is designed and fabricated. The electrochemical NH_3 synthesis in SPE cell gives higher NH_3 yields than that in THF solution in H-type cell. Moreover, to confirm that the generation of NH_3 in the electrochemical reaction is derived from N_2 gas, the isotopic labeling experiment was also performed. The comparison of the electrochemical synthesis of NH_3 in

non-coordinating IL with that in coordinating IL indicates that the efficiency of the NH_3 synthesis in non-coordinating IL is higher than that in coordinating IL.

In Chapter 3, the electrochemical reduction of [Cp_2TiCl_2] in ILs is evaluated using UV/vis/NIR spectroscopy, and furthermore, N_2 coordination of titanocene monochloride, [Cp_2TiCl], in ILs is also discussed. UV-vis/NIR spectra of [Cp_2TiCl_2] during the electrochemical reduction clearly suggest that dimeric species, [$(Cp_2TiCl)_2$], is generated via formation of monomeric [Cp_2TiCl] even in non-coordinating IL. To confirm whether an equilibrium reaction between dimeric [$(Cp_2TiCl)_2$] and monomeric [Cp_2TiCl] in IL exists or not, the frozen solution EPR spectrum of [$(Cp_2TiCl)_2$] in Pyr_4FAP was measured. Surprisingly, the hyperfine splitting derived from N_2 coordination to [Cp_2TiCl] was observed only in IL. The effect of ILs toward the N_2 coordination to [Cp_2TiCl] is evaluated by DFT calculations, and it was suggested that the polar domain in non-coordinating IL promotes the N_2 coordination to [Cp_2TiCl] through weak interaction between FAP anion and [Cp_2TiCl].

In Chapter 4, the electrochemical oxidation reaction of molybdenum(0)–N_2 complex supported with bidentate phosphine ligands in Pyr_4FAP is described. To examine the effect of Pyr_4FAP, the electrochemical oxidation reaction in THF solution was also evaluated. Resonance Raman, FT-IR and UV-vis/NIR spectroscopic studies during electrochemical oxidation reaction and their evaluation by DFT and TDDFT calculations revealed that the subsequent reaction after the electrochemical oxidation of the Mo(0)-N_2 complex proceeded to form the dimeric species, Mo(II)–N=N–Mo(II) in THF solution. On the other hand, a mononuclear Mo(I)–N_2 complex in Pyr_4FAP was stabilized due to its weak interaction with FAP anion of the non-coordinating IL.

In Chapter 5, the conclusions in this thesis are described.

List of Publications

1. Electrochemical conversion of dinitrogen to ammonia induced by a metal complex–supported ionic liquid
   Akira Katayama, Tomohiko Inomata, Tomohiro Ozawa, Hideki Masuda,
   Electrochem. Commun., **2016**, *67*, 6–10.
   (Reference in Chapter 3)

2. Electrochemical Evaluation of Titanocenes in Ionic Liquids with Non-coordinating and Coordinating Anions and Application for NH_3 Synthesis
   Akira Katayama, Tomohiko Inomata, Tomoniro Ozawa, Hideki Masuda,
   ChemElectroChem., **2017**, *4*, 3053–3060.
   doi: 10.1002/celc.201700557
   (Reference in Chapter 2)

3. Ionic liquid promotes N_2 coordination to titanocene(III) monochloride
   Akira Katayama, Tomohiko Inomata, Tomohiro Ozawa, Hideki Masuda,
   Dalton Trans., **2017**, *46*, 7668–7671.
   (Reference in Chapted 2)

Table of Contents

Detailed Table of Contents

Page

List of Figures

Chapter 1

Chapter 2

Chapter 3

Chapter 4

Appendix A

Appendix B

Appendix C

List of Schemes

Chapter 3

Chapter 4

Appendix C

List of Tables

Chapter 2

Chapter 3

Chapter 4

Appendix A

Appendix B

Appendix C

List of Abbreviations

Abs.	Absorbance
Ag/AgCl	Silver/silver(I) chloride electrode (reference electrode)
Ag	Silver
AgCl	Silver(I) chloride
$AgClO_4$	Silver(I) perchlorate
$AgNO_3$	Silver(I) nitrate
Al_2O_3	Aluminium oxide
aq.	Aqueous solution
Ar	Argon
atm	Standard atmosphere
BF_4^-	Tetrafluoro borate
BP86	functional for DFT
B3LYP	functional for DFT
B3LYP*	functional for DFT
C	Coulomb
calcd	Calculated
CE	Counter electrode
Cl^-	Chloride anion
cm	Centimeter
cm^{-1}	Wavenumver
CO_2	Carbon dioxide
CO	Carbon monoxide
CPE	Controlled-potetial electrolysis
Cp	Cyclopentagienyl ligand
$[Cp_2TiCl_2]$	Titanocene dichloride
$[(Cp_2TiCl)_2]$	Dimeric bis[(cyclopentadienyl)titanium(III) chloride]
$[Cp_2TiCl]$	Bis[(cyclopentadienyl)titanium(III) chloride]
$[Cp^*_2TiCl_2]$	Bis(pentamethylcyclopentadienyl)titanium(IV) dichloride
$[Cp_2VCl_2]$	Bis(cyclopentadienyl)vanadium(IV) dichloride
$CrCp_2^*$	Decamethylchromocene
CT	Charge transfer
Cu	Copper

CV	Cyclic voltammogram
C_4mim	1-butyl-3-methylimidazolium
D	Diffusion coefficient
D_2	Deuterium dihydrogen
deg.	Degree
depe	1,2-Bis(diethylphosphino)ethane
DFT	Density functional theory
dppe	1,2-Bis(diphenylphosphino)ethane
e^-	Electron
EC	Heterogeneous electron transfer followed by homogeneous chemical reaction
Eq.	Equation
ESI-MS	Electrospray ionization mass spectroscopy
EtOH	Ethanol
EMIM	1-ethyl-3methylimidazolium
EPR	Electron Paramagnetic Resonance
eV	Electron volt
$E_{1/2}$	Measured or expected half-wave potential in voltammetry
E_{ox}	Oxidation peak potential
E_{red}	Reduction peak potential
F	Fluorine atom
FAP	Tris(pentafluoroethyl)trifluorophosphate
Fc^+	ferrocenium ion
Fc	ferrocene
Fe	Iron
Fe_3O_4	Triiron tetraoxide
FeMoco	Iron-Molybdenum cofactor
g	Electron g-factor
G	Gauss, Gibbs free energy
GCE	Glassy carbon electrode
GD3BJ	D3 version of Grimme’s dispersion with Becke–Johnson damping (empirical correction for DFT)
h	Hour

H	Enthalpy, hydrogen atom
H^+	Proton
H_2	Dihydrogen
HD	Hydrogen deuteride
Hg	Mercury
HIPT	Hexa-isopropyl-terphenyl
HOMO	Highest-Occupied Molecular Orbital
Hz	Hertz
H_2SO_4	Sulfic acid
H_2O	Water
IL	Ionic liquid
IR	Infrared
K	Potassium, Kelvin
kcal/mol	Kilocalorie per mole
KC_8	Potassium graphite
K_2O	Potassium oxide
$LiClO_4$	Lithium perchlorate
LMCT	Ligand to metal charge transfer
LSV	Linear sweep voltammogram
LUMO	Lowest-Unoccupied Molecular Orbital
[LutH]BAr$_4$F	2,6-lutidinium tetrakis[3,5-bis(trifluoromethyl)phenylborate]
M	Concentration in molarity
MeOH	Methanol
mg	Milligram
min	Minute
mL/min	Millilitter per minutes
MMCT	Metal to metal charge transfer
mM	Millimolar
mol	Mole
Mo	Molybdenum
mT	Millitesra
mV	Millivolt
N	Nitrogen atom
NaCl	Sodium chloride

NBO	Natural Bond Orbital
NBu_4	Tetrabutylammonium
NH_3	Ammonia
nm	Nanometer
NO	Nitric oxide
NOx	Nitrogen oxides
NTf_2	Bis(trifuloromethane)sulfonate
N_2	Dinitrogen
OTf	Triflate
O_2	Dioxygen
P	Phosphorus atom
PCM	Polarized continuum model
PF_6^-	Hexafluorophosphate
PTFE	Polytetrafluoroethylene
Pt	Platinum
Pyr_4FAP	1–butyl–1–methylpyrrolidinium tris(pentafluoroethyl)trifluorophosphate
Pyr_4OTf	1−butyl−1−methylpyrrolidinium tris(pentafluoroethyl)trifluorophosphate
Pyr_4NTf_2	1-butyl-1-methylpyrrolidinium bis(trifluoromethylsulfonyl)imide
RE	Reference electrode
redox	Reduction and oxidation
r.t.	Room temperature
Ru	Ruthenium
QRE	Quasi-reference electrode
s	Second
SDD	Stuttgart/Dresden ECP (basis sets for DFT)
SCE	Saturated Calomel Electrode
SPE	Solid polymer electrolyte
$TBABF_4$	Tetrabutyl ammonium tetrafluoroborate
TDDFT	Time-dependent density functional theory
THF	Tetrahydrofuran
Ti	Titanium

TMS	Trimethylsilane
TZVP	Polarized valence triple-ζ (basis sets for DFT)
UV-vis/NIR	UltraViolet-visible/Near InfraRed
V	Volt
vs.	Versus
W	Tungsten
WE	Working electrode
%	Percent
ε	Electric permittivity
μM	Micromolar
ΔG	Gibbs energy change in a chemical process
ΔH	Enthalpy change in a chemical process
Å	Ångström
(D)	Depth
(W)	Width
(H)	Height
ϕ	Diameter
°C	Degree Celsius
π	Pi symmetry orbital
π*	Pi symmetry antibonding interaction
ε	Extinction coefficient in units of $M^{-1}cm^{-1}$, dielectric permittivity
η	Hapcity of order,
λ	Wavelength
λ_{max}	Wavelength
6-31G	Basis sets for DFT
0.2 M Pyr_4FAP/THF	THF containing 0.2 M Pyr_4FAP

Chapter 1: Introduction

1.1 Motivation

A unifying theme described in this thesis concerns the effect of ionic liquid (IL) on the N_2 activation by a transition metal complex and its application to electrochemical ammonia (NH_3) synthesis. In 2011, when this subject was first given to me, the N_2 activation in IL had not been presented yet although various studies on dinitrogen fixation had been reported. Since I believed the breakthrough and new discovery in this research area on both of the N_2 activation and ILs, I decided to tackle the issues as my Ph.D. study.

1.2 Potential roles of NH_3 as hydrogen carrier in H_2 economy

NH_3 is one of the most important chemicals produced exceeding 200 million tons/year.[1] ca. 80% of NH_3 produced is used for the fertilizer, and it is utilized to maintain the growth of human population in the world.[2] Beyond using it as fertilizer, the use of NH_3 as energy carrier has recently been expected, because it contains 17.6 wt% of H atom.[3] From the potential roles of NH_3 in dihydrogen (H_2) economy that is the energy system mainly utilizing H_2 as energy carrier,[3] the use of NH_3 has been energetically developed. In comparison with their physical properties, some advantages of NH_3 with respect to H_2 are its lower cost for stored energy, higher volumetric energy density and easier handling.[3] Moreover, since completely burned NH_3 does not emit CO_2, the use of NH_3 as energy storage media is expected from the viewpoint of safety and environment.[4] In Japan, the utilization method of NH_3 as a fuel instead of fossil fuel has been studied in the field of the vehicle industry, electric power plant, and so on.[5,6] It is considered that NH_3 as energy carrier is competitive with hydrogen or electricity in terms of its efficiency, CO_2 emissions, and supply cost for energy systems.[5] In electric power plant, since the reducing the CO_2 emission at coal-fired power generating plant has succeeded in 2017, NH_3 has been expected as a fuel instead of powdered coal.[6] Especially, in the case of firing 80% of coal with 20% of NH_3 in a test plant, the generated nitrogen oxides (NOx) and electrical energy are similar to those by firing 100% of coal, indicating that 20% of CO_2 emission is reduced.[6] Accordingly, the use of NH_3 as hydrogen carrier will contribute to the realization of the sustainable energy society in the future.

1.3 Current major NH_3 synthesis method

A lot of chemical plants that produce NH_3 consume up to 5% of the world's natural gas and release hundreds of millions of CO_2.[7] To reduce CO_2 emission, chemists have developed various alternative methods to use renewable energy.[7] In this section, we describe major industrial and biological NH_3 syntheses in addition to the conversion of N_2 into NH_3 by using transition metal complexes. Furthermore, electrochemical NH_3 syntheses are also introduced, which is especially promised to the energy storage technique for renewable energy such as solar power, wind power and so on.[8]

1.3.1 Industrial ammonia synthesis

The Haber-Bosch process is the main method to produce NH_3 from N_2 and H_2 gases in industry (Eq. 1).[8]

$$N_2 + 3H_2 \leftrightarrow 2NH_3 \qquad (1)$$

The Haber-Bosch process was developed 100 years ago, which adopts $Fe_3O_4/K_2O/Al_2O_3$ catalyst in the temperature range of 400–500 ℃ under 130–170 bar.[8,9] Nowadays, although the process requires very severe conditions, it produces about 120 million tons of NH_3 per year for fertilizer. The energy consumption for the synthesis is estimated to be about 1.4% of all energy consumed in the world.[7,10,11] Additionally, more than 90% of the total energy for industrial NH_3 production is consumed for the H_2 generation as a raw material from fossil fuels, and more than 300 million tons of CO_2 are produced per year.[11] Therefore, an alternative NH_3 synthesis process consuming less energy would be highly desirable.

1.3.2 Biological NH_3 synthesis

As opposed to the Haber-Bosch process carried out under severe conditions, in nature, plants and bacteria can convert N_2 gas into NH_3 under mild conditions. In biological system, nitrogenase enzyme is well known to proceed the conversion of N_2 to ammonia at ambient temperature and pressure (eq. 2).[12] The active site structure of nitrogenase is composed of $Fe_7MoS_{10}CNO_2$ cluster, as shown in Figure 1-1.

$$N_2 + 8H^+ + 8e^- + 16ATP \rightarrow 2NH_3 + H_2 + 16ADP + 16Pi \quad (2)$$

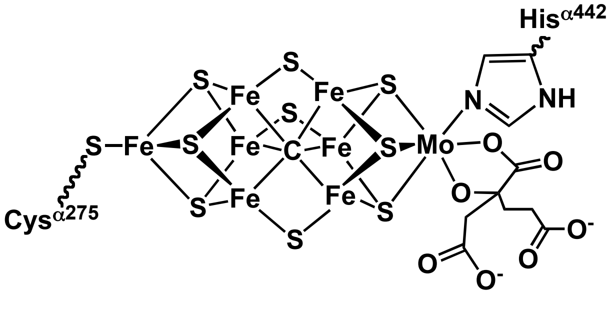

Figure 1-1. Schematic structure of the active site of nitrogenase (FeMoco).

Though X-ray structure of the active site of FeMo cofactor in nitrogenase has been confirmed in 2011, the detailed reaction mechanism and pathway have not been elucidated yet.[12] Currently, the scheme has been proposed that N_2 is coordinated and activated at the thiolate-bridged Fe sites to be converted into NH_3 through the stepwise protonation and reduction.[12(a)]

Although 8 equiv. of ATP is required to produce 1 equiv. of NH_3 (244 kJ/mol), it is still better than the industrial method (ca. 485 kJ/mol, where it includes the whole process such as H_2 production from steam reforming, pressurizing of the reaction mixture, and so on).[8,10] Moreover, the rate of NH_3 generation by nitrogenase enzyme from *Klebsiella pneumoniae* (0.25 mmol min^{-1} $(g\text{-protein})^{-1}$) is 100000 times higher than that from N_2 and H_2 by using Ru-K/C as heterogeneous catalyst.[13] Interestingly, even though H_2 evolution by the reduction of proton is extremely favor reaction for NH_3 production, nitrogenase enzyme produces 2 equiv. NH_3 and 1 equiv. H_2, as shown in eq. (2). FeMo nitrogenase under D_2 atmosphere generated HD, suggesting that the scrambling reaction of H^+ with D_2 occurs and that the H_2 evolution is not just a side reaction in NH_3 generation.[14,15]

On the basis of the attractive NH_3 synthesis system by nitrogenase in nature, many scientists have considered that to imitate and learn it are a key to realize an environment-friendly alternative process instead of the Haber−Bosch process for NH_3 production under mild reaction conditions.

1.3.3 NH_3 synthesis using transition metal complexes

Toward the development of N_2 activation method under mild condition, many chemists have engaged in studying on various transition-metal N_2 complexes so far.[16,17,18] Notably, the Mo-N_2 and W-N_2 complexes supported with four monodentate phosphines as ligands, which achieved a stoichiometric conversion of the coordinated N_2 into NH_3 by treatment with strong acid such as sulfuric acid, have energetically been studied.[19,20] The reaction utilizing change in the oxidation states of Mo(0) to Mo(IV) is known as Chatt cycle.[21] In 2003, Yandulov and Schrock reported that a catalytic conversion of N_2 into NH_3 was achieved by using Mo(III) supported with trisamidoamine ligand with sterically bulky substituent groups as the catalyst.[22] The structure of catalysts is shown in Figure 1-2. The catalytic reaction gave 8 equiv. of NH_3 per Mo ion by using decamethylchromocene ($CrCp_2$*) as a reducing agent and 2,6-lutidinium tetrakis[3,5-bis(trifluoromethyl)phenylborate] ([LutH]BAr_4F; ArF = 3,5-bis(trifluoromethyl)phenyl)) as a proton source with the catalyst.[22] In the Schrock cycle, the catalytic reaction is accompanied by change in the oxidation state of Mo(III) to Mo(VI) by the stepwise protonation and reduction.[23]

In 2011, Nishibayashi and co-workers reported the catalytic conversion of N_2 into NH_3 by using Mo complexes supported with PNP-type pincer (2,6-bis(di-tert-butylphosphinomethyl)pyridine)) ligand (Figure 1-2).[24] Although in the initial report, the TON was ca. 12 equiv. of NH_3 per Mo atoms, the tuning of the ligand and reaction conditions improved the catalytic activity up to 415 equiv.[11(d),25] From both of theoretical and experimental studies, some catalytic reaction pathways, such as the stepwise protonation and reduction for the coordinated N_2 and the protonation to the Mo-nitride complex via directly N≡N bond cleavage, are proposed.

Although these studies show catalytic NH_3 synthesis under 1 atm at r.t., more improvement of reaction conditions are required. The energy consumption of the added protonation and reducing agent (for Schrock system, 580 kJ mol^{-1} as calculated as a 65% efficiency; for Nishibayashi system, 700 kJ mol^{-1} as 50% efficiency)[15] is not mild still as compared with the industrial and biological reactions. Moreover, the chemicals, such as protonation source and reducing agent, should be replaced by proton derived from H_2O and electron supplied from electrode using a renewable energy.

Recently, bio-inspired Fe complexes having catalytic activity for conversion of N_2 into NH_3 have also been reported by Peter's group. In that case, the Fe–N_2 complex, $[Fe(BP_3)(N_2)]^-$ ($BP_3 = B[2-(\mathit{i}Pr_2P)C_6H_4]_3$, generated NH_3 from excess amount of strong acid and reducing agent under N_2.[26] Such robust system gave larger turnover of 64 equiv. of NH_3 production at −78 °C. Interestingly, the resting state of the catalyst was detected as the Fe-N_2 hydride species that was proposed as the active intermediate of the nitrogenase enzyme.[26(b)] In this way, the study of N_2 fixation by transition metal complex is also useful in understanding the biological N_2 fixation.

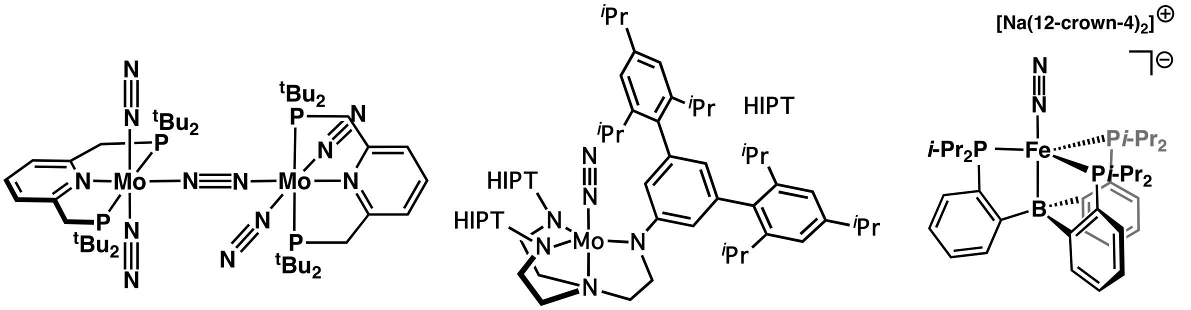

Figure 1-2. Molecular catalysts for N_2 fixation reported by (a) Nishibayashi *et al.*, (b) Schrock *et al.* and (c) Peters *et al.*.

1.3.4 Electrochemical NH_3 synthesis at room temperature under 1 atm

As described above, NH_3 is promised as energy storage media for next renewable ones, therefore, the development of efficient electrochemical NH_3 synthesis is prospective. So far, numerous researchers have studied the electrochemical NH_3 synthesis under high temperature and pressure conditions under N_2. There, however, are few reports on the electrochemical NH_3 generation from N_2 and H_2O at r.t. and 1 atm (Figure 1-3).

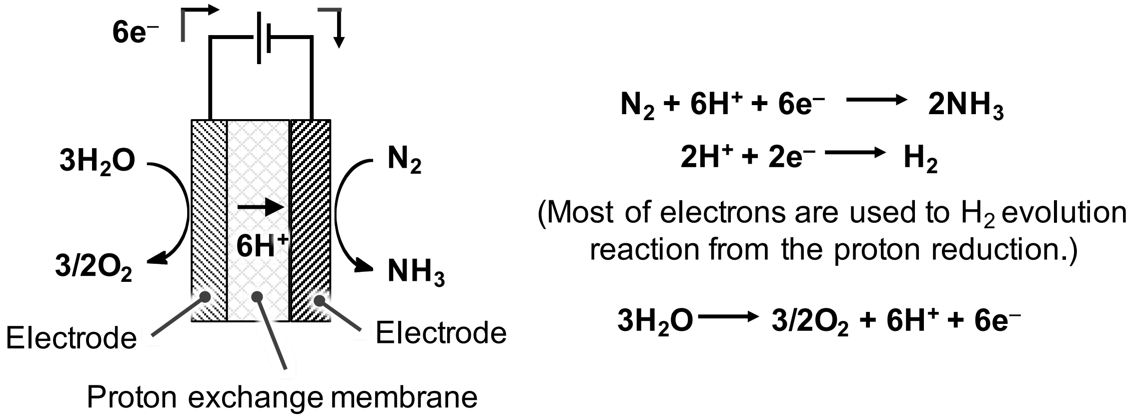

Figure 1-3. Schematic drawing of electrochemical synthesis of NH_3 using proton exchange membrane.

In the case of using heterogeneous catalyst as the electrode, the electrochemical reaction proceeds in a solid polymer electrolyte (SPE) cell with the proton exchange membrane and the gas diffusion electrode. For example, Kyriacou and co-workers reported the electrochemical NH_3 synthesis derived from N_2 and H_2O in SPE cell using a Ru/C cathode by gas diffusion electrode as the working electrode (WE).[27] in this system, the proton generated in the oxidation of H_2O at the counter electrode reacted with N_2 at WE, and its current efficiency was 0.28% at 20 °C when the controlled-potential electrolysis was performed at −1.10 V (vs. Ag/AgCl). The rate of NH_3 generated was 0.21 μg•h^{-1}cm^{-2}. The standard potential for the N_2 reduction to NH_3, as calculated from the Nernst equation, was reported to be −0.88 V (vs. Ag/AgCl).[27] The conversion of N_2 to NH_3 in their experiments was carried out from −0.96 V, which is slightly higher (by 0.08 V) than the calculated value (−0.88 V (vs. Ag/AgCl)). Recently, Tao and co-workers reported the direct synthesis of NH_3 from air and H_2O at r.t. and 1 atm by using Pt/C electrode in SPE cell.[28] The current efficiency was ca. 0.2 % by applying the voltage at 1.6 V.

The electrochemical NH_3 synthesis by using transition metal complexes under mild conditions have also been reported by Pickett and co-worker first in 1985, which was carried out through protonation to *trans*-$[W(N_2)_2(dppe)_4]$ at r.t.[29] The reaction was proceeded in THF containing $[NBu_4][BF_4]$ in the controlled-potential electrolysis at −2.6 V (vs. Fc/Fc$^+$) on Hg-pool electrode. Besides, Becker and co-workers reported the electrochemical reduction of $[Cp_2TiCl_2]$ in H-type cell under N_2 atmosphere to generate NH_3. The current efficiency was 0.28% in MeOH containing 0.1 M $LiClO_4$ as electrolyte by using Pt electrode in the controlled potential electrolysis at −2.2 V (vs. Ag wire).[30]

Though these reactions proceeded in low current efficiency, it would be improved if the experimental conditions were optimized by changing the H-type cell to SPE cell that the proton derived from H_2O was used and the gas diffusion electrode was introduced for efficient supply of N_2 gas. In addition, they required a large amounts of energy, because the energy required for activations of *cis*-$[W(N_2)_2(PMe_2Ph)_4]$ and $[Cp_2TiCl_2]$ is higher than heterogeneous catalysts, such as Ru and Pt electrodes. Therefore, the electrochemical NH_3 synthesis by using transition metal complexes without consuming large amounts of energy is extremely challenging theme. In addition to the fundamental understanding of the reduction of N_2 in the protonation, it requires development of new catalytic systems.

1.4 Ionic liquid

As a breakthrough method of conversion of N_2 into NH_3, we have paid attention to ionic liquid (ILs), because the reactions in ILs are different from those in conventional solvents. In this session, we describe their physical properties and small molecule activation reactions in ILs to refer to our purpose in this thesis.

1.4.1 Property of ionic liquid[31]

An IL is a salt composed of organic cation and anion in the liquid state. The following typical structures are studied as the cation parts of ILs; (a) imidazolium, (b) pyridinium, (c) pyrrolidinium, (d) ammonium, and (e) phosphonium types, as shown in Figure 1-4. Although the substituent groups around N or P atom are basically constructed by alkyl groups, they are tunable by changing the length of alkyl chains and introducing various functional groups. The control of structures affects their physical properties, such as viscosity, melting point, and so on. Thus, ILs are called as “designable solvent”. A positive electric charge in (a) or (b) is delocalized on the aromatic rings, while that in (c), (d) and (e), which are non-aromatic type, is localized on N or P atom. Thus, the physical property for (a) and (b) is somewhat different from those in (c), (d) and (e). Typical anions of ILs, which are mainly inorganic compound, are summarized in Figure 1-4 ((f), (g), (h), and (i)). In ILs containing a halogen anion, they have higher melting points, viscosity, and hydrophilicity as compared with other ILs. These types of ILs were firstly paid attention, because cellulose was dissolved in [C_4mim]Cl. BF_4^- and PF_6^- anions are also often used as anion of ILs. However, they generate a small amount of HF due to hydrolysis by mixing with H_2O. The IL containing [NTf_2] anion is hydrophobic, which shows low melting point and viscosity. This is because their anions are flexible for rotation of CF_3-SO_2- group around N atom by delocalization of negative charge.

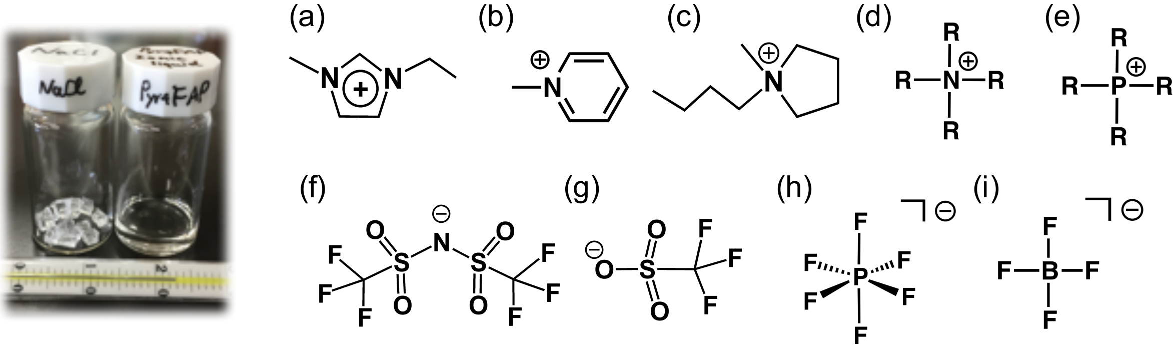

Figure 1-4. A photo of IL (left) and chemical structures of cation and anion parts of ILs (right); for the cation part, (a) imidazolium, (b) pyridinium, (c) pyrrolidinium, (d) ammonium, and (e) phosphonium cations (R = alkyl group), and for the anion part, (f) bis(trifluoromethanesulfonyl)imide, (g) trifluorometansulfonate, (h) hexafluorophosphate, and (i) tetrafluoroborate.

Characteristic physical property of IL is summarized as follows.

i) A low melting point and difficulty of crystallization

The physical properties of low melting point and difficult crystallization are derived from the steric hindrance of ions, the delocalization of the charges and the asymmetric character in the structures of ions.

ii) A low vapor pressure

The physical property of low vapor pressure is different from those of ordinary solvents. The non-volatility brings about a great merit especially when using as reaction field under vacuum condition.

iii) A wide range of electrochemical window

In aprotic IL, the stabilities in the reduction and oxidation depend on the kinds of cations and anions, respectively. In the reduction reaction, aliphatic type cations such as pyridinium and ammonium are more stable than aromatic cations such as imidazolium and pyrridinium.

iv) Viscosity

Viscosity is very important factor when using as a solvent. The viscosity of IL is more than 100 times as high as H_2O and other organic solvents on the account of working electrostatic interaction among ions. In the case of using as electrolyte and reaction solvent, the low viscosity is preferred due to reduction in the diffusion constant.

v) High ionic conductivity and thermal stability[31(e)]

Ionicity is affected by both of the Lewis basicity of anions and the Lewis acidity of cations and the van der Waals forces between them. Increase in their parameters lead to decrease in ionicity of ILs. Typical IL is constructed of quite low Lewis basicity and Lewis acidity. Therefore, their coordination abilities are very low. Although the electrostatic interaction among their ion pairs is estimated to be ca. 80 kcal/mol, which competes with those of covalent bonds (single bond: 50-100 kcal/mol), each ion is dissociated. Accordingly, low vaporization and high ionic conductivity bring about high thermal stability.

vi) Nanostructure organized by polar and non-polar domain[31f, 31g]

The nanostructure of ILs are organized by polar domain, which is constructed of ionic parts, and non-polar domain, which is constructed of hydrophobic alkyl groups.[31h] The electric permittivity (ε), therefore, is locally different. For instance, in the case of 1-butyl-3-methylimidazolium hexafluorophosphate, [C_4mim][PF_6], the total dielectric permittivity has been reported to be ca 14.0 Debye,[31i] but those in nonpolar and polar domains have been reported as ca. 2.5 and 20 Debye, respectively.[31g]

1.4.2 Small molecule activation reaction in ionic liquids

Small molecule activation reactions in ILs have also been a hot research topic.[32] For example, the reduction of CO_2 to CO by Ag electrode in 1-ethyl-3methylimidazolium tetrafluoroborate, [EMIM]BF_4, is achieved at low overpotential due to the electrostatic interaction between the one-electron reduced CO_2 intermediate and imidazolium ring.[33] Regarding the reduction of $O_{2,}$ the reversible one electrochemical reduction and oxidation are observed by cyclic voltammetry, even though the phosphonium-type IL contains H_2O. This specific behavior is also attributed to the stabilization by electrostatic interaction in IL.[34]

The catalytic electrochemical conversion of CO_2 to CO by *fac*-[ReCl(2,2'-bipyridine)$(CO)_3$] in 1-ethyl-3-methylimidazolium tetracyanoborate,

[emim][TCB] was achieved at lower overpotential (−1.74 V vs. Fc/Fc$^+$) than that in acetonitrile (−2.11 V vs. Fc/Fc$^+$). The mechanism has been proposed as follows; the interaction between imidazolium cation and two-electron reduced Re complex promotes the rapid dissociation of chloride and the decrease in the activation energy for CO_2 reduction.[35]

Numerous studies involving small molecule activation reactions by transition metal complexes in ILs have been reported[36] and they revealed that the ILs interact with substrates through the electrostatic interaction. However, the reduction of N_2 to NH_3 by using transition metal complex in ILs have never been reported yet.

1.5 Purpose of this study

The purpose of this study is (i) to construct the electrochemical conversion system for N_2 to NH_3 by using transition metal complexes under mild conditions in ILs and (ii) to evaluate the effect of ILs toward formation of transition metal-N_2 complexes. As described in the session 1.4.2, small molecule activation reactions, such as CO_2 and O_2, in ILs have been studied previously. However, the N_2 reduction by transition metal complexes and the evaluation of transition metal-N_2 complexes in the ILs have never been reported before. Therefore, we have evaluated that the N_2 molecule coordinated to a transition metal complex in IL would affect to the reactivity by its electrostatic interaction and the reactivity in the IL would be different from those in conventional organic solvents.

1.6 Chapter summaries

On the basis of the above-mentioned backgrounds, the construction of the electrochemical conversion system from N_2 and proton derived from H_2O to NH_3 using transition metal complexes in ILs under mild conditions and the evaluation of the effect of ILs toward transition metal-N_2 complex have been described as below.

In Chapter 2, the electrochemical NH_3 synthesis by using titanocene dichloride, $[Cp_2TiCl_2]$, in the ILs in solid polymer electrolyte (SPE) cell is described based on the results of the electrochemical redox reaction of $[Cp_2TiCl_2]$ in ILs. To carry out the electrochemical reaction, a SPE cell having a proton exchange membrane and a gas diffusion electrode coated with ILs containing $[Cp_2TiCl_2]$ has been designed and fabricated. The electrochemical NH_3 synthesis in the SPE cell resulted in higher NH_3 production than that in THF solution in H-type cell. Moreover, to confirm that the generation of NH_3 in the electrochemical reaction has been derived from N_2 gas, the isotopic labeling experiment has also been performed. Furthermore, the electrochemical NH_3 production in non-coordinating IL has been compared with that in coordinating IL. It indicated that the efficiency of the NH_3 synthesis in non-coordinating IL has been higher than that in coordinating IL.

In Chapter 3, N_2 coordination by titanocene monochloride, $[Cp_2TiCl]$, in ILs are described in addition to the evaluation of electrochemical reduction of $[Cp_2TiCl_2]$ in ILs by using UV/vis/NIR spectroscopy. UV-vis/NIR spectral changes of $[Cp_2TiCl_2]$ during the electrochemical reduction clearly suggest that dimeric species, $[(Cp_2TiCl)_2]$, are generated via formation of monomeric $[Cp_2TiCl]$ even in non-coordinating IL. To confirm whether an equilibrium reaction between dimeric $[(Cp_2TiCl)_2]$ and monomeric $[Cp_2TiCl]$ in IL exists or not, the frozen solution EPR spectroscopy of $[(Cp_2TiCl)_2]$ in ILs under N_2 was measured. Surprisingly, the hyperfine splitting derived from N_2 coordination to [Cp_2TiCl] was detected only in IL. The effect of ILs toward [Cp_2TiCl] was evaluated using DFT calculations, and we concluded that the polar domain in non-coordinating IL promoted the N_2 coordination to [Cp_2TiCl] due to complex formation with anion parts of IL through the weak interaction.

In Chapter 4, the electrochemical oxidation reaction of molybdenum(0)-N_2 complex supporting with bidentate phosphine ligands in ILs is described. To consider the effect of the ILs, the electrochemical oxidation reaction of molybdenum(0)-N_2 complex in organic solvents is also evaluated. Resonance Raman, FT-IR and UV-vis/NIR spectroscopic studies during the electrochemical oxidation reaction and their evaluation by DFT and TDDFT calculations have revealed that the subsequent reaction after the electrochemical oxidation reaction proceeded to form the dimeric structure, Mo(II)-N_2-Mo(II). On the other hand, a mononuclear Mo(I)-N_2 complex is stabilized due to weak interaction between F atoms of anion in IL and H atoms on ethyl group in the depe ligand during the oxidation process, which suppressed the formation of the dimeric structure

In Chapter 5, the conclusion in this thesis is described and the perspective for the reactivity of transition metal complexes in ILs are stated.

1.7 References

1. S. Giddey, S. P. S. Badwal, A. Kulkarni, *Int. J. Hydrogen Energ.*, **2013**, *38*, 14576.
2. J. H. Montoya, C. Tsai, A. Vojvodic, J. K. Norskov, *ChemSusChem.*, **2015**, 8, 2180.
3. G. Thomas and G. Parks, Potential Roles of Ammonia in a Hydrogen Economy A

Study of Issues Related to the Use Ammonia for On-Board Vehicular Hydrogen Storage, U.S. Department of Energy, 2006, <https://www.hydrogen.energy.gov/pdfs/nh3_paper.pdf>

4. A. Valera-Medina, R. Marsh, J. Runyon, D. Pugh, P. Beasley, T. Hughes, P. Bowen, *Applied Energy,* **2017**, *185*, 1362.
5. D. Miura and T. Tezuka, *Energy*, **2014**, *68*, 428.
6. <http://criepi.denken.or.jp/press/pressrelease/2017/01_10press.pdf>, 10 Jan 2017, Press in central research institute of electric power industry.
7. R. F. Service, *Science*, **2014**, *345*, 610.
8. V. Kyriakou, I. Garagounis, E. Vasileiou, A. Vourros, M. Stoukides, *Catal. Today*, **2017**, *286*, 2.
9. Liu, H. Ammonia Synthesis Catalysts; Chemical Industry Press & World Scientific: Singapore, 2013.
10. (a) C. J. M. van der Ham, M. T. M. Koper, D. G. H. Hetterscheid, *Chem. Soc. Rev.,* **2014**, *43*, 5183. (b) M. Appl, Ullmann's Encyclopedia of Industrial Chemistry, Wiley-VCH Verlag GmbH & Co. KGaA, 2006
11. (a) I. Rafiqul, C. Weber, B. Lehman, A. Voss, *Energy*, **2005**, *30*, 2487. (b) N. Gruber, J. N. Galloway, *Nature*, **2008**, *451*, 293. (c) Annual Energy Outlook 2012: with Projections to 2035; U.S. Energy Information Administration: Washington, DC, 2012. (d) Y. Nishibayashi, *Inorg. Chem.*, **2015**, *54*, 9234.
12. (a) B. M. Hoffman, D. Lukoyanov, Z. Yang, D. R. Dean, and L. C. Seefeldt, *Chem. Rev.*, **2014**, *114*, 4041. (b) T. Spatzal, M. Aksoyoglu, L. Zhang, S. L. A. Andrade, E.

Schleicher, S. Weber, D. C. Rees, O. Einsle, *Science*, **2011**, *334*, 940. (c) K. M. Lancaster, M. Roemelt, P. Ettenhuber, Y. Hu, M. W. Ribbe, F. Neese, U. Bergmann, S. DeBeer, *Science*, **2011**, *334*, 974. (d) K. M. Lancaster, Y. Hu, U. Bergmann, M. W. Ribbe, S. DeBeer, *J. Am. Chem. Soc*., **2013**, *135*, 610. (e) J. A. Wiig, Y. Hu, C. C. Lee, M. W. Ribbe, *Science*, **2012**, *337*, 1672.

13. (a) K. Aika, *Angew. Chem. Int. Ed.*, **1986**, *25*, 558. (b) R. R. Eady, B. E. Smith in R. W. F. Hardy, F. Bottomley, R. C. Burns (Eds.): A Treatise on Dinitrogen Fixation. Sections 1 and 2. Wiley. New York 1979, p. 466.
14. (a) S. Wherland, B. K. Burgess, E. I. Stiefel and W. E. Newton, *Biochemistry*, **1981**, *20*, 5132. (b) B. K. Burgess, S. Wherland, W. E. Newton and E. I. Stiefel, *Biochemistry*, **1981**, *20*, 5140.
15. C. J. M. van der Ham, M. T. M. Koper and D. G. H. Hetterscheid, *Chem. Soc. Rev.*, **2014**, *43*, 5183.
16. A. D. Allen, C. V. Senoff, *Chem. Commun*., **1965**, 621.
17. (a) S. Hinrichsen, H. Broda, C. Gradert,; L. Söncksen, F. Tuczek, *Annu. Rep. Prog. Chem. Sect. A: Inorg. Chem*., **2012**, *108*, 17. (b) Y. Nishibayashi, *Dalton Trans*., **2012**, *41*, 7447. (c) K. C. MacLeod, P. L. Holland, *Nat. Chem*., **2013**, *5*, 559. (d) M. D. Fryzuk, *Chem. Commun*., **2013**, *49*, 4866. (e) Y. Tanabe, Y. Nishibayashi, *Coord. Chem. Rev*., **2013**, *257*, 2551. (f) H.-P. Jia, E. A. Quadrelli, *Chem. Soc. Rev*., **2014**, *43*, 547. (g) C. Köthe, C. Z. Limberg, *Anorg. Allg. Chem*., **2015**, *641*, 18. (h) N. Khoenkhoen, B. de Bruin, J. N. H. Reek, W. I. Dzik, *Eur. J. Inorg. Chem*., **2015**, 567. (i) S. F. McWilliams, P. L. Holland, *Acc. Chem. Res.*, **2015**, *48*, 2059. (j) R. J.

Burford and M. D. Fryzuk, *Nat. Chem. Rev.*, **2017**, *1*, 1.

18. (a) T. Shima, S. Hu, G. Luo, X. Kang, Y. Luo, Z. Hou, *Science,* **2013**, *340*, 1549. (b) S. P. Semproni, P. J. Chirik, *J. Am. Chem. Soc*., **2013**, *135*, 11373. (c) M. T. Mock, S. Chen, M. O'Hagan, R. Rousseau, W. G. Dougherty, W. S. Kassel, R. M. Bullock, *J. Am. Chem. Soc*., **2013**, *135*, 11493. (d) T. Miyazaki, Y. Tanabe, M. Yuki, Y. Miyake, K. Nakajima, Y. Nishibayashi, *Chem.—Eur. J.*, **2013**, *19*, 11874. (e) I. Klopsch, M. Finger, C. Würtele, B. Milde, D. B. Werz, S. Schneider, *J. Am. Chem. Soc*., **2014**, *136*, 6881. (f) A. J. Keane, B. L. Yonke, M. Hirotsu, P. Y. Zavalij, L. R. Sita, *J. Am. Chem. Soc*., **2014**, *136*, 9906. (g) K. C. MacLeod, D. J. Vinyard, P. L. Holland, *J. Am. Chem. Soc*., **2014**, *136*, 10226. (h) J. Rittle, C. C. L. McCrory, J. C. Peters, *J. Am. Chem. Soc*., **2014**, *136*, 13853. (i) Y. Ishida, H. Kawaguchi, *J. Am. Chem. Soc.,* **2014**, *136*, 16990. (j) T. Miyazaki, H. Tanaka, Y. Tanabe, M. Yuki, K. Nakajima, K. Yoshizawa, Y. Nishibayashi, *Angew. Chem. Int. Ed*., **2014**, *53*, 11488. (k) G. W. Margulieux, Z. R. Turner, P. J. Chirk, *Angew. Chem. Int. Ed*., **2014**, *53*, 14211. (l) C. Gradert, N. Stucke, J. Krahmer, C. Näther, F. Tuczek, *Chem.—Eur. J.*, **2015**, *21*, 1130. (m) Y. Lee, F. T. Sloane, G. Blondin, K. A. Abboud, R. García-Serres, L. J. Murray, *Angew. Chem. Int. Ed*., **2015**, *54*, 1499. (n) I. Pappas and P. J. Chirik, *J. Am. Chem. Soc*., **2015**, *137*, 3498.
19. (a) J. Chatt, A. J. Pearman, R. L. Richards, *Nature,* **1975**, *253*, 39. (b) J. Chatt, A. J. Pearman, R. L. Richards, *J. Chem. Soc., Dalton Trans*., **1977**, 1852.
20. T. Takahashi, Y. Mizobe, M. Sato, Y. Uchida, M. Hidai, *J. Am. Chem. Soc*., **1979**, *101*, 3405.

21. (a) J. Chatt, R. L. Richard, *J. Organomet. Chem*., **1982**, *239*, 65. (b) C. J. Pickett, *J. Biol. Inorg. Chem*., **1996**, *1*, 601. (c) F. Tuczek, K. H. Hom, N. Lehnert, *Coord. Chem. Rev.,* **2003**, *245*, 107.
22. (a) D. V. Yandulov, R. R. Schrock, *Science,* **2003**, *301*, 76. (b) V. Ritleng, D. V. Yandulov, W. W. Weare, R. R. Schrock, A. S. Hock, W. M. Davis, *J. Am. Chem. Soc*., **2004**, *126*, 6150. (c) R. R. Schrock, *Acc. Chem. Res*., **2005**, *38*, 955. (d) W. W. Weare, X. Dai, M. J. Byrnes, J. M. Chin, R. R. Schrock, P. Müller, *Proc. Natl. Acad. Sci. U.S.A*., **2006**, *103*, 17099. (e) R. R. Schrock, Angew. Chem. Int. Ed., **2008**, *47*, 5512.
23. (a) R. L. McNaughton, M. Roemelt, J. M. Chin, R. R. Schrock, F. Neese and B. M. Hoffman, *J. Am. Chem. Soc*., **2010**, *132*, 8645. (b) R. A. Kinney, R. L. McNaughton, J. M. Chin, R. R. Schrock and B. M. Hoffman, *Inorg. Chem*., **2011**, *50*, 418. (c) R. R. Schrock, *Angew. Chem. Int. Ed*., **2008**, *47*, 5512. (d) S. Schenk, B. L. Guennic, B. Kirchner and M. Reiher, *Inorg. Chem*., **2008**, *47*, 3634.
24. K. Arashiba, Y. Miyake and Y. Nishibayashi, *Nat. Chem*., **2011**, *3*, 95.
25. K. Arashiba, A. Eizawa, H. Tanaka, K. Nakajima, K. Yoshizawa, and Y. Nishibayashi, *Bull. Chem. Soc. Jpn.*, **2017**, *90*, 1111.
26. (a) J. S. Anderson, J. Rittle and J. C. Peters, *Nature*, **2013**, *501*, 84. (b) T. J. D. Castillo, N. B. Thompson, and J. C. Peters, *J. Am. Chem. Soc*., **2016**, 138, 5341.
27. V. Kordali, G. Kyriacou and Ch. Lambrou, *Chem. Commun.,* **2000**, 1673.
28. R. Lan, J. T. S. Irvine and S. Tao, *Sci. Rep.*, **2013**, *3*, 1145.
29. C. J. Pickett and J. Talarmin, *Nature*, **1985**, *317*, 652.

30. J. Y. Becker, S. Avraham and B. Posin, *J. Electroanal. Chem.,* **1987**, *230*, 143.

31. (a) P. Hapiot and C. Lagrost, *Chem. Rev.*, **2008**, *108*, 2238. (b) M. Armand, F. Endres, D. R. MacFarlane, H. Ohno and B. Scrosati, *Nat. Mater.*, **2009**, *8*, 621. (c) F. V. Rantwijk and R. A. Sheldon, *Chem. Rev.*, **2007**, *107*, 2757. (d) J. P. Hallett and T. Welton, *Chem. Rev.*, **2011**, *111*, 3508. (e) S. Tsyzuki, H. Tokuda, K. Hayamizu, M. Watanabe, *J. Phys. Chem. B*, **2005**, *109*, 16474. (f) O. Yamamuro, T. Yamada, M. Kofu, M. Nakakoshi and M. Nagao, *J. Chem. Phys.*, **2011**, *135*, 054508. (g) M. Mizoshiri, T. Nagao, Y. Mizoguchi and M. Yao, *J. Chem. Phys.*, **2010**, *132*, 164510. (h) J. N. A. C. Lopes and A. A. H. Pádua, *J. Phys. Chem. B*, **2006**, *110*, 3330. (i) M. Huang, Y. Jiang, P. Sasisanker, G. W. Driver, and H. Weingärtner, *J. Chem. Eng. Data*, **2011**, *56*, 1494.

32. C. D. Hubbard, P. Illner and R. V. Eldik, *Chem. Soc. Rev.*, **2011**, *40*, 272.

33. (a) B. A. Rosen, A. S. Khojin, M. R. Thorson, W. Zhu, D. T. Whipple, P. J. A. Kenis and R. I. Masel, *Science*, **2011**, *334*, 643. (b) B. A. Rosen, J. L. Haan, P. Mukherjee, B. Braunschweig, W. Zhu, A. S. Khojin, D. D. Dlott and R. I. Masel, *J. Phys. Chem. C*, **2012**, *116*, 15307.

34. C. Pozo-Gonzalo, A. A. J. Torriero, M. Forsyth, D. R. MacFarlane, and P. C. Howlett, *J. Phys. Chem. Lett.*, **2013**, *4*, 1834.

35. (a) D. C. Grills, Y. Matsubara, Y. Kuwahara, S. R. Golisz, D. A. Kurtz, and B. A. Mello, *J. Phys. Chem. Lett.,* **2014**, *5*, 2033. (b) Y. Matsubara, D. C. Grills and Y. Kuwahara, *ACS Catal.*, **2015**, *5*, 6440.

36. (a) M. Schmeisser and R. van Eldik, *Inorg. Chem.*, **2009**, *48*, 7466. (b) S. Kern, R.

van Eldik, *Inorg. Chem.*, **2012**, *51*, 7340. (c) M. Schmeisser, F. W. Heinemann, P. Illner, R. Puchta, A. Zahl, and R. van Eldik, *Inorg. Chem.*, **2011**, *50*, 6685. (d) S. Begel, F. W. Heinemann, G. Stopa, G. Stocheland, R. van Eldik, *Inorg. Chem.*, **2011**, *50*, 3946. (e) S. Begel, P. Illner, S. Kern, R. Puchta, and R. van Eldik, *Inorg. Chem.*, **2008**, *47*, 7121. (f) P. Illner, S. Begel, S. Kern, R. Puchta, and R. van Eldik, *Inorg. Chem.*, **2009**, *48*, 588. (g) K. Pokornv, M. Schmeisser, F. Hampel, A. Zahl, R. Puchta, and R. van Eldik, *Inorg. Chem*., **2013**, *52*, 13167. (h) S. Begel, R. Puchta, J. Sutter, F. W. Heinemann, L. Dahlenburgand, and R. van Eldik, *Inorg. Chem.*, **2015**, *54*, 6763. (i) C. Sievers, O. Jimenez, T. E. Müller, S. Steuernagel, and J. A. Lercher, *J. Am. Chem. Soc.*, **2006**, *128*, 13990.

Chapter 2: Electrochemical ammonia synthesis by using titanocene in ionic liquid

2.1 Introduction

Numerous researchers in various chemical fields have investigated electrochemical NH_3 synthesis under mild conditions.[1] The electrochemical synthesis of NH_3 by using transition metal complex is one of the promising methods because the reaction can proceed under mild conditions.[2,3] As well as development of the catalyst,[4] we must rethink the reaction conditions to achieve more efficient synthesis of NH_3. Disadvantages of the electrochemical NH_3 synthesis by using transition metal complexes are inefficient supply of N_2 gas in ordinary electrolysis cell such as H-type cell using hydrogen source derived from fossil fuel. For example, Becker and co-workers reported previously that titanocene dichloride, $[Cp_2TiCl_2]$, could convert N_2 into NH_3 when the controlled potential electrolysis (CPE) was carried out at −2.2 V (vs. Ag wire) in MeOH solution containing 0.3 M $LiClO_4$ and 0.25 M catechol.[3] Although the reaction proceeds at r.t. under 1 atm using hydrogen source from catechol and/or MeOH, the yield of NH_3 per $[Cp_2TiCl_2]$ and the current efficiency were quite low (1.45% and 0.28 %, respectively). To improve the bottleneck, we paid attention to the electrochemical synthesis of NH_3 in solid polymer electrolysis (SPE) cell.

As described on the electrochemical NH_3 synthesis in SPE cell in Section 1.3.4,[1d] a proton generated by oxidation of H_2O at the counter electrode (CE) was transferred to the working electrode (WE) and it reacts with N_2.[1d] It has advantages that the proton originating from H_2O oxidation is employed and the generated O_2 is separated from the WE by proton exchange membrane.

Electrochemical NH_3 synthesis by using a transition metal complex on gas-diffusion electrode in SPE cell would achieve the highly conversion of N_2 to NH_3 because the supplying of N_2 gas is improved compared with that in the H-type electrolysis cell. Hence, we considered that an ionic liquid (IL) would be applied as the supporting material of transition metal complex on gas-diffusion electrode in SPE cell.

ILs that are salts in a liquid state at r.t. have recently been employed in a number of different research efforts, because they have several unique properties such as low volatility, an electrochemical window, high thermal and chemical stability, and electric conductivity, as described in Section 1.4.[5] In particular, 1−butyl−1−methylpyrrolidinium tris(pentafluoroethyl)trifluorophosphate (Pyr_4FAP) is appropriate for use as a supporting material because of its high stability.[6] Hence, we devised fabrication of the WE by coating the Pyr_4FAP supported with a transition metal complex on the gas diffusion electrode.

Regarding the transition metal complex, $[Cp_2TiCl_2]$, group 4 metallocene, was chosen. Group 4 metallocenes have been widely studied because they have a coordinating ability toward N_2 molecule.[4c-f] In addition, since the characteristic of $[Cp_2TiCl_2]$ in organic solvents has been investigated and well-known, the redox behavior of $[Cp_2TiCl_2]$ in ILs will be able to easily evaluate.[7] To consider the influence of the coordinating ability of ILs to the reactivity, the electrochemical NH_3 synthesis is also performed not only in Pyr_4FAP as non-coordinating IL but also in 1-butyl-1-methylpyrrolidinium triflate (Pyr_4OTf) as coordinating IL, as shown in Figure 2-1. Here, we report the electrochemical reduction of N_2 to NH_3 using a WE coated with a transition metal complex-supported ILs in the SPE cell under ambient conditions.

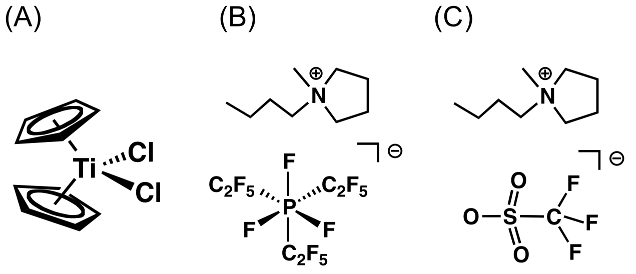

Figure 2-1. The structures of titanocene complexes, (A) [Cp_2TiCl_2] and ILs, (B) Pyr_4FAP, and (C) Pyr_4OTf.

2.2 Results and Discussion

2.2.1 Design and fabrication of solid polymer electrolyte cell (SPE cell)

SPE cell was fabricated as shown in Figure 2-2, which was designed by modification of the previous literature.[1d] The gas diffusion electrode is made from carbon paper coated with 10 mM [Cp_2TiCl_2]. Since WE is in the gas flow channel, N_2 gas is supplied effectively.

2.2.2 Cyclic voltammograms of [Cp_2TiCl_2] in ionic liquids with non-coordinating FAP$^-$ or coordinating OTf$^-$ anion

To understand redox potential of [Cp_2TiCl_2] in ILs, cyclic voltammetry of [Cp_2TiCl_2] in Pyr_4FAP and Pyr_4OTf were measured. The cyclic voltammograms (CVs) are shown in Figure 2-3 and the parameters obtained are summarized in Table 2-1. The redox waves of [Cp_2TiCl_2] in Pyr_4FAP, as shown in Figure 2-3(A), have oxidation and reduction waves at −1.14 and −1.06 V (vs. Fc/Fc$^+$), respectively, as a reversible redox wave ($E_{1/2}$ value: −1.10 V) assigned to the Ti(IV)/Ti(III) couple. This potential is in good agreement with the previously measured value in THF containing electrolyte,[3,8] indicating that the reaction Eq. (1) (see below) has proceeded.

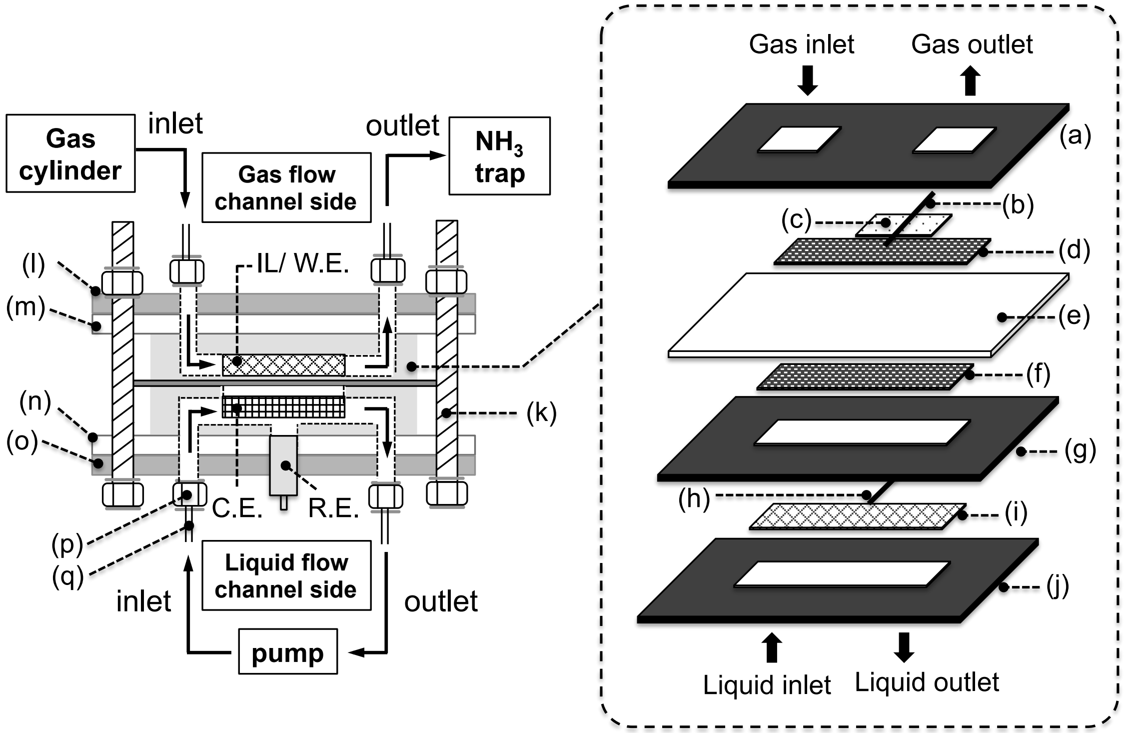

Figure 2-2. A schematic diagram of the constructed SPE cell (left) and the internal structure of electrolysis cell (right); (a) gasket (30 mm (D) × 55 mm (W) × 1 mm (H)), (b) Cu wire, (c) parafilm (10 mm (D) × 10 mm (W)), (d) carbon paper (TORAY, TGP–H–120) as the working electrode (10 mm (D) × 20 mm (W) × 0.37 mm (H)) coated with 50 μL of IL containing 10 mM [Cp_2TiCl_2], (e) Nafion®212 membrane, (f) carbon paper (10 mm (D) × 20 mm (W) × 0.37 mm (H)) that is used as support to bind membrane, (g) gasket, (h) Pt wire, (i) Pt mesh as the counter electrode, (j) gasket, (k) bolt, (l) aluminum plate (70 mm (D) × 50 mm (W) × 5 mm (H)), (m) polytetrafluoroethylene (PTFE) plate (70 mm (D) × 50 mm (W) × 5 mm (H)), (n) PTFE plate that has a hole (1/4 28UNF) at the center to screw the reference electrode, (o) aluminum plate that has a hole (1.2 cm diameter) at the center, (p) teflon connector, and (q) silicon tube (1 mm diameter). The reference electrode is Ag/AgCl one (3 M NaCl aq.) that is a screw type to attach in teflon body. The inlet of gas channel is connected by gas cylinder and the outlet is connected to 10 mM HCl aqueous solution as NH_3 trap. The flow rate of gas was kept at 5 mL/min. The inlet and outlet of liquid channels are connected by pump, and the 0.2 M H_2SO_4 aqueous solution is circulated.

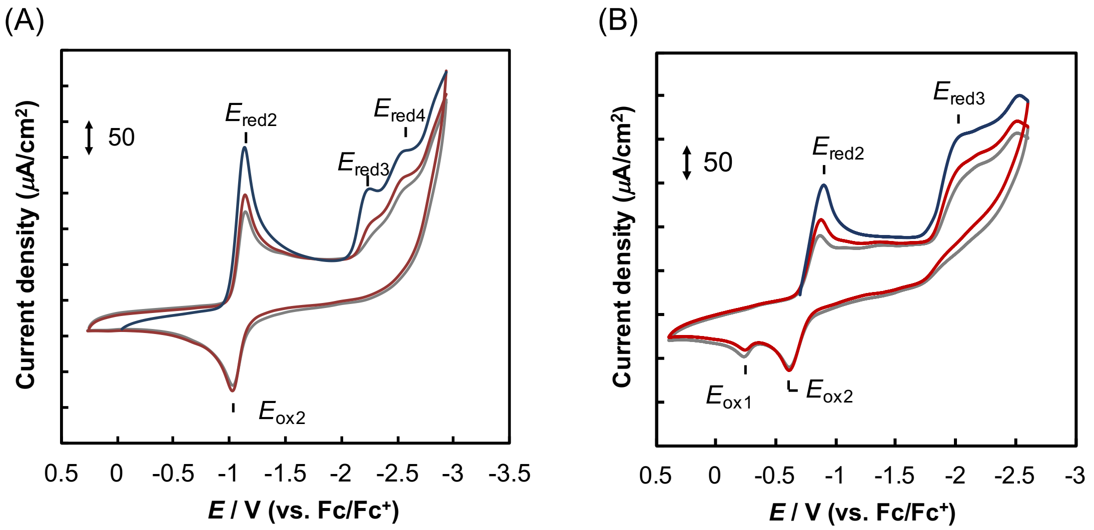

Figure 2-3. CVs of 10 mM [Cp_2TiCl_2] in (A) Pyr_4FAP and (B) Pyr_4OTf (WE: GCE (1 mm diameter), CE: Pt wire, RE:Ag/Ag^+ electrode, scan rate: 100 mV/s, 1st cycle: blue, 2nd cycle: red, and 3rd cycle: gray). The potentials were referenced to the ferrocene/ferrocenium (Fc/Fc^+) couple in Pyr_4FAP and Pyr_4OTf, respectively.

Table 2-1. Summary of redox potentials for [Cp_2TiCl_2]

Complex	**Anion of IL**	**Redox potential (V vs. Fc/Fc^+)**					
		E_{ox1}	E_{red2}	E_{ox2}	$E_{1/2}$	E_{red3}	E_{red4}
[Cp_2TiCl_2]	FAP	–	−1.14	−1.06	−1.10	−2.31	−2.54
	OTf	−0.41	−0.99	−0.76	−0.88	−2.14	–

$$[Cp_2TiCl_2] + e^- \rightleftharpoons [Cp_2TiCl_2]^- \qquad (1)$$

$$[Cp_2TiCl_2]^- \rightleftharpoons [Cp_2TiCl] + Cl^- \qquad (2)$$

$$[(Cp_2TiCl)_2] \rightleftharpoons 2\,[Cp_2TiCl] \qquad (3)$$

In more negative potential region, two irreversible reduction waves, E_{red3} and E_{red4}, were observed at −2.31 and −2.54 V (vs. Fc/Fc$^+$) in Pyr$_4$FAP, which were reduced with increase in cycles. As described in the previous literatures,[8,9] the irreversible wave at E_{red3} is attributed to Ti(III)/Ti(II) reduction. The reduced titanocene(II) is unstable and the C–H bond in cyclopentadienyl group was activated, and Ti–C bonds among titanocenes was formed. The reduction wave at E_{red4} would be derived from Ti(III)/Ti(II) reduction of the uncharacterized titanocene species.

The cyclic voltammetry of [Cp$_2$TiCl$_2$] in Pyr$_4$OTf was also measured and the CV was shown in Figure 2-3(B). The reduction and oxidation waves of [Cp$_2$TiCl$_2$] in Pyr$_4$OTf, which were assigned to Ti(IV)/Ti(III) redox couple, were observed at −0.99 and −0.76 V (vs. Fc/Fc$^+$), respectively. The $E_{1/2}$ value is −0.88 V (vs. Fc/Fc$^+$). The irreversible reduction wave observed at −2.14 V was assigned to Ti(III)/Ti(II) reduction. The oxidation wave (E_{ox1}) was observed at −0.41 V (vs. Fc/Fc$^+$), although it was not detected in Pyr$_4$FAP (Figure 2-3(A)). This oxidation wave (E_{ox1}) is explained in terms of difference in the coordination behaviors to the reduced titanocene between FAP and OTf anions. Oldham Jr. and co-workers have reported that the [Cp$_2$Ti]$^{2+}$ species is coordinated by bis(trifluoromethylsulfonyl)imide anion, [(SO$_2$CF$_3$)$_2$N]$^-$, through η^1–O binding modes.[10] Though the anion of the IL used in this study was OTf anion instead of [(SO$_2$CF$_3$)$_2$N]$^-$, the chemical property of [(SO$_2$CF$_3$)$_2$N]$^-$ are similar to that of OTf anion. Accordingly, OTf anion can coordinate to the Ti center during the electrochemical reaction and the titanocene complex coordinated with OTf anion may be generated, as shown in Figure 2-4. The oxidation wave (E_{ox1}) observed at −0.41 V originates from oxidation of [Cp$_2$TiCl(OTf)] (Ti(IV)/Ti(III)), which is the [Cp$_2$Ti]$^+$ species coordinated with [CF$_3$SO$_3$]$^-$ in the η^1-O binding mode (Figure 2-4).

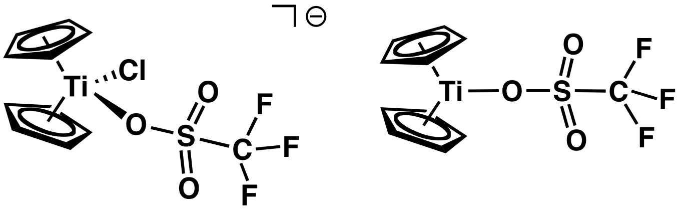

Figure 2-4. Possible structures of titanocene(III) species coordinated with OTf anion.

Previously, Daasbjerg and co-workers reported the redox behavior of [Cp_2TiX_2] (X = Cl, Br, I) in THF containing electrolyte.[11] The oxidation waves, which were derived from the generated [Cp_2TiX], were observed in the range of −0.6 to −0.9 V (vs. Fc/Fc^+) as a subsequent reaction of Eq. (1) when the Ti–X bond was cleaved to generate the monomeric species, [Cp_2TiCl] according to Eq. (2). Moreover, the monomeric species reacted each other to generate the dimeric species, [$(Cp_2TiCl)_2$], as shown in Eq. (3).[11]

To consider the dissociation reaction of the Cl anion from [Cp_2TiCl_2]$^-$, DFT calculations for [Cp_2TiCl_2]$^-$ and [Cp_2TiCl] are also carried out and the quantitative energy profile is shown in Figure 2-5. *Δ*G value of [Cp_2TiCl_2]$^-$ (1.27 kcal/mol) is higher than that of monomeric [Cp_2TiCl], indicating that monomeric [Cp_2TiCl] is more stable than [Cp_2TiCl_2]$^-$

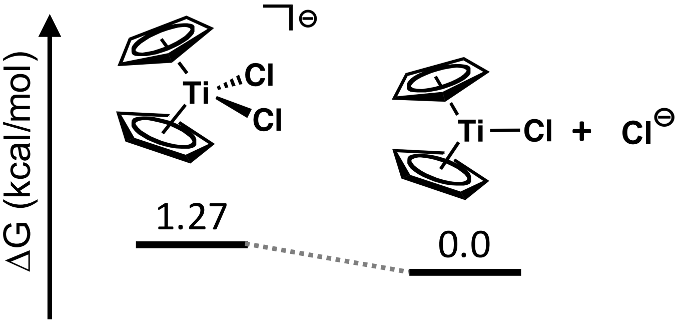

Figure 2-5. Energies estimated by DFT studies of the [Cp_2TiCl_2]$^-$ and monomeric [Cp_2TiCl] with Cl^-.

In Chapter 3, UV-vis/NIR spectra during the electrochemical reduction of [Cp_2TiCl_2] in THF, Pyr_4OTf, Pyr_4FAP, and IL are described to consider the subsequent reaction in the electrochemical reduction.

2.2.3 Linear sweep voltammograms of [Cp_2TiCl_2] in SPE cell

The linear sweep voltammograms (LSVs) of [Cp_2TiCl_2] in Pyr_4FAP in the SPE cell were investigated and the results are displayed in Figure 2-6(A) together with the results of control experiments: The LSVs were measured under N_2 and Ar atmospheres, respectively, and it without [Cp_2TiCl_2] under N_2 is also carried out for comparison. Under both N_2 and Ar atmosphere, broadened peaks were observed at –1.13 V (vs. Ag/AgCl), but no peaks were observed without [Cp_2TiCl_2]. Accordingly, it is clear that the observed peaks originate from the oxidation of Ti(IV) to Ti(III) in [Cp_2TiCl_2]. The current under N_2 is considerably greater than that under Ar. The noisy pattern in the peak is due to the generation of H_2 gas. These findings indicate that the reduced Ti(III) species reacts with N_2, accompanied by an H_2 evolution reaction.

In order to investigate the influence of coordinating anion in the electrochemical reduction of [Cp_2TiCl_2], the LSV of [Cp_2TiCl_2] in Pyr_4OTf was also carried out in SPE cell. The LSV before the CPE is shown in Figure 2-6(B). The current in the range of the −1.0 to −1.5 V (vs. Ag/AgCl) under N_2 atmosphere is larger than that under Ar atmosphere, suggesting that reduced [Cp_2TiCl_2] is reacted with N_2 even in Pyr_4OTf. Hence, the potential in the CPE was decided to carry out in the range of –1.0 to –1.5 V.

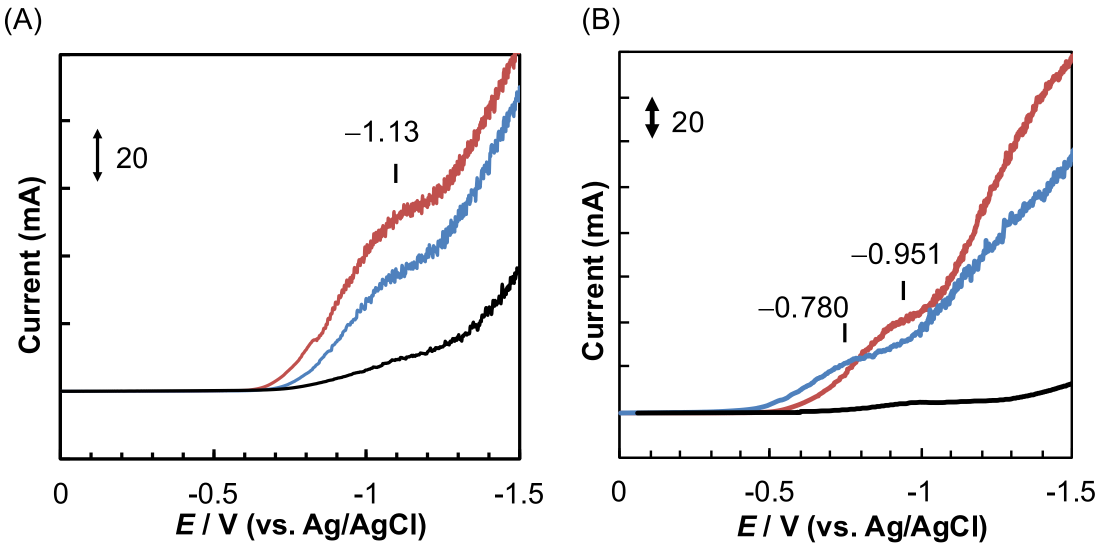

Figure 2-6. LSVs of 10 mM [Cp_2TiCl_2] in (A) Pyr_4FAP and in (B) Pyr_4OTf in SPE under N_2 (red line) and Ar (blue line) (Scan rate: 5 mV/s). Black one is carried out without [Cp_2TiCl_2].

2.2.4 Electrochemical NH_3 synthesis in Pyr_4FAP and Pyr_4OTf

Although in the CPE in the range of –1.0 V to –1.4 V (vs. Ag/AgCl), NH_3 was not detected, it was detected in the CPE at –1.5 V (vs. Ag/AgCl). The quantification of produced NH_3 was evaluated using the indophenol method.[12]

As expected, the CPE at –1.5 V under Ar did not gave NH_3 generation. Performing the CPE at −1.5 V (vs. Ag/AgCl) by using Pyr_4FAP without [Cp_2TiCl_2] under N_2 also did not give NH_3. These results indicate that the conversion of N_2 into NH_3 was occurred by [Cp_2TiCl_2] during the CPE at −1.5 V (vs. Ag/AgCl).

The plots of the yields of NH_3 per [Cp_2TiCl_2] (%) against the consumed electric charges (C) in the CPE at –1.5 V are displayed in Figure 2-7. The yield of NH_3 was found to increase gradually and the maximum yield reached ca. 27%. The yield of NH_3

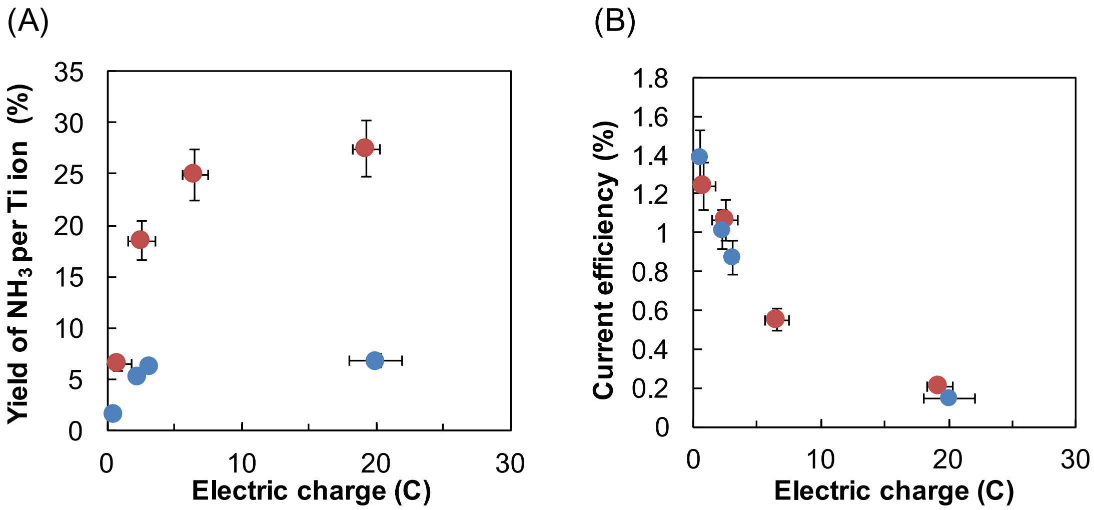

Figure 2-7. (A) Plots of NH_3 yields per Ti ion (%) against the consumed electric charge (C) and plots of current efficiency (%) (B) against the consumed electric charge (C) (blue plots: [$(Cp_2TiCl)_2$] in Pyr_4FAP, red plots: [Cp_2TiCl_2] in Pyr_4FAP, blue plots: [Cp_2TiCl_2] in Pyr_4OTf).

saturated when the 400 equiv. of electric charge (20 C, 0.2 mmol) was consumed against the amount of the used [Cp_2TiCl_2] (500 nmol). The plots of the current efficiency (%) against consumed electric charge (C) in CPE at –1.5 V (vs. AgAgCl) are displayed in Figure 2-7(B). The current efficiency (%) was found to be ca. 1.2% at the early stage in CPE with a gradual decrease to ca. 0.2% at 20 C. These results indicate that [Cp_2TiCl_2] is converted to an inactive species after the reaction, and that the consumed electric charge (C) is employed for the H_2 evolution reaction.

Hydrazine is also believed to be produced as an incomplete reduction product of nitrogen. Though the quantification of hydrazine was carried out according to the published procedure,[13] it could not be detected during the CPE. This selective formation of NH_3 is similar to that in organic solvent reported in previous literature.[3] The yield of NH_3 is much higher than the previous yield, 1.45%. Moreover, the applied potential in the electrochemical reduction, –1.5 V (vs. Ag/AgCl), is positive than that of the previous report, –2.2 V (vs. Ag wire).[3] In addition, our system, in which H_2O was used as the proton source, is carried out under milder conditions than the previous experiment which used catechol as the proton source.

Although the CPEs by using Pyr_4OTf containing 10 mM $[Cp_2TiCl_2]$ in the range of −1.0 to −1.5 V (vs. Ag/AgCl) are also conducted, the generation of the NH_3 was confirmed only in the CPE at −1.5 V (vs. Ag/AgCl). The yield per Ti atom (%) and current efficiency are shown in Figure 2-7. The maximum yields of NH_3 per Ti ion is 6.8% at 20 C, which is lower than that in Pyr_4FAP, suggesting that the coordination of OTf anion prevents the reaction. Though the current efficiency at early stage is 1.38% at 0.5 C, it gradually decreased to 0.15% at 20 C, which are similar to those in Pyr_4FAP. The quantification of H_2 was also performed, and the current efficiency was estimated to be 84% at 5.0 C under N_2 atmosphere. The quantification of hydrazine was also carried out but was not detected, which is similar to that in the case of using Pyr_4FAP.

The small molecules activation reactions by a transition metal complex in ILs have been recently reported.[5j,14,15] The reduction of CO_2 to CO by *fac*–ReCl(bpy)$(CO)_3$ (bpy = 2,2'–bipyridine) was found to lower the activation energy in the presence of ILs against the same reaction in the absence of IL.[15] This is because the IL, 1–ethyl–3–methylimidazolium tetracyanoborate, assists in the dissociation of Cl anion from the *fac*–ReCl(bpy)$(CO)_3$ and decrease the activation energy for reduction of CO_2. Accordingly, also in our system, the electrostatic interaction of the IL toward $[Cp_2TiCl_2]$ would have an effect on the reaction. (see Chapter 3) To the best of our knowledge, this is the first example of reduction of N_2 by a transition metal complex in IL. The obtained current efficiency is similar to that in previous literature.[3] The yield of NH_3, however, is higher than the previous one.[3] In electrochemical synthesis of NH_3 using N_2 and protons, previously reported current efficiencies have been quite low,[1d,1e,5j] because most of the electric charge is consumed in the H_2 evolution reaction. Accordingly, the low current efficiency obtained in this system is explained in terms of having most of the available electric charge used for H_2 evolution reaction.

2.2.5 Isotopic labeling experiment under $^{15}N_2$ atomosphere

To confirm that the generated NH_3 was originated from N_2 gas, the controlled experiments under $^{15}N_2$ atmosphere and Ar atmosphere are also carried out. The ESI-MS spectrum of indophenol anion derived from NH_3 prepared by the CPE by using [Cp_2TiCl_2] in Pyr_4FAP at −1.5 V (vs. Ag/AgCl) under $^{14}N_2$ or $^{15}N_2$ are shown in Figure 2-8. The ^{14}N–indophenol (m/z = 198) and ^{15}N–indophenol anions were detected when the CPEs under $^{14}N_2$ or $^{15}N_2$ were carried out, respectively. These results clearly indicate that the obtained NH_3 was derived from N_2 gas.

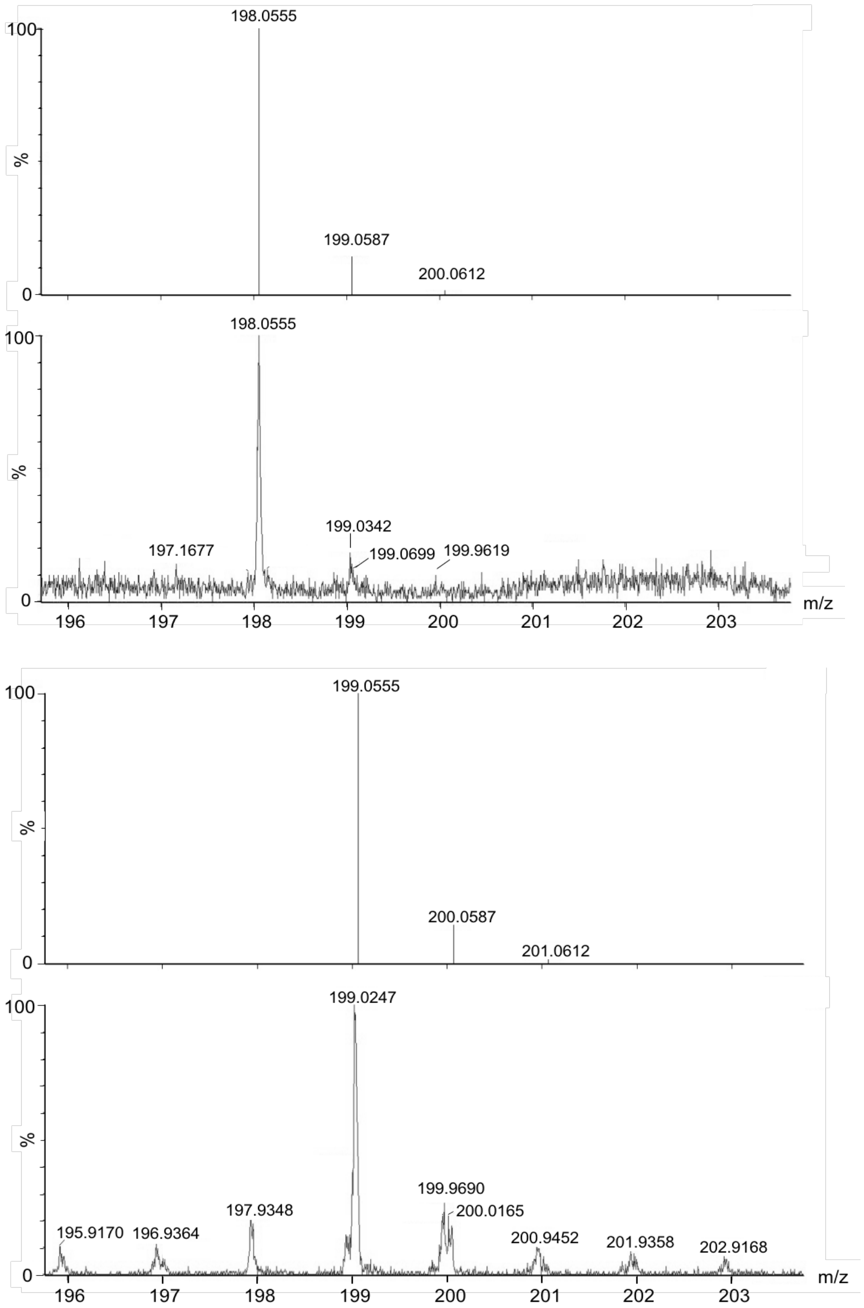

Figure 2-8. ESI-MS spectrum (negative mode) of indophenol anion derived from ammonia prepared by CPE at $-$1.5 V (vs. Ag/AgCl) under $^{14}N_2$ or $^{15}N_2$. The expanded views of the range of m/z = 196$-$203 for (A) the simulation of ^{14}N-indophenol anion (m/z = 198), for (B) the measurement of ^{14}N-indophenol anion, for (C) the simulation of ^{15}N-indophenol (m/z = 199), and for (D) the measurement of ^{15}N-indophenol.

2.3 Conclusion

The electrochemical properties of monomeric [Cp_2TiCl_2] were investigated in two different types of ILs, Pyr_4FAP with the non-coordinating FAP^- anions and Pyr_4OTf with the coordinating OTf^- anion, by measuring cyclic voltammetry. In the CVs of [$(Cp_2TiCl)_2$] in Pyr_4FAP and Pyr_4OTf, a difference was observed in the ratio of the current densities between Pyr_4OTf and Pyr_4FAP, indicating that $[Cp_2Ti]^{2+}$ was stabilized in Pyr_4OTf by the coordination of OTf^- anion in the η^1–O binding mode.

Toward development of the electrochemical NH_3 synthesis by using transition metal complexes in IL under mild conditions, the SPE cell, where WE is supported with IL containing a transition metal complex on gas diffusion, was designed and fabricated. LSV in SPE cell showed that the current density under N_2 was larger than that under Ar in the range of −1.0 to −1.5 V (vs. Ag/AgCl). In the case of using Pyr_4FAP, the maximum yield of NH_3 per [Cp_2TiCl_2] was 27% at 20 C and the maximum current efficiency was 1.24% at early stage, but it is gradually decreased to 0.2% at 20 C.

The yield of NH_3 per Ti ion (%) and current efficiency in the CPE of [Cp_2TiCl_2] in Pyr_4OTf was lower than that in Pyr_4FAP, indicating that the synthesis of NH_3 by using transition metal complex is preferred in non-coordinating IL, Pyr_4FAP, as a solvent. The unique property of Pyr_4FAP will be applied not only to electrochemical NH_3 synthesis but also to various electrochemical reactions by using transition metal complexes, because Pyr_4FAP acts as a polar non-coordinating IL.

2.4 Experimental

2.4.1 Chemicals

Bis(cyclopentadienyl)titanium(IV) dichloride, [Cp_2TiCl_2], was purchased from Tokyo

Chemical Industry Co., Ltd. and used without further purification. 1–Butyl–1–methylpyrrolidinium tris(pentafluoroethyl)trifluorophosphate, Pyr_4FAP, was purchased from Merck Ltd., which was purified according to the previous literature as follows.[16] Pyr_4FAP (50 g) was dissolved in distilled EtOH (100 mL), and to the solution was added an activated charcoal (5g, Sigma-Aldrich). And then, the activated charcoal was removed by filtrate and the remaining solvent was removed by evaporator. If the color was not colorless, the purification was repeated using the activated charcoal. After the purification was finished, Pyr_4FAP was vacuumed at 80 °C for 3 days and dried over molecular sieves (4 Å) for 1 week. 1−Butyl−1−methylpyrrolidinium triflate, Pyr_4OTf, was synthesized according to the literature,[16] based on the metathesis reaction of 1−butyl−1−methylpyrrolidinium chloride and lithium triflate (Wako Pure Chemical Industries Ltd.), where 1−butyl−1−methylpyrrolidinium chloride was also synthesized according to the literature[16] by using N_2 methylpyrrolidine (TCI Co. Ltd) distilled with KOH under N_2 atmosphere and 1−chlorobutane (TCI Co. Ltd) distilled from CaH_2 under N_2 atmosphere. $[Cp_2TiCl_2]$ and ILs were stored in a glove box (mBRAUN MB 150B−G glovebox) under Ar atmosphere (< 1 ppm O_2/H_2O). The reagents used for quantification of NH_3 and N_2H_4, including sodium nitroprusside, sodium hydroxide, sodium hypochlorite, ammonium chloride, *p*–dimethylaminobenzaldehyde, hydrazine monohydrochloride, and hydrogen chloride, were purchased from Wako Pure Chemical Industries Ltd. These reagents were used without further purification. Nafion®212 was purchased from Sigma Aldrich. N_2 (99.999%) and Ar (99.999 %) gases (Nagoya Kousan. Ltd.) were employed as inlet gas.

2.4.2 Instrumentation

Milli−Q water was obtained from a Millipore Biosil system connected to an EYELA SA−2100E automated water distillation apparatus. Solvents were purified by the method of Grubbs,[17] where the solvents were passed over columns of activated alumina and supported copper catalyst supplied by ultimate purification system (Glass Contour System, NIKKO HANSEN & CO., LTD), transferred to the glovebox without exposure to air, and stored over molecular sieves (4Å). Electrochemistry was conducted using a potentiostat (BAS, ALS/1100C). UV−vis/NIR spectra were measured with a Jasco V−770 spectrophotometer. ESI-TOF/MS were obtained with a Micromass LCT spectrometer.

2.4.3 Measurements of cyclic voltammetry

Cyclic voltammetry was measured in a glove box under a purified Ar atmosphere at 25 ℃. The cyclic voltammetry was recorded using a GCE (1 mm diameter) as a working electrode (WE). Pt spiral wire was used as a counter electrode (CE). Ag/Ag^+ electrode (Ag wire + 10 mM $AgNO_3$ in 0.2 M Pyr_4FAP/THF) was used as a reference electrode (RE). The potentials are referenced to the Fc/Fc^+ redox couple, which was measured by adding ferrocene to the sample solution. The concentrations of $[Cp_2TiCl_2]$ were adjusted to 10 mM in Pyr_4FAP and Pyr_4OTf.

2.4.4 Electrochemical N_2 reduction in SPE cell

The electrochemical reduction of N_2 was carried out with a solid polymer electrolyte (SPE) cell as shown in Figure A2 (see Appendix A).[18] The SPE cell used in these experiments was constructed of a aluminum plate, a teflon plate (70 mm (D) × 50 mm

(W) × 5 mm (H)), a gasket made of Viton (fluoropolymer elastomer, (30 mm (D) × 55 mm (W) × 1 mm (H)), a Nafion®212 membrane, carbon paper (TORAY, TGP–H–120) as a WE, Pt mesh as a CE, and Ag/AgCl (3 M NaCl aq., ALS Co., Ltd, RE–3VP) as a RE that is a screw type to attach to Teflon body. The gas and liquid channels were constructed using Viton gaskets. Cu wire was used as the lead line of the WE that was coated with 50 μL of IL containing 10 mM [Cp_2TiCl_2]. The gas inlet and outlet were jointed with Swagelok SS Ball Valve 1/4" straight (SW-SS-43GS4). The setting was carried out in the glove box. The flow rate of N_2 and Ar gases was kept in 5 mL/min. 10 mL of 10 mM HCl aq. was set at N_2 gas outlet for collecting NH_3. The inlet and outlet of liquid channels are connected by pump, and the 0.2 M H_2SO_4 aqueous solution is circulated.

2.4.5 Quantification of NH_3 and N_2H_4

The NH_3 generated during the CPE measurement was collected in the NH_3 trap (1 mL of 10 mM HCl aq.). The concentration of NH_3 trapped was evaluated by the indophenol method.[12] A calibration curve was made from 10 mM HCl containing NH_4Cl. Then, 2 mL of a solution of reagent A (5 g of phenol with 25 mg of sodium nitroprusside per 500 mL of solution) and 2 mL of a solution of reagent B (2.5 g of sodium hydroxide with 4.2 mL sodium hypochlorite to 500 mL of solution) were added to 1 mL of each sample. The visible spectrum was recorded, and the amounts of produced NH_3 were estimated from the maximum absorption peak at 635 nm after 30 min when reagents A and B were added to the sample solution.

The current efficiency (CE) for formation of NH_3 was calculated as following scheme.[19]

$$CE\,(\%) = \frac{Moles\ of\ NH_3\ produced}{Consumed\ Coulombs\ /Faraday\ constant} \times \frac{1}{3} \times 100$$

In order to confirm the formation of hydrazine in the N_2 reduction reaction, the quantification of hydrazine was carried out as follows.[13] 2 mL of a solution of p–dimethylaminobenzaldehyde (2 g of p–dimethylaminobenzaldehyde with 2 mL of conc. HCl to 100 mL ethanol solution) was added to a 1 mL sample of unknown hydrazine concentration and then diluted to 5 mL by adding 1 M HCl. Immediately, a yellow–orange color with an absorption peak at λ_{max} = 458 nm appeared. The concentration of hydrazine was estimated from the intensity of the maximum absorption at 458 nm.

2.4.6 Detection of ^{15}N–labeled indophenol

The aqueous solution containing indophenol anion prepared by indophenol method after the CPE at −1.5 V was added to tetrabutylammonium bromide, which was extracted with $CHCl_3$. The $CHCl_3$ solution was evaporated, and then acetonitrile was added. The acetonitrile solution was used for measurement of ESI-MS. The obtained spectrum (m/z = 199) was noisy. This is because the rate of supplying of $^{15}N_2$ (< 1 mL/min) is slower than that of $^{14}N_2$ (5 mL/min) and the amount of ^{15}N-labeled indophenol anion was quite low compared with ^{14}N-labeled indophenol anion.

2.4.7 DFT calculation

All electronic structure calculations were performed with the Gaussian 09 package[20] on the Fujitsu HX600 system at the Nagoya University Information Technology Center. Geometry optimizations of dimeric $[Cp_2TiCl]^-$ and the monomeric $[Cp_2TiCl]$ as model complexes were performed using BP86 functional[21] in combination with a polarized valence triple-ζ basis set (TZVP) [22] for all atoms.

Contribution of solvents for the DFT calculations was applied with polarized continuum model (PCM).[23] In the DFT calculation with solvent effect of ILs, the dielectric permittivity (ε) of 14.7 at 25 °C, which is that of 1-butyl-1-methylpyrrolidinium bis(trifluoromethylsulfonyl)imide (Pyr_4NTf_2), was employed, because structure of Pyr_4NTf_2 is similar to that of Pyr_4FAP.[24]

2.5 References

1. (a) D. B. Kayan, F. Köleli, *J. Electroanal. Chem.* **2010**, *638*, 119. (b) G. Marnellos, M. Stoukides, *Science* **1998**, *282*, 98. (c) T. Murakami, T. Nishikiori, T. Nohira, Y. Ito, *J. Am. Chem. Soc.* **2003**, *125*, 334. (d) V. Kordali, G. Kyriacou, C. Lambrou, *Chem. Commun.* **2000**, 1673. (e) R. Lan, J. T. S. Irvine, S. Tao, *Sci. Rep.* **2013**, *3*, 1145. (f) A. Tsuneto, A. Kudo, and T. Sakata, *Chem. Lett.* **1993**, *22*, 851. (g) V. Kyriakou, I. Garagounis, E. Vasileiou, A. Vourros, M. Stoukides, *Catal. Today*, **2017**, *286*, 2. (h) C. J. M. van der Ham, M. T. M. Koper and D. G. H. Hetterscheid, *Chem. Soc. Rev.*, **2014**, *43*, 5183.
2. C. J. Pickett and J. Talarmin, *Nature*, **1985**, *317*, 652.
3. J. Y. Becker, S. Avraham (Tsarfaty) and B. Posin, *J. Electroanal. Chem.*, **1987**, *230*, 143.

4. (a) Y. Nishibayashi, *Inorg. Chem.*, **2015**, *54*, 9234. (b) R. J. Burford and M. D. Fryzuk, *Nat. Chem. Rev.*, **2017**, *1*, 1. (c) P. J. Chirik, *Organometallics*, **2010**, *29*, 1500. (d) I. Pappas and P. J. Chirik, *J. Am. Chem. Soc.*, **2015**, *137*, 3498. (e) S. P. Semproni and P. J. Chirik, *J. Am. Chem. Soc.*, **2013**, *135*, 11373. (f) S. P. Semproni, C. Milsmann and P. J. Chirik, *Organometallics*, **2012**, *31*, 3672.
5. (a) P. Hapiot and C. Lagrost, *Chem. Rev.*, **2008**, *108*, 2238. (b) M. Armand, F. Endres, D. R. MacFarlane, H. Ohno and B. Scrosati, *Nat. Mater.*, **2009**, *8*, 621. (c) F. V. Rantwijk and R. A. Sheldon, *Chem. Rev.*, **2007**, *107*, 2757. (d) J. P. Hallett and T. Welton, *Chem. Rev.*, **2011**, *111*, 3508. (e) S. Tsyzuki, H. Tokuda, K. Hayamizu, M. Watanabe, *J. Phys. Chem. B*, **2005**, *109*, 16474. (f) O. Yamamuro, T. Yamada, M. Kofu, M. Nakakoshi and M. Nagao, *J. Chem. Phys.*, **2011**, *135*, 054508. (g) M. Mizoshiri, T. Nagao, Y. Mizoguchi and M. Yao, *J. Chem. Phys.*, **2010**, *132*, 164510. (h) J. N. A. C. Lopes and A. A. H. Pádua, *J. Phys. Chem. B*, **2006**, *110*, 3330. (i) M. Huang, Y. Jiang, P. Sasisanker, G. W. Driver, and H. Weingärtner, *J. Chem. Eng. Data*, **2011**, *56*, 1494. (j)C. D. Hubbard, P. Illner and R. V. Eldik, *Chem. Soc. Rev.*, **2011**, *40*, 272.
6. N.V. Ignat'ev, U. Welz−Biermann, A. Kucheryna, G. Bissky, and H. Willner, *J. Fluorine Chem.,* **2005**, *126*, 1150.
7. (a) R. J. Enemærke, J. Larsen, T. Skrydstrup, K. Daasbjerg, *J. Am. Chem. Soc*. **2004**, *126*, 7853−7864. (b) J. Larsen, R. J. Enemærke, T. Skrydstrup, K. Daasbjerg, *Organometallics,* **2006**, *25*, 2031−2036.
8. J. Langmaier, Z. Samec, V. Varga, M. Horáček, K. Mach, *J. Organomet. Chem.,* **1999**, *579*, 348.
9. G. P. Pez, P Apgar, R. K. Crissey, *J. Am. Chem. Soc*. **1982**, *104*, 482.
10. D. B. Williams, M. E. Stoll, B. L. Scott, D. A. Costa, W. J. Oldham, Jr., *Chem.*

Commun., **2005**, 1438.

11. R. J. Enemærke, J. Larsen, T. Skrydstrup, K. Daasbjerg, *Organometallics,* **2004**, *23*, 1866.
12. M. W. Weatherburn, *Anal. Chem.*, **1967**, *39*, 971.
13. G. W. Watts and J. D. Chrisp, *Anal. Chem.*, **1952**, *24*, 2006.
14. (a) M. Schmeisser and R. van Eldik, *Inorg. Chem.*, **2009**, *48*, 7466. (b) S. Kern, R. van Eldik, *Inorg. Chem.*, **2012**, *51*, 7340. (c) M. Schmeisser, F. W. Heinemann, P. Illner, R. Puchta, A. Zahl, and R. van Eldik, *Inorg. Chem.*, **2011**, *50*, 6685. (d) S. Begel, F. W. Heinemann, G. Stopa, G. Stocheland, R. van Eldik, *Inorg. Chem.*, **2011**, *50*, 3946. (e) S. Begel, P. Illner, S. Kern, R. Puchta, and R. van Eldik, *Inorg. Chem.*, **2008**, *47*, 7121. (f) P. Illner, S. Begel, S. Kern, R. Puchta, and R. van Eldik, *Inorg. Chem.*, **2009**, *48*, 588. (g) K. Pokornv, M. Schmeisser, F. Hampel, A. Zahl, R. Puchta, and R. van Eldik, *Inorg. Chem*., **2013**, *52*, 13167. (h) S. Begel, R. Puchta, J. Sutter, F. W. Heinemann, L. Dahlenburgand, and R. van Eldik, *Inorg. Chem.*, **2015**, *54*, 6763.
15. (a) D. C. Grills, Y. Matsubara, Y. Kuwahara, S. R. Golisz, D. A. Kurtz, and B. A. Mello, *J. Phys. Chem. Lett.,* **2014**, *5*, 2033. (b) Y. Matsubara, D. C. Grills and Y. Kuwahara, *ACS Catal.*, **2015**, *5*, 6440.
16. A. K. Burrell, R. E. Del Sesto, S. N. Baker, T. M. McCleskeya, G. A. Baker, *Green Chem*., **2007**, *9*, 449.
17. A. B. Pangborn, M. A. Giardello, R. H. Grubbs, R. K. Rosen, F. J. Timmers, *Organometallics* **1996**, *15*, 1518.
18. A. Katayama, T. Inomata, T. Ozawa, H. Masuda, *Electrochem. Commun*. **2016**, *67*, 6.
19. K. Tanaka, Y. Hozumi, T. Tanaka, *Chem. Lett*. **1982**, 1203.

20. M. J. Frisch, G. W. Trucks, H. B. Schlegel, G. E. Scuseria, M. A. Robb, J. R. Cheeseman, G. Scalmani, V. Barone, B. Mennucci, G. A. Petersson, H. Nakatsuji, M. Caricato, X. Li, H. Hratchian, A. F. Izmaylov, J. Bloino, G. Zheng, J. L. Sonnenberg, M. Hada, M. Ehara, K. Toyota, R. Fukuda, J. Hasegawa, M. Ishida, T. Nakajima, Y. Honda, O. Kitao, H. Nakai, T. Vreven, J. A. Jr. Montgomery, J. E. Peralta, F. Ogliaro, M. Bearpark, J. J. Heyd, E. Brothers, K. N. Kudin, V. N. Staroverov, T. Keith, R. Kobayashi, J. Normand, K. Raghavachari, A. Rendell, J. C. Burant, S. S. Iyengar, J. Tomasi, M. Cossi, N. Rega, J. M. Millam, M. Klene, J. E. Knox, J. B. Cross, V. Bakken, C. Adamo, J. Jaramillo, R. Gomperts, R. E. Stratmann, O. Yazyev, A. J. Austin, R. Cammi, C. Pomelli, J. W. Ochterski, R. L. Martin, K. Morokuma, V. G. Zakrzewski, G. A. Voth, P. Salvador, J. J. Dannenberg, S. Dapprich, A. D. Daniels, O. Farkas, J. B. Foresman, J. V. Ortiz, J. Cioslowski, D. J. Fox, Gaussian 09, Revision E.01,; Gaussian, Inc.: Wallingford, CT, 2013.
21. J. P. Perdew, *Phys. Rev. B*, **1986**, *33*, 8822.
22. A. Schäfer, C. Huber, R. Ahlrichs, *J. Chem.Phys.*, **1994**, *100*, 5829.
23. J. Tomasi, , B. Mennucci, and R. Cammi, *Chem. Rev.*, **2005**, *105*, 2999.
24. M. Huang, Y. Jiang, P. Sasisanker, G. W. Driver, and H. Weingärtner, *J. Chem. Eng. Data*, **2011**, *56*, 1494.

Chapter 3: Ionic liquid promotes N_2 coordination to titanocene(III) monochloride

3.1 Introduction

In Chapter 2, the electrochemical synthesis of ammonia (NH_3) by using titanocene(IV) in ionic liquid (IL) was investigated. The yield of NH_3 per Ti ion (%) and current efficiency in the CPE of titanocene dichloride ([Cp_2TiCl_2]) in 1-butyl-1-methylpyrrolidinium tris(pentafluoroethyl)trifluorophosphate (Pyr_4FAP) is higher than that in 1-butyl-1-methylpyrrolidinium triflate (Pyr_4OTf), indicating that the synthesis of NH_3 by using transition metal complex is preferred in non-coordinating IL, Pyr_4FAP, as a solvent. The yield of NH_3 in Pyr_4FAP is significantly improved compared with that in organic solvents reported in previous literature.[1] The N_2 reduction to NH_3 is believed to occur during the electrochemical reduction of Ti(IV) to Ti(III) and/or Ti(II) species in titanocene. This reaction is not observed for the same complex in organic solvents such as THF and toluene, suggesting that the IL contributes to the highly efficient N_2 reduction reaction.

Hence, in Chapter 3, the electrochemical reduction of [Cp_2TiCl_2] in Pyr_4FAP, Pyr_4OTf, and THF containing 0.2 M Pyr_4FAP (0.2 M Pyr_4FAP/THF) were discussed by using UV-vis/NIR spectroscopy during the electrochemical reduction of [Cp_2TiCl_2] to understand the electrochemical N_2 reduction promoted by [Cp_2TiCl_2] in Pyr_4FAP as described in Chapter 2. Besides the UV-vis/NIR spectroscopy during the electrochemical reduction, bis[(dicyclopentadienyl)titanium(III) chloride], [$(Cp_2TiCl)_2$], was prepared and its reactivity toward N_2 in the IL was examined by using UV-vis/NIR and frozen solution EPR spectroscopies. Moreover, to consider the equilibrium reaction containing N_2 coordination from theoretical viewpoints, we describe the density functional theory (DFT) and time-dependent density functional theory (TDDFT) studies for [($Cp_2TiCl)_2$], [Cp_2TiCl], and [Cp_2TiClN_2], which are the possible structures in the equilibrium reaction of [($Cp_2TiCl)_2$] in toluene and IL.

3.2 Results and Discussion

3.2.1 UV-vis/NIR spectra of [Cp_2TiCl_2] in ionic liquids during electrochemical reduction

To understand the electrochemical reduction reaction of [Cp_2TiCl_2] from Ti(IV) to Ti(III), UV-vis/NIR spectra of [Cp_2TiCl_2] in Pyr_4FAP, Pyr_4OTf and 0.2 M Pyr_4FAP/THF were measured during the controlled-potential electrolysis (CPE). The results in Pyr_4FAP are shown in Figure 3-1. The rest potential before the LSV measurement was observed at 0 V (vs. Pt wire). Thus, the LSV was started to sweep from 0 V (vs. Pt wire). The LSV (Figure 3-1(A)) before UV-vis/NIR and CPE measurement showed increase in the current assigned to the reduction of Ti(IV) to Ti(III). Therefore, the reduction potential of CPE was decided to be −1.2 V (vs. Pt wire). The time courses (s) of electric charge (mC), UV-vis/NIR spectra and its difference spectra are shown in Figures 3-1(B), 3-1(C) and 3-1(D), respectively. The difference spectra shown in Figure 3-1(D) clearly revealed intensity changes in absorbances at 462, 531, 821, and 1194 nm.

The results in Pyr_4OTf and 0.2 M Pyr_4FAP/THF are also shown in Figures 3-2 and 3.3, respectively. The LSVs before UV-vis/NIR and CPE measurements are shown in Figures 3-2(A) and 3-3(A), respectively, and the increase in the currents were observed from −0.8 V (vs. Pt wire) in the LSVs, which are assigned to the reduction of Ti(IV) to Ti(III). The wave seen in Figure 3-1(A) is not wave-shaped, as seen in Figure 3-2(A), suggesting that IR drop was occurred due to the higher viscosity of Pyr_4FAP than that of

Pyr_4OTf. In addition, the setting of 3 electrodes in UV-vis/NIR cell cannot provide the best cell geometry allowing minimizing of IR drop. The current value is different from in all three solvents due to the difference in their viscosities (Pyr_4FAP: η= 333.789 mPa•s at 293.15K, Pyr_4OTf: η= 217 mPa•s at 293.15 K)[2,3]. The influence due to the viscosities was also observed in the consumed electric charge of CPE, as shown in Figures 3-2(B) and 3-3(B), and in the intensity change in absorbances in UV-vis/NIR spectra shown in Figures 3-2(C), 3-2(D), 3-3(C) and 3-3(D). In the difference UV-vis/NIR spectra in Pyr_4OTf (Figure 3-2(D)), intensity changes were observed in the bands at 525, 783, 874, and 1154 nm. In the difference UV-vis/NIR spectra in 0.2 M Pyr_4FAP/THF (Figure 3-3(D)), the intensity change is observed in the bands at 519, 737, 811, 1171 nm, which is similar to that in Pyr_4OTf. The species generated in 0.2 M Pyr_4FAP/THF is therefore similar to that in Pyr_4OTf.

All the UV-vis/NIR and difference spectra in Pyr_4FAP, Pyr_4OTf and 0.2 M Pyr_4FAP/THF showed increase in the broad bands at around 1000 ~ 1400 nm, which are characterized to metal to metal charge transfer (MMCT) band derived from $[(Cp_2TiCl)_2]$ generated after the electrochemical reduction (see Section 3.2.2).[4,5] Moreover, other peaks at around 800 nm were also characterized to d-d transition of Ti(III) for $[(Cp_2TiCl)_2]$ and $[Cp_2TiCl]$. These observations are consistent with the UV-vis/NIR spectra of $[(Cp_2TiCl)_2]$ as shown in Figures A13-A15 in Appendix A.[4] Accordingly, Ti–Cl bond of $[Cp_2TiCl_2]^-$ was obviously cleaved even in Pyr_4FAP that is non-coordinating solvent. To the best of our knowledge, although such a behavior in 0.2 M Bu_4NPF_6/THF has been reported before,[6] that in non-coordinating solvent has not been reported yet. Accordingly, the generation of $[Cp_2TiCl]$, which was estimated as the active intermediate in the electrochemical NH_3 synthesis as described in Chapter 2,[4,7] was also confirmed clearly by UV-vis/NIR spectra observed during electrochemical reduction of [Cp_2TiCl_2] in Pyr_4FAP.

Interestingly, increase in intensity of the absorbance observed at 462 nm in Pyr_4FAP (Figure 3-1(D)), which is derived from [Cp_2TiCl], was not observed in Pyr_4OTf (Figure 3-2(D)) and 0.2 M Pyr_4FAP/THF (Figure 3-3(D)), suggesting that equilibrium reactions between [Cp_2TiCl] and [$Cp_2TiCl(S)$] (S: solvent), as shown in Eqs.(2) and (3),[8] exist in addition to Eq. (1).

$$[(Cp_2TiCl)_2] \rightleftharpoons 2\,[Cp_2TiCl] \tag{1}$$

$$[Cp_2TiCl] + [Pyr_4]^+[OTf]^- \rightleftharpoons [Pyr_4]^+[Cp_2TiCl(OTf)]^- \tag{2}$$

$$[Cp_2TiCl] + THF \rightleftharpoons [Cp_2TiCl(THF)] \tag{3}$$

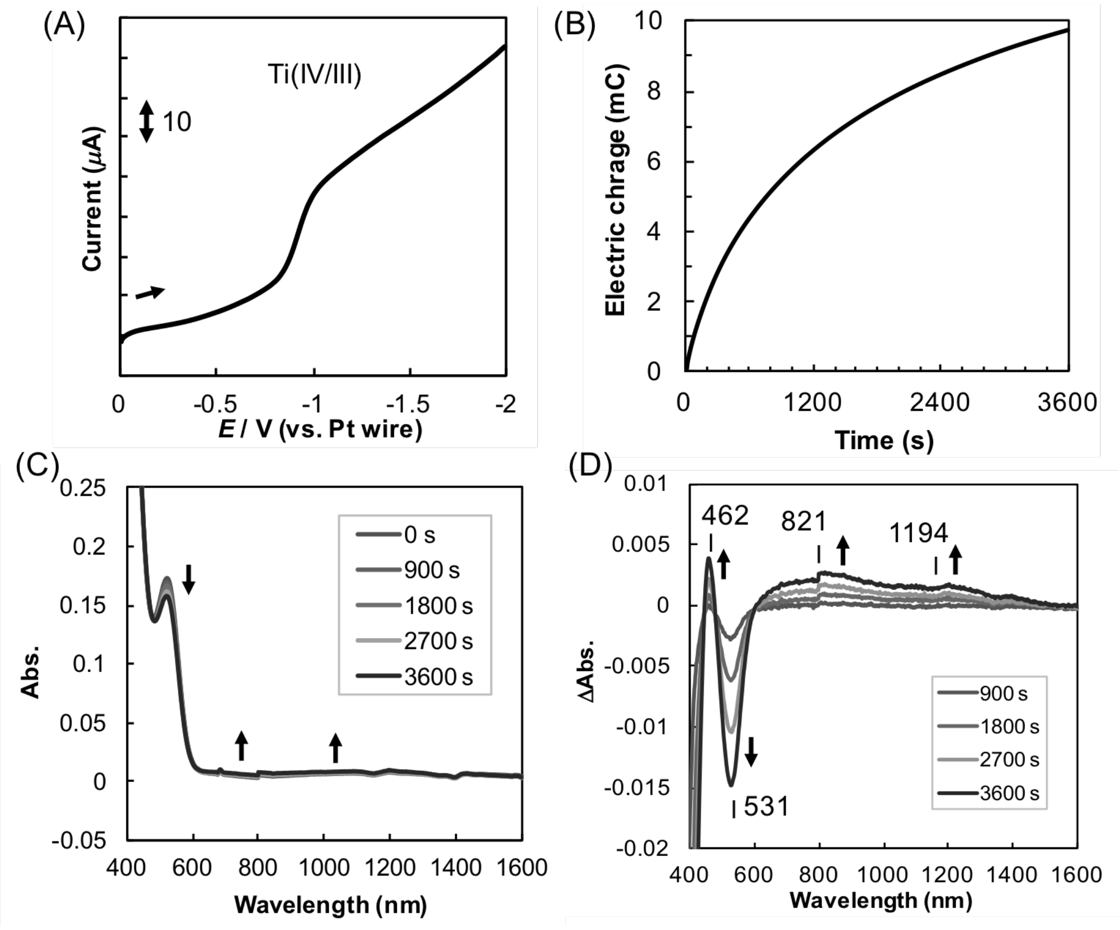

Figure 3-1. UV-vis/NIR spectra of 10 mM $[Cp_2TiCl_2]$ in Pyr$_4$FAP during CPE at −1.2 V (vs. Pt wire) under Ar atmosphere. (A) Linear sweep voltammogram of $[Cp_2TiCl_2]$ in Pyr$_4$FAP (scan rate: 10 mV/s) before CPE, (B) plots of consumed electric charge (mC) vs. time (s) during CPE at −1.2 V (vs. Pt wire), (C) UV-vis/NIR spectra of 10 mM $[Cp_2TiCl_2]$ (**1**) in Pyr$_4$FAP during CPE at −1.2 V (vs. Pt wire) under Ar atmosphere at 0, 900, 1800, 2700, and 3600 s, and (D) the difference UV-vis/NIR spectra of 10 mM $[Cp_2TiCl_2]$ in Pyr$_4$FAP at 900, 1800, 2700, and 3600 s.

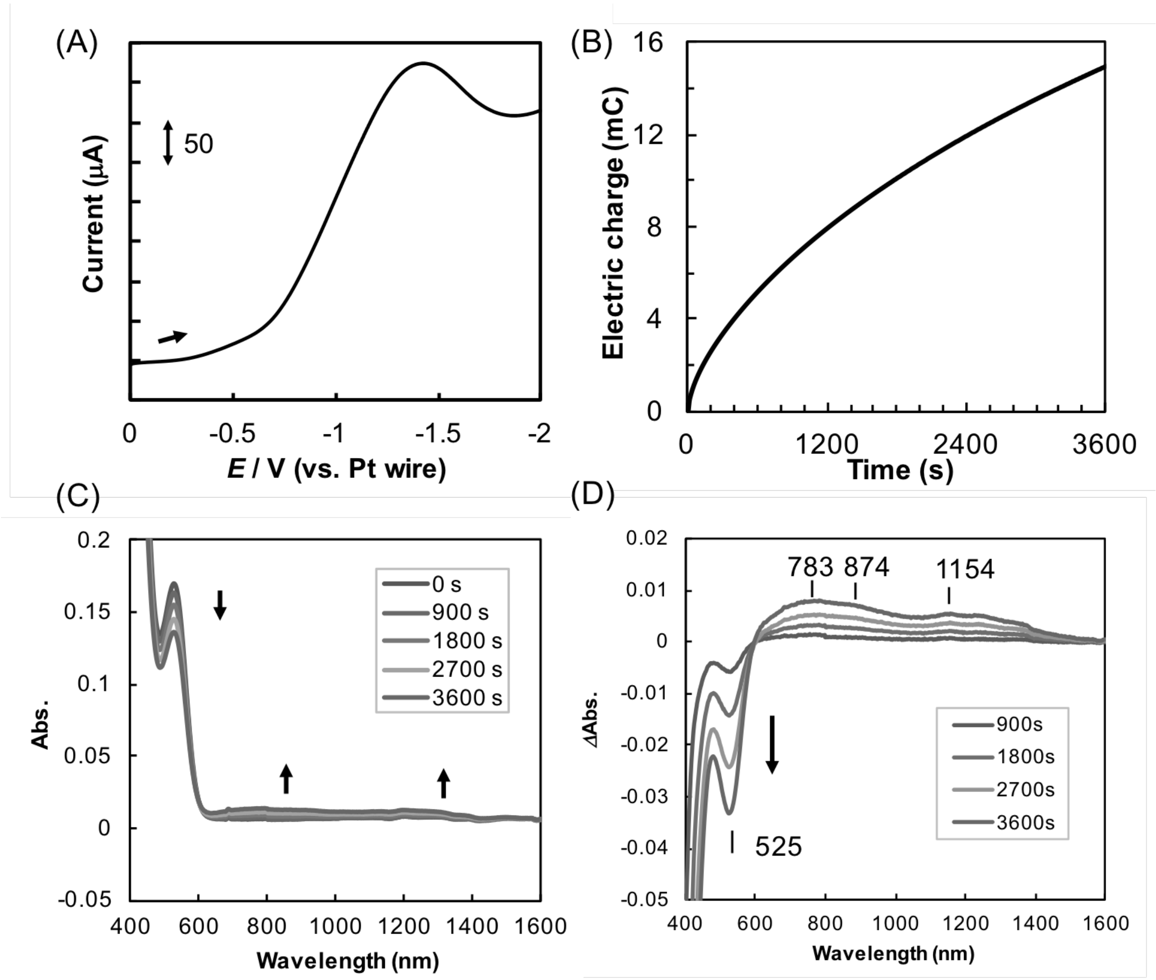

Figure 3-2. (A) Linear sweep voltammogram of [Cp_2TiCl_2] in Pyr_4OTf (scan rate: 100 mV/s) before CPE, (B) plots of consumed electric charge (mC) vs. time (s) during CPE at −1.2 V (vs. Pt wire), (C) UV-vis/NIR spectra of 10 mM [Cp_2TiCl_2] in Pyr_4OTf during CPE at −1.2 V (vs. Pt wire) under Ar atmosphere at 0, 900, 1800, 2700, and 3600 s, and (D) difference UV-vis/NIR spectra of 10 mM [Cp_2TiCl_2] in Pyr_4OTf at 900, 1800, 2700, and 3600 s.

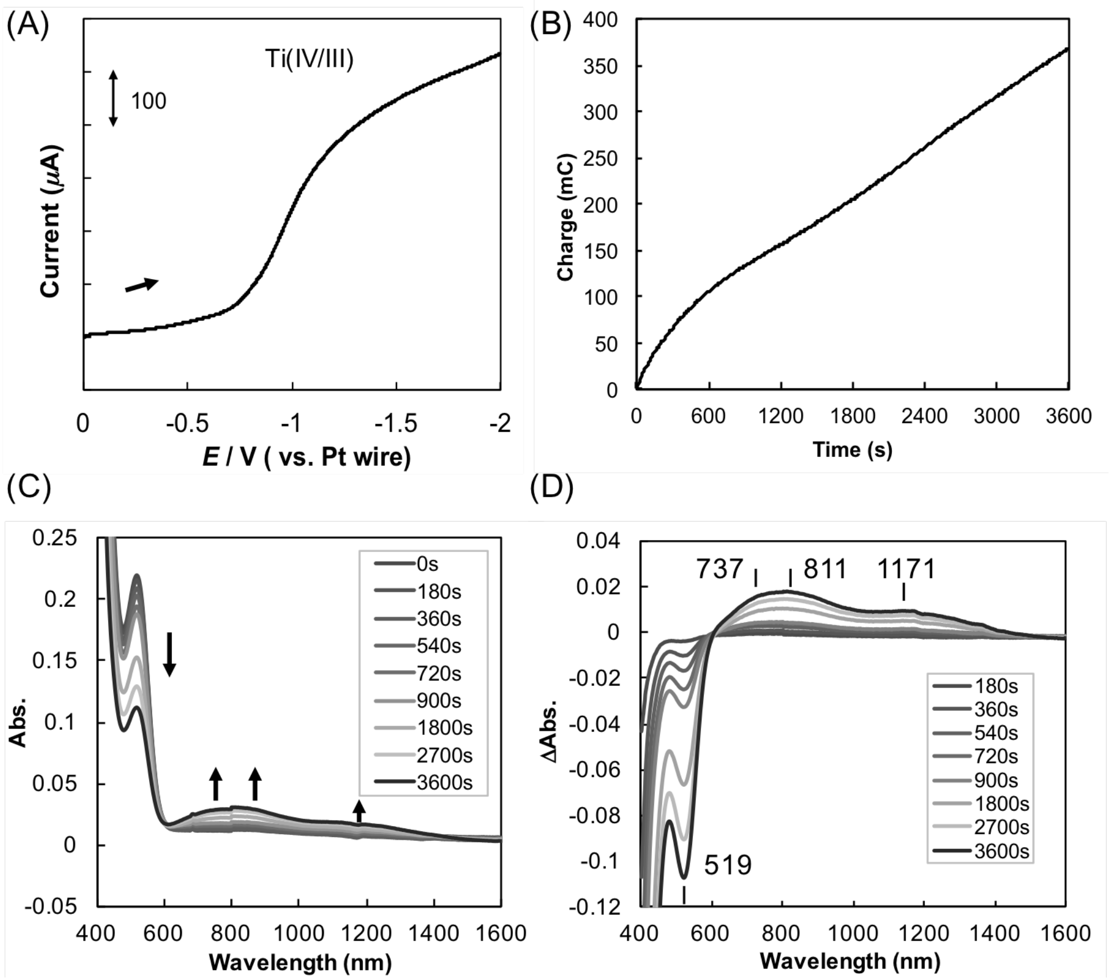

Figure 3-3. UV-vis/NIR spectra of 10 mM [Cp_2TiCl_2] in 0.2 M Pyr_4FAP/THF during CPE at −1.2 V (vs. Pt wire) under Ar atmosphere. (A) Linear sweep voltammogram of [Cp_2TiCl_2] in 0.2 M Pyr_4FAP/THF (scan rate: 10 mV/s) before CPE, (B) plots of consumed electric charge (mC) vs. time (s) during CPE at −1.2 V (vs. Pt wire), (C) UV-vis/NIR spectra of 10 mM [Cp_2TiCl_2] in 0.2 M Pyr_4FAP/THF at 0, 180, 360, 540, 720, 900, 1800, 2700, and 3600 s, and (D) the difference UV-vis/NIR spectra of 10 mM [Cp_2TiCl_2] in 0.2 M Pyr_4FAP/THF at 180, 360, 540, 720, 900, 1800, 2700, and 3600 s.

3.2.2 UV-vis/NIR spectra of [$(Cp_2TiCl)_2$]

UV-vis/NIR spectra of 5 mM [$(Cp_2TiCl)_2$] in Pyr_4FAP and in 0.2 M Pyr_4FAP-containing THF solution (0.2 M Pyr_4FAP/THF) and toluene for comparison were measured under a dinitrogen atmosphere. These spectra are shown in Figure 3-4 and summarized in Table A10 in Appendix A. All spectra have an intense peak at about 450 nm, two weak bands in the range of 690 ~ 820 nm and a broadened band at about 1150 nm, which are quite similar to each other, except for a small absorption band at 449 nm observed in 0.2 M Pyr_4FAP/THF. The former intense bands and two weak bands were previously assigned as CT and d-d bands, respectively.[9] Although the broadened band at about 1150 nm was also assigned as a d-d band, it is in a longer wavelength region. Therefore, we measured UV-vis/NIR spectra of [Cp^*_2TiCl] and [Cp_2VCl_2] in toluene in order to assign the broadened bands, in which metal ions are both in the same electronic state (d^1 electronic configuration) and do not form any dimeric structure.[10] These complexes have intense bands below 400 nm and two weak bands in the d-d transition band range of 550 – 910 nm; 558 (ε 110 $M^{-1}cm^{-1}$) and 640 nm (ε 77 $M^{-1}cm^{-1}$) for [Cp^*_2TiCl] and 755 (ε 82 $M^{-1}cm^{-1}$) and 905 nm (ε 93 $M^{-1}cm^{-1}$) for [Cp_2VCl_2], (see Figures A16 and A17 and Table A10 in Appendix A). However, there are no absorption bands in the NIR region of 900−1500 nm. Therefore, the absorption bands observed in the range of 1100–1200 nm are assigned as metal-metal charge transfer (MMCT) bands. Furthermore, UV-vis/NIR spectra of [$(Cp_2TiCl)_2$] in Pyr_4FAP, toluene and THF were measured in various concentrations (see Figures A18-A20 in Appendix A). The MMCT bands in all three solvents were increased in the higher concentrations. These behaviors are reasonable because the equilibrium is biased toward the formation of the dimeric species. Thus, the results also suggest that the bands in the range of 1100-1200 nm are MMCT bands. The detailed assignments of the UV-vis/NIR spectra by TD-DFT calculations are described in Section 3.2.8 and Appendix B.

The CT band indicates that the equilibrium reaction between the dimeric and monomeric species exists also in non-coordinating solvent. As described above, the intense band at about 450 nm decreases in intensity according to the following order of solvents; toluene (456 nm (ε 1300)) > Pyr$_4$FAP (449 nm (ε 930)) > 0.2 M Pyr$_4$FAP/THF (452 nm (ε 120)).

The decrease in peak intensity of the CT band observed in 0.2 M Pyr$_4$FAP/THF solution may indicate release of a chloride atom from the Ti(III) center upon coordination of a THF molecule, resulting in transformation from dimeric [(Cp$_2$TiCl)$_2$] to monomeric [Cp$_2$TiCl]. The small decay of the CT band observed for the complex in Pyr$_4$FAP may indicate dissociation from the dimeric species to the monomeric species and weak coordination of the dinitrogen molecule.

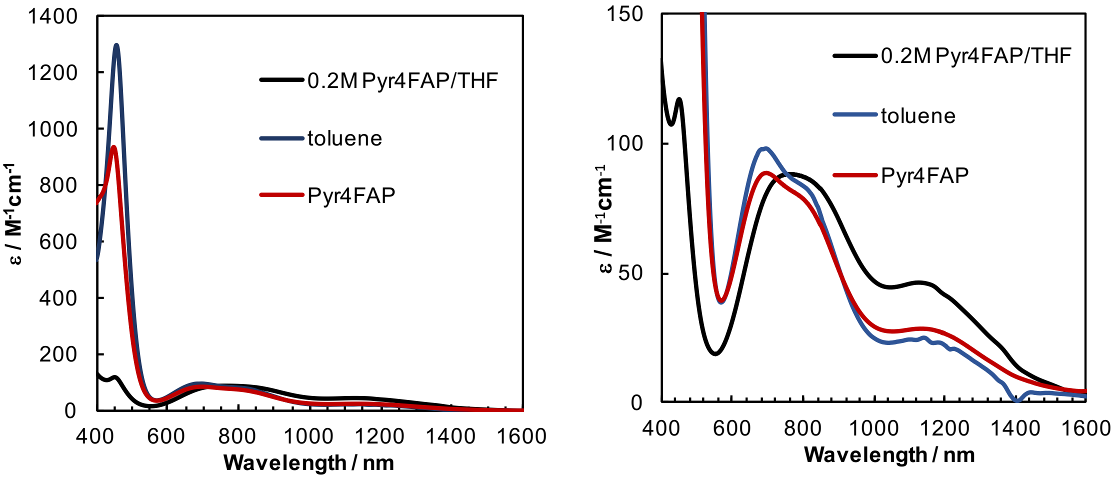

Figure 3-4. UV-vis/NIR spectra of 5 mM [(Cp$_2$TiCl)$_2$] in 0.2 M Pyr$_4$FAP /THF (black), toluene (blue) and Pyr$_4$FAP (red).

3.2.3 Frozen solution EPR spectroscopy of dimeric [($Cp_2TiCl)_2$] in Pyr_4FAP, THF and toluene

To understand the equilibrium reaction between dimeric [($Cp_2TiCl)_2$] and monomeric [Cp_2TiCl] in Pyr_4FAP, EPR spectrum for [($Cp_2TiCl)_2$] in Pyr_4FAP was measured. Regarding the ground state of the [($Cp_2TiCl)_2$], it has been known to be in the singlet state at low temperature.[11-14] Accordingly, [($Cp_2TiCl)_2$] in the singlet state is stabilized at lower temperature due to the strong intermolecular spin-spin interaction of titanium-titanium. The unusual phenomenon observed in Pyr_4FAP would involve the switch of the spin state in [($Cp_2TiCl)_2$] from the singlet state to the triplet state. Therefore, if there is the monomeric species generated by the equilibrium reaction of dimeric [($Cp_2TiCl)_2$] in Pyr_4FAP, [($Cp_2TiCl)_2$] would be EPR active.

To confirm the existence of equilibrium reaction between monomeric [Cp_2TiCl] and dimeric [($Cp_2TiCl)_2$] in Pyr_4FAP, the EPR spectrum of [($Cp_2TiCl)_2$] under N_2 atmosphere was measured at 77 K. The yellow color of [($Cp_2TiCl)_2$] in Pyr4FAP is changed to yellow-green when it was cooled at 77K. This color change was not observed upon cooling the complex in organic solvents, 0.2 M Pyr_4FAP/THF and toluene. The color change observed for the complex in pure ionic liquid suggests N_2 coordinates to [Cp_2TiCl]. Interestingly, the EPR spectrum of the complex in Pyr_4FAP is obviously different from that of the complex in organic solvents, as described below (see Figures 3-5, 3-6 and 3-7). The EPR spectrum of [($Cp_2TiCl)_2$] in Pyr_4FAP under $^{14}N_2$ (Figure 3-5) was a rhombic signal with $g_x = 1.997$, $g_y = 1.977$, $g_z = 1.946$, and $A_z(N) = 17$ G. This spectrum exhibits clear triplet hyperfine splitting at the g_z signal. This is a strong indication of dinitrogen binding to the Ti(III) center, because the hyperfine splitting is a triplet pattern induced by the coordination of ^{14}N with a nuclear spin $I = 1$. This spectrum agrees well with the simulation ($g_x = 1.995$, $g_y = 1.974$, $g_z = 1.944$ and $A_z(N) = 16$ G). To confirm this finding, we also carried out the same experiment under $^{15}N_2$ ($I = 1/2$ for ^{15}N). The spectrum for the complex measured under $^{15}N_2$ is also a rhombic type spectrum with $g_x = 1.994$, $g_y = 1.975$, and $g_z = 1.940$, in which the g_z signal was doubly split with $A_z(N) = 22$. The doubly split signal clearly indicates coordination of $^{15}N_2$ to the Ti(III) species. This spectrum is consistent with the simulated spectrum ($g_x = 1.994$, $g_y = 1.975$, $g_z = 1.940$, $A_z(N) = 21$). Further support for coordination of N_2 is provided by the ratio of coupling constants, $^{14}N/^{15}N$, because the ratio (0.77) is close to the theoretical value estimated from the ratio for nuclear spin moments, $^{14}N/^{15}N$, (0.7128).[15] These experimental data demonstrate that $[(Cp_2TiCl)_2]$ dissociates to monomeric $[Cp_2TiCl]$ and N_2 coordinates to the monomeric species in Pyr_4FAP. Although the reactivity of the lower valent titanocene(II) with N_2 has previously been studied,[16] reactivity of titanocene(III) ligated to a Cp ring without any substituent groups such as a methyl group has never been reported.

For comparison, EPR spectra of $[(Cp_2TiCl)_2]$ were also studied in toluene and 0.2 M Pyr_4FAP/THF at 77 K, which are shown in Figures 3-6 and 3-7. Both spectra have a rhombic signal with $g_x = 1.998$, $g_y = 1.980$, $g_z = 1.950$ and with $g_x = 1.997$, $g_y = 1.977$, $g_z = 1.946$, respectively. These spectra are similar to the simulated spectra and in agreement with spectra in the literature.[17] These spectra, however, do not include hyperfine splitting at the g_z peak. If $[(Cp_2TiCl)_2]$ were retained in the dimer structure, it would be EPR silent due to the antiferromagnetic interaction. These findings at least indicate that $[(Cp_2TiCl)_2]$ also exists as the monomeric species. Although the EPR spectrum of $[(Cp_2TiCl)_2]$ in Pyr_4FAP (Figure 3-5) has a hyperfine split derived from coordination of N_2, similar hyperfine splitting was not observed for the complex in organic solvents.

A plausible reaction scheme for [(Cp_2TiCl)$_2$] in IL is illustrated in Scheme 3.1. [(Cp_2TiCl)$_2$] is in equilibrium between the dimeric species, [(Cp_2TiCl)$_2$], and the monomeric species, [Cp_2TiCl], not only in organic solvents[6] but also in Pyr_4FAP. The monomeric species is coordinated to dinitrogen at 77 K. Increase in the amount of the monomeric species promotes the coordination of N_2. The UV-vis/NIR spectra at various concentrations, as shown in Figures A18-A20 in the Appendix A, indicate that more monomeric species exists in the lower concentrations. Accordingly, the coordination can be enhanced in lower concentrations.

The results of this work suggest that the IL affects the reactivity of titanocene(III) monochloride with N_2. Although the detailed structure of the titanocene(III)-N_2 species in the ionic liquid remains unknown, it appears that the ionic liquid promotes and stabilizes the formation of the N_2-coordinated Ti(III) species. To the best of our knowledge, the similar coordination behavior of N_2 with a Ti(III) complex has not been reported although the reactivity of other transition metal complexes with small molecules such as NO and CO_2 in ionic liquid has been investigated.[18]

Scheme 3-1. Possible reaction scheme of [(Cp_2TiCl)$_2$] in Pyr_4FAP under N_2

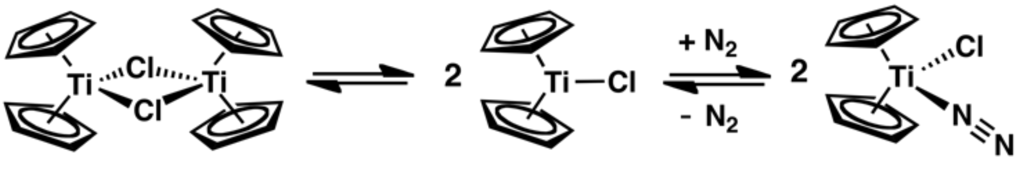

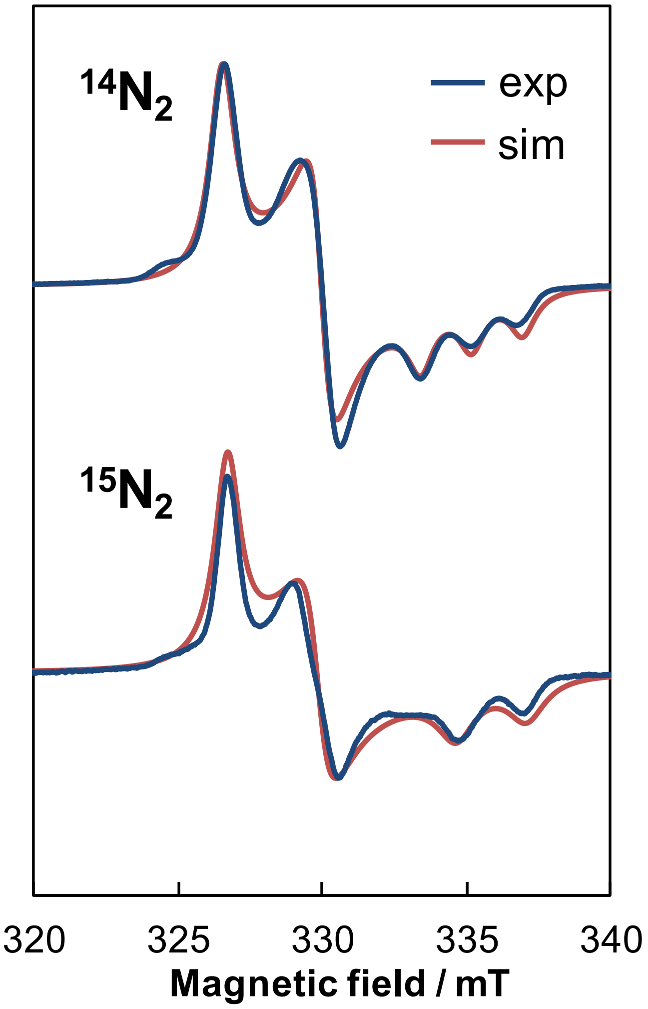

Figure 3-5. Experimental (blue) and simulated (red) frozen solution EPR spectra of $[(Cp_2TiCl)_2]$ in Pyr_4FAP under $^{14}N_2$ (upper) and $^{15}N_2$ atmospheres (bottom). Experimental conditions are as follows: $^{14}N_2$; temperature $T = 77$ K, power 1 mW, and modulation 0.63 mT, $^{15}N_2$; temperature $T = 77$ K, power 1 mW, and modulation 0.63 mT. The observed spectrum (blue) and simulation (red) are as follows; $^{14}N_2$; g values estimated from the spectrum are $g_x = 1.998$, $g_y = 1.977$, g_z =1.946, $A_z(N) = 17$ G and simulated g values are $g_x = 1.995$, $g_y = 1.974$, g_z =1.944, Az(N) = 16 G, $^{15}N_2$; g values estimated from the spectrum are $g_x = 1.994$, $g_y = 1.975$, g_z =1.940, Az(N) = 22 G, and simulated g values are $g_x = 1.994$, $g_y = 1.975$, g_z =1.940, Az(N) =21 G.

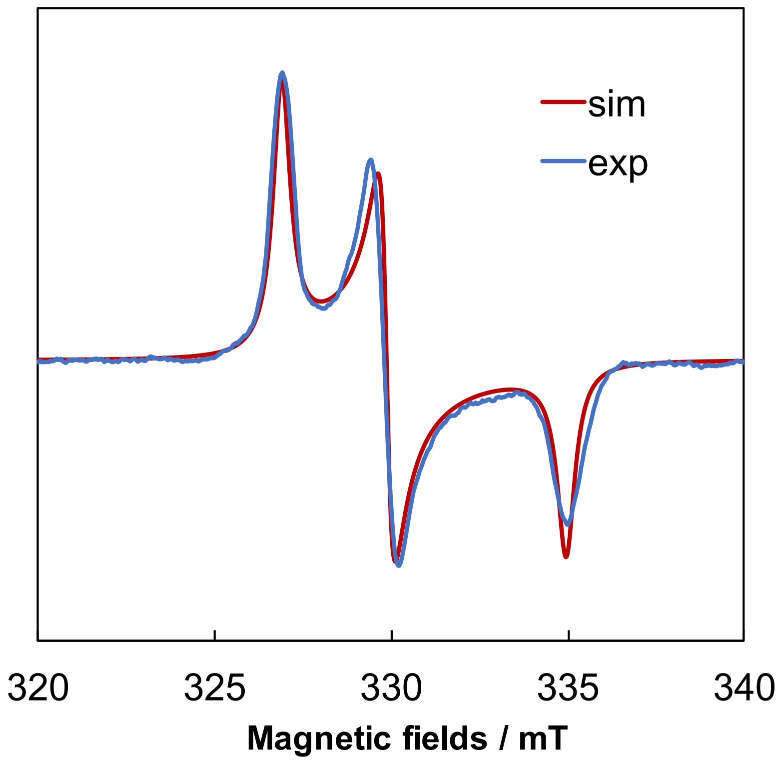

Figure 3-6. Frozen solution EPR spectrum of 0.5 mM [($Cp_2TiCl)_2$] in toluene. Experimental conditions are as follows: temperature T = 77 K, frequency ν = 9.142 GHz, power 1 mW, and modulation 0.63 mT. The observed spectrum (blue) and simulation (red) are as follows; g values estimated from the spectrum are as follows; g_x = 1.998, g_y = 1.980, g_z =1.950, and simulated g values are g_x = 1.998, g_y = 1.980, g_z =1.950.

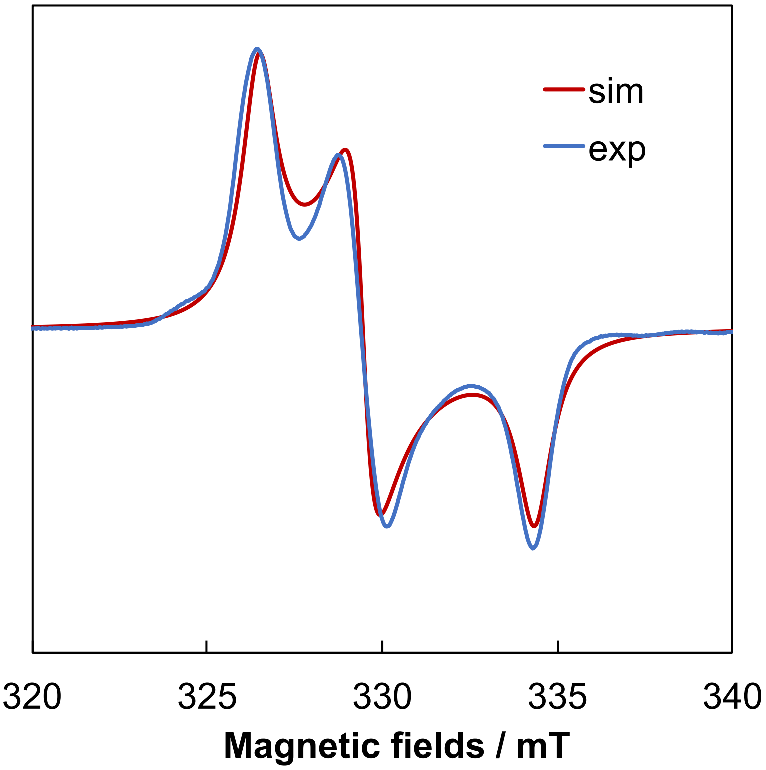

Figure 3-7. Frozen solution EPR spectrum of 1 mM $[(Cp_2TiCl)_2]$ in 0.2 M Pyr_4FAP/THF. Experimental conditions are as follows; temperature T = 77 K, frequency ν = 9.125 GHz, power 1 mW, and modulation 0.63 mT. The observed spectrum (blue) and simulation (red) are as follows; g values estimated from spectrum are g_x = 1.997, g_y = 1.977, g_z =1.946, and simulated g values are g_x = 1.997, g_y = 1.979, g_z =1.950.

3.2.4 Full geometry optimizations of titanocene derivatives, 1, 2, 3, 4, and 4-TS by DFT calculations.

In order to understand the N_2 coordination to titanocene in IL, which was previously studied by EPR spectroscopy, full geometry optimizations of the following model complex structures were carried out by using DFT calculations; $[(Cp_2TiCl)_2]$ in the singlet (**1**) and triplet states (**2**), $[Cp_2TiCl]$ in the doublet state (**3**), $[Cp_2TiCl(N_2)]$ in the doublet state (**4**), and the transition state of **4** in the doublet state (**4-TS**). DFT calculations were performed using BP86/TZVP basis set for all atoms,[19,20] because DFT calculations for titanocene complexes were studied previously using the same basis set.[21,22] The calculations were carried out with applying with the dielectric permittivity (ε) as solvation effects of toluene ($\varepsilon = 2.3741$) and IL ($\varepsilon = 14.7$). The value ε of IL employed in this study was applied with that of 1-butyl-1-methyl pyrrolidinium bis(trifluoromethansulfonyl)imide reported previously.[23] The transition state in the formation of **4**, **4-TS**, was calculated by gradual elongation of Ti···N distance for **4**.

The structures of model complexes optimized with solvent effect of IL ($\varepsilon = 14.7$) are shown in Figure 3-8, and the structural information are summarized in Tables B2-B4 and described in the Appendix B. The optimized structures in toluene were similar to those in toluene and IL, and the bond parameters among them were almost the same within ±0.02 Å (see Appendix B). Although the structures of **1** and **2** were similar to each other, the Ti-Ti distance (4.0153 Å) for **1** was shorter than that of **2** (4.0657 Å). This difference was found in the difference between their molecular orbitals as follows. For **1**, the density population analysis revealed that the HOMO−1 in the molecular orbital 109 was constructed of d orbitals on two Ti atoms to form the metal-metal interaction (see Figure B10 in Appendix B). On the other hand, for **2**, the spin density demonstrated that the HOMO−1 in the molecular orbital 109α displayed the metal-metal interaction on Ti atoms *via* molecular orbitals of the bridged Cl atoms (see supporting information). The Ti-Ti distances in the optimized structures for **1** (4.0153 Å) and **2** (4.063 Å) were slightly elongated in comparison with that (3.943 Å and 3.968 Å) in the crystal structure of dimeric [$(Cp_2TiCl)_2$] complex in the triplet state reported previously (see Table B1 in Appendix B).[13] In comparison with [$(Cp_2TiCl)_2$] in the singlet and triplet states calculated by using B3LYP/def2-TZVP, the Ti-Ti distances are also slightly elongated in comparison with those model complexes (3.91615 Å for singlet state, 3.94936 Å for triplet state) (see Table B1). Accordingly, the structures of model complexes **1** and **2** calculated by BP86/TZVP are almost agreement with those of [$(Cp_2TiCl)_2$] calculated by B3LYP/def-TZVP reported in previous literature.[14]

The optimized structure of **3** is similar to the crystal structure of [Cp^*_2TiCl] previously reported.[24] Although the Ti−Cl bond length (2.380 Å) for **3** is similar to that (2.363 Å) of [Cp^*_2TiCl] crystal, the angle of Cp ring centroid−Ti−Cp ring centroid for **3** (134.70 deg) is smaller than that (143.6 deg) in [Cp^*_2TiCl] crystal, which may have been widen by steric hindrance of methyl groups on Cp* rings. In the optimization of [$Cp_2TiCl(N_2)$] complex (**4**) coordinated with N_2, the N-N bond length was calculated to be 1.120 Å, which was slightly longer than that (1.0977 Å) of free N_2 molecule. The distances of Ti−N and Ti−Cl bonds were estimated to be 2.116 and 2.477 Å, respectively. The angle Ti−N−N (178.26 deg.) was almost linear and the Cl−Ti−N was 84.88 deg. In the optimized structure of **4-TS**, N-N bond length was calculated to be 1.1069 Å, which is slightly shorter than that of **4**. The distances of Ti−N and Ti−Cl bonds were estimated to be 2.9406 and 2.4175 Å, respectively. The angle Ti−N−N (158.70 deg.) and Cl−Ti−N (79.60 deg) were smaller than those of **4**.

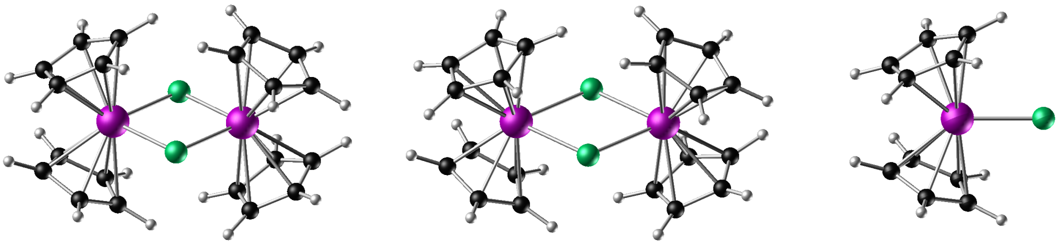

[$(Cp_2TiCl)_2$] (singlet) (**1**) [$(Cp_2TiCl)_2$] (triplet) (**2**) [Cp_2TiCl] (**3**)

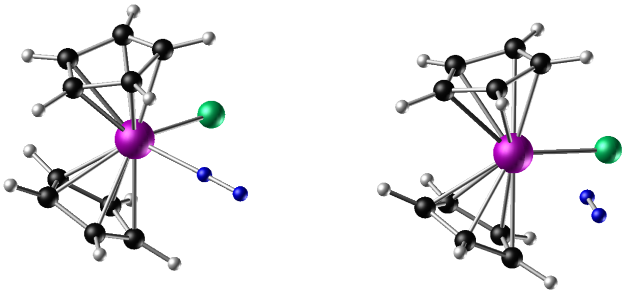

[Cp_2TiClN_2] (**4**) [Cp_2TiClN_2]-TS (**4-TS**)

Figure 3-8. Optimized structures of [$(Cp_2TiCl)_2$] in the singlet (**1**) and triplet states (**2**), [Cp_2TiCl] (**3**), [Cp_2TiClN_2] (**4**) and [Cp_2TiClN_2] in the transition state (**4-TS**) (purple: Ti atom, green: Cl atom, black: C atom, blue: N atom and White: H atom). The bond lengths and angles are presented in Å and degree, respectively. Important bond parameters for **1**: Ti···Ti 4.0153, Ti-Cl 2.5953. For **2**: Ti···Ti 4.063, Ti-Cl 2.597. For **3**: Ti-Cl 2.380. For **4**: Ti-Cl 2.477, Ti-N 2.116, N-N 1.120, Ti-N-N 178.26, N-Ti-Cl 84.88. For **4-TS**: Ti-Cl 2.477, Ti-N 2.116, N-N 1.107, Ti-N-N 158.96, N-Ti-Cl 79.53.

3.2.5 Evaluation of equilibrium reactions based on calculated Gibbs energies of the titanocene derivatives.

Next, we tried to evaluate the equilibrium reactions among species **1**- **4** in toluene and IL under N_2, and the computed reaction profiles of the equilibrium reactions were analyzed. The equilibrium reactions among these complexes were discussed by using *Δ*H (kcal/mol) instead of ΔG (kcal/mol) (see Figure B24 in Appendix B), because of the well-known erroneous computational analyses of the variation of entropy for a reaction where two reactants give only one product in solution.[25] The *Δ*Hs for **1-5** at 298.15 K in toluene and IL are shown in Figure 3-9.

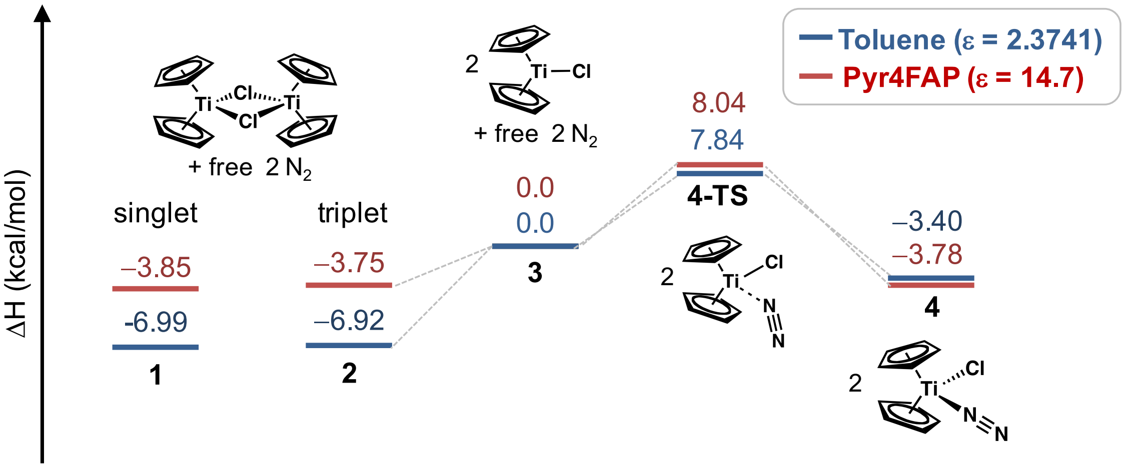

Figure 3-9. Computed profile of the equilibrium reactions among **1**, **2**, **3**, **4**, and **4-TS** in toluene (ε = 2.3741) (red) and Pyr$_4$FAP (ε = 14.7) (black), as estimated at 298.15 K.

The *Δ*H values (kcal/mol), as estimated based on the sum of enthalpies of the two monomeric [Cp_2TiCl] (**3**) and two free N_2 molecules, were evaluated in each solvent. In toluene, the calculated ΔH value for **1** was estimated to be −6.92 kcal/mol and that for **2** was −6.99 kcal/mol, indicating that **2** is slightly stable at 298.15 K as compared with **1**. For the equilibrium reaction between **1** and **2**, it is known that the ground state of **2** in the triplet state is close to the singlet state at a low temperature.[11-14]

Interestingly, the *Δ*H values of **1** (−3.85 kcal/mol) and **2** (−3.75 kcal/mol) in IL are higher than those (−6.99 and −6.75 kcal/mol, respectively) in toluene. On the other hand, those of **4-TS** (8.04 kcal/mol) and **4** (−3.78 kcal/mol) in IL are similar to those (7.84 and −3.40 kcal/mol, respectively) in toluene. To further discuss the influence of the dielectric permittivity for model complexes, the dipole moments (Debye) for the optimized all model complexes are summarized in Table 3-1 and compared. Interestingly, it suggests that the model complex with a small dipole moment, such as **1** and **2**, is stabilized by non-polar solvent with a small dielectric permittivity, in other words, a polar solvent destabilizes **1** and **2** with small dipole moment.

Table 3-1. Summary of dipole moments (Debye) for model complexes

Solvent (dielectric permittivity)	**1**	**2**	**3**	**4-TS**	**4**
Pyr_4FAP (14.7)	0.14	0.058	5.0	5.5	6.4
Toluene (2.3741)	0.0022	0.0005	4.2	4.3	5.6

3.2.6 Evaluation of the effect of IL toward 3, 4 and 4-TS.

In order to understand the interaction between titanocene and FAP anion, DFT calculations for model complexes **3, 4** and **4-TS** with FAP anion were performed by using BP86/TZVP with empirical corrections (GD3BJ)[26] and dielectric permittivity of IL ($\varepsilon = 14.7$). The model complexes **3**, **4** and **4-TS** calculated using empirical corrections (GD3BJ) again for comparison are described as **3’**, **4’** and **4’-TS**, and their FAP adducts for **3’**, **4’**, **4’-TS** are described as **3’-FAP**, **4’-FAP** and **4’-FAP-TS.**

The optimized structures for **3’**, **4’**, **4’-TS**, **3’-FAP**, **4’-FAP,** and **4’-FAP-TS** and their structural information are shown in Figures 3-10, B1, B2, B3 and Table B5 in Appendix B. The structures of titanocene in **3’** and **4’** without FAP are similar to those in **3’-FAP** and **4’-FAP** (see Table B5). Interestingly, F atoms in FAP anion have weak interactions with H atoms in Cp rings. The structure of **4’-FAP** is shown in Figure 3-10. The F···H distances between FAP anion and Cp ring are in the range of ca. 2.5 to 2.9 Å as follows; F15···H2 2.4596, F15···H6 2.7927, F15···H7 2.7080, F5···H2 2.6499, F5···H1 2.8546, F10···H1 2.7475, F10···H6 2.6748, and F9···H6 2.5828 Å. Such interactions are also observed in structure of **3’-FAP**. Although we also expected weak interaction of F atom with the coordinated N_2, the N-N bond distance (N1-N2 1.119 Å) for **4’-FAP** is the same as that of **4** (N1-N2 1.119 Å) and the F atom in FAP anion is near the coordinated N_2 atoms (F10···N1 3.2935, F10···N2 3.2999 Å). To confirm the interaction between FAP anion and the N_2 molecule coordinated to [Cp_2TiCl], Mulliken charges on N atoms of **4’-FAP** were estimated. However, the charges on N atoms of **4’-FAP** (N1: 0.071401, N2: −0.172722) were unfortunately similar to those of **4’** (N1: 0.074238, N2: −0.173357), indicating that the F atom has only little interaction toward N_2 molecule.

To consider the effect of the interaction in the energy profile, the computed profile of the equilibrium reactions among **3’**, **4’**, **4’-TS**, **3’-FAP**, **4’-FAP**, and **4’-FAP-TS** were shown in Figure 3-11. The ΔH values (kcal/mol) are based on the enthalpy of **3’** with free FAP anion and free N_2 molecule. ΔH of **3’-FAP** is estimated to be −2.54 kcal/mol, indicating that FAP anion stabilized **3’** through weak interaction between H atoms on the Cp ring and F atoms in FAP anion. The ΔH of **4’-TS** as the transition state of N_2 adduct of **3’** is estimated to be −0.37 kcal/mol, which is very close to that of **3**’ with free

N_2 molecule. The *Δ*H value of **4’-TS** in the transition state might be estimated to be low due to the dispersion corrections. The *Δ*H value of **4’-FAP-TS** (−3.46 kcal/mol) is also affected by the weak interaction, and therefore, the *Δ*H is lower than that of **4’-TS**. In addition, the *Δ*H of **4’-FAP** (−11.3 kcal/mol) is lower than that of **4’** (−7.81 kcal/mol), also suggesting that FAP anion stabilized **4’**. These findings suggest that the N_2 coordination to [Cp_2TiCl] is occurred in polar domain of Pyr_4FAP that weakly interacts to the transition metal complex.

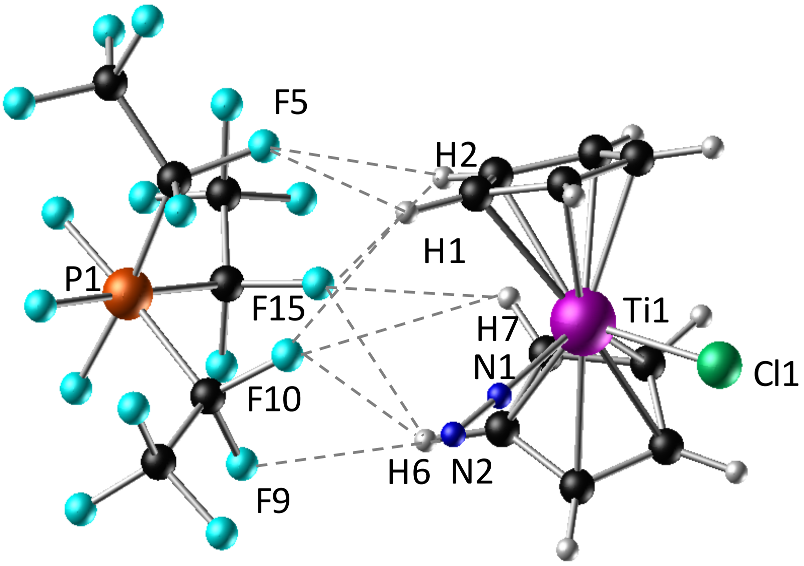

Figure 3-10. The optimized structure of **4’-FAP**. Selected bond lengths (Å) and angles (deg.) for **4’-FAP**: Ti1-Cl1 2.4779, Cp1(centroid)-Ti1 2.0529, Cp1(centroid)-Ti1-Cp2(centroid) 134.6, Cp1(centroid)-Ti-Cl1 107.8, N1-N2 1.1196, Ti1-N1 2.0987, Ti1-N1-N2 178.77, N1-Ti1-Cl1 84.9, F15···H1 3.8974, F15···H2 2.4596, F15···H6 2.7927, F15···H7 2.7080, F5···H2 2.6499, F5···H1 2.8546, F10···H1 2.7475, F10···H6 2.6748, F10···N1 3.2935, F10···N2 3.2999, F9···H6 2.5828.

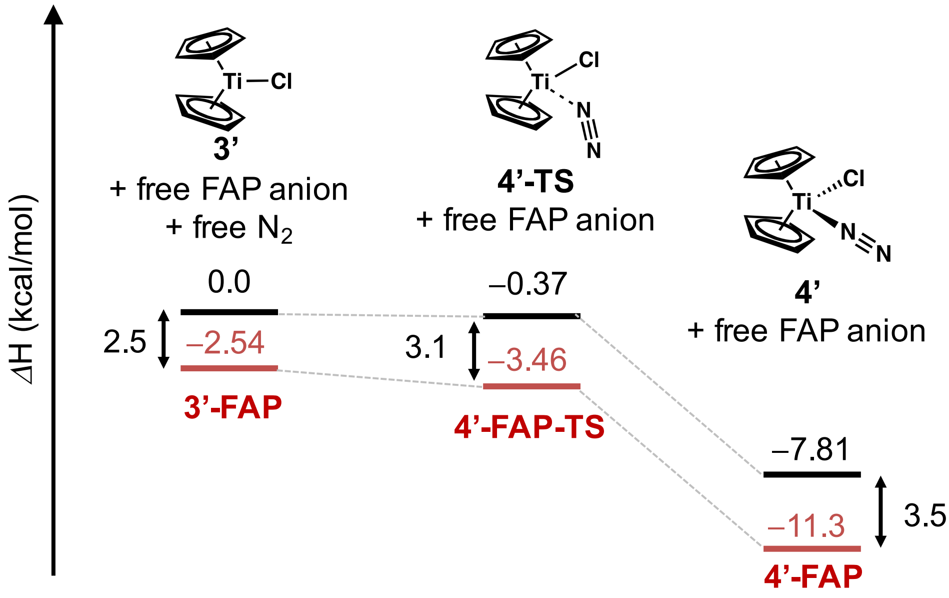

Figure 3-11. Computed reaction profile of the equilibrium reaction calculated by BP86/TZVP with empirical corrections (GD3BJ) among **3'**, **4'** and **4-TS** without FAP anion (black) and **3'-FAP**, **4'-FAP** and **4'-FAP-TS** with FAP (red) in Pyr$_4$FAP (ε=14.7) at 298.15 K.

3.2.7 Mechanism of N_2 coordination to 3 achieved in IL

On the basis of the above findings obtained by DFT calculations, we evaluated the mechanism of N_2 coordination to **3** in IL, as shown in Scheme 3.2. The IL is known to have both of polar and nonpolar domains.[27,28] For instance, in the case of 1-butyl-3-methylimidazolium hexafluorophosphate, [C$_4$mim][PF$_6$], the total dielectric permittivity has been reported to be ε = ca.14.0 but those in polar and nonpolar domains have been estimated to be ca. 20 and 2.5, respectively.[23] For Pyr$_4$FAP, it would also have domain structures, although the accurate ε values of polar and nonpolar domains have been unknown. Accordingly, the equilibrium reaction in nonpolar domain of IL would be similar to that in nonpolar non-coordinating solvent, such as toluene. On the other hand, the equilibrium reaction in polar domain of IL would be affected by forming a complex with anion. Therefore, other reaction mechanism would exist in IL unlike in conventional organic solvents. In this study, we can propose that the equilibrium reaction in polar domain of IL has that between **3** and **4** in addition to those among **1**, **2** and **3**. As a result, the N_2 coordination to [Cp_2TiCl] would be observed in non-coordinating IL by frozen solution EPR spectroscopy.[9]

Scheme 3.2. Schematic drawing of (A) the estimated equilibrium reactions among **1**, **2** and **3** in nonpolar domain of in Pyr_4FAP and (B) that between **3** and **4** in polar domain of Pyr_4FAP

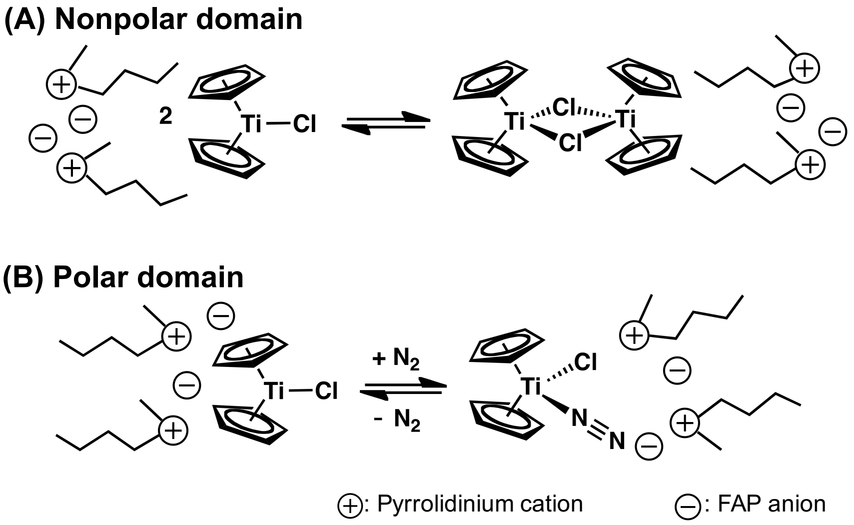

3.2.8 TD-DFT calculations for [Cp_2TiCl] and [$(Cp_2TiCl)_2$] in ionic liquid

UV-vis/NIR spectrum of [$(Cp_2TiCl)_2$] in Pyr_4FAP (Figure 3-4) gave the absorption bands at 449, 697, 817, and 1167 nm, respectively. To characterize the absorption bands, TD-DFT calculations for **1**, **2**, **3**, and **4** in IL were carried out. The calculated TD-DFT absorption bands are shown in Figure 3-12 and Table B6-B9 in Appendix B. In the range of 900 to 1100 nm, the absorption band for **2** in the excited state 2 are in good agreement with the absorption band at 1167 nm as shown in Figure 3-12 (see Figure B7, B8, B9, B10 and Table B7). The excited state 2 consists of the transition from molecular orbital 109α (HOMO−1) to 111α (LUMO). Accordingly, the absorption bands at 1167 nm is characterized to MMCT. In the range of 500 to 900 nm, the absorption bands of **2** in the excited states 3 and 5 (see Figure B7, B8, B9, B10 and Table B7), **3** in the excited states 2 and 3 (see Figures B11, B12, B13 and Table B8), and **4** in the excited states 1 and 4 (see Figures B14, B15, B16 and Table B10) were observed. These absorption bands are characterized to the d-d transitions on Ti atom except for the absorption band of **4** in the excited state 4.

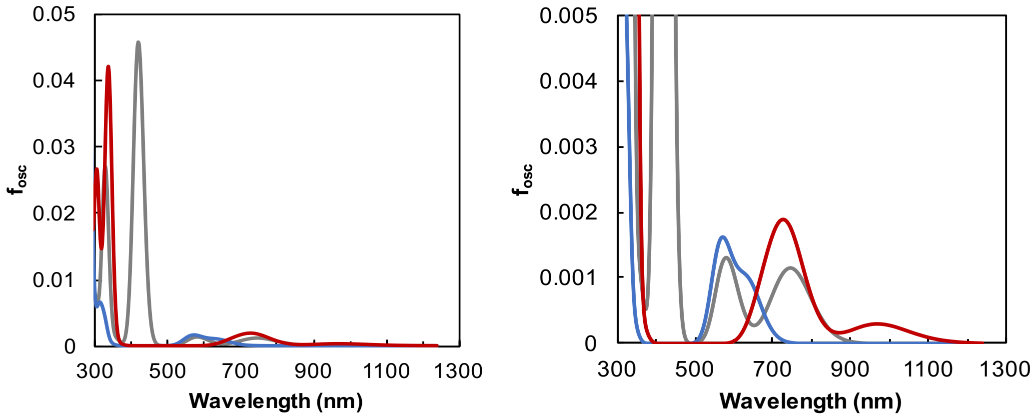

Figure 3-12 Absorption spectra of complex **2** (red), **3** (blue), and **4** (grey) in Pyr$_4$FAP (ε = 14.7) calculated by TD-DFT

The absorption band of **4** in the excited state 4 is characterized to the charge transfer from d-orbital on Ti atom to π* orbital on N atom of the coordinating N_2 (MLCT). Therefore, absorption bands at 697 and 817 nm shown in Figure 3-4 are characterized to the d-d transitions for **2** and **3**. The absorption bands for **2** and **3** have strong absorption bands at around 300 nm derived from the charge transfer from the π orbitals on Cp ring to the d orbital on Ti atom (LMCT). Therefore, the absorption band at 449 nm shown in Figure 3-4 is characterized to the LMCT. The absorption band of **4** in the excited state 6 is observed the transition at 418 nm, which is closer to the absorption band at 449 nm shown in Figure 3-4 than LMCT of **2** and **3** at ca. 300 nm. The N_2 coordination to [Cp_2TiCl] would be occurred at lower temperature than r.t. or the amounts of **4** in IL at r.t. might be not so much to detect it.

3.3 Conclusion

To understand the electrochemical synthesis of ammonia by using [Cp_2TiCl_2] in ionic liquids described in Chapter 2, the electrochemical reduction of [Cp_2TiCl_2] in both of conventional organic solvents and the ionic liquids were investigated by using UV-vis/NIR spectroscopy during electrochemical reduction. Even in non-coordinating Pyr_4FAP, the absorption band at 1194 nm was observed by electrochemical reduction from Ti(IV) to (III) in [Cp_2TiCl_2]. The observed absorption band at ca. 1200 nm is also observed in the UV-vis/NIR spectrum of dimeric [$(Cp_2TiCl)_2$] in Pyr_4FAP, which is in good agreement with the absorption bands calculated with TDDFT method, which was assigned to MMCT. The characteristic absorption band at ca. 1200 nm was also observed in THF and Pyr_4OTf, which can be coordinated with [Cp_2TiCl] via Ti-O bond. Accordingly, the UV-vis/NIR spectra of [Cp_2TiCl_2] (**1**) in Pyr_4FAP, Pyr_4OTf and 0.2 M Pyr_4FAP/THF during the electrochemical reduction of Ti(IV) to Ti(III) demonstrate [$(Cp_2TiCl)_2$] (**2**) was generated from [Cp_2TiCl_2]$^-$ in these three solvents.

To understand the equilibrium reaction between dimeric [$(Cp_2TiCl)_2$] and monomeric [Cp_2TiCl], frozen solution EPR spectroscopy for [$(Cp_2TiCl)_2$] in Pyr_4FAP was studied in non-coordinating ionic liquid, 1-butyl-1-methylpyrrolidinium tris(pentafluoroethyl) trifluorophosphate (Pyr_4FAP), and organic solvents of 0.2 M Pyr_4FAP/THF and toluene under N_2. Interestingly, the spectrum measured in non-coordinating ionic liquid under $^{14}N_2$ gave a triplet hyperfine splitting of the g_z signal, which was changed to a doublet pattern in the isotopic labeling experiment using $^{15}N_2$. However, the EPR spectra in organic solvents did not have such a hyperfine splitting at the g_z signal.

These observations demonstrate that [$(Cp_2TiCl)_2$] is in the equilibrium between monomeric and dimeric species in both ionic liquid and organic solvents, and furthermore that the monomeric species is coordinated to dinitrogen in the non-coordinating ionic liquid, Pyr_4FAP. These findings may also indicate that Pyr_4FAP has special properties capable of stabilizing the N_2 coordinated-[Cp_2TiCl] species.

With a view to understanding the effect of ILs toward the N_2 coordination to monomeric [Cp_2TiCl], DFT calculations were carried out for dimeric [$(Cp_2TiCl)_2$] in the singlet (**1**) and triplet states (**2**), monomeric [Cp_2TiCl] (**3**), [$Cp_2TiCl(N_2)$] (**4**), and [$Cp_2TiCl(N_2)$]‡ in the transition state (**4-TS**) in toluene and IL, in which the effects of solvents were examined with applying their dielectric permittivities. The DFT studies revealed that ΔH values for **1** (−6.99 kcal/mol) and **2** (−6.92 kcal/mol) in toluene were lower than those in IL (−3.85 kcal/mol for **1** and −3.75 kcal/mol for **2**, respectively). These results are well consistent with the experimental findings that the model complexes with a small dipole moment have been stabilized by the solvents with a small dielectric permittivity. Moreover, to consider the effect of FAP anion toward N_2

coordination to titanocenes, we further calculated **3**, **4** and **4-TS** with FAP anion (**3'-FAP**, **4'-FAP** and **4'-FAP-TS)** with empirical corrections (GD3BJ). Though the structures of titanocene in **3'-FAP** and **4'-FAP** are similar to those of **3'** and **4'** without FAP anion, respectively, F atoms in FAP anion had weak interactions toward H atoms on Cp ring. It suggests that the interactions have contributed to stabilize **3'-FAP** and **4'-FAP** and lowered the activation energy of the N_2 coordination reaction in **4'-FAP-TS**. The N_2 coordination to [Cp_2TiCl] was occurred in polar domain of Pyr_4FAP due to formation of a complex with anion of IL, and therefore, it would have been observed by frozen solution EPR spectroscopy.[9]

In general, the IL is known to have polar and nonpolar domain structures, which are composed of ionic parts and alkyl chain parts, respectively. In nonpolar domain, **3** is in equilibriums with **1** and **2** that have only a small dipole moment. Although most of polar conventional solvents act as coordinating solvent against unsaturated transition metal complexes, the polar domain in Pyr_4FAP acts as non-coordinating polar solvent toward transition metal center. However, Pyr_4FAP weakly interacts with titanocene to form a complex with anion of IL. Such weak interactions with anion parts of IL would be observed in the case of using conventional anion, such as triflate and so on. Therefore, it is one of the key factors and reason why the reactivity in IL is different from those in conventional organic solvents.

3.4 Experimental

All manipulations were performed using standard Schlenk-line techniques or in an MBraun dry box under Ar or N_2 atmosphere (< 1 ppm O_2 /H_2O).

3.4.1 Chemicals

Bis(cyclopentadienyl)titanium(IV) dichloride, [Cp_2TiCl_2], was purchased from Tokyo Chemical Industry Co., Ltd. Bis(pentamethylcyclopentadienyl)titanium(IV) dichloride, [$Cp^*{}_2TiCl_2$], was purchased from Wako Pure Chemical Industries Ltd. Bis(cyclopentadienyl)vanadium(IV) dichloride, [Cp_2VCl_2], was purchased from Sigma-Aldrich. These reagents were used after recrystallization from hexane. 1-Butyl-1-methylpyrrolidinium tris(pentafluoroethyl)trifluorophosphate, Pyr_4FAP,[29] was purchased from Merck Ltd. and purified referring to previous literature (see Section 3.4.2 purification of ionic liquid).[30] KC_8 was prepared according to the literature.[31] Solvents were purified by the method of Grubbs,[32] where the solvents were passed over columns of activated alumina and supported copper catalyst supplied by ultimate purification system (Glass Contour System, NIKKO HANSEN & CO., LTD), transferred to the glovebox without exposure to air, and stored over molecular sieves 4Å. Bis[(dicyclopentadienyl)titanium(III) chloride], [$(Cp_2TiCl)_2$], and bis[(dipentamethylcyclopentadienyl)titanium(III) chloride], [$Cp^*{}_2TiCl$], were synthesized according to the literature.[33, 34]

3.4.2 Purification of ionic liquid

Pyr_4FAP (50 g) was dissolved in distilled EtOH (100 mL), and to the solution was added an activated charcoal (5g, Sigma-Aldrich). And then, the activated charcoal was remove by filtrate and the solvent was removed by evaporator. If the color was not colorless, the purification was repeated using the activated charcoal. After the purification was finished, Pyr_4FAP was vacuumed at 80°C for 3 days and dried over molecular sieves (4 Å) for 1 week.

3.4.3 Instrumentation

Electrochemistry was studied using a potentiostat (BAS, ALS/600). UV−vis/NIR absorption spectra were measured with a Jasco V−770 spectrophotometer using a 1 mm light-pass−length quartz cell. X-band EPR spectra of frozen solution were recorded at 77 K using JEOL RE-1X ESR spectrometer.

3.4.4 Measurement of EPR spectra under $^{14}N_2$ atmosphere

The sample preparation was carried out in the glove box under $^{14}N_2$ atmosphere. Pyr$_4$FAP, which was stirred for 1 week under $^{14}N_2$, was used for EPR measurement. The concentration of [(Cp$_2$TiCl)$_2$] was adjusted to 1 mM for each solvent. EPR tube (ϕ 4 mm) with a ground glass joint (15/25) was employed as the glass stopper (15/25) for measurement under $^{14}N_2$.

3.4.5 Measurement of EPR spectra under $^{15}N_2$ atmosphere

The sample preparation was carried out in the glove box under Ar atmosphere. Pyr$_4$FAP used was vacuumed overnight, and then, stirred for 1 week under $^{15}N_2$ before use. The $^{15}N_2$ gas (99.9 Atom %), which was purchased from SI Science Co., Ltd., was purified by passing the column containing KC$_8$ (see Figure C1 in Appendix C), and used after replacement of the gas from Ar to $^{15}N_2$ by using vacuum line equipped in the glovebox. The replacement is carried out by connecting the gas outlet with vacuum line and the gas inlet with $^{15}N_2$ gas cylinder. The concentration of [(Cp$_2$TiCl)$_2$] was adjusted to 1 mM for each solvent. EPR tube (ϕ 4 mm) with a ground glass joint (15/25) was used with a three-way glass stopcock (15/25) for measurement under $^{15}N_2$ atmosphere. After adding the sample in EPR tube, the atmosphere in EPR tube was replaced from Ar to $^{15}N_2$.

3.4.6 UV-vis/NIR spectra during controlled potential electrolysis (CPE)

UV-vis/NIR spectra during electrochemical reduction were measured by using 1 mm length quartz cell welded with the Pyrex glass tube with an interchangeable ground joint (15/25), a Teflon adapter and electrodes (Figure A1 in Appendix A). Pt mesh and Pt wire were purchased from Nilaco Co., Ltd. Pt mesh (diameter: φ0.08 mm, 80 mesh, 0.8 cm × 3 cm) connected with Pt wire (diameter: φ0.25 mm, length: 6 cm) was used as working electrode (WE). Pt mesh, whose reaction area is three times larger than WE, connected with Pt wire was used as the counter electrode (CE). Pt wire (diameter: φ0.25 mm, length: 3 cm) was used as quasi-reference electrode (QRE). The Cu wires as lead line for connection between electrodes and potentiostat were fixed to PTFE tube (outside diameter: 6.0 mm, inside diameter: 5.0 mm, FLON INDUSTRY CO., LTD.) by using one-component RTV rubber (KE45, Shin-Etsu Silicon). PTFE tube containing three Cu wire was kept overnight for fixing the RTV rubber. The PTFE tube with Cu wires was jointed to the quartz cell by using a Teflon tube adapter (F-5005-004, outside diameter: φ6 mm, inside diameter: 5.0 mm, interchangeable ground joint: 15/25, FLON INDUSTRY CO., LTD.). For increasing the airtightness of the connecter with PTFE tube containing Cu wires, a silicon grease was coated. For preventing a contact of electrodes and lead lines each other, the Pt wire of the electrodes were covered by PTFE tube (outside diameter: 1.0 mm, inside diameter: 0.5 mm, FLON INDUSTRY CO., LTD.), and Cu wires bared partly in UV-vis/NIR cell side were wrapped with parafilm. The setting was performed in the globe box. Therefore, the measurements were carried out under Ar atmosphere. The blank solution without [Cp_2TiCl_2], which is containing only solution in the quartz cell with electrodes as shown in Figure A1, was measured as base line. To decide the potential of CPE, a linear sweep voltammogram (LSV) was measured. The initial UV-vis/NIR spectra, which are described as 0 s in Figures 3-1, 3-2 and 3-3, were recorded after the LSV measurement. The subsequent UV-vis/NIR spectra were measured during the controlled potential electrolysis.

3.4.7 DFT and TDDFT calculations

All electronic structure calculations were performed with the Gaussian 09 package[35] on the Fujitsu HX600 system at the Nagoya University Information Technology Center. Geometry optimizations of dimeric [$(Cp_2TiCl)_2$] in the singlet (**1**) and triplet states (**2**), monomeric [Cp_2TiCl] (**3**), [$Cp_2TiCl(N_2)$] (**4**), and [$Cp_2TiCl(N_2)$] in the transition state (**4-TS**) as model complexes were performed using BP86 functional[19] in combination with a polarized valence triple-ζ basis set (TZVP) for all atoms.[20] Contribution of solvents of toluene and THF were applied using the polarized continuum model (PCM).[36] In the DFT calculation with solvation effect of IL, the dielectric permittivity of Pyr_4FAP was applied with ε =14.7 at 25 °C for 1-butyl-1-methylpyrrolidinium bis(trifluoromethylsulfonyl)imide (Pyr_4NTf_2), which is similar structure to Pyr_4FAP.[37] DFT calculations of **3**, **4** and **4-TS** added with FAP anion, **3-FAP**, **4-FAP**, and **4-FAP-TS,** were further carried out. In the DFT calculations for **3-FAP**, **4-FAP**, and **4-FAP-TS**, BP86/TZVP as functional and basis sets treated with the D3 version of Grimme's dispersion with Becke − Johnson damping (GD3BJ)[27] with dielectric permittivity of IL (ε = 14.7) was applied to consider the interaction between titanocene and FAP anion. To assign the absorption bands of electronic transitions, time-dependent density functional theory (TD-DFT) calculations[38] were performed, and the results are described in Supporting Information. For simulation of UV-vis spectra, the absorption profiles were calculated as a sum of Gaussian functions, where the heights and centers of the peaks were oscillator strengths and excitation energies, respectively, and the standard deviations were 0.1 eV. The isosurfaces of the molecular orbitals were drawn using the MOPLOT and MOVIEW programs.[39]

3.5 References

1. J. Y. Becker, S. Avraham (Tsarfaty) and B. Posin, *J. Electroanal. Chem.*, **1987**, *230*, 143.
2. S. Stevanoic, and M. F. Costa Gomes, *J. Chem. Thermodynamics* **2013**, *59* 65.
3. M. Okuniewski, K. Paduszyński, and U. Domańska, *J. Chem. Eng. Data*, **2016**, *61*, 1296.
4. A. Katayama, T. Inomata, T. Ozawa and H. Masuda, *Dalton Trans.*, **2017**, *46*, 7668-7671.
5. Metal to metal charge transfer (MMCT) transition: An electronic transition of a bi- or poly-nuclear metal complex that corresponds to excitation populating an electronic state in which considerable electron transfer between two metal centres has occurred. PAC, 1996, 68, 2223 (Glossary of terms used in photochemistry (IUPAC Recommendations 1996)) on page 2254.
6. (a) R. J. Enemærke, J. Larsen, T. Skrydstrup and K. Daasbjerg, *J. Am. Chem. Soc.*, **2004**, *126*, 7853. (b) R. J. Enemærke, J. Larsen, T. Skrydstrup and K. Daasbjerg, *Organometallics*, **2004**, *23*, 1866.
7. A. Katayama, T. Inomata, T. Ozawa and H. Masuda, *Electrochem. Commun.* **2016**, *67*, 6.

8. A. Rosales, I. Rodríguez-García, J. Muñoz-Bascón, E. Roldan-Molina, N. M. Padial, L. P. Morales, M. García-Ocaña, and J. E. Oltra, *Eur. J. Org. Chem.*, **2015**, 4567.
9. R. S. P. Coutts, P. C. Wailes and R. L. Martin, *J. Organomet. Chem.*, **1973**, *47*, 375.
10. F. J. Liotta, G. V. Duyne, and B. K. Carpenter., *Organometallics*, **1987**, *6*, 1010.
11. R. S. P. Coutts, R. L. Martin, and P. C. Wailes, *Aust. J. Chem.*, **1973**, *26*, 2101.
12. $\chi_m=(g^2N\beta^2/3k_BT)\{1+1/3\exp(-J/k_BT)\}^{-1}$ in B. N. Figgis and R. L. Martin, *J. Chem. Soc*. **1956**, 3837.
13. R. Jungst, D. Sekutowski, J. Davis, M. Luly and G. Stucky, *Inorg. Chem.*, **1977**, *16*, 1645.
14. (a) R. L. DeKock, M. A. Peterson, L. E. L. Reynolds, L. H. Chen, E. J. Baerends and P. Vernooijs, *Organometallics*, **1993**, *12*, 2794. (b) M. Benard and M. M. Rohmer, *J. Am. Chem. Soc.*, **1992**, *114*, 4785. (c) C. Wolff, A. Gottschlich, J. England, K. Wieghardt, W. Saak, D. Haase and R. Beckhaus, *Inorg. Chem.*, **2015**, *54*, 4811.
15. A. Gunn, E. R. Derbyshire, M. A. Marletta and R. D. *Britt, Biochemistry*, **2012**, *51*, 8384. (b) J. Hüttermann, C. Burgard, and R. Kappl, *J. Chem. Soc. Faraday Trans*, **1994**, *90*, 3077.
16. (a) N. Beydoun, R. Duchateau, and S. Gambarotta, *J. Chem. Soc., Chem. Commun.*, **1992**, 244. (b) J. R. Hagadorn and J. Arnold, *J. Am. Chem. Soc.*, **1996**, *118*, 893. (c) L. Morello, P. Yu, C. D. Carmichael, B. O. Patrick, and M. D. Fryzuk, *J. Am. Chem. Soc.*, **2005**, *127*, 12796. (d) T. Kurogi, Y. Ishida and H. Kawaguchi, *Chem. Commun.*, **2013**, *49*, 11755.
17. E. Samuel and J. Vedel, *Organometallics*, **1989**, *8*, 237.

18. (a) M. Schmeisser and R. van Eldik, *Inorg. Chem.*, **2009**, *48*, 7466. (b) S. Kern and R. van Eldik, *Inorg. Chem.*, **2012**, *51*, 7340. (c) M. Schmeisser, F. W. Heinemann, P. Illner, R. Puchta, A. Zahl, and R. van Eldik, *Inorg. Chem.*, **2011**, *50*, 6685. (d) S. Begel, F. W. Heinemann, G. Stopa, G. Stocheland and R. van Eldik, *Inorg. Chem.*, **2011**, *50*, 3946. (e) S. Begel, P. Illner, S. Kern, R. Puchta, and R. van Eldik, *Inorg. Chem.*, **2008**, *47*, 7121. (f) P. Illner, S. Begel, S. Kern, R. Puchta, and R. van Eldik, *Inorg. Chem.*, **2009**, *48*, 588. (g) K. Pokornv, M. Schmeisser, F. Hampel, A. Zahl, R. Puchta, and R. van Eldik, *Inorg. Chem.*, **2013**, *52*, 13167. (h) S. Begel, R. Puchta, J. Sutter, F. W. Heinemann, L. Dahlenburgand, and R. van Eldik, *Inorg. Chem.*, **2015**, *54*, 6763. (i) C. Sievers, O. Jimenez, T. E. Müller, S. Steuernagel, and J. A. Lercher, *J. Am. Chem. Soc.*, **2006**, *128*, 13990.
19. (a)A. D. Becke, *Phys. Rev. B*, **1988**, *38*, 3098. (b) J. P. Perdew, *Phys. Rev. B*, **1986**, *33*, 8822.
20. A. Schäfer, C. Huber, and R. Ahlrichs, *J. Chem.Phys*., **1994**,*100*, 5829.
21. A. Gansäuer, A. Barchuk, F. Keller, M. Schmitt, S. Grimme, M. Gerenkamp, C. Mück-Lichtenfeld, K. Daasbjerg and H. Svith, *J. Am. Chem. Soc.*, **2007**, *129*, 1359.
22. J. Larsen, R. J. Enemærke, T. Skrydstrup and K. Daasbjerg, *Organometallics*, **2006**, *25*, 2031.
23. M. Huang, Y. Jiang, P. Sasisanker, G. W. Driver and H. Weingärtner, *J. Chem. Eng. Data*, **2011**, *56*, 1494.
24. J. W. Pattiasina, H. J. Heeres, F. Van Bolhuis, A. Meetsma, J. H. Teuben and A. L. Spek, *Organometallics*, **1987**, *6*, 1004.
25. L. Watson and O. Eisenstein, *J. Chem. Educ*. **2002**, *79*, 1269.
26. (a) S. Grimme, J. Antony, S. Ehrlich and H. Krieg, *J. Chem. Phys.* **2010**, *132*,

154104－1－154104－19. (b) S. Grimme, S. Ehrlich and L. Goerigk, *J. Comput. Chem.* **2011**, *32*, 1456－1465.

27. O. Yamamuro, T. Yamada, M. Kofu, M. Nakakoshi and M. Nagao, *J. Chem. Phys.*, **2011**, *135*, 054508.
28. M. Mizoshiri, T. Nagao, Y. Mizoguchi and M. Yao, *J. Chem. Phys.*, **2010**, *132*, 164510.
29. N.V. Ignat'ev, U. Welz-Biermann, A. Kucheryna, G. Bissky and H. Willner, *J. Fluorine Chem.*, **2005**, *126*, 1150.
30. K. Burrell, R. E. Del Sesto, S. N. Baker, T. M. McCleskeya and G. A. Baker, *Green Chem.*, **2007**, *9*, 449.
31. D. E. Bergbreiter and J. M. Killough, *J. Am. Chem. Soc.*, **1978**, *100*, 2126–2134.
32. B. Pangborn, M. A. Giardello, R. H. Grubbs, R. K. Rosen and F. J. Timmers, *Organometallics*, **1996**, *15*, 1518.
33. R. P. Spencer, C. L. Cavallaro, and J. Schwartz, *J. Org. Chem.*, **1999**, *64*, 3987.
34. J. W. Pattiasina, H. J. Heeres, F. V. Bolhuis, A. Meetsma, J. H. Teuben and A. L. Spek, *Organometallics*, **1987**, *6*, 1004.
35. M. J. Frisch, G. W. Trucks, H. B. Schlegel, G. E. Scuseria, M. A. Robb, J. R. Cheeseman, G. Scalmani, V. Barone, B. Mennucci, G. A. Petersson, H. Nakatsuji, M. Caricato, X. Li, H. Hratchian, A. F. Izmaylov, J. Bloino, G. Zheng, J. L. Sonnenberg, M. Hada, M. Ehara, K. Toyota, R. Fukuda, J. Hasegawa, M. Ishida, T. Nakajima, Y. Honda, O. Kitao, H. Nakai, T. Vreven, J. A. Jr. Montgomery, J. E. Peralta, F. Ogliaro, M. Bearpark, J. J. Heyd, E. Brothers, K. N. Kudin, V. N. Staroverov, T. Keith, R. Kobayashi, J. Normand, K. Raghavachari, A. Rendell, J. C. Burant, S. S. Iyengar, J. Tomasi, M. Cossi, N. Rega, J. M. Millam, M. Klene, J.

E. Knox, J. B. Cross, V. Bakken, C. Adamo, J. Jaramillo, R. Gomperts, R. E. Stratmann, O. Yazyev, A. J. Austin, R. Cammi, C. Pomelli, J. W. Ochterski, R. L. Martin, K. Morokuma, V. G. Zakrzewski, G. A. Voth, P. Salvador, J. J. Dannenberg, S. Dapprich, A. D. Daniels, O. Farkas, J. B. Foresman, J. V. Ortiz, J. Cioslowski and D. J. Fox, Gaussian 09, Revision E.01,; Gaussian, Inc.: Wallingford, CT, 2013.

36. J. Tomasi, B. Mennucci, and R. Cammi, *Chem. Rev.* **2005**, *105*, 2999.
37. M. Huang, Y. Jiang, P. Sasisanker, G. W. Driver and H. Weingärtner, *J. Chem. Eng. Data*, **2011**, *56*, 1494.
38. A. Dreuw and M. Head-Gordon, *Chem. Rev.* **2005**, *105*, 4009.
39. (a) H. Wasada, Y. Tsutsui, *Bull. Coll. Gen. Educ.* **1996**, *33*, 145. (b) I. Takahashi, H. Wasada and Y. Tsutsui, MOVIEW: Program of Nagoya University Information Technology Center Representing Molecular Orbitals and Electron Density Maps by Isosurfaces.

Chapter 4: Electrochemical oxidation of molybdenum(0)-N_2 complex in THF solution and ionic liquid

4.1 Introduction

The effect of ionic liquids toward N_2 coordination of [Cp_2TiCl] is discussed in Chapters 2 and 3. In Chapter 4, the effect of ionic liquids for that of other transition metal-N_2 complex during electrochemical reaction is described.

As described in Chapter 1, Nishibayashi and co-worker reported the turnover numbers for the ammonia production is drastically improved up to 830 equiv based on a dinitrogen-bridged dimolybdenum complex (415 equiv / Mo ion) in the Mo-N_2 complex with PNP pincer ligand and iodide by addition of proton source and reductant in a stepwise fashion.[1] The catalytic cycle, where a protonation for terminal N_2 ligand of dinitrogen complex (M-N_2), formations of diazenide (M-NNH), hydrazide (M≡NNH_2), and hydrazium (M-NNH_3^+), nitride (M≡N) and ammonia (M-NH_3) complexes by protonation and reduction, and regeneration for M-N_2 complex, is proposed. Another novel reaction pathway, where generation of nitride (M≡N) complex via dinitrogen cleavage of the bridging N_2 ligand and formation of ammonia by protonation for five coordinate nitride (M≡N) complex, is proposed as a key point for high catalytic activity. The precursor that is molybdenum (I) bearing tridentate ligands with halogen were able to cleavage the bridging N_2 ligand under N_2.[1]

Inspired by these findings, we considered that five coordinate dimeric molybdenum(I) complex bridging N_2 ligand supporting with only neutral phosphine ligand will cleavage the N_2 ligand and generate molybdenum (IV) nitride complex. Hence, we decided to investigate the electrochemical one electron oxidation reaction for *trans*–[Mo(depe)$_2$(N$_2$)$_2$] (**1**) (depe = 1,2–bis(diethyl)phosphinoethane) to understand reactivity of di-molybdenum(I) bridging N$_2$ ligand supporting neutral phosphine ligand. Herein, we report the UV-vis, FT-IR and resonance Raman spectra during the electrochemical oxidation reaction for **1** in THF solution and DFT calculations for Mo-N$_2$ complexes and discuss the generation of dimeric (μ–N$_2$)[Mo(depe)$_2$(N$_2$)$_2$].

From the obtained findings in Chapter 3, the reactivity of **1** with N$_2$ in Pyr$_4$FAP was described to be different from that in 0.2 M Pyr$_4$FAP/THF. In this Chapter, besides the electrochemical oxidation reaction of **1** in 0.2 M Pyr$_4$FAP/THF, the UV-vis, FT-IR and resonance Raman spectra during the electrochemical oxidation of the Mo-N$_2$ complex, **1**, in Pyr$_4$FAP were discussed on the influence of ionic liquids toward structure and reactivity of Mo-N$_2$ complex by using DFT calculations.

4.2 Results and Discussion

4.2.1 Electrochemical oxidation of Mo-N$_2$ complex in THF solution

4.2.1.1 FT-IR spectra during electrochemical oxidation

To understand the redox behaviors of *trans*–[Mo(depe)$_2$(N$_2$)$_2$] (**1**), cyclic voltammogram (CV) of **1** in THF containing 0.2 M Pyr$_4$FAP (0.2 M Pyr$_4$FAP/THF) was measured, which is shown in Figure 4-1. The redox potential, $E_{1/2}$, assignable to Mo(0)/Mo(I) is observed at −1.01 V (vs. Fc/Fc$^+$), and the oxidation wave assignable to Mo(I)/Mo(II) is observed at −0.02 V (vs. Fc/Fc$^+$), which is in good agreement with the $E_{1/2}$ for Mo(0)/Mo(I) of *trans*–[Mo(depe)$_2$(N$_2$)$_2$] measured using Pt electrode in THF containing 0.2 M [NBu$_4$][BF$_4$] (−0.43 V vs. SCE).[2,3]

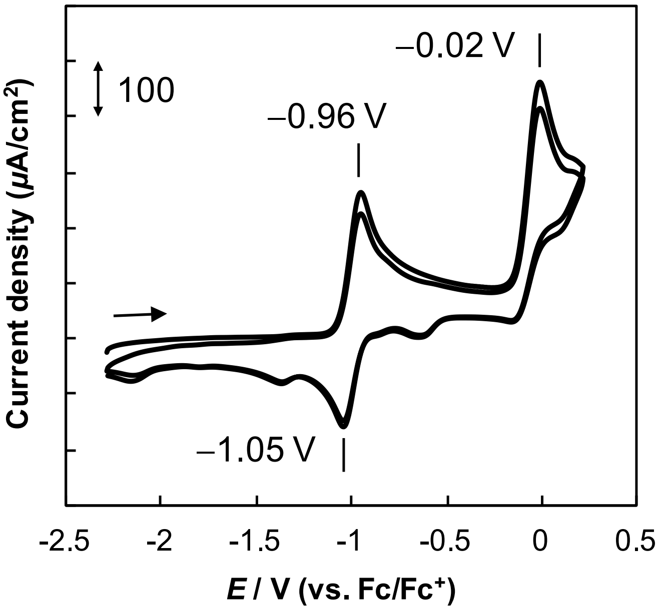

Figure 4-1. Cyclic voltammogram of 1 mM *trans*–[Mo(depe)$_2$(N$_2$)$_2$] in 0.2 M Pyr$_4$FAP/THF. (WE: GCE (ϕ 1mm, CE: Pt coil, RE: Ag/Ag$^+$ (10 mM AgClO$_4$ in 0.2 M Pyr$_4$FAP/THF) and scan rate: 100 mV/s).

In order to understand the structure change of **1** during the electrochemical oxidation, the FT-IR spectral changes during the same oxidation reaction were also measured. The FT-IR spectra for **1** during electrochemical oxidation was carried out by using Pt mesh (WE and CE) and Pt wire (quasi-RE) in a hand-made Nylon film cell (see Figure C2 in Appendix C). To determine the oxidation potential from Mo(0) to Mo(I), CV for **1** was measured before the controlled-potential electrolysis (CPE). The CV before CPE and plots of electric charge consumed with time during CPE are shown in Figures 4-2 (A) and 4.2(B). In Figure 4-2(A), the two oxidation waves are observed at +0.355 and +1.48 V (vs. Pt wire), and one reduction wave is observed at +0.125 V (vs. Pt wire). The rest potential was observed at ca. 0 V (vs. Pt wire), because the three electrodes used are Pt electrodes. Accordingly, the $E_{1/2}$ in the redox for Mo(0)/Mo(I) of

1 is observed at +0.24 V (vs. Pt wire). The difference in the two oxidation waves is +1.125 V. Thus, the observed redox waves are assigned to the redox waves for Mo(0)/Mo(I) and Mo(I)/Mo(II). On the basis of the observed results, the oxidation potential was decided to be +0.5 V (vs. Pt wire). The consumed electric charge is 90 mC (0.93 μmol), which is less than the total amount of *trans*-Mo$[(depe)_2(N_2)_2]$ (1.0 μmol) used, meaning that one electron oxidation reaction proceeds.

The time-dependent difference IR spectra for **1** in 0.2 M Pyr_4FAP/THF during CPE at +0.5 V are shown in Figure 4-2(C). The base line was measured after measuring CV described above. The difference FT-IR spectra are measured in the range of 1700 to 2200 cm^{-1}, because a nylon does not have any vibration in the region. The intensities of peaks at 2008 and 1938 cm^{-1} were changed with time during CPE at +0.5 V (vs. Pt wire). The decrease in the peak intensity at 1938 cm^{-1} is assigned to the stretching frequency of N_2 coordinated to **1**, which is consistent with the wavenumber (1938 cm^{-1}) reported in the previous literature.[4] The peak at 2008 cm^{-1} is assigned to $\nu(N_2)$ in the oxidized **1**. In the case of *trans*-$[Mo(dppe)_2(N_2)_2]$ that keeps the six-coordinate octahedral structure before and after the oxidation,[34] the difference in the $\nu(N_2)$ between *trans*-$[Mo(dppe)_2(N_2)_2]$ (1975 cm^{-1}) and *trans*-$[Mo(dppe)_2(N_2)_2]I_3$ (2047 cm^{-1}) was 72 cm^{-1}. In our case, the change in wavenumbers during CPE at +0.5 V (Pt wire) is 70 cm^{-1}, suggesting that the oxidized **1** is six-coordinate octahedral structure.

The plots of the intensities of IR peaks at 2008 and 1938 cm^{-1} for times are shown in Figure 4-2(D). The peak at 1938 cm^{-1} is decreased during CPE at +0.5 V. On the other hand, although the peak at 2008 cm^{-1} increased at early stage, the peak is gradually reduced and disappears, suggesting that the structure of the oxidized **1** is changed during CPE at +0.5 V (Pt wire). Thus, the electrochemical oxidation reaction for **1** has a subsequent reaction after electrochemical oxidation (EC reaction). Moreover, some air bubbles from working electrode were observed during CPE, therefore, the subsequent reaction would be involved dissociation of N_2 from the oxidized species.

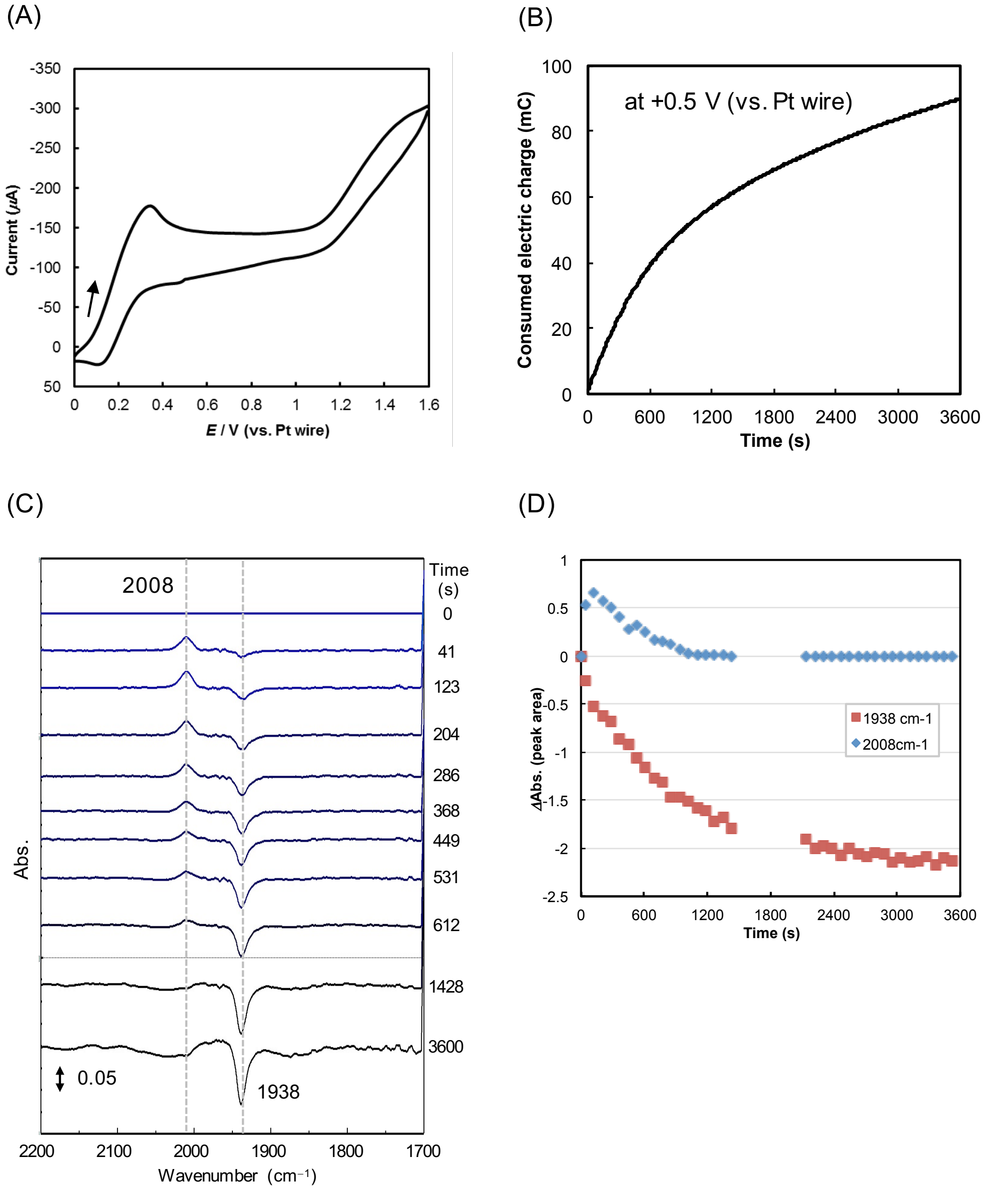

Figure 4-2. (A) Cyclic voltammogram of 10 mM *trans*–[Mo(depe)$_2$(N$_2$)$_2$] in 0.2 M Pyr$_4$FAP/THF (WE and CE: Pt mesh, RE: Pt wire, cell: Nylon film and scan rate: 10 mV/s), (B) the plots of consumed electric charge (mC) against time (s) by CPE at +0.5 V (vs. Pt wire), (C) The difference FT-IR spectra during CPE at +0.5 V (vs.Pt wire) (WE and CE: Pt mesh, RE: Pt wire, FT-IR cell: Nylon film) based on the spectrum at 0 s and (D) the plots of ΔAbs. in peak area at 1938 (red) and 2008 cm^{-1} (blue) against time during CPE. Amount of solution 0.1 mL

Scheme 4-1. Equilibrium reaction mechanism of *trans*-[Mo(depe)$_2$(N$_2$)$_2$] in 0.2 M Pyr$_4$FAP/THF

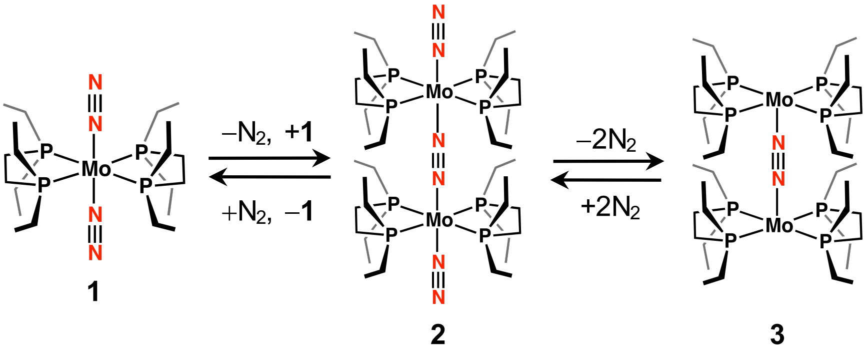

4.2.1.2 Resonance Raman spectra during electrochemical oxidation

To clarify whether a dimeric species is formed in 0.2 M Pyr$_4$FAP/THF or not, the resonance Raman spectroscopy are measured. Those of **1** and *trans*–[Mo(depe)$_2$(^{15}N$_2$)$_2$] (**^{15}N$_2$-1**) in 0.2 M Pyr$_4$FAP/THF are displayed in Figure 4-3(A). The Raman bands of **1** attributed to ν(N$_2$) are observed at 1816 and 2006 cm^{-1} and those for **^{15}N$_2$-1** are observed at 1754 and 1942 cm^{-1} (calcd 1754 and 1938 cm^{-1}), respectively. In Raman spectrum for **^{15}N$_2$-1**, the weak Raman band attributed from **1** is also observed, because substitution reaction between coordinating ^{15}N$_2$ and atmospheric ^{14}N$_2$ is occurred while the measurement is carried out under ^{14}N$_2$ atmosphere. The Raman bands at 1816 cm^{-1} suggest that two N$_2$ bridged dimeric Mo complexes, (μ–N$_2$)[Mo(depe)$_2$(N$_2$)]$_2$ (**2**) and/or (μ–N$_2$)[Mo(depe)$_2$]$_2$ (**3**), are generated in THF solution, and **1** is not stable in THF solution and has an equilibrium reaction for releasing N$_2$ from **1** as shown in Scheme 4-1. Fryzuk, Loehr and co-workers reported correlation between N$_2$ bond distance, d(N$_2$), and Raman shift, ν(N$_2$)[6] and proposed the following equation; ν(N$_2$) = $-1840[d(\mathrm{N_2})]^{3/2} + 4130$.[7] It led to a prediction of N-N bond from Raman band at 1816

cm^{-1} to be ca. 1.165 Å. Judging from the N_2 bond distance (1.0977 Å), the bond order for N_2 in these species is estimated to be triple bond. The Raman band at 2006 cm^{-1} is assignable to the symmetric vibration of N_2 in **1**, which is good agreement in DFT calculation as shown in Table 4-1 (see Section 4.2.1.4. Computational Studies).

To evaluate the electrochemical oxidation reaction for **1**, the resonance Raman spectroscopy was also carried out. The CV for **1** before CPE and plots of electric charge consumed with time during CPE are shown in Figures 4-3 (B) and 4.3(C). The $E_{1/2}$ value assigned to the redox couple for Mo(0)/Mo(I) is observed at +0.17 V (vs. Pt wire), which is negatively shifted compared to the $E_{1/2}$ = +0.24 V (vs. Pt wire), as shown in Figure 4-2(A), due to using quasi-reference electrode. From the obtained $E_{1/2}$ value, the oxidation potential in CPE was decided to be +0.5 V (vs. Pt wire). The consumed electric charge is 91 mC (0.94 μmol) at 7200 s, which is less than the total amount of **1** (1.0 μmol), suggesting that one electron oxidation reaction proceeded.

The time-dependent resonance Raman spectra for **1** during CPE at +0.5 V (vs. Pt wire) is shown in Figures 4-3(D). The Raman spectra are measured in the range of 1000 to 2200 cm^{-1} every 20 min during CPE. The Raman band at 1816 and 2006 cm^{-1} decreased during CPE along with the increase in those at 1292 and 1509, and 1574 cm^{-1}, suggesting that the N_2 molecule bridged between Mo complexes was activated by electrochemical oxidation. To confirm these Raman bands attributed to that of N_2 molecule coordinated with Mo complex, the isotopic labeling experiment was also performed. The Raman spectra for **$^{15}N_2$-1** are shown in Figure 4-3(E). Although the Raman bands derived from **1** are also observed, decrease in the Raman bands for **$^{15}N_2$-1** at 1752 and 1942 cm^{-1} (calcd 1756 and 1937 cm^{-1}) and increase in those at 1245, 1453 and 1530 cm^{-1} (calcd 1248, 1457 and 1520 cm^{-1}) are observed during CPE. The difference spectrum between **1** and **$^{15}N_2$-1** is displayed in Figure 4-3(E). The intensity of Raman band for **1** at 1292 cm^{-1}, which is between the value for free hydrazine (1076 cm^{-1}) and trans–diazene (1529 cm^{-1}),[8] is increased during CPE continuously, and it has the strongest intensity among the bands, indicating that it is attributed from the main species generated by electrochemical oxidation. Previously, Chirik and co-workers reported that the ν(N_2) value for $[\{(^{Ph}Tpy)(PPh_2Me)_2Mo\}_2(\mu_2\text{-}N_2)][BArF^{24}]$ [^{Ph}Tpy =4'-Ph-2,2',6',2"-terpyridine; ArF^{24} = $(C_6H_3\text{-}3,5\text{-}(CF_3)_2)_4$] is 1563 cm^{-1}, which is described as Mo(II) complex bridged with a modestly activated $[N_2]^{2-}$ ligand, and the ν(N_2) for the 2 electron oxidized species is 1477 cm^{-1}.[9] Therefore, the Raman band observed at 1577 cm^{-1} is assigned to the stretching vibration in a dimeric $(\mu\text{–}N_2)[Mo(depe)_2]^{2+}$. The Raman band observed at 1292 cm^{-1} is attributed to strongly activated N_2 ligand in dimeric $(\mu\text{–}N_2)[Mo(depe)_2]^{2+}$ species, which is similar to that in $[\{(PNP)ClMo\}(N_2)]$ (PNP = $N(CH_2CH_2P^tBu_2)_2$)) (1343 cm^{-1}) reported by Schneider and co-workers.[10] Accordingly, N_2 molecule bridged with the electrochemically oxidized **1** is estimated as $[N_2]^{2-}$ ligand. Although the excitation laser at 355 nm was kept irradiating for 1 hour after the electrochemical oxidation reaction, the obtained spectra were not changed. Thus, the generated dimeric Mo species is supposed to be stable under irradiation of the laser at 355 nm. Moreover, the Raman spectrum of **1** irradiated for 1 hour did not change without the CPE, also suggesting that the species with a peak at 1292 cm^{-1} was generated by CPE.

The proposed subsequent reaction mechanism in the electrochemical oxidation reaction for **1** is shown in Scheme 4-2. $[Mo(depe)_2(N_2)]^+$ (**4**) was generated in electrochemical oxidation of **1**, and then, the intermolecular reaction of molybdenum complexes proceeded to generate $(\mu\text{–}N_2)[Mo(depe)_2(N_2)_2]^{2+}$ (**5**), $(\mu\text{–}N_2)$ $[Mo(depe)_2]^{2+}$

(**6**) whose bridged N_2 is triple bond, and $(\mu\text{–}N_2)[Mo(depe)_2]^{2+}$ (**7**) whose bridged N_2 is double bond. Although the electrochemical oxidation products for **2** and **3** were not observed in FT-IR spectra, the dimeric species **2** and **3** would also be oxidized to generate **6** and **7**, respectively.

Scheme 4-2. Proposed subsequent reaction mechanism of the oxidized *trans*-$[Mo(depe)_2(N_2)_2]$ in 0.2 M Pyr_4FAP/THF during the controlled-potential electrolysis at +0.5 V (vs. Pt wire)

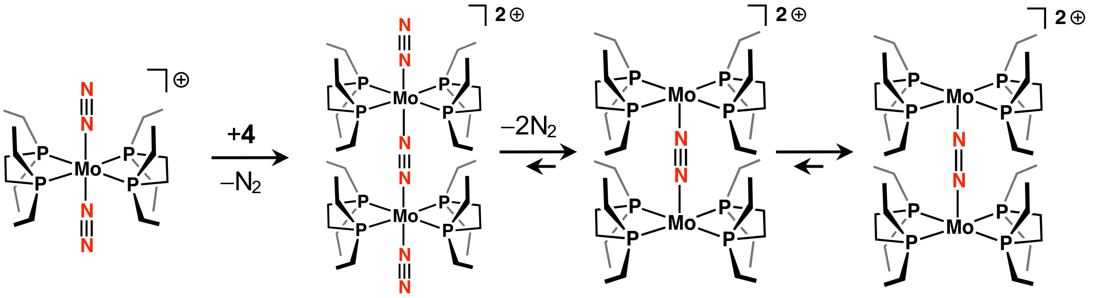

4 **5** **6** **7**

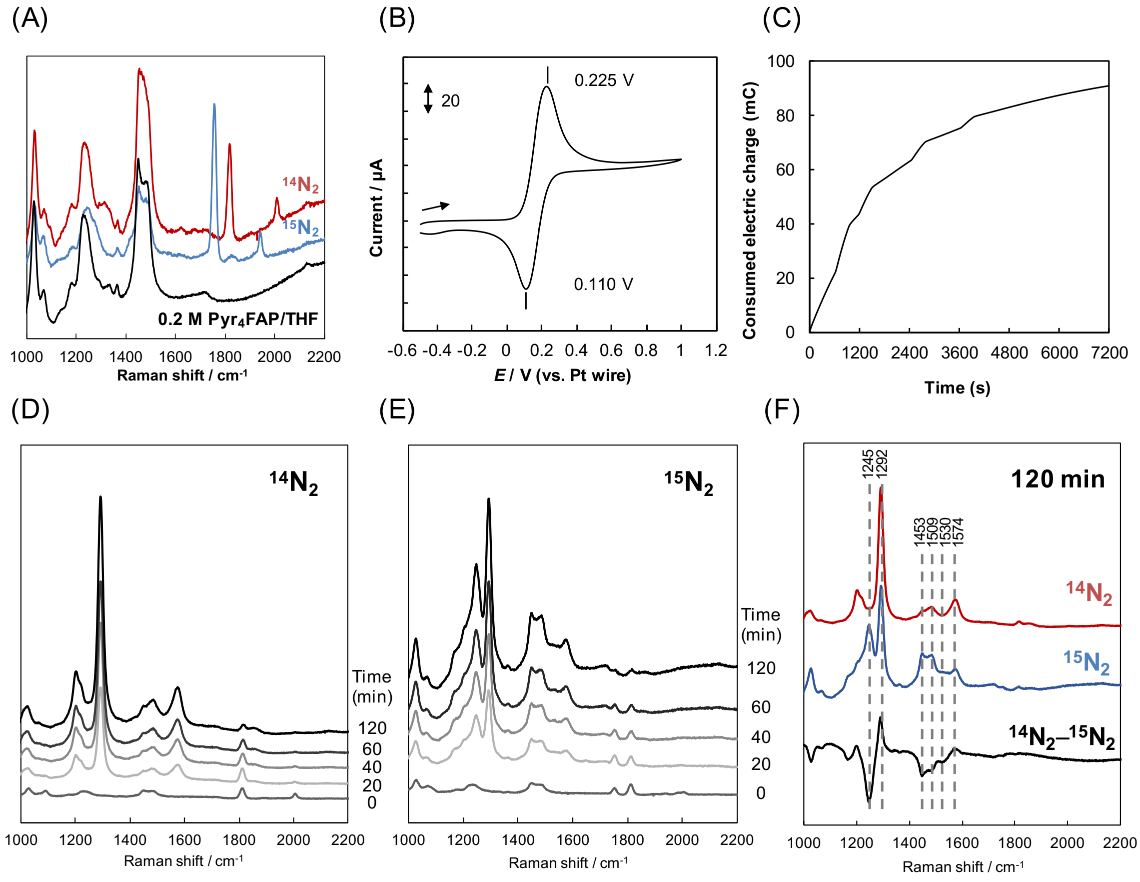

Figure 4-3. (A) Resonance Raman spectra of 2 mM *trans*–[Mo(depe)$_2$($^{14}N_2$)$_2$] (red) and *trans*–[Mo(depe)$_2$($^{15}N_2$)$_2$] (blue) in 0.2 M Pyr$_4$FAP/THF and 0.2 M Pyr$_4$FAP/THF (black), (B) cyclic voltammogram of 2 mM *trans*–[Mo(depe)$_2$($^{14}N_2$)$_2$] in 0.2M Pyr$_4$FAP/THF (WE: Pt mesh, CE: Pt coil, quasi-RE: Pt wire, cell: handmade Raman cell (diameter: 4 mm) (see Supporting Information), scan rate: 10 mV/s), (C) the plots of consumed electric charge (mC) against time (s) in CPE at +0.5 V (vs. Pt wire), (D) the resonance Raman spectra of 2 mM *trans*–[Mo(depe)$_2$($^{14}N_2$)$_2$] in 0.2 M Pyr$_4$FAP/THF during CPE at +0.5 V at 0, 20, 40, 60, and 120 min, (E) the resonance Raman spectra of 2 mM *trans*–[Mo(depe)$_2$($^{15}N_2$)$_2$] in 0.2 M Pyr$_4$FAP/THF during CPE at +0.5 V at 0, 20, 40, 60 and 120 min, and (F) the Raman spectrum of *trans*–[Mo(depe)$_2$($^{14}N_2$)$_2$] (red) and *trans*–[Mo(depe)$_2$($^{15}N_2$)$_2$] (red) in 0.2 M Pyr$_4$FAP/THF in CPE at 120 min and those difference spectra (black). The resonance Raman spectroscopic measurements were performed under $^{14}N_2$ by using an excitation wavelength at 355 nm. The excitation laser was irradiated at 0, 20, 40, 60, and 120 min after the CPE started (exposure times: 30 (s) and accumulation times: 10 (s). Amount of solution: 0.5 mL.

4.2.1.3 UV-vis spectra during electrochemical oxidation

To consider the EC reaction of **1** in detail, UV-vis spectroscopy for **1** during electrochemical oxidation was also measured. The UV-vis spectra for **1** during electrochemical oxidation was carried out by using Pt mesh (WE and CE) and Pt wire (quasi-RE) in UV-vis cell (see Figure A1 in Appendix A). To determine the oxidation potential from Mo(0) to Mo(I), the linear sweep voltammetry for **1** was performed before the CPE. The linear sweep voltammogram (LSV) at the scan rate of 100 mV/s before CPE and plots of electric charge consumed with time during CPE are shown in Figures 4-4 (A) and 4-4(B). The current in the LSV (Figure 4-4(A)) increased from 0.2 V (vs. Pt wire) and the oxidation wave was observed at +0.677 V (vs. Pt wire). The wave shape is different from that in Figure 4-3(A) due to IR drop because electrodes are not close each other in the UV-vis cell. The consumed electric charge is 100 mC (1.0 μmol) at 3600 s, which is less than the total amount of **1** (3.0 μmol), suggesting that one electron oxidation reaction was proceeded.

UV-vis spectral changes of **1** during CPE at +0.5 V (vs. Pt wire) for electrochemical oxidation are shown in Figures 4-4(C) and 4-4(D). In Figure 4-4(C), the absorption bands derived from **1** are observed at 323 and 417, 457 and 493 nm before CPE. The absorption band at 323 nm decreased during CPE, which was shifted to 300 nm and then decreased. Interestingly, absorption bands at 417 and 457 nm increased once, and then, these bands decreased from 1200 s. The absorption band at 493 nm also decreased during CPE. Plots of intensity changes for these bands with time are displayed in Figures 4-4(E) and 4-4(F). The plots at 323 and 493 nm decreased and those at 417 and 457 nm increased until 1200 s. In the range of 1200 to 3600 s, the changes for the intensities at 323 and 493 nm are not observed. On the other hands, the changes for the intensities at 417 and 457 nm are switched from increase to decrease at 1200 s and they decreased until 3600 s. Therefore, we judged that the absorption bands at 300, 417 and 457 nm are derived from the oxidized **1**. In addition, the absorbances at 417 and 458 nm are started to change at around 1200 s, suggesting that subsequent reactions for the oxidized **1** are occurred. Moreover, a new band at 353 nm appeared with decrease in the band of the oxidized **1**, suggesting that the subsequent reactions proceed and some new species were generated after CPE. The assignments of these absorption bands in detail are described in Section 4.2.1.4.

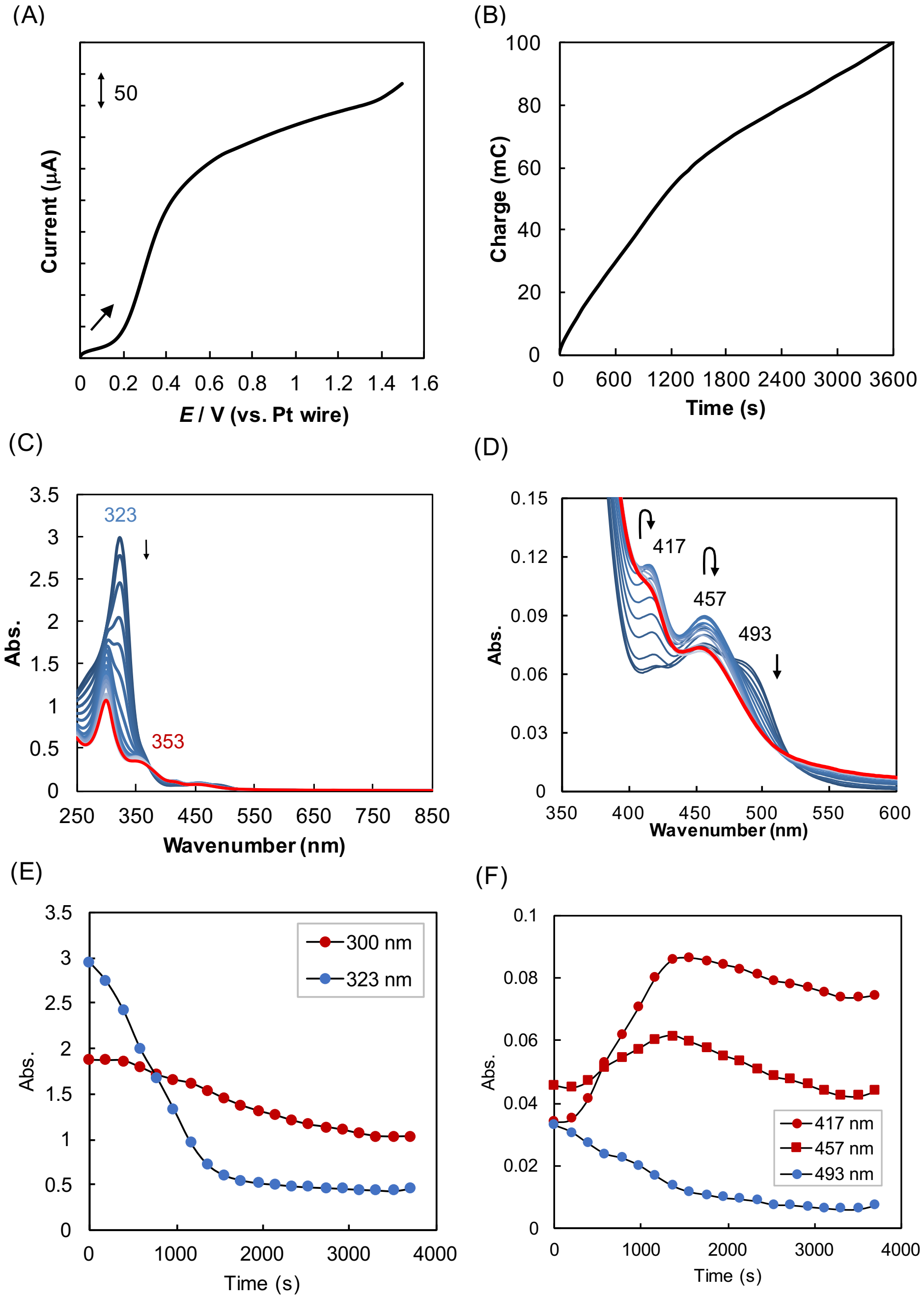

Figure 4-4. (A) Cyclic voltammogram of 1 mM *trans*–[Mo(depe)$_2$(N$_2$)$_2$] in Pyr$_4$FAP (WE: Pt mesh, CE: Pt coil, quasi-RE: Pt wire, cell: UV-vis cell (see Supporting Information), scan rate: 100 mV/s), (B) the plots of consumed electric charge (mC) against time (s) by CPE at +0.5 V (vs. Pt wire), (C) Time-dependent UV-vis spectra of 1 mM *trans*-[Mo(depe)$_2$(N$_2$)$_2$] in 0.2 M Pyr$_4$FAP/FAP during CPE at +0.5 V (*vs*. Pt wire) (WE: Pt mesh, CE: Pt coil, quasi-RE: Pt wire, amount of solution : 3 mL) in the range of 250 to 850 nm and (D) that in the range of 350 to 600 nm, (E) the plots of abs. against time at 300 and 323, and (F) those at 417, 457 and 493 nm.

4.2.1.4 Assignment of FT-IR, resonance Raman and UV-vis spectra for electrochemical oxidation products of *trans*–[Mo(depe)$_2$(N$_2$)$_2$] by DFT and TDDFT calculations

To understand the obtained time-dependent FT-IR, resonance Raman and UV-vis spectra for **1** and its oxidation reactions, DFT and TDDFT calculations were performed using the model complexes **1** (singlet state), **2** (singlet state), and **3** (singlet state) as Mo(0)-N$_2$ complexes and [Mo(depe)$_2$(N$_2$)]$^+$ (**4**) (doublet state), (μ–N$_2$)[Mo(depe)$_2$(N$_2$)$_2$]$^{2+}$ (**5**) (singlet and triplet states) and (μ–N$_2$)[Mo(depe)$_2$]$^{2+}$ (**6** in the singlet and triplet states) and **7** in the singlet and triplet states) as the oxidized complexes, and [Mo(depe)$_2$(N$_2$)]$^+$ (**8**) as nitride complex. These calculations were adopted with B3LYP* as hybrid functional and Stuttgart/Dresden ECP (SDD) on the Mo atom, 6-311G(d) on N and P atoms, and 6-31G(d) on C and H atoms as the basis set (see Experimental Section). These model complexes coordinating with THF are not considered because the distance between O atom of THF and Mo ion are ca. 4Å after optimizing structure of the model complexes as six coordinate structure. The parameters estimated by the calculations are summarized in Table 4-1.

In FT-IR spectra during the electrochemical oxidation reaction, the intensity of peak at 2008 cm^{-1} was increased and that at 1938 cm^{-1} was decreased, respectively, as described above. The ν(N$_2$) for **1** was estimated to be 1940 cm^{-1}, which is in good agreement with the experimental result (1938 cm^{-1}). For electrochemical oxidation of **1**, **4** would be generated and the ν(N$_2$) was estimated to be 2015 cm^{-1}, which is also in good agreement with experimental one (2008 cm^{-1}).

In resonance Raman spectra shown in Figure 4-3(A), we estimated that **2** and/or **3** exist in THF solution in addition to **1**. Although we expected that the Raman shift assigned to stretching vibration of N_2 ligand for **2** is different from that for **3**, the calculated values are 1881 and 1880 cm^{-1}, respectively. Thus, we cannot distinguish them. The Raman band at 1816 cm^{-1}, as shown in Figure 4-3, is assigned to the bridging N_2 ligand in **2** and/or **3**, which are close to the estimated values (1881 and 1880 cm^{-1}). However, we estimate that **2** did not almost exist in THF solution because the decreasing peak is observed only at 1938 cm^{-1} in FT-IR spectra during electrochemical oxidation. If **2** mainly exist in THF, the decreasing peak in FT-IR spectra would be observed in the lower region than 1938 cm^{-1}, because the estimated $\nu(N_2)$ for **2** is 1905 cm^{-1}. Therefore, we estimated that the peak at 1816 cm^{-1} in Raman spectrum is derived from **3**. The band at 2006 cm^{-1} observed in Raman spectra shown in Figure 4-3(A) is attributed to the symmetric stretching vibration of terminal N_2 ligand in **1**, which is consistent with the calculated Raman shift for **1** (2011 cm^{-1}). In the resonance Raman spectra during electrochemical oxidation (Figure 4-3), the Raman bands at 1816 and 2006 cm^{-1} decreased along with increase in those at 1292, 1509, and 1574 cm^{-1}, suggesting that bridging N_2 ligand was activated, and $[N_2]^{2-}$ ligands were generated. The observed Raman band at 1574 and 1509 cm^{-1} is consistent with the estimated Raman bands for **6** in the triplet and singlet states (1562 and 1568 cm^{-1}). Moreover, the observed Raman band at 1292 cm^{-1} is also in good agreement in the estimated Raman bands for **7** in the triplet and singlet states (1306 and 1311 cm^{-1}). Although **5** might be generated during electrochemical oxidation, the estimated Raman bands for **5** are not consistent with experimental results. In addition, the generation for **7** via **6** is considerable because intensity for Raman band at 1292 cm^{-1} is larger than that at 1509 and 1574 cm^{-1}, as described above. Therefore, dimeric Mo complex bridged with $[N_2]^{2-}$ ligand, **7**, is main species in electrochemical oxidation for **1**.

To consider the UV-vis spectra during electrochemical oxidation of **1** shown in Figure 4-4, electronic absorption spectra estimated by TDDFT calculations for models **1**–**7** are shown in Figure 4-5. The calculated absorption bands for **1** gave peaks at 270, 309 and 500 nm (Figure 4-5(A) and 4-5(B)), which are very similar to those of experimentally obtained bands at 323 and 493 nm (Figures 4-4(C) and 4-4(D)) except for the peak at 270 nm. The estimated band at 309 and 500 nm are assigned to the transition d_{xz}, d_{yz} and d_{xy} orbitals on Mo ion to π^* orbital on N atom (MLCT) (see Appendix C). The estimated band at 270 nm is assigned to the transition for d_{xz} and d_{yz} orbitals on Mo to π^* orbital on N atom (MLCT), although the absorption band in UV-vis spectrum is not observed. The band at 270 nm would be slightly shifted to a longer wavelength region.

The estimated electronic absorption bands for **2** and **3** are detected at 397 nm and at 368 and 433 nm, as shown in Figure 4-5(C). These bands are overlapped with the strong absorption band at 323 nm for **1** as shown in Figure 4-4(C), even if these absorption bands for **2** and **3** are detected in the range of 350 to 450 nm.

The electronic absorption spectrum estimated for **4** generated by the oxidation of **1** gave absorption bands at 266, 398 and 440 nm as shown in Figures 4-5(A) and 4-5(B). These bands are similar to the absorbance appearing at 300 nm and the increased peaks observed at 417 and 457 nm (Figure 4-4(C) and 4-4(D)). Therefore, these observed absorption bands are decided to be derived from **4**. The absorption bands assigned to **4** is gradually decreased, suggesting that **4** has been changed to dimeric species **5**, **6** and **7**. The electronic absorption spectra estimated for **5**, **6**, and **7** are shown in Figures 4-5(D), 4.5(E), and 4.5(F). These spectra have the electronic absorption bands at around 350 nm, suggesting that the bands appeared around 353 nm in Figure 4-4(C) are attributed from dimeric species **5**, **6**, and **7**. The electronic absorption spectrum in Figure 4-4(C) does not have any bands in the range of 500 to 700 nm, therefore, **7** in the singlet state is mainly generated by electrochemical oxidation for **1** via generating **4**.

Table 4-1. Summary for DFT and TDDFT calculations results for complex **1-7**[c]

Complex	Multiplicity	$\nu(N_2)$ /cm^{-1}	Raman shift /cm^{-1}	Wavelength /nm	N–N /Å	Mo–N /Å
1	singlet	1940	2011 (1871)	270 (MLCT)[a] 309 (MLCT)[a] 500 (MLCT)[a]	1.1348	2.0208
2	singlet	1905	1881 (48000) 1932 (18000)	397 (MLCT)[a]	1.1478 (bridged) 1.1428(terminal)	2.1682 (bridged) 1.9822(terminal)
3	singlet	–	1880	368 (MLCT)[a]	1.1547	2.0650 2.0725
4	doublet	2015	2072	266 (MLCT)[a] 398 (MLCT)[a] 440 (LMCT)[b]	1.1262 1.1262	2.0307
5	triplet	2008	1886	374 (MLCT)[a]	1.1459 (bridged) 1.1292 (terminal)	2.1307(bridged) 2.0090(terminal)
	singlet	2067	1669 (bridged) 2091 (terminal)	432 (MLCT)[a] 684 (d-d)	1.1791 (bridged) 1.1202 (terminal)	2.0069 (bridge) 2.0143 (bridge) 2.0924 (terminal) 2.0868 (terminal)
6	triplet	–	1562	349 (MLCT)[a] 564 (d-d)	1.2086	1.9309 1.9290
	singlet	–	1568	360 (MLCT)[a] 491 (d-d)	1.2086	1.9250 1.9085
7	triplet	–	1306	351 (MLCT)[a] 543 (d-d)	1.2586	1.9164 1.9143
	singlet	–	1311	371 (MLCT)[a]	1.2586	1.9119 1.8938

[a] MLCT: charge transfer from d orbital on Mo atom to π* orbital on N atom

[b] LMCT: charge transfer from depe ligand to d orbital on Mo atom

[c] FT-IR frequencies and Raman shifts assigned to $\nu(N_2)$ / cm^{-1}, electronic absorption band / nm, and N_2 and Mo–N bond length / Å.

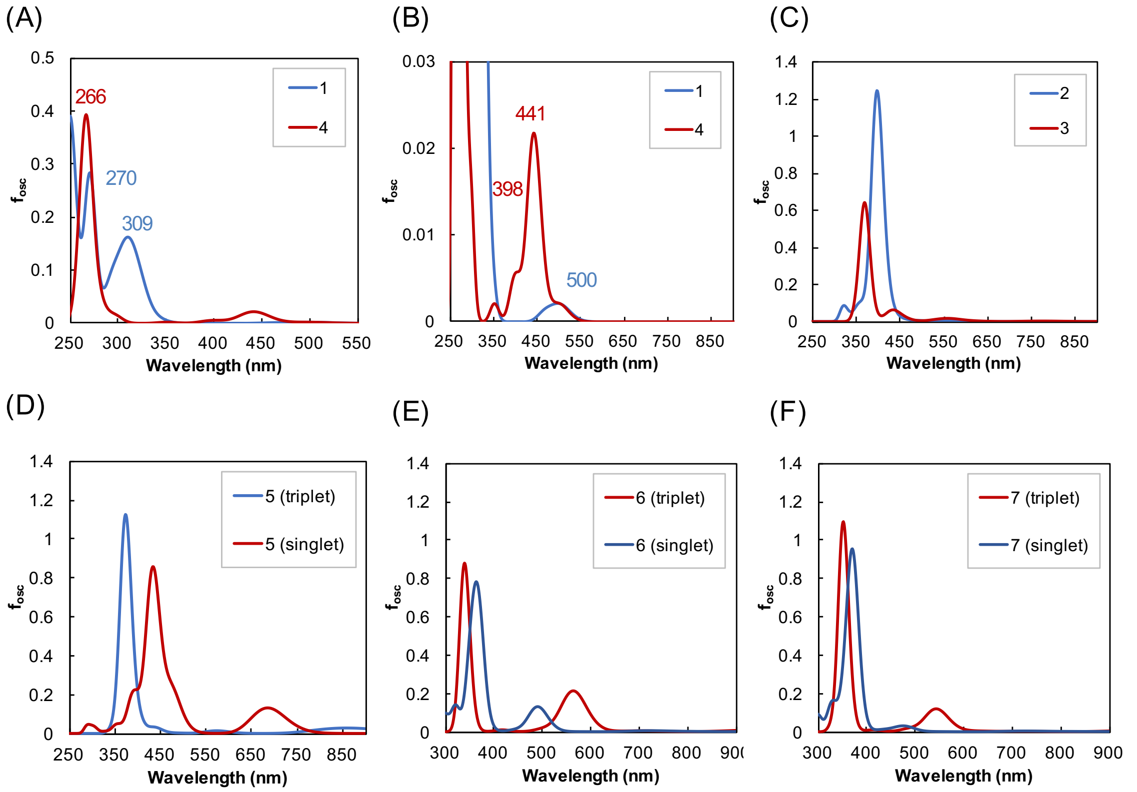

Figure 4-5. (A) Electronic absorption spectra estimated by TD-DFT calculations for complexes **1** and **4**, (B) expansion of Figure 4-5(A), (C) those for **2** and **3**, (D) **5** in the triplet and singlet states, (E) **6** in the triplet and singlet states, and (F) **7** in the triplet and singlet states.

4.2.1.5 Quantitative molecular orbital diagram and energy profile for (μ–N_2)[Mo(depe)$_2$]$^{2+}$ in the singlet state (7)

A qualitative molecular orbital diagram for **7** in the singlet state is shown in Figure 4-6. The DFT-computed highest molecular orbitals (HOMO) and the lowest occupied molecular orbital (LUMO) are principally molybdenum based and bridged N_2 bonding orbital. HOMO−1 and HOMO−2 display d_{xy} orbitals on Mo atoms and LUMO+1 also show d_{z2} orbital on Mo atom. HOMO−3 and HOMO−4 is constructed π_x* and π_y*

orbitals on N_2 coupled with d_{xz} and d_{yz} orbitals on Mo atoms, indicating that bridged N_2 bonded by π back donation from Mo center and bridged N_2 is reduced to $[N_2]^{2-}$. The Wiberg bond index of 1.76 for N_2 indicate the bond order of bridged N_2 is 2. LUMO+3 and LUMO+6 display $\pi_x^*(N_2)$ and $\pi_y^*(N_2)$ orbitals at −0.35 and −0.66 eV, which is higher than HOMO at −4.0 eV, suggesting that generation of $[N_2]^{2-}$ by reduction of bridged N_2 ligand from π back donation from Mo center has high activation barrier.

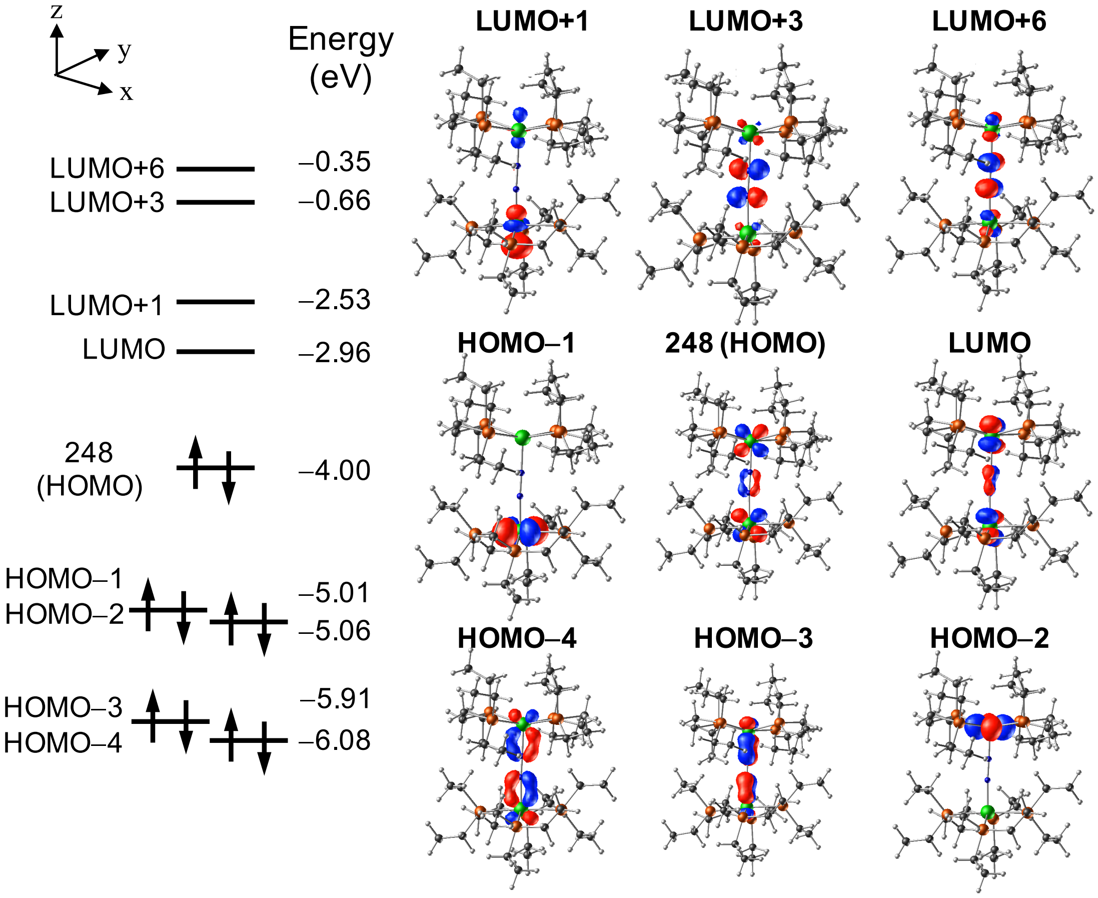

Figure 4-6. Qualitative frontier molecular orbital diagram of **7** in the singlet state estimated from DFT calculation. The z axis is defined as the Mo-N2-Mo vector.

To understand whether the electrochemically generated **7** gives the nitride complex, **8**, or not, the reaction profile was analyzed and evaluated, which are shown in Figure

4-7. The energy profile lets us expect that **8** may be generated by the electrochemical oxidation reaction, because ΔG value based on **7** in the singlet is 3.0 kcal/mol higher than that of **8** in the triplet state and −69.1 kcal/mol lower than that of **8** in the singlet state. However, **7-TS**, which is the transition state from **7** in the singlet to **8**, is 11.8 kcal/mol higher than it in the singlet and 34.2 kcal/mol higher than it in the triplet state, indicating that it must pass through the higher activation energy barrier. Therefore, it is difficult to generate **8** just as it is, although the ΔG (kcal/mol) of **8** in the singlet state is lower than that of **7**.

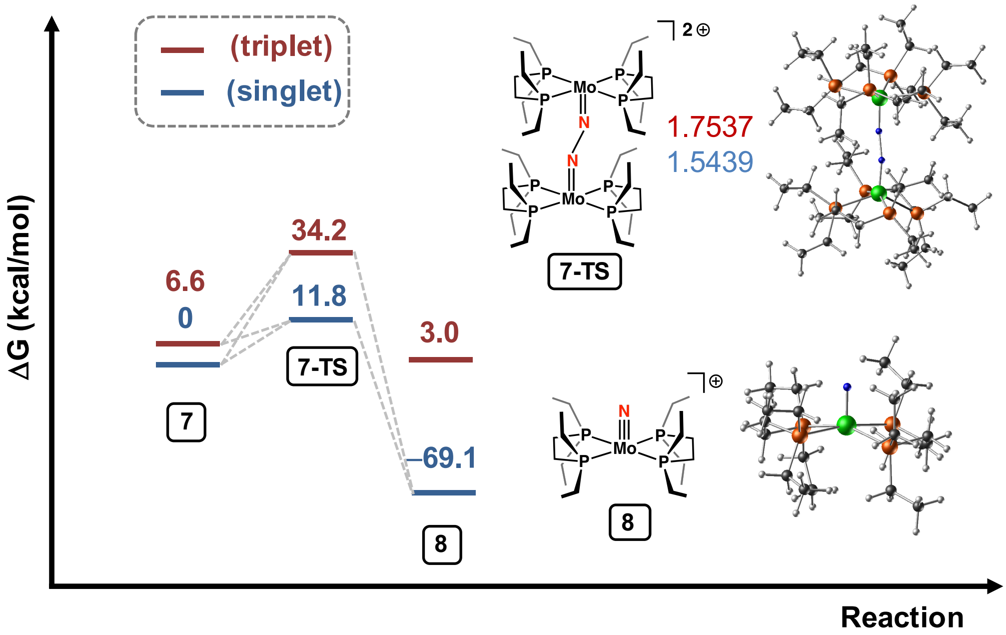

Figure 4-7. Computed reaction profile from **7** to the nitride **8**. Free energy profile as estimated at 298.15 K (ΔG, kcal/mol).

4.2.2 Electrochemical oxidation of Mo-N$_2$ complex in Pyr$_4$FAP

4.2.2.1 FT-IR spectra during electrochemical oxidation

To understand the redox behaviors of *trans*–[Mo(depe)$_2$(N$_2$)$_2$] (**1**), cyclic voltammogram (CV) of **1** in Pyr$_4$FAP was measured. The result is shown in Figure 4-8. The redox potential, $E_{1/2}$, assignable to Mo(0)/Mo(I) is observed at −1.11 V (vs. Fc/Fc$^+$), and the oxidation wave assignable to Mo(I)/Mo(II) is observed at +0.005 V (vs. Fc/Fc$^+$), which is similar to that in THF as described in Section 4.2.1.1.

In order to understand the structure change of **1** during the electrochemical oxidation from Mo(0) to Mo(I), the FT-IR spectra of **1** in Pyr$_4$FAP during the electrochemical oxidation reaction was also measured. Its difference IR spectra based on the spectrum when the electrochemical oxidation reaction started are shown in Figure 4-9. The CV before controlled potential electrolysis (CPE) and plots of electric charge consumed with time during CPE are shown in Figure 4-9(B). The intensities in peaks at 1955 and

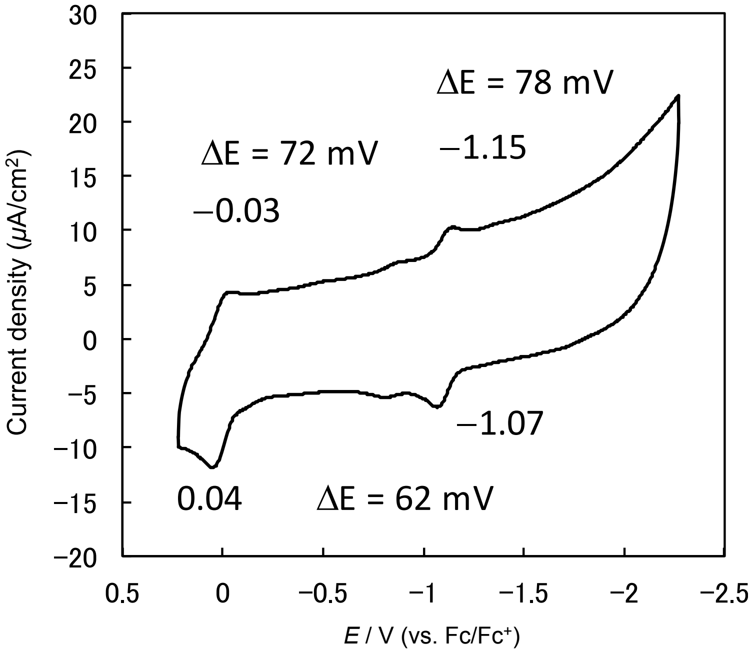

Figure 4-8. Cyclic voltammograms of 1 mM *trans*-Mo(depe)$_2$(N$_2$)$_2$ in Pyr$_4$FAP (WE.: GC (φ 1 mm), CE: Pt wire, RE: Ag/Ag$^+$ electrode, and scan rate: 100 mV/s). The potentials were referenced to the ferrocene/ferrocenium (Fc$^+$/Fc) couple in Pyr$_4$FAP.

1919 cm^{-1} were changed with time during CPE at +0.5 V (vs. Pt wire), as shown in Figure 4-9(A). Since it is lower than those of **1** detected in the solid state (1928 cm^{-1})[4] and in THF solution (1939 cm^{-1})[4] that were reported previously, the decrease in peak at 1919 cm^{-1} was assigned to ν(N_2) of **1**. The increase in peak intensity at 1955 cm^{-1} is assignable to stretching vibration of N_2 molecule for the one-electron oxidized species. In addition, since generation of gases are observed during the electrochemical oxidation of **1** in both Pyr$_4$FAP and 0.2 M Pyr$_4$FAP/THF solution, the species generated in the electrochemical oxidation reaction released one molar N_2 at least from **1**. The increase in peak at 1955 cm^{-1} is clearly correlated to decrease in peak at 1919 cm^{-1}, suggesting that five coordinate [Mo(depe)$_2$(N_2)] was oxidized with coordinating N_2. In oxidation reaction for *trans*-[Mo(N_2)$_2$(dppe)$_2$] by using an oxidant, the ν(N_2) stretching of *trans*-[Mo(N_2)$_2$(dppe)$_2$] in nujol was observed at 1975 cm^{-1} and the ν(N_2) stretching of *trans*-[Mo(N_2)$_2$(dppe)$_2$]I_3 in nujol, which is chemically oxidized Mo complex, was detected at 2047 cm^{-1}.[5] The difference in wavenumber was 72 cm^{-1} in one electron oxidation, where the core structure was not changed (see Table C14 in Appendix). In the electrochemical oxidation for **1** in Pyr$_4$FAP shown in Figure 4-9, the difference wavenumber was 36 cm^{-1}, suggesting that the structure of Mo(I)-N_2 complex changed after the electrochemical oxidation reaction. Interestingly, the peak at 1955 cm^{-1} was not decreased after the electrochemical oxidation, indicating that Mo(I)–N_2 species after the structure change is stabilized and kept in Pyr$_4$FAP.

4.2.2.2 Resonance Raman spectra

As described in Section 4.2.1, the bridged N_2 is detected by measuring the resonance Raman spectroscopy. We therefore studied to clarify whether a dimeric species is formed in Pyr_4FAP by using resonance Raman spectroscopy. The resonance Raman spectra of *trans*–$[Mo(depe)_2(N_2)_2]$ and *trans*–$[Mo(depe)_2(^{15}N_2)_2]$ in Pyr_4FAP are shown in Figure 4-10. The resonance Raman spectra of *trans*–$[Mo(depe)_2(N_2)_2]$ in Pyr_4FAP after electrochemical oxidation reaction were also measured, but the spectra were not changed, suggesting that Mo(I)-N_2 species was stabilized as monomeric cation species by electrostatic interaction with Pyr_4FAP.

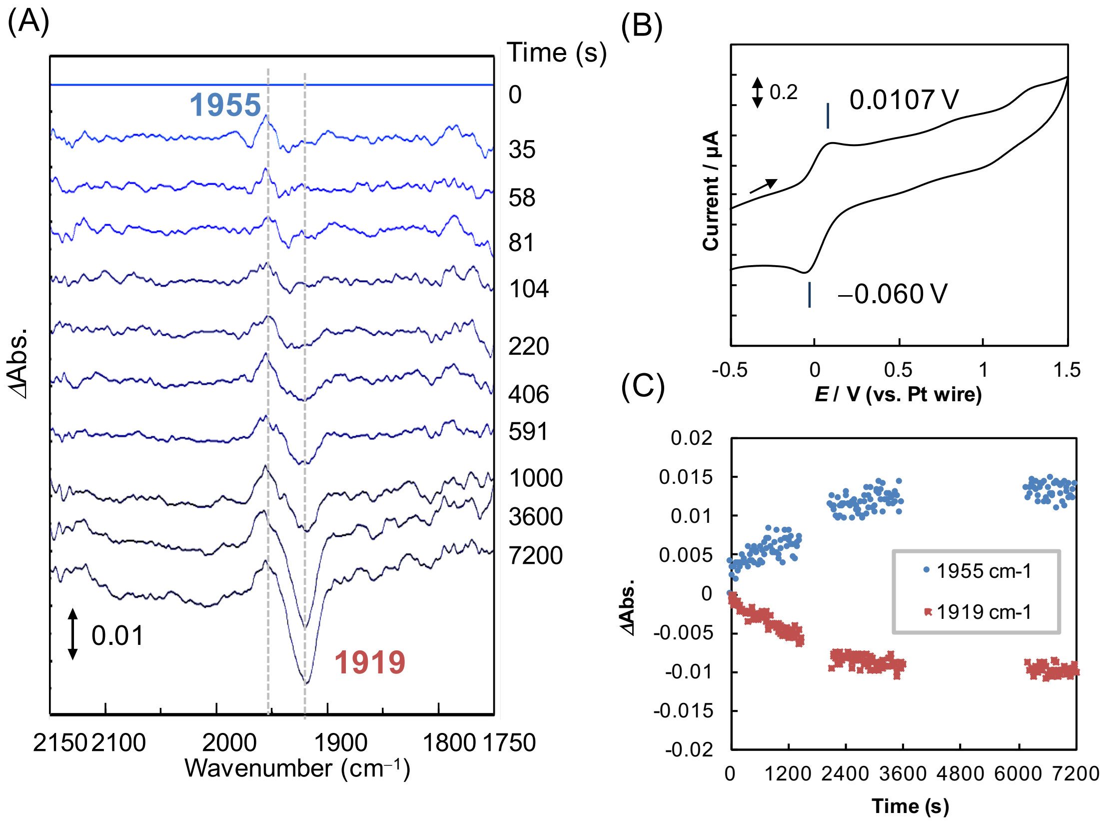

Figure 4-9. (A) The difference FT-IR spectra during CPE at +0.5 V (vs.Pt wire) (WE and CE: Pt mesh, RE: Pt wire, FT-IR cell: Nylon film) based on the spectrum at 0 s, (B) CV of **1** in Pyr_4FAP before electrochemical oxidation, and (C) the plots of *Δ*Abs. in the peaks at 1955 (red) and 1919 cm^{-1} (blue) against time during CPE.

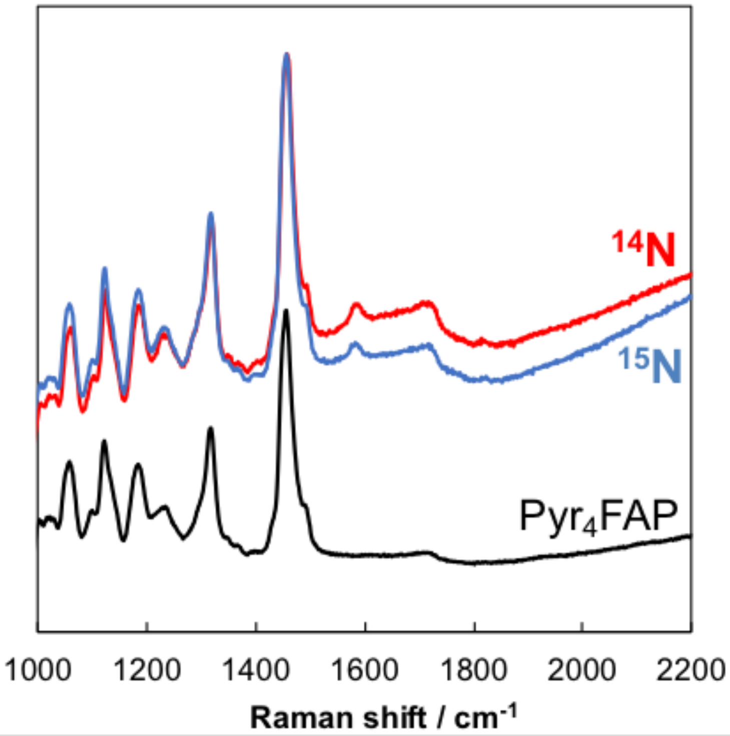

Figure 4-10 Resonance Raman spectra of 2 mM *trans*-[Mo(depe)($^{14}N_2$)$_2$] (red), 2 mM *trans*-[Mo(depe)($^{15}N_2$)$_2$] (blue) and used solvent, Pyr$_4$FAP (black).

4.2.2.3 The effect of FAP anion toward Mo complex

To consider the effect of FAP anion toward Mo-N_2 complex, DFT calculations for [Mo(depe)$_2$N$_2$]$^+$(**9'**), [Mo(depe)$_2$N$_2$ ⋯ FAP] (**10'**), [FAP ⋯ Mo(depe)$_2$N$_2$] (**11'**) and [FAP⋯Mo(depe)$_2$N$_2$⋯FAP] (**12'**) were carried out. These calculations were adopted with B3LYP* as hybrid functional and Stuttgart/Dresden ECP (SDD) on the Mo atom, 6-311G(d) on N and P atoms, and 6-31G(d) on C and H atoms as the basis set with empirical corrections (GD3BJ) in ionic liquid (ε=14.7) (see Experimental Section). The energy profile for **9'–12'** is shown in Figure 4-11. The ΔH and ΔG (kcal/mol) for **9'–12'** are calculated based on those of **9'**. The ΔH values for **10'**, **11'** and **12'** are estimated to be −18.4, −28.3 and −41.8 kcal/mol, respectively, and the ΔG values for **10’**, **11’** and **12’** are estimated to be −3.4, −15.1 and −16.0 kcal/mol, respectively, indicating that **12’** is the most stable among the four complexes. This is because FAP anions weakly interact to the oxidized Mo(I) complexes.

The structure of **12’** is shown in Figure 4-12 (see Appendix C). The structure of **12’** reveals that some F atoms on FAP anion weakly interact with ethyl group in depe ligand; F93···H73 2.8278, F93···H71 2.3380, F89···H64 2.9302, F89···H63 2.6904, F90···H63 2.3938, F90···H21 2.9037, F90···H30, F92···H73 2.6136, F88···H21 2.2994, F88···H22 2.6106, F86···H22 2.8267, F106···H27 2.4178, F106···H66 2.4039, F106···H29 2.8833, F103···H66 2.4849, F125···H29 2.5953, F110···H29 2.7437, F110···H27 2.8770, F122···H66 2.4211, F121···H68 2.7540, F122···H54 2.3705. In addition, the Mo(I) ion may also have weak interaction with FAP anion (Mo1···F90 3.5837). Such weak interactions stabilize **9’** and contribute to suppression for the formation of dimeric species observed in THF solution, as described in Section 4.1.2. Therefore, the electrochemical oxidation of Mo(0) to Mo(I) for **1** in Pyr$_4$FAP gives **12’**.

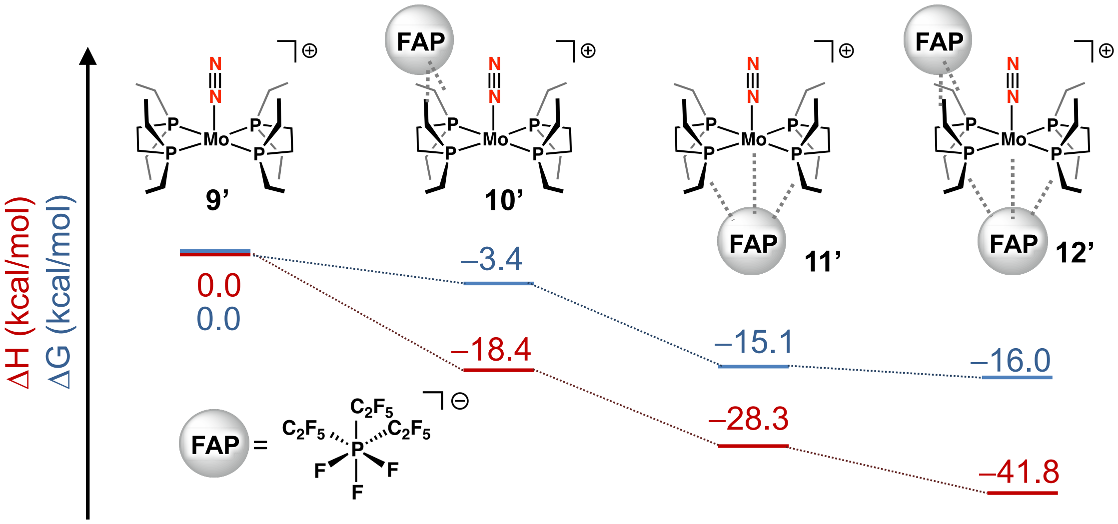

Figure 4.11. Energy profile for model complexes **9’**, **10’**, **11’** and **12’**.

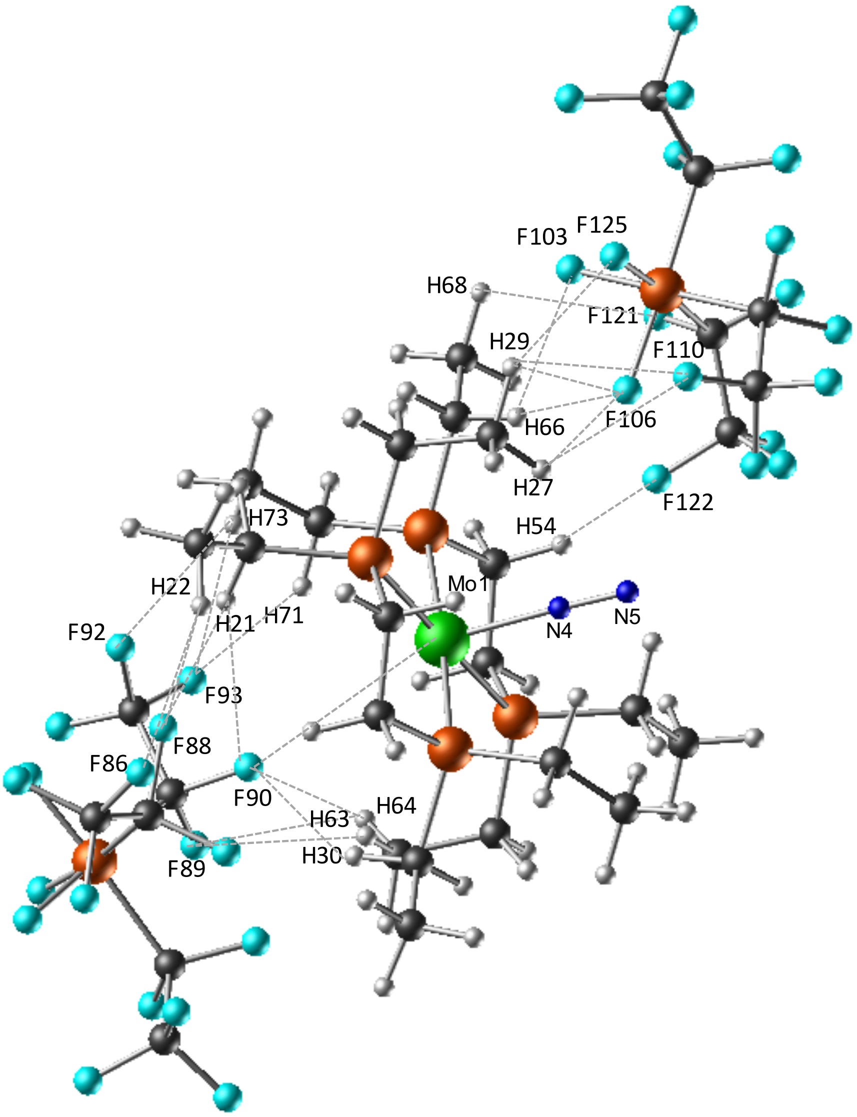

Figure 4-12. The optimized structure of **12'**. Selected bond lengths for the complex; F93···H73 2.8278, F93···H71 2.3380, F89···H64 2.9302, F89···H63 2.6904, F90···H63 2.3938, F90···H21 2.9037, F90···H30, Mo1···F90 3.5837, F92···H73 2.6136, F88···H21 2.2994, F88···H22 2.6106, F86···H22 2.8267, F106···H27 2.4178, F106···H66 2.4039, F106···H29 2.8833, F103···H66 2.4849, F125···H29 2.5953, F110···H29 2.7437, F110···H27 2.8770, F122···H66 2.4211, F121···H68 2.7540, F122···H54 2.3705.

To assign the obtained FT-IR spectra of **1** during the electrochemical oxidation described in Section 4.2.2.1, the ν(N_2) for **1** is also estimated with empirical corrections (GD3BJ)[26b,26c] in the IL (ε = 14.7). The estimated ν(N_2) for **1** (1937 cm^{-1}) is consistent with the experimental result (1919 cm^{-1}) (see Figure 4-9). The calculated ν(N_2) for **12'** is 1984 cm^{-1}, which is close to the increasing peak at 1955 cm^{-1} as shown in Figure 4-9. Accordingly, **12'**, which is a complex with FAP anion, would be generated.

4.3 Conclusion

Electrochemical oxidation reaction for *trans*–$[Mo(depe)_2(N_2)_2]$ (**1**) (depe = $Et_2PCH_2CH_2PEt_2$) is carried out and the generation of dimeric molybdenum complex bridging $[N_2]^{2-}$ ligand is revealed. The one electron electrochemical oxidation reaction is studied by time-dependent FT-IR, resonance Raman and UV-vis spectroscopies during controlled-potential electrolysis (CPE). The time dependent FT-IR spectra during CPE shows decrease in the peak at 1938 cm^{-1} assignable to ν(N_2) for **1** and increase in the peak at 2008 cm^{-1} assigned to the ν(N_2) for the electrochemically-oxidized **1**. However, the increased peak at 2008 cm^{-1} disappeared after electrochemical oxidation reaction. The time-dependent resonance Raman spectra during CPE gave three bands at 1574, 1509 and 1294 cm^{-1}, suggesting that N_2 is activated by forming dimeric species, (μ–N_2)$[Mo(depe)_2(N_2)_2]$. Time-dependent UV-vis spectra during CPE shows decrease in the absorption bands at 323 and 493 nm derived from **1** and increase in the absorption bands at 417 and 457 nm assigned to those of the oxidized **1**, and an absorption band at 353 nm assigned to (μ–N_2)$[Mo(depe)_2(N_2)_2]$ appeared. To consider the assignment for these spectra, DFT and TDDFT calculations are also performed and they are in good agreement with experimental results. Unfortunately, the generation of nitride complex by N_2 cleavage was not observed, because the transition state has a high-energy barrier. However, to the best of our knowledge, the activation of bridging N_2 ligand through the electrochemical oxidation of the terminally-coordinated N_2 metal complex has not been reported yet.

On the contrary, in the electrochemical oxidation of **1** in Pyr_4FAP, the resonance Raman spectra of **1** and its oxidized species in Pyr_4FAP have revealed that a dimeric structure bridged with N_2 is not generated before and after electrochemical oxidation. Since generation of gas was seen during the electrochemical oxidation of **1** in both Pyr_4FAP and 0.2 M Pyr_4FAP/THF solutions, the species generated in the electrochemical oxidation reaction is supposed to be one molar amount of N_2 gas at least from **1**. Although the FT-IR spectra during the one-electron oxidation reaction in Pyr_4FAP showed increase in the peak at 1955 cm^{-1} and decrease in the peak at 1919 cm^{-1}, there is no increasing peaks unlike that in THF solution. Accordingly, the Mo(I)–N_2 species generated after the structure change was stabilized and kept in Pyr_4FAP. DFT calculations for five-coordinate $[Mo(depe)_2(N_2)]^+$ with FAP anion are also performed with empirical correction (GD3BJ) in ionic liquid (ε=14.7) to understand the effect of FAP anion. The DFT calculations reveal that the ΔG of $[Mo(depe)_2(N_2)]^+$ interacted with FAP anion is 16.0 kcal/mol lower compared with that without FAP anion. In addition, the estimated $\nu(N_2)$ for five-coordinate $[Mo(depe)_2(N_2)]^+$ with FAP anions (1984 cm^{-1}) is in good agreement with the experimental result (1955 cm^{-1}). These results indicate clearly that the weak interaction between them contributed to stabilize the monomeric $[Mo(depe)_2(N_2)]^+$ and suppressed the dimerization reaction of **1** in the electrochemical oxidation reaction.

4.4 Experimental

All manipulations were performed using standard Schlenk-line techniques or in an MBraun dry box under Ar or N_2 atmosphere (< 1 ppm O_2 /H_2O).

4.4.1 Chemicals

N_2 (99.999%) and Ar (99.999 %) (Nagoya Kousan. Ltd.) were employed as inlet gas for the reaction vessel. 1,2−bis(diethyl)phosphinoethane, depe, was purchased from Sigma-Aldrich and used without the purification. *Trans*-[Mo(depe)$_2$(N_2)$_2$] was prepared according to the literature.[11] 1-Butyl-1-methylpyrrolidinium tris(pentafluoroethyl) trifluorophosphate, Pyr_4FAP,[12] was purchased from Merck Ltd. and purified referring to previous literature as follows.[13] Pyr_4FAP (50 g) was dissolved in distilled EtOH (100 mL), and to the solution was added an activated charcoal (5g, Sigma-Aldrich). And then, the activated charcoal was removed by filtrate and the remaining solvents were evaporated. If the color was not colorless, the purification was repeated using the activated charcoal. After the purification was finished, Pyr_4FAP was vacuumed at 80 °C for 3 days and dried over molecular sieves (4 Å) for 1 week. *Trans*-[Mo(depe)$_2$(N_2)$_2$] and Pyr_4FAP were stored in a glove box (mBRAUN MB 150B−G glovebox) under N_2 atmosphere (< 1 ppm O_2/H_2O). KC_8 was prepared according to the literature.[14] Solvents were purified by the method of Grubbs,[15] where the solvents were passed over columns of activated alumina and supported copper catalyst supplied by ultimate purification system (Glass Contour System, NIKKO HANSEN & CO., LTD), transferred to the glovebox without exposure to air, and stored over molecular sieves 4Å. The *trans*-[Mo(depe)$_2$($^{15}N_2$)$_2$] is prepared under $^{15}N_2$ atmosphere by the same procedure in case of *trans*-[Mo(depe)$_2$(N_2)$_2$]. The $^{15}N_2$ gas (99.9 Atom %), which was purchased from SI Science Co. Ltd., was purified by passing the column containing KC_8 (see Figure C1 in Appendix C), and used after replacement of the gas from Ar to $^{15}N_2$ by using vacuum line equipped in the glovebox.

4.4.2 Instrumentation

The electrochemical study was evaluated using a potentiostat (BAS, ALS/1100C). Cyclic voltammograms were measured in the glove box under a purified Ar atmosphere at 25°C. The CVs were recorded using a GCE (diameter: 1 mm) as a WE. Pt spiral wire was used as a CE. Ag/Ag^+ electrode (Ag wire + 10 mM $AgNO_3$ in 0.2 M Pyr_4FAP/THF) was used as a RE. The working electrode was polished by using aluminum slurry before the CV measurement according to the previous literature.[16] The counter electrode was dipped in concentrated nitric acid for 1 day, and then, rinsed by Milli-Q water and dried in an oven at 190 °C. The potentials are referenced to the Fc/Fc^+ redox couple, which was measured by adding ferrocene to the sample solution. The concentrations of each samples were adjusted to 1 mM. FT-IR spectra of the solid compounds were measured with a JASCO FT/IR−4200 spectrophotometer. UV−vis absorption spectra were measured with a Jasco V−770 spectrophotometer using a 1 mm light-pass−length quartz cell shown in Figure A1 of Appendix A. Resonance Raman spectra were obtained using a liquid nitrogen cooled CCD detector (CCD-1024 × 256-OPEN-1LS, HORIBA Jobin Yvon) attached to a 1 m single polychromator (MC-100DG, Ritsu Oyo Kogaku) with a 1200 grooves/mm holographic grating. An excitation wavelength of 355 nm was provided by an Nd:YAG laser (Photonic Solutions, SNV-20F), with 5 mW power at the sample point. All measurements were carried out with a hand-made glass tube (ϕ 4 mm, length: 30 cm) at room temperature. Raman shifts were calibrated with indene and potassium ferricyanide, and the accuracy of the peak positions of the Raman bands was ±1 cm^{-1}. The concentration of each sample was adjusted to 2 mM.

4.4.3 FT-IR spectroscopy during the controlled potential electrolysis

FT- IR measurements were carried out in Nylon film cell as shown in Figure C2 of Appendix C. The nylon film (thickness 75 μm) is purchased from Asahi KASEI Pax Co. Ltd. The cut nylon film (6.5 cm × 2.4 cm) was brought together by using the laminating machine (Clip selaler z-1, Technoimpulse Co. Ltd). The Pt mesh (80mesh, 0.08 × 5 × 10 mm, Nilaco Co. Ltd.) connected with Pt wire (ϕ 0.25 mm diameter, length: 10cm, Nilaco Co. Ltd.) was used as the working electrode. The Pt mesh (80mesh, 0.08×10×10 mm, Nilaco Co. Ltd.) connected with Pt wire (ϕ 0.25 mm diameter, length: 10 cm, Nilaco Co. Ltd.) was used as the counter electrode. Pt wire was used as a quasi-reference electrode (ϕ 0.25 mm diameter, Nilaco Co. Ltd.).

The nylon film cell is soft, and the thickness of liquid is easily changeable, therefore, the exchanging of solutions affects the baseline. Thus, the baseline of sample solutions is measured before the CPE and the obtained results during CPE are displayed as difference spectrum against it. The set of nylon film cell containing the sample solution was carried out in the glove box and the measurements were carried out outside of glove box. The top of Nylon film cell is coated with silicon grease and closed by the laminating machine. Thus, the inside in Nylon film cell is kept under inert atmosphere. The nylon film cell is prepared every time and it was disposed after measurement. The nylon film is transparent for the infrared light in the range of 1700 ~ 2200 cm^{-1}.

4.4.4 Resonance Raman spectroscopy during the controlled potential electrolysis

Resonance Raman spectroscopy was carried out in hand-made electrolysis cell (Raman cell) as shown in Figure C3 of Appendix C. The glass tube (diameter: 4 mm, length: 30 cm) is made of quarts (downside, length 10 cm) and pylex (upper side, length: 20 cm). The upper part is welded with ground glass joint (15/25, female) for setting electrode by using Teflon tube adaptor (F-5005-004, outside diameter: ϕ6 mm, inside diameter: ϕ5.0 mm, interchangeable ground joint: 15/25, FLON INDUSTRY CO., LTD.). Pt mesh and Pt wire as using electrodes were purchased from Nilaco Co., Ltd. Pt mesh (diameter: ϕ0.08 mm, 80 mesh, 0.4 cm × 1 cm) connected with Pt wire (diameter: ϕ0.25 mm, length: 25 cm) was used as working electrode (WE). Pt mesh, whose reaction area is three times larger than WE, connected with Pt wire (diameter: ϕ0.25 mm, length: 25 cm) was used as the counter electrode (CE). Pt wire (diameter: ϕ0.25 mm, length: 25 cm) was used as quasi-reference electrode (QRE). The Cu wires as lead line for connection between electrodes and potentiostat were fixed to PTFE tube (outside diameter: 6.0 mm, inside diameter: 5.0 mm, FLON INDUSTRY CO., LTD.) by using one-component RTV rubber (KE45, Shin-Etsu Silicon). PTFE tube containing three Cu wires was kept overnight for fixing the RTV rubber. The PTFE tube with Cu wires was jointed to the resonance Raman cell by using a Teflon tube adapter (F-5005-004, outside diameter: ϕ6 mm, inside diameter: ϕ5.0 mm, interchangeable ground joint: 15/25, FLON INDUSTRY CO., LTD.). For increasing the airtightness of the connecter with PTFE tube containing Cu wires, a silicon grease was coated. For preventing a contact of electrodes and lead lines each other, the Pt wire of the electrodes were covered by PTFE tube (outside diameter: ϕ1.0 mm, inside diameter: ϕ0.5 mm, FLON INDUSTRY CO., LTD.), and Cu wires bared partly in Raman cell side were wrapped with parafilm. The setting before measurement was performed in the globe box under $^{14}N_2$ atmosphere. To decide the potential of CPE, a linear sweep voltammogram (LSV) was measured. The initial Raman spectra, which are described as 0 s in Figure 4-3, were recorded after the LSV measurement. The Raman laser at 355 nm was irradiated only in measuring resonance Raman spectroscopy.

4.4.5 UV-vis spectroscopy during the controlled potential electrolysis

UV-vis spectra during electrochemical reduction were measured by using 1 mm length quartz cell welded with the Pyrex glass tube with an interchangeable ground joint (15/25), a Teflon adapter and electrodes (Figure A1 in Appendix A). Pt mesh and Pt wire were purchased from Nilaco Co., Ltd. Pt mesh (diameter: ϕ 0.08 mm, 80 mesh, 0.8 cm × 3 cm) connected with Pt wire (diameter: ϕ 0.25 mm, length: 6 cm) was used as working electrode (WE). Pt mesh, whose reaction area is three times larger than WE, connected with Pt wire was used as the counter electrode (CE). Pt wire (diameter: ϕ 0.25 mm, length: 3 cm) was used as quasi-reference electrode (QRE). The Cu wires as lead line for connection between electrodes and potentiostat were fixed to PTFE tube (outside diameter: ϕ 6.0 mm, inside diameter: ϕ 5.0 mm, FLON INDUSTRY CO., LTD.) by using one-component RTV rubber (KE45, Shin-Etsu Silicon). PTFE tube containing three Cu wires was kept overnight for fixing the RTV rubber. The PTFE tube with Cu wires was jointed to the quartz cell by using a Teflon tube adapter (F-5005-004, outside diameter: ϕ 6 mm, inside diameter: ϕ 5.0 mm, interchangeable ground joint: 15/25, FLON INDUSTRY CO., LTD.). For increasing the airtightness of the connecter with PTFE tube containing Cu wires, a silicon grease was coated. For preventing a contact of electrodes and lead lines each other, the Pt wire of the electrodes were covered by PTFE tube (outside diameter: ϕ 1.0 mm, inside diameter: ϕ 0.5 mm, FLON INDUSTRY CO., LTD.), and Cu wires bared partly in UV-vis cell side were wrapped with parafilm. The setting was performed in the globe box. Therefore, the measurements were carried out under Ar atmosphere. The blank solution without **1**, which contains only solution in the quartz cell with electrodes, was measured as base line. To decide the potential of CPE, a linear sweep voltammogram (LSV) was measured. The initial UV-vis spectra, which are described as 0 s in Figure 4-4, were recorded after the LSV measurement. The subsequent UV-vis spectra were measured during the controlled potential electrolysis.

4.4.6 DFT and TDDFT calculations

All electronic structure calculations were performed with the Gaussian 09 package[17] on the Fujitsu HX600 system at the Nagoya University Information Technology Center. Geometry optimizations of dinitrogen complexes were performed using B3LYP* functional, which is a reparametrized version of the B3LYP hybrid functional[18] developed by Reiher and co-workers[19]

The B3LYP and B3LYP* energy expressions are given as equation (1):

$$E_{XC}^{B3LYP} = a_0 E_X^{HF} + (1 - a_0) E_X^{LSDA} + a_x E_X^{B88} + a_c E_c^{LYP} + (1 - a_c) E_C^{VWN} \quad (1)$$

where a_0 = 0.20 (B3LYP) or 0.15 (B3LYP*), a_x = 0.72, a_c = 0.81 and in which E_X^{HF} is the Hartree-Fock exchange energy; E_X^{LSDA} is the local exchange energy from the local spin density approximation; E_X^{B88} is Becke's gradient correction[20] to the exchange functional; E_c^{LYP} is the correlation functional developed by Lee and co-workers[21]; and E_C^{VWN} is the correlation energy calculated using the local correlation functional of Vosko, Wilk and Nusair (VWN)[22].

We used Stuttgart/Dresden ECP and basis set on Mo[23] together with 6-311G(d) on P and N[24a,24b], 6-31G(d)[25a,25b] on C, F and H. The results of frequency calculations at the same level confirmed that each of the optimized structures was at a minimum on the potential energy surface. For solvent calculation, the polarized continuum model (PCM)[26a] was applied, using a dielectric constant ε of 7.4257 for THF. DFT calculations for **9'**,**10'**, **11'**, and **12**' were performed by using the above functional and basis sets with the D3 version of Grimme's dispersion with Becke − Johnson damping (GD3BJ)[26b,26c] in addition to the solvent effects of ionic liquid (ε = 14.7). The dielectric constants of 1-butyl-1-methylpyrrolidinium bis(trifluoromethylsulfonyl)imide reported in previous literature[26d] is used instead of that of $\mathrm{Pyr_4FAP}$, because the dielectric permittivity of Pyr4FAP is not reported yet.

To assign the absorption bands of electronic transitions, time-dependent density functional theory (TDDFT)[27] calculations were performed. For the simulation of UV-vis spectra, the absorption profile was calculated as a sum of Gaussian functions where the heights and centers of the peaks were oscillator strengths and excitation energies, respectively, and the estimated standard deviation was 0.1 eV. The isosurfaces of the molecular orbitals were drawn using the MOPLOT and MOVIEW programs.[28]

4.5 References

1. K. Arashiba, A. Eizawa, H. Tanaka, K. Nakajima, K. Yoshizawa, Y. Nishibayashi, *Bull. Chem. Soc. Jpn.*, **2017**, *90*, 1111.
2. (a) J. Chatt, W. Hussain, G. J. Leigh, H. Neukomm, C. J. Pickett, D. A. Rankin, *J.*

Chem. Soc., Chem. Commun. **1980**, 1024. (b) G. J. Leigh, C. J. Pickett, *J. Chem. Soc., Dalton Trans*., **1977**, 1797.

3. (a) Considering that the formal potentials (V) for the ferrocene/ferrocenium couple vs. SCE is 0.56 V in THF containing $[NBu_4][PF_6]$. The obtained $E_{1/2}$ measured by glassy carbon electrode (GCE) (−1.01 V) is good agreement with the $E_{1/2}$ reported by Chatt and co-worker (–0.99 V (vs. Fc/Fc^+). (b) N. G. Connelly, W. E. Geiger, *Chem. Rev*. **1996**, *96*, 877.
4. A. C. Filippou, G. Schnakenburg, A. I. Philippopoulos, N. Weidemann, *Angew. Chem. Int. Ed.* **2005**, *44*, 5979.
5. T. A. George, C. D. Sebold, *Inorg. Chem.* **1973**, *12*, 2548.
6. J. D. Cohen, M. Mylvaganam, M. D. Fryzuk, T. M. Loehr, *J. Am. Chem. Soc.*, **1994**, 116, 9529.
7. C. E. Laplaza, M. J. A. Johnson, J. C. Peters, A. L. Odom, E. Kim, C. C. Cummins, G. N. George, I. J. Pickering, *J. Am. Chem. Soc.*, **1996**, *118*, 8623.
8. (a) J. R. Durig, M .G. Griffin, R. W. MacNamee, *J. Raman Spectrosc.*, **1975**, *3*, 133. (b) N. C. Craig, I. W. Levin, *J. Chem. Phys.*, **1979**, *71*, 400.
9. (a) M. J. Bezdek, S. Guo, P. J. Chirik, *Inorg. Chem.*, **2016**, *55*, 3117.
10. G. A. Silantyev, M. Förster, B. Schluschaß, J. Abbenseth, C. Würtele, C. Volkmann, M. C. Holthausen, S. Schneider, *Angew. Chem., Int. Ed.* **2017**, *56*, 5872.
11. T. A. George, M. E. A. Noble, *Inorg. Chem.* **1978**, *17*, 1678.
12. N. V. Ignat'ev, U. Welz-Biermann, A. Kucheryna, G. Bissky, H. Willner, *J. Fluorine Chem.* **2005**, *126*, 1150.
13. A. K. Burrell, R. E. Del Sesto, S. N. Baker, T. M. McCleskeya, G. A. Baker,

Green Chem. **2007**, *9*, 449.

14. D. E. Bergbreiter, J. M. Killough, *J. Am. Chem. Soc.* **1978**, *100*, 2126.
15. A. B. Pangborn, M. A. Giardello, R. H. Grubbs, R. K. Rosen, F. J. Timmers, *Organometallics*, **1996**, *15*, 1518.
16. I. Hu, D. H. Karweik, T. Kuwana, *J. Electroanal. Chem.* **1985**, *188*, 59.
17. M. J. Frisch, G. W. Trucks, H. B. Schlegel, G. E. Scuseria, M. A. Robb, J. R. Cheeseman, G. Scalmani, V. Barone, B. Mennucci, G. A. Petersson, H. Nakatsuji, M. Caricato, X. Li, H. Hratchian, A. F. Izmaylov, J. Bloino, G. Zheng, J. L. Sonnenberg, M. Hada, M. Ehara, K. Toyota, R. Fukuda, J. Hasegawa, M. Ishida, T. Nakajima, Y. Honda, O. Kitao, H. Nakai, T. Vreven, J. A. Jr. Montgomery, J. E. Peralta, F. Ogliaro, M. Bearpark, J. J. Heyd, E. Brothers, K. N. Kudin, V. N. Staroverov, T. Keith, R. Kobayashi, J. Normand, K. Raghavachari, A. Rendell, J. C. Burant, S. S. Iyengar, J. Tomasi, M. Cossi, N. Rega, J. M. Millam, M. Klene, J. E. Knox, J. B. Cross, V. Bakken, C. Adamo, J. Jaramillo, R. Gomperts, R. E. Stratmann, O. Yazyev, A. J. Austin, R. Cammi, C. Pomelli, J. W. Ochterski, R. L. Martin, K. Morokuma, V. G. Zakrzewski, G. A. Voth, P. Salvador, J. J. Dannenberg, S. Dapprich, A. D. Daniels, O. Farkas, J. B. Foresman, J. V. Ortiz, J. Cioslowski, D. J. Fox, Gaussian 09, Revision E.01,; Gaussian, Inc.: Wallingford, CT, 2013.
18. A. D. Becke, *J. Chem. Phys.* **1993**, *98*, 5648.
19. (a) M. Reiher, O. Salomon, B. A. Hess, *Theor. Chem. Acc.* **2001**, *107*, 48. (b)M. Reiher, *Inorg. Chem.* **2002**, *41*, 6928.
20. A. D. Becke, *Phys. Rev. A*, **1988**, *38*, 3098.
21. C. Lee, W. Yang, R. G. Parr, *Phys. Rev. B* **1988**, *37*, 785.

22. S. H. Vosko, L. Wilk, M. J. Nusair, *Can. J. Phys*. **1980**, *58*, 1200.

23. D. Andrae, U. Haüssermann, M. Dolg, H. Stoll, H. Preuss, *Theor. Chim. Acta*, **1990**, *77*, 123.

24. (a) A. D. McLean, G. S. Chandler, *J. Chem. Phys*. **1980**, *72*, 5639. (b) M. M. Francl, W. J. Pietro, W. J. Hehre, J. S. Binkley, M. S. Gordon, D. J. DeFrees, J. A. Pople, *J. Chem. Phys*. **1982**, *77*, 3654.

25. (a) P. C. Hariharan, J. A. Pople, *Theor. Chim. Acta* **1973**, *28*, 213. (b) W. J. Hehre, R. Ditchfield, J. A. Pople, *J. Chem. Phys*. **1972**, *56*, 2257.

26. (a) J. Tomasi, B. Mennucci, R. Cammi, R. *Chem. Rev*. **2005**, *105*, 2999. (b) S. Grimme, J. Antony, S. Ehrlich, H. Krieg, *J. Chem. Phys.* **2010**, *132*, 154104－1－154104－19. (c) S. Grimme, S. Ehrlich, L. Goerigk, *J. Comput. Chem.* **2011**, *32*, 1456. (d) M. M. Huang, Y. Jiang, P. Sasianker, G. W. Driver, and H. Weingärtner, *J. Chem. Eng. Data*, **2011**, *56*, 1494.

27. A. Dreuw, M. Head-Gordon, *Chem. Rev*. **2005**, *105*, 4009.

28. (a) H. Wasada, Y. Tsutsui, *Bull. Coll. Gen. Educ.* **1996**, 33, 145−158. (b) I. Takahashi, H. Wasada, Y. Tsutsui, MOVIEW: Program of Nagoya University Information Technology Center Representing Molecular Orbitals and Electron Density Maps by Isosurfaces.

Chapter 5: Conclusions

In this thesis, the effect of ionic liquids (ILs) on the N_2 activation by a transition metal complex and its application to electrochemical ammonia (NH_3) synthesis are described and discussed. It is happy for me to report some findings in my Ph.D. study. The conclusions obtained from each chapter are summarized as below.

In Chapter 2, the electrochemical property of monomeric [Cp_2TiCl_2] was investigated in two different types of ILs, Pyr_4FAP with the non-coordinating FAP^- anions and Pyr_4OTf with the coordinating OTf anion, by measuring cyclic voltammetry. In the CVs of [$(Cp_2TiCl)_2$] in Pyr_4FAP and Pyr_4OTf, a difference was observed in the ratio of the current densities between Pyr_4OTf and Pyr_4FAP, indicating that $[Cp_2Ti]^{2+}$ was stabilized in Pyr_4OTf by the coordination of OTf anion in the η^1–O binding mode.

Toward development of the electrochemical NH_3 synthesis by using transition metal complexes in IL under mild conditions, the SPE cell, where WE is supported with IL containing a transition metal complex on gas diffusion, was designed and fabricated. LSV in SPE cell showed that the current density under N_2 was larger than that under Ar in the range of −1.0 to −1.5 V (vs. Ag/AgCl). In the case of using Pyr_4FAP, the maximum yield of NH_3 per [Cp_2TiCl_2] was 27% at 20 C and the maximum current efficiency was 1.24% at early stage, but it was gradually decreased to 0.2% at 20 C. The yield of NH_3 per Ti ion (%) and current efficiency in the CPE of [Cp_2TiCl_2] in Pyr_4OTf were lower than that in Pyr_4FAP, indicating that the synthesis of NH_3 by using a transition metal complex is preferred in non-coordinating IL, such as Pyr_4FAP, as a solvent. The unique property of Pyr_4FAP will be applied not only to electrochemical NH_3 synthesis but also to various electrochemical reactions by using transition metal complexes, because Pyr_4FAP acts as a polar non-coordinating IL.

In Chapter 3, to understand the electrochemical synthesis of ammonia by using $[Cp_2TiCl_2]$ in ILs that was described in Chapter 2, the electrochemical reduction of $[Cp_2TiCl_2]$ in both of conventional organic solvents and ILs were investigated by using UV-vis/NIR spectroscopy during electrochemical reduction. Even in non-coordinating Pyr_4FAP, the absorption band at 1194 nm was observed by electrochemical reduction from Ti(IV) to (III) in $[Cp_2TiCl_2]$. The absorption band at ca. 1200 nm is also observed in the UV-vis/NIR spectrum of dimeric $[(Cp_2TiCl)_2]$ in Pyr_4FAP, which is in good agreement with the absorption bands calculated with TDDFT method, which was assigned to MMCT. The characteristic absorption band at ca. 1200 nm was also observed in THF and Pyr_4OTf, which can be coordinated with $[Cp_2TiCl]$ via Ti-O bond. Accordingly, the UV-vis/NIR spectra of $[Cp_2TiCl_2]$ in Pyr_4FAP, Pyr_4OTf and 0.2 M Pyr_4FAP/THF during the electrochemical reduction of Ti(IV) to Ti(III) demonstrate that $[(Cp_2TiCl)_2]$ was generated from $[Cp_2TiCl_2]^-$ in these three solvents.

To understand the existence of equilibrium reaction between dimeric $[(Cp_2TiCl)_2]$ and monomeric $[Cp_2TiCl]$, frozen solution EPR spectroscopy for $[(Cp_2TiCl)_2]$ in Pyr_4FAP was studied in non-coordinating IL, 1-butyl-1-methylpyrrolidinium tris(pentafluoroethyl) trifluorophosphate (Pyr_4FAP), and organic solvents of 0.2 M Pyr_4FAP/THF and toluene under N_2. Interestingly, the spectrum measured in non-coordinating IL under $^{14}N_2$ gave a triplet hyperfine splitting of the g_z signal, which was changed to a doublet pattern in the isotopic labeling experiment using $^{15}N_2$. However, the EPR spectra in organic solvents did not give such a hyperfine splitting at the g_z signal.

These observations demonstrate that $[(Cp_2TiCl)_2]$ is in the equilibrium between monomeric and dimeric species in both IL and organic solvents, and furthermore that the monomeric species is coordinated to dinitrogen in the non-coordinating IL, Pyr_4FAP. These findings may also indicate that Pyr_4FAP has unique properties capable of stabilizing the N_2 coordinated-$[Cp_2TiCl]$ species.

With a view to understanding the effect of ILs toward the N_2 coordination to monomeric $[Cp_2TiCl]$, DFT calculations were carried out for dimeric $[(Cp_2TiCl)_2]$ in the singlet (**1**) and triplet states (**2**), monomeric $[Cp_2TiCl]$ (**3**), $[Cp_2TiCl(N_2)]$ (**4**), and $[Cp_2TiCl(N_2)]^{\ddagger}$ in the transition state (**4-TS**) in toluene and IL, in which the effects of solvents were examined with applying their dielectric permittivities. The DFT studies revealed that ΔH values for **1** (−6.99 kcal/mol) and **2** (−6.92 kcal/mol) in toluene were lower than those in IL (−3.85 kcal/mol for **1** and −3.75 kcal/mol for **2**, respectively). These results are well consistent with the experimental findings that the model complexes with a small dipole moment have been stabilized by the solvents with a small dielectric permittivity. Moreover, to consider the effect of FAP anion toward N_2 coordination to titanocene, we further calculated **3**, **4** and **4-TS** with FAP anion (**3'-FAP**, **4'-FAP** and **4'-FAP-TS)** with empirical corrections (GD3BJ). Though the structures of titanocene in **3'-FAP** and **4'-FAP** are similar to those of **3'** and **4'** without FAP anion, respectively, F atoms in FAP anion had weak interactions toward H atoms on Cp ring. It suggests that the interactions have contributed to stabilize **3'-FAP** and **4'-FAP** and lowered the activation energy of the N_2 coordination reaction in **4'-FAP-TS**. The N_2 coordination to $[Cp_2TiCl]$ was occurred in polar domain of Pyr_4FAP due to formation of a complex with anion of IL, and as a result, it would have been obtained by frozen solution EPR spectroscopy.

In Chapter 4, electrochemical oxidation reaction for *trans*−$[Mo(depe)_2(N_2)_2]$ (depe =

$Et_2PCH_2CH_2PEt_2$) was carried out and the generation of dimeric molybdenum complex bridging $[N_2]^{2-}$ ligand was revealed. The one electron electrochemical oxidation reaction of *trans*–$[Mo(depe)_2(N_2)_2]$ was followed by time-dependent FT-IR, resonance Raman, and UV-vis spectroscopies during controlled-potential electrolysis (CPE). The time dependent FT-IR spectra during CPE showed decrease in the peak at 1938 cm^{-1} assigned to $\nu(N_2)$ in *trans*–$[Mo(depe)_2(N_2)_2]$ and increase in the peak at 2008 cm^{-1} assigned to $\nu(N_2)$ in the electrochemically-oxidized *trans*–$[Mo(depe)_2(N_2)_2]$. However, the increased peak at 2008 cm^{-1} disappeared after electrochemical oxidation reaction. The time-dependent resonance Raman spectra during CPE gave three bands at 1574, 1509 and 1294 cm^{-1}, suggesting that N_2 is activated by forming dimeric species, $(\mu–N_2)[Mo(depe)_2(N_2)_2]$. Time-dependent UV-vis spectra during CPE showed decrease in the absorption bands at 323 and 493 nm derived from *trans*–$[Mo(depe)_2(N_2)_2]$ and increase in the absorption bands at 417 and 457 nm assigned to the oxidized *trans*–$[Mo(depe)_2(N_2)_2]$, and the absorption band appeared at 353 nm assigned to $(\mu–N_2)[Mo(depe)_2(N_2)_2]$. To consider the assignment for these spectra, DFT and TDDFT calculations were also performed and they were in good agreement with the experimental results. Unfortunately, a nitride complex that will be generated by N_2 cleavage was not observed. This is because the transition state of the reaction has high energy barrier. However, to the best of our knowledge, the finding that the bridging N_2 ligand rather than the terminal N_2 coordinated to the metal complex was activated by electrochemical oxidation reaction have not been reported yet. Understanding and control of the reactivity for N_2 complex by electrochemical method are very important for realizing catalytic N_2 fixation by using renewable energy.

On the contrary, in the electrochemical oxidation of *trans*–$[Mo(depe)_2(N_2)_2]$ in

Pyr_4FAP, the resonance Raman spectra of *trans*–$[Mo(depe)_2(N_2)_2]$ and its oxidized species in Pyr_4FAP have revealed that a dimeric structure bridged with N_2 is not generated before and after electrochemical oxidations. Since the generation of gases were observed in the electrochemical oxidation of *trans*–$[Mo(depe)_2(N_2)_2]$ in both Pyr_4FAP and 0.2 M Pyr_4FAP/THF solutions, one molar amount of N_2 at least from *trans*–$[Mo(depe)_2(N_2)_2]$ is supposed to have been released by the electrochemical oxidation reaction. The FT-IR spectrum during the one-electron oxidation reaction in Pyr_4FAP showed increase in peak at 1955 cm^{-1} and decrease in peak at 1919 cm^{-1} and the increased peak did not disappear unlike that in THF solution. Accordingly, the Mo(I)–N_2 species formed after the structure change was stabilized and kept in Pyr_4FAP. DFT calculations for five-coordinate $[Mo(depe)_2(N_2)]^+$ with FAP anion were also performed with empirical correction (GD3BJ) in IL (ε=14.7) to consider the effect of FAP anion. The DFT calculations revealed that the ΔG of $[Mo(depe)_2(N_2)]^+$ interacted with FAP anion was 16.0 kcal/mol lower compared with that without FAP anion. The weak interaction may have contributed to stabilize monomeric $[Mo(depe)_2(N_2)]^+$ and suppressed the dimerization reaction of *trans*–$[Mo(depe)_2(N_2)_2]$ in the electrochemical oxidation reaction.

In general, the IL is known to have polar and nonpolar domain structures, which are composed of ionic parts and alkyl chain parts, respectively. Although most of polar conventional solvents act as coordinating solvent against unsaturated transition metal complexes, the polar domain in Pyr_4FAP acts as non-coordinating polar solvent toward transition metal center. Interestingly, Pyr_4FAP weakly interacts with the transition metal complex to form a complex with anion of IL. Such weak interactions with anion parts of IL would be observed in the case of using IL. Therefore, it is one of the key factors for reason why the reactivity in ILs is different from those in conventional organic solvents.

The conversion of N_2 into NH_3 is one of the most important topics in the view of scientific and engineering fields. The electrochemical NH_3 synthesis in IL gave new findings in the research field involving N_2 activation and ionic liquids. Therefore, in the future, this work will contribute to realize the sustainable energy society.

Appendix A: Supporting information in Chapters 2 and 3

A.1 Design of the cell for UV-vis spectroscopy during CPE

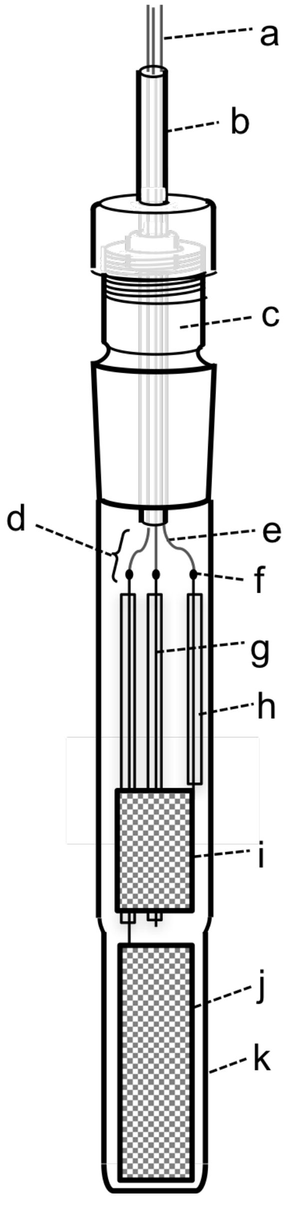

Figure A1. Schematic drawing of UV-vis spectral cell made of quarts (bottom part) and pyrex glass (upper part). (a) Cu wires as a lead line, (b) PTFE tube filled by RTV rubber, (c) Teflon adapter (15/25), (d) a wrapped parafilm, (e) Cu wires as a lead line, (f) joint coiled by Cu wire, (g) QRE (Pt wire), (h) PTFE tube, (i) CE (Pt mesh), (j) WE (Pt mesh), and (k) quart cell (cell length: 1 mm).

A.2 Design of SPE cell

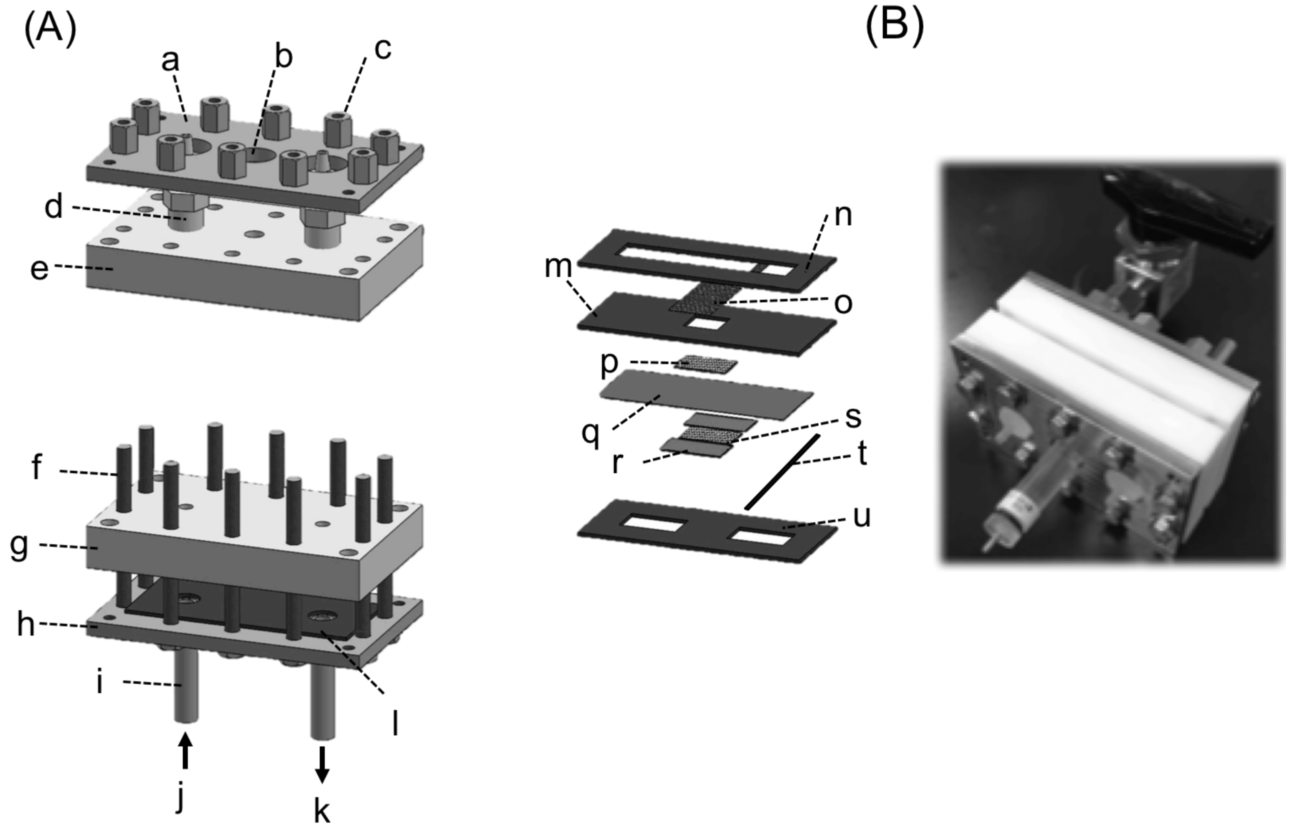

Figure A2. (A) A schematic diagram and (B) picture of the SPE cell. (a) Aluminum plate with three holes (1.2 cm diameter), (b) a center hole for RE, (c) high nut, (d) Teflon connector (R 1/8, inside diameter: 3 mm), (e) Teflon plate with a hole (1/4 28UNF) at the center for screwing the RE and two holes for connector, (f) stainless bolt, (g) Teflon plate with two holes for gas channel, (h) aluminum plate welded, (i) stainless steel seamless tubing (1/4 inch), (j) gas inlet, (k) gas outlet, (l) gasket, (m) gasket with square window of 10 mm, (n) gasket in anode side, (o) CE: Pt mesh, (p) carbon paper (10 mm (D) × 20 mm (W) × 0.37 mm (H)) for fixing of Nafion membrane, (q) Nafion®212 membrane, (r) parafilm (10 mm (D)×10 mm (W)), (s) WE: carbon paper (10 mm × 20 mm) coated with 50 μL of IL containing 10 mM [Cp_2TiCl_2] or [$(Cp_2TiCl)_2$], (t) Cu wire as a lead line, and (u) gasket in cathode side.

A.3 Quantification of H_2

All generated H_2 gas and flowed N_2 gas were collected in the balloon, and the amount of the generated H_2 gas was quantified by gas chromatography (SHIMADZU CORPORATION, GC-8A). The controlled potential electrolysis was performed under N_2 at flow rate of 1.0 mL/min. The outlet of the SPE cell was jointed to the balloon with a ball valve (Swagelok SS Ball Valve 1/4" straight, SW-SS-43GS4), a reducing port connector (Stainless Steel Swagelok Tube Fitting, Reducing Port Connector, 1/4 in. x 1/8 in. Tube OD, SS-401-PC-2), and a union tee (Stainless Steel Swagelok Tube Fitting, Union Tee, 1/8 in. Tube OD, SS-200-3) having a septum made of silicon (diameter: 6 mm, thickness: 4.5 mm, GL Sciences Inc., 3007-15101), and a male tube adapter (Stainless Steel Swagelok Tube Fitting, Male Tube Adapter, 1/8 in. Tube OD x 1/4 in. Male ISO Tapered Thread, SS-2-TA-1-4RT), as shown in Figure A3. The balloon was jointed with ISO tapered thread of the male tube adapter. When the quantification of H_2 was performed, the ball valve connected to the gas outlet was closed and disconnected from the SPE cell. The GC analysis conditions are shown as follows. Column: SHINCARBON ST 50/80, stainless column 4.0 m (2.0 m × 2) 3.0mm I.C., column temperature: 100 °C, carrier gas: Ar, detecter: TCD, 80 mA, sample volume: 500 μL. The gas tight syringe was used and subjected to GC analysis. Retention time for H_2 was 5.7 min.

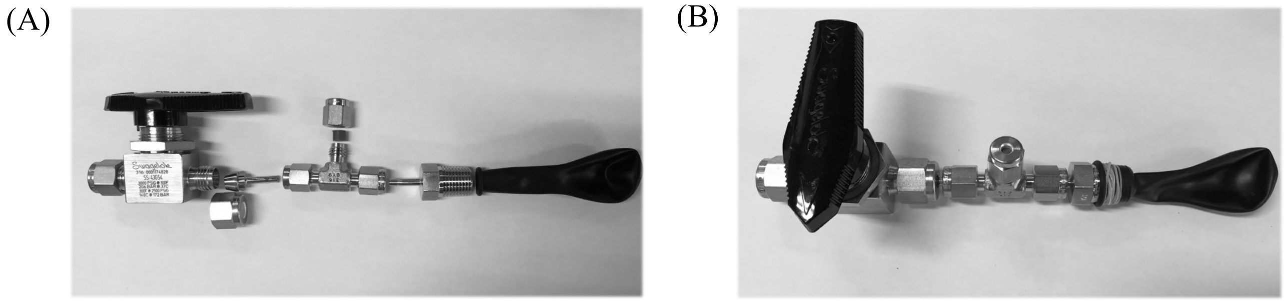

Figure A3. Pictures of parts for collecting H_2 gas (A) before and (B) after assembling.

To understand the electrochemical reduction of [Cp_2TiCl_2] in ionic liquid, diffusion coefficients and electrochemical rate constants of [Cp_2TiCl_2] in ionic liquids were determined as follows.

A.4 Calculation of diffusion coefficients (D / cm^2 s^{-1})

Diffusion coefficients of [Cp_2TiCl_2] in Pyr_4FAP, Pyr_4OTf and 0.2 M Pyr_4FAP/THF were determined from Cottrell equation by measuring chronoamperometry.[1]

$$i = \frac{nFA\sqrt{D}c^*}{\sqrt{\pi t}}$$

i = current (A)

n = number of electrons

F = Faraday constant, 96,485 (C/mol)

A = electrode area (cm^2)

c^* = concentration of electroactive species (mol/cm^3)

D = diffusion coefficient for species (cm^2/s)

t = time (s)

The chronoamperograms are shown in Figures A4, A5 and A6. Diffusion coefficient (D/cm^2 s^{-1}) of [Cp_2TiCl_2] was calculated from the slope in i-$t^{-1/2}$ plots. The parameter used in calculation and calculated D are summarized in Table A1.

Table A1. Parameters obtained from chronoamperograms.

Parameter	Pyr_4FAP	Pyr_4OTf	0.2 M Pyr_4FAP/THF
slope in i-$t^{-1/2}$ plot	0.169	0.1735	0.1845
A (cm^2)	7.85×10^{-3}		7.07×10^{-2}
c^* (mol/cm^{-3})	1.0×10^{-5}	1.0×10^{-6}	1.0×10^{-5}
D (cm^2/s)	9.6×10^{-8}	1.0×10^{-7}	1.2×10^{-5}

All calculations were carried out as n = 1.

Diffusion coefficient for [Cp_2TiCl_2] in 0.2 M Pyr_4FAP/THF (1.2×10^{-5} cm^2 s^{-1}) obtained in this study is similar to the value (7.2×10^{-6} cm^2 s^{-1}) in 0.2 M Bu_4NPF_6/THF reported in previous literature.[2]

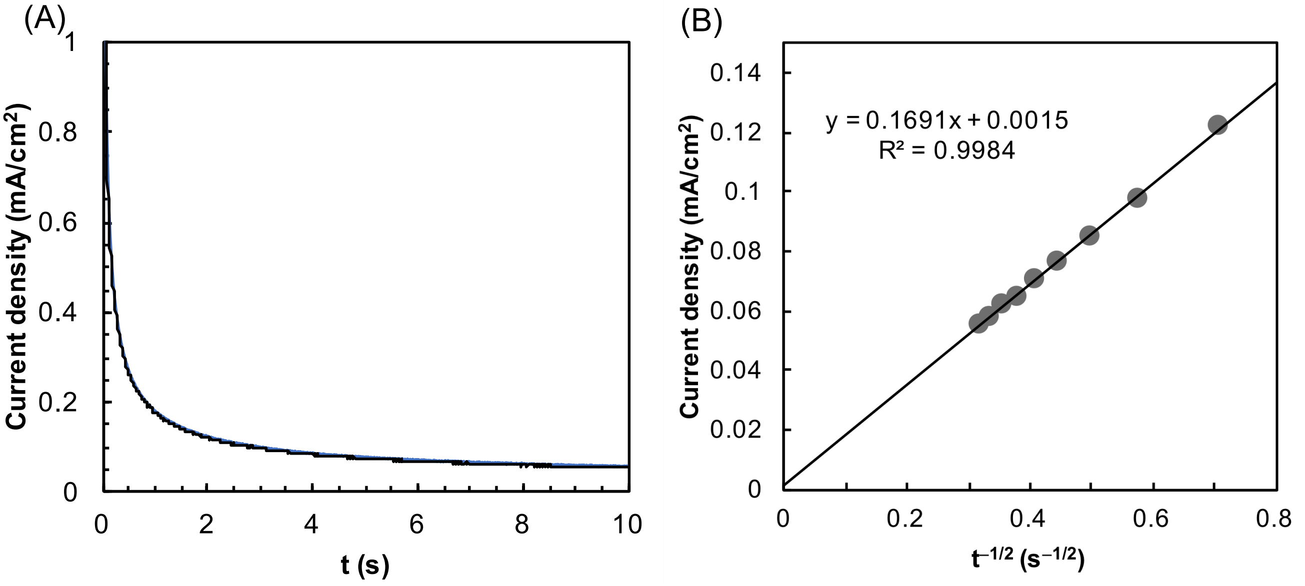

Figure A4. (A) Chronoamperogram of 10 mM [Cp_2TiCl_2] in Pyr_4FAP after the potential was stepped from 0 to −1.6 V (vs. Fc/Fc$^+$) and (B) i-$t^{-1/2}$ plots calculated from Figure A4(A).

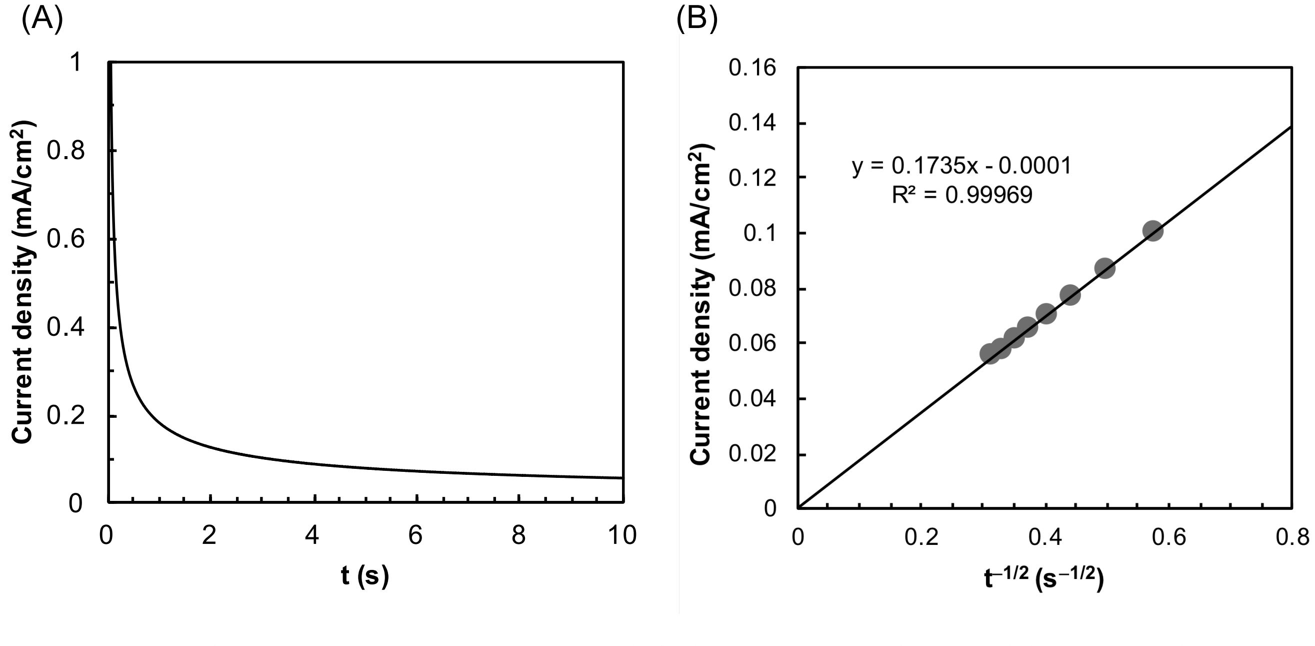

Figure A5. (A) Chronoamperogram of 10 mM [Cp_2TiCl_2] in Pyr_4OTf after the potential was stepped from 0 to −1.3 V (vs. Fc/Fc$^+$) and (B) i-$t^{-1/2}$ plots calculated from Figure A5(A).

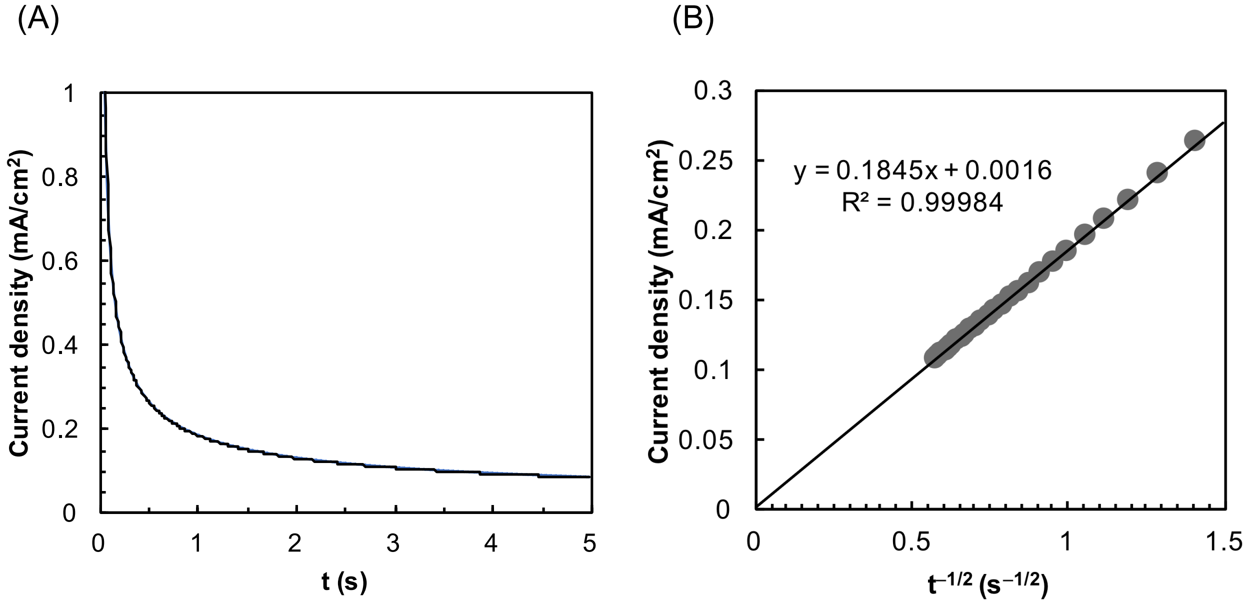

Figure A6. (A) Chronoamperogram of 1 mM [Cp$_2$TiCl$_2$] in 0.2 M Pyr$_4$FAP/THF (GCE: φ3 mm) after the potential was stepped from 0 to −1.6 V (vs. Fc/Fc$^+$) and (B) i-$t^{-1/2}$ plots calculated from Figure A6(A).

A.5 Calculation of electrochemical rate constant (k^0 / cm s^{-1})

Calculation of the electrochemical rate constant was performed using the peak separation of anodic and cathodic potentials, $\Delta E_p = E_{pa} - E_{pc}$, in the voltammograms according to the following equation reported in the previous literature.[1,3]

$$\Psi = \frac{k^0}{[\pi D \nu (F/RT)]^{1/2}} = f(\Delta E_p)$$

Ψ = *dimensionless rate parameter*
k^0 = *electrochemical rate constant* (cm s^{-1})
F = Faraday constant, 96,485 (C/mol)
ν = scan rate (V)
D = diffusion coefficient for species (cm^2/s)
R = gas constant, 8.314 (J · K^{-1} · mol^{-1})
T = absolute temperature (K)

Ψ value was estimated using the parameters listed in Table 1 that was reported in previous literature.[3] The ΔE was determined from the CVs shown in Figures A8, A9, and S10 and Tables A6, A7 and A8. The obtained rate constants were summarized in Table A2.

Table A2. Parameters used in the calculation for $k^{0'}$

Parameter	Pyr_4FAP	Pyr_4OTf	0.2 M Pyr_4FAP/THF
ΔE	103	105	75
Ψ	0.5	0.5	1.5
D	9.64×10^{-8}	1.01×10^{-7}	1.15×10^{-5}
ν	0.3	0.2	0.1
$k^{0'}$	9.4×10^{-4}	7.8×10^{-4}	$1.8 \times 10^{-2*}$

T = 298 was used in calculation.

*The calculated electrochemical rate constant (1.8×10^{-2} cm s^{-1}) is slightly smaller than the heterogeneous rate constant, k_s, of [Cp_2TiCl_2] in the redox of Ti(IV)/Ti(III) (0.04 cm s^{-1}) that was reported in the previous literature.[2] Therefore, the obtained $k^{0'}$ values in Table A2 could be affected by IR drop and they were underestimated.

Table A3. Relationship between Ψ function parameter and peak potential separation, ΔE_p[*3]

ΔE_p / mV	Ψ	ΔE_p / mV	Ψ	ΔE_p / mV	Ψ	ΔE_p / mV	Ψ
61.6	6.0	82.8	1.0	220	0.10	620	2.0×10^{-3}
62.5	5.0	90.6	0.75	288	5.0×10^{-2}	691	1.0×10^{-3}
63.8	4.0	105	0.50	382	2.0×10^{-2}	763	5.0×10^{-4}
66.0	3.0	123	0.35	454	1.0×10^{-2}	857	2.0×10^{-3}
70.3	2.0	144	0.25	525	5.0×10^{-3}	929	1.0×10^{-3}

*The table is constructed by utilizing the digital simulation package DigiSim 3.0 (Bioanalytical System). (One-electron reduction, $D_O = D_R$, $\alpha_c = 0.5$, $E_\lambda - E^{0'} = -1$) α_c: transfer coefficient, E_λ: switching potential.

A.6 Influence of viscosity of solvents against *D*

Ferrocene in ionic liquid has been reported that a plot of D versus $1/\eta$ is predicted to be linear according to Stokes-Einstein equation[4,5]

$$D = \frac{k_B T}{6\pi\eta r_H}$$

k_B: Bolzmann constant, $1.38064852(79)\times10^{-23}$ (J K^{-1})

T: absolute temperature (K)

η: Viscosity (Pa s)

r_H: Stokes radius

If the D value obtained in this study is reasonable, a plot of D versus $1/\eta$ is predicted to be linear. The plots are shown in Figure A7, and the linear relationship between D and $1/\eta$ is obtained. Therefore, the obtained D is reasonable and the diffusion of [Cp_2TiCl_2] in ionic liquid is according to Stokes-Einstein equation as well as ferrocene.

Table A4. Viscosity of ionic liquids and diffusion coefficients of [Cp_2TiCl_2]

Solvent	η^* /mPa s	$1/\eta$ /Pa^{-1} s^{-1}	D /10^{-7} cm^2 s^{-1}
Pyr_4FAP [6]	333	3.00	0.964
Pyr_4OTf [7]	217	4.61	1.02
0.2 M Pyr_4FAP/THF [8]	0.480	2083	115

*Viscosity at 293.15 K

Table A5.* Diffusion coefficients of ferrocene, Fc, and cobaltocene hexafluorophosphate, $CcPF_6$

Ionic liquid	viscosity / mPa s	D_{Fc} / 10^{-7} cm^{2}s^{-1}	D_{CcPF6} / 10^{-7} cm^{2}s^{-1}
[C_4mim][BF_4]	112	1.83	1.11
[C_4mim][NO_3]	266	0.83	0.58
[C_4mim][PF_6]	371	0.59	0.47
[$P_{14,6,6,6}$][FAP]	464	0.86	0.33

*The parameters are reported in the previous literature.[5]

[C_4mim]: 1-butyl-3-methylimidazolium cation [$P_{14,6,6,6}$]: tris(n-hexyl)tetradecylphosphonium cation

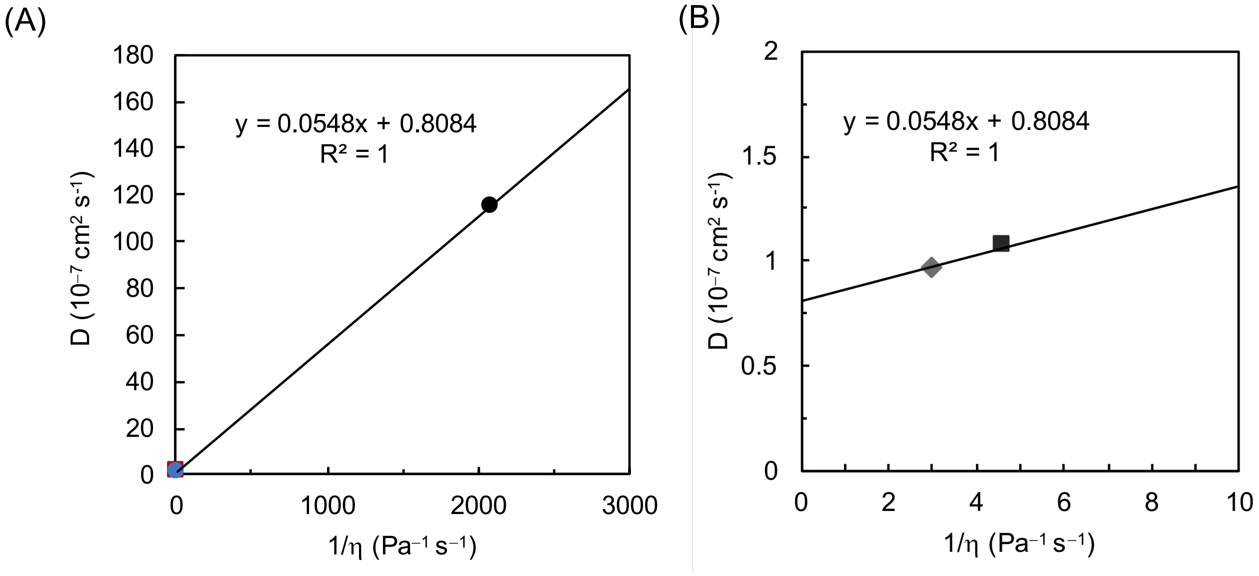

Figure A7. (A) Plots of *D* versus $1/\eta$ and (B) expanded version of Figure A7(A) (●: 0.2 M Pyr_4FAP/THF, ■: Pyr_4OTf and ◆: Pyr_4FAP).

A.7 Cyclic voltammograms of [Cp_2TiCl_2]

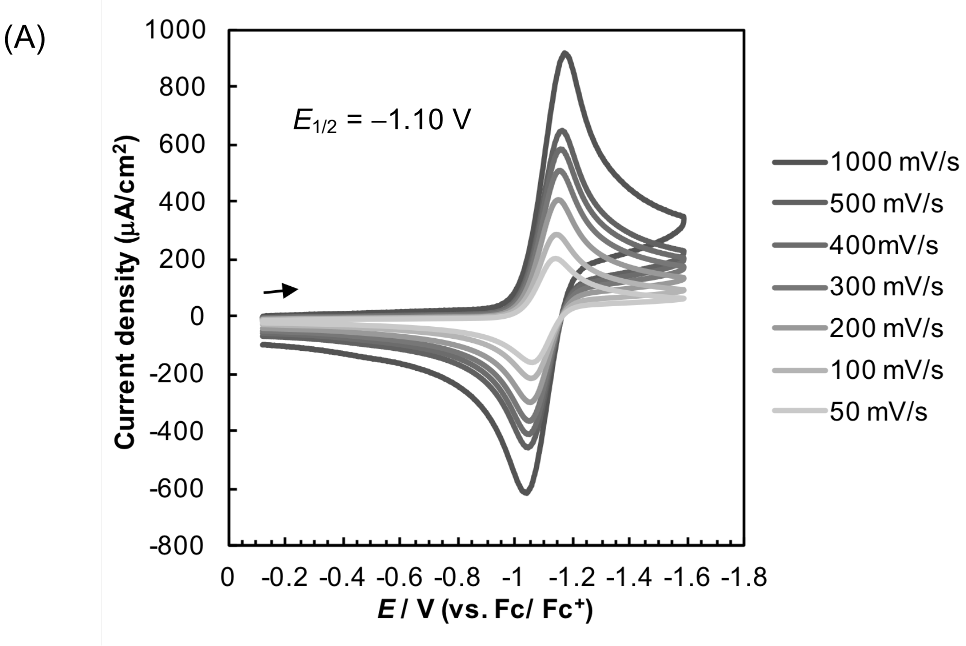

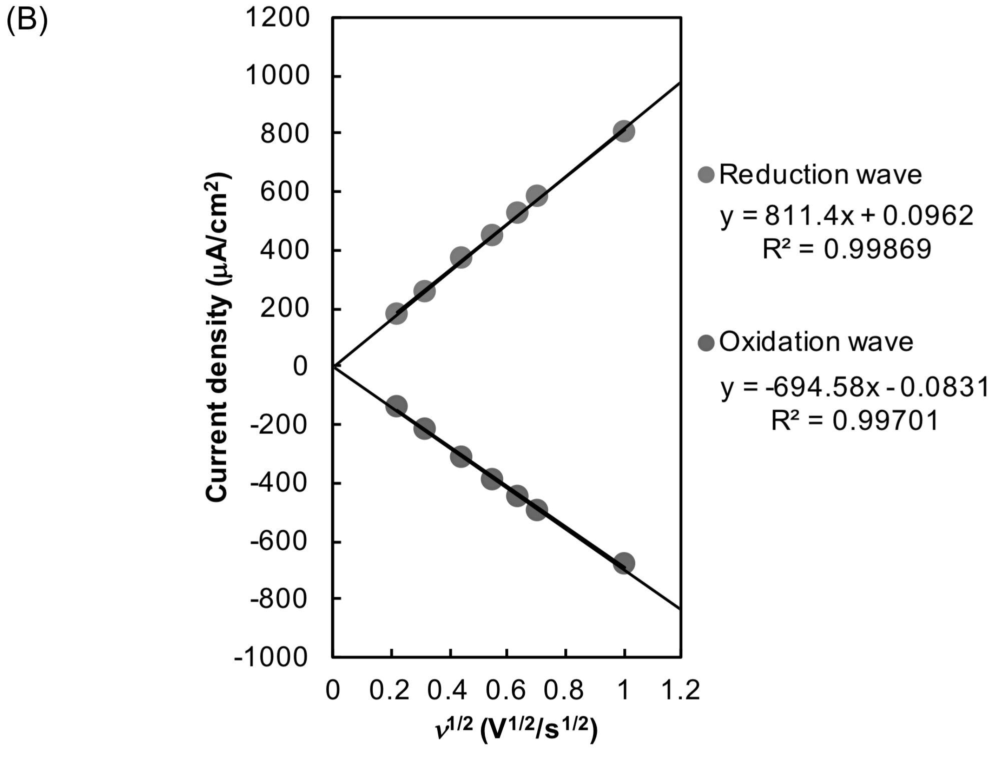

Figure A8. (A) Cyclic voltammograms of 10 mM [Cp_2TiCl_2] in Pyr_4FAP at scan rates of 50, 100, 200, 300, 400, 500, and 1000 mV/s (WE: GCE ϕ1 mm, CE: Pt wire, RE: Ag/Ag^+ electrode). The potential is referred to the ferrocene/ferrocenium (Fc/Fc^+) couple in Pyr_4FAP. (B) Plots of current density (μA/cm^2) against $v^{1/2}$ ($V^{1/2}/s^{1/2}$) calculated from Figure A8(A) (reduction wave: plots of positive current and oxidation wave: plots of negative one).

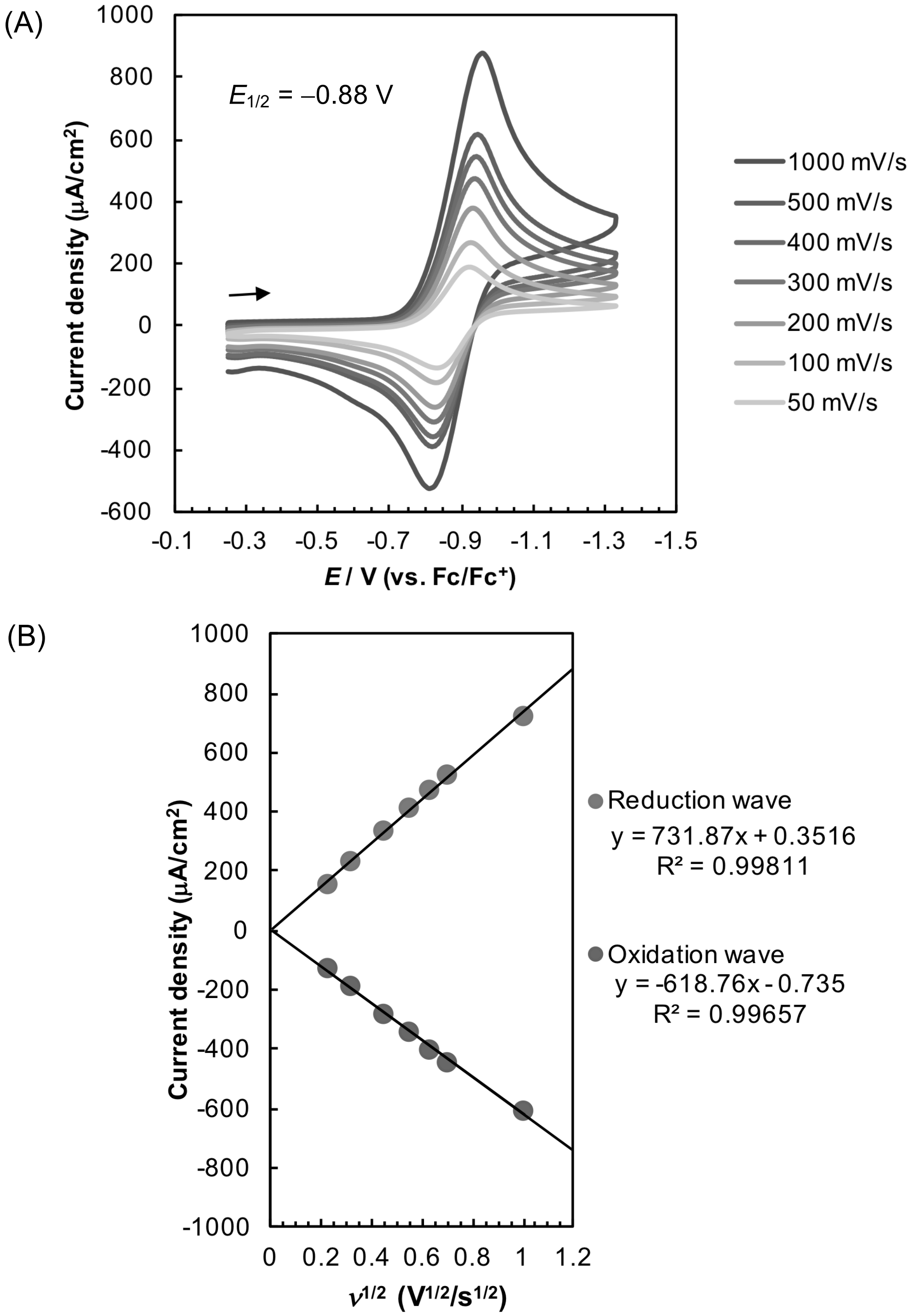

Figure A9. (A) Cyclic voltammograms of 10 mM [Cp_2TiCl_2] in Pyr_4OTf at scan rates of 50, 100, 200, 300, 400, 500, and 1000 mV/s (WE: GCE ϕ1 mm, CE: Pt wire, RE: Ag/Ag^+ electrode). The potential is referred to the ferrocene/ferrocenium (Fc/Fc^+) couple in Pyr_4OTf. (B) Plots of current density ($\mu A/cm^2$) against $v^{1/2}$ ($V^{1/2}/s^{1/2}$) calculated from Figure A9(A) (reduction wave: plots of positive current and oxidation wave: plots of negative one).

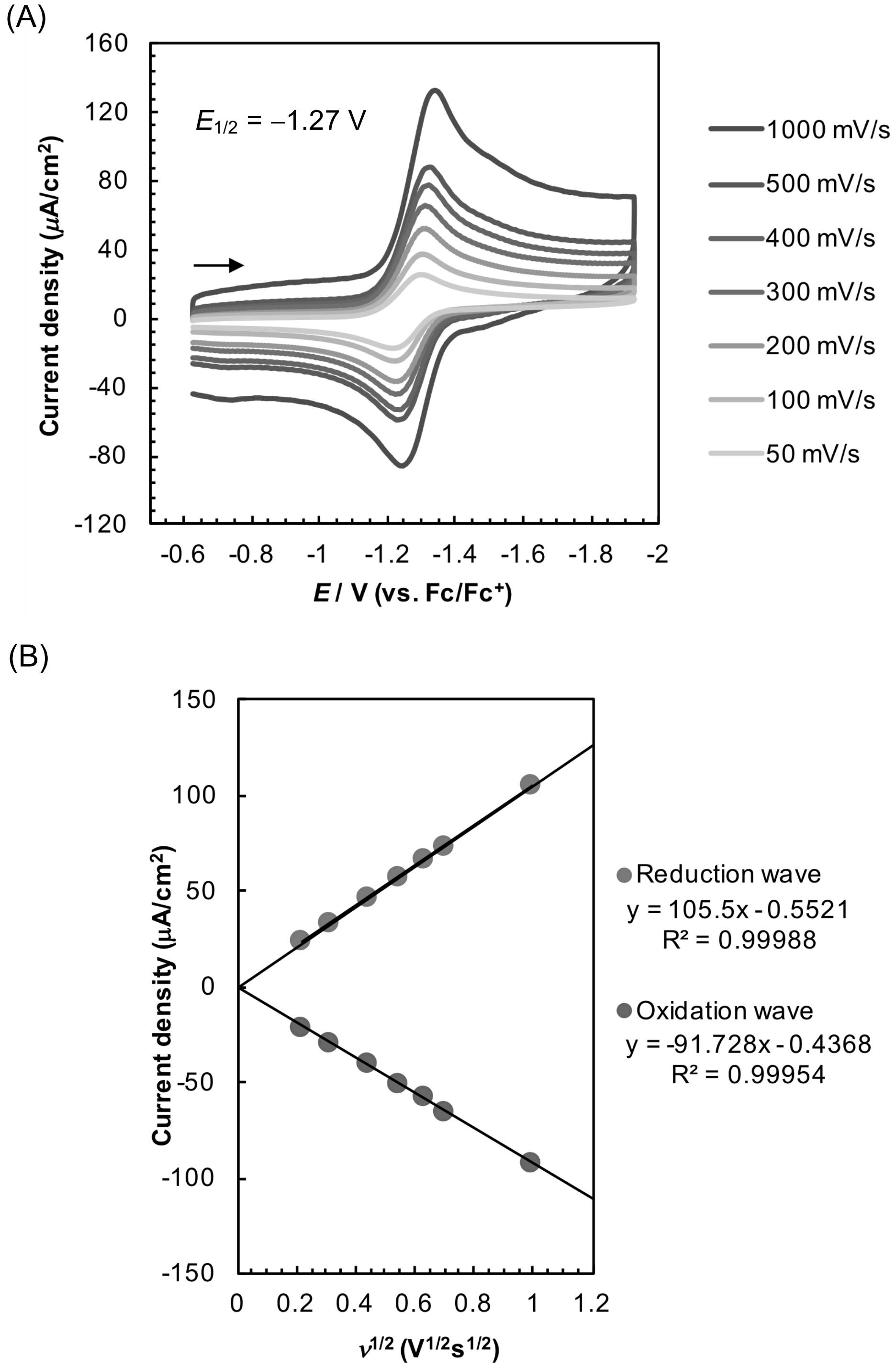

Figure A10. (A) Cyclic voltammograms of 0.15 mM [Cp_2TiCl_2] in 0.2 M Pyr_4FAP/THF at scan rates of 50, 100, 200, 300, 400, 500, and 1000 mV/s (WE: GCE ϕ1 mm, CE: Pt wire, RE: Ag/Ag^+ electrode). The potential is referred to the ferrocene/ferrocenium (Fc/Fc^+) couple in 0.2 M Pyr_4FAP/THF. (B) Plots of current density (μA/cm^2) against $\nu^{1/2}$ ($V^{1/2}/s^{1/2}$) calculated from Figure A10(A) (reduction wave: plots of positive current and oxidation wave: plots of negative one).

Table A6. Parameters obtained from CV in Pyr_4FAP shown in Figure A8.

Scan rate / V	j_c / μA cm^{-2}	j_a / μA cm^{-2}	ΔE_p / mV
1	801	–680	130
0.5	580	–498	118
0.4	521	–449	108
0.3	451	–388	103
0.2	366	–316	98
0.1	253	–216	85
0.05	172	–143	80

Table A7. Parameters obtained from CV in Pyr_4OTf shown in Figure A9.

Scan rate / V	j_c / μA cm^{-2}	j_a / μA cm^{-2}	ΔE_p / mV
1	720	–606	147
0.5	595	–446	126
0.4	471	–401	120
0.3	407	–348	114
0.2	331	–282	105
0.1	229	–194	96
0.05	154	–127	87

Table A8. Parameters obtained from CV in 0.2 M Pyr_4FAP/THF shown in Figure A10.

Scan rate / V	j_c / μA cm^{-2}	I_a / μA cm^{-2}	ΔE_p / mV
1	105	–92.5	96
0.5	73.6	–65.5	85
0.4	66.2	–57.8	84
0.3	57.2	–50.9	79
0.2	46.3	–40.8	78
0.1	32.7	–29.3	75
0.05	23.4	–21.6	75

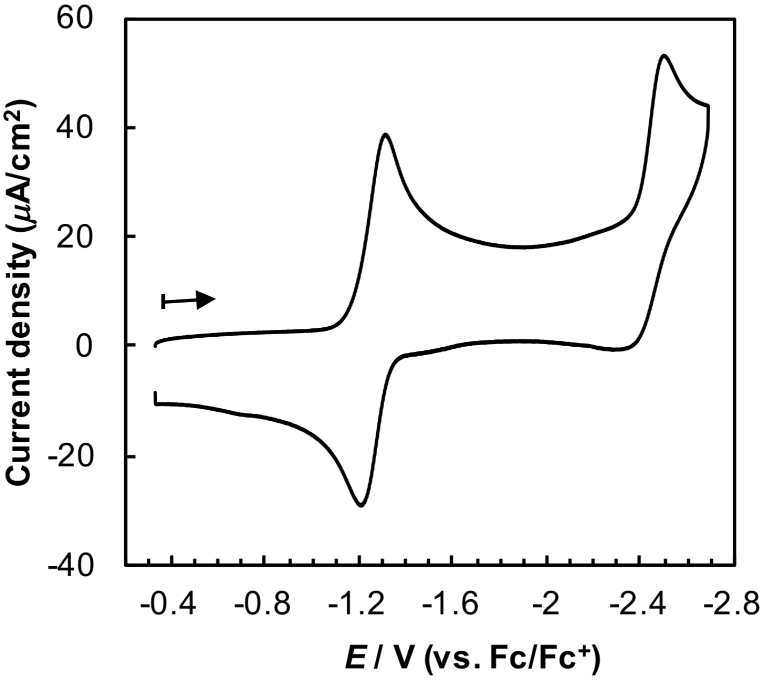

Figure A11. Cyclic voltammograms of 0.15 mM [Cp_2TiCl_2] in 0.2 M Pyr_4FAP/THF at 100 mV/s (WE: GCE ϕ1 mm, CE: Pt wire, RE: Ag/Ag^+ electrode). The potential was refered to the ferrocene/ferrocenium (Fc/Fc^+) couple in 0.2 M Pyr_4FAP/THF. The redox potential of Ti(IV/III) is observed at −1.317 and −1.223 V, ($E_{1/2}$: −1.27 V) and the reduction of Ti(III)/Ti(II) is observed at −2.470 V.

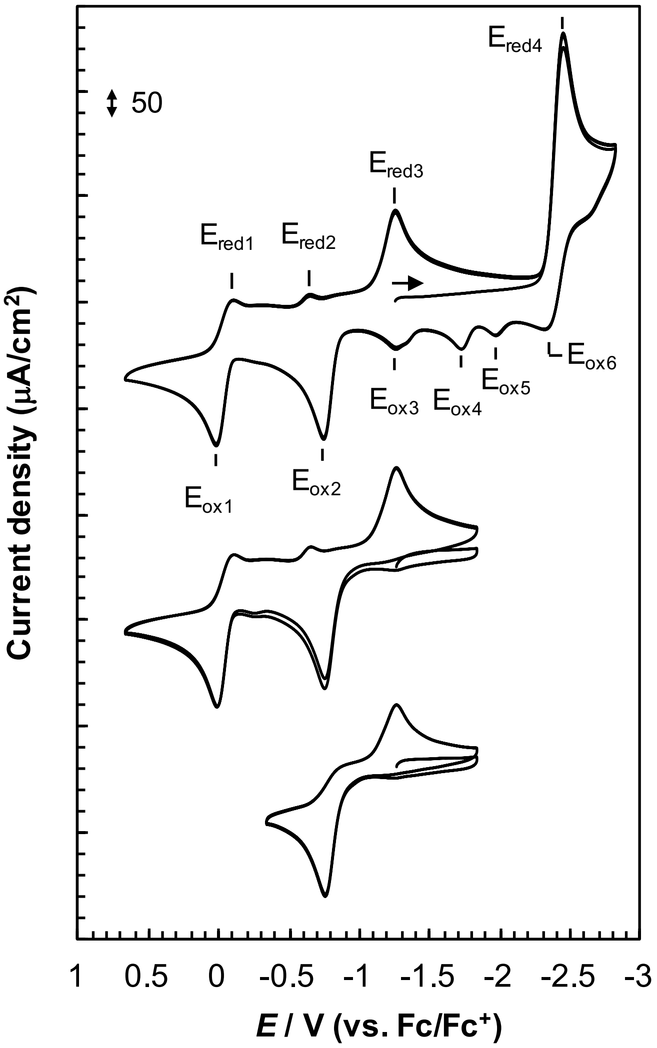

Figure A12. Cyclic voltammograms of 1 mM [$(Cp_2TiCl)_2$] in 0.2 M Pyr$_4$FAP/THF at 100 mV/s (WE: GCE ϕ1 mm, CE: Pt wire, RE: Ag/Ag$^+$ electrode). The potential was refered to the ferrocene/ferrocenium (Fc/Fc$^+$) couple in 0.2 M Pyr$_4$FAP/THF.

Table A9. Redox potentials of [$(Cp_2TiCl)_2$] in 0.2 M Pyr$_4$FAP/THF that was obtained from Figure A12.

	E_{red1}	E_{red2}	E_{red3}		E_{red4}	
Potential*	−0.106	−0.653	−1.259		−2.463	
	E_{ox1}	E_{ox2}	E_{ox3}	E_{ox4}	E_{ox5}	E_{ox6}
Potential*	0.017	−0.750	−1.263	−1.735	−1.983	−2.333

*Potential vs. Fc/Fc$^+$

A.8 UV-vis/NIR spectra of [($Cp_2TiCl)_2$], [$Cp^*{}_2TiCl$] and [Cp_2VCl_2]

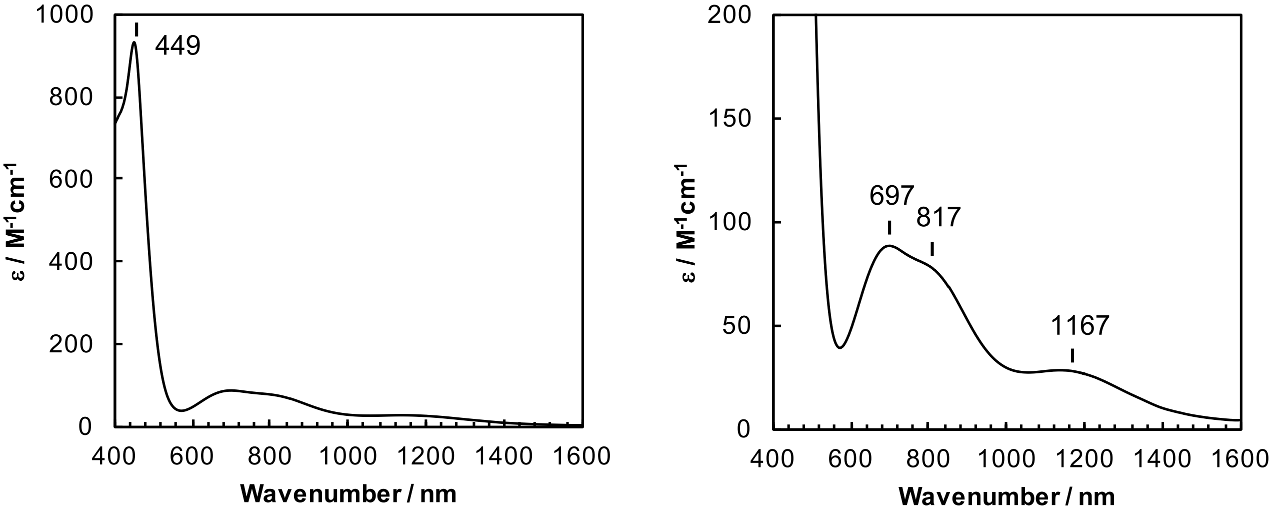

Figure A13. UV-vis/NIR spectra of 5 mM [$(Cp_2TiCl)_2$] in Pyr_4FAP.

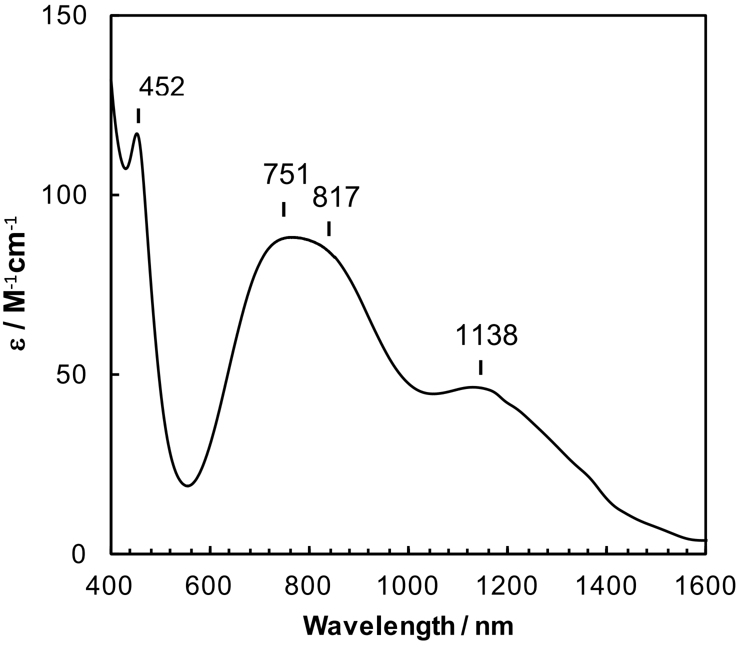

Figure A14. UV-vis/NIR spectrum of 5 mM [$(Cp_2TiCl)_2$] in 0.2 M Pyr_4FAP/THF.

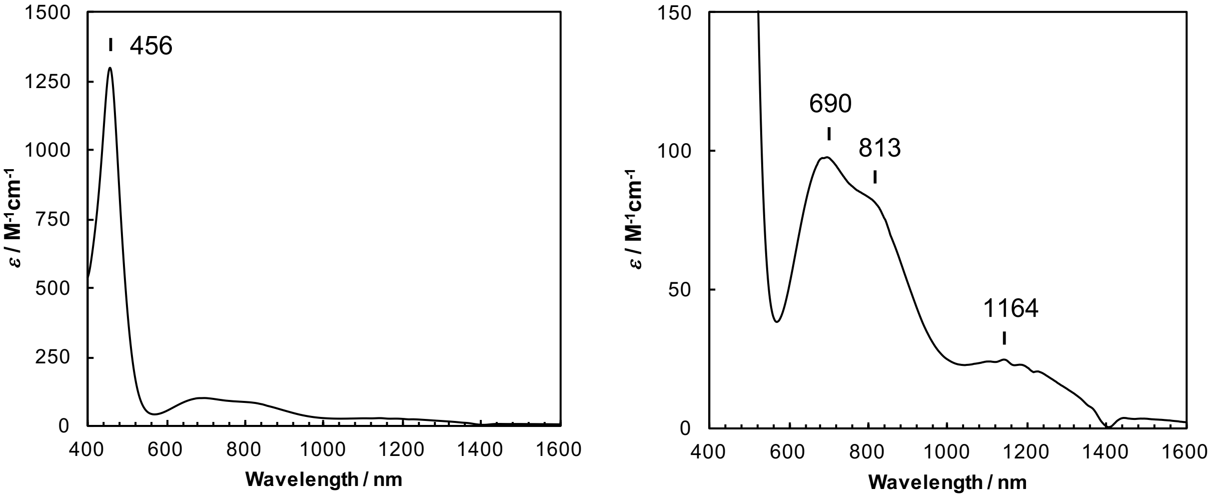

Figure A15. UV-vis/NIR spectrum of 5 mM [$(Cp_2TiCl)_2$] in toluene.

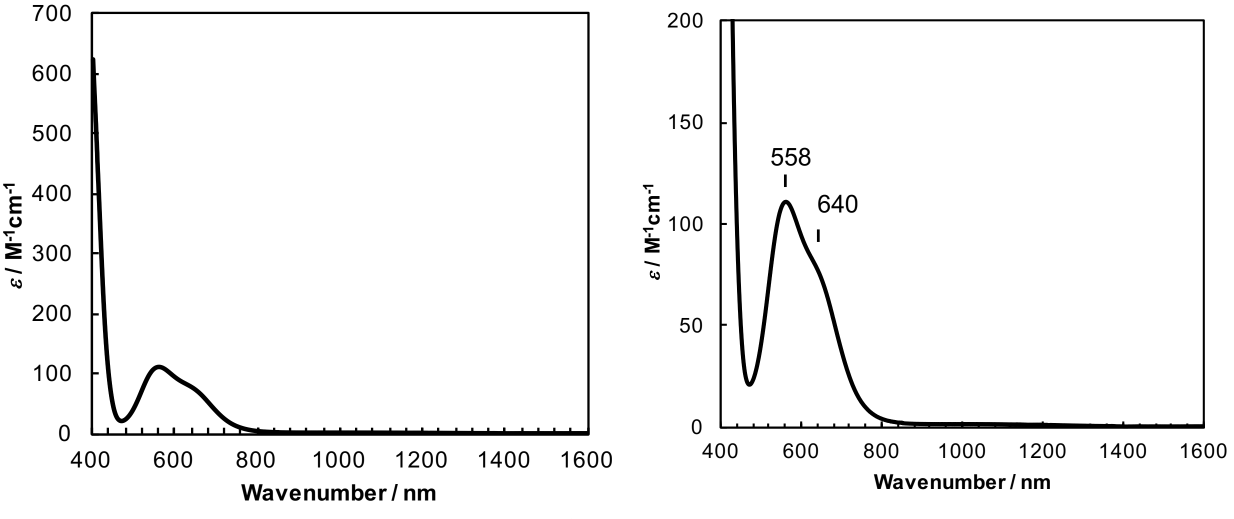

Figure A16. UV-vis/NIR spectrum of 5 mM [Cp^*_2TiCl] in toluene.

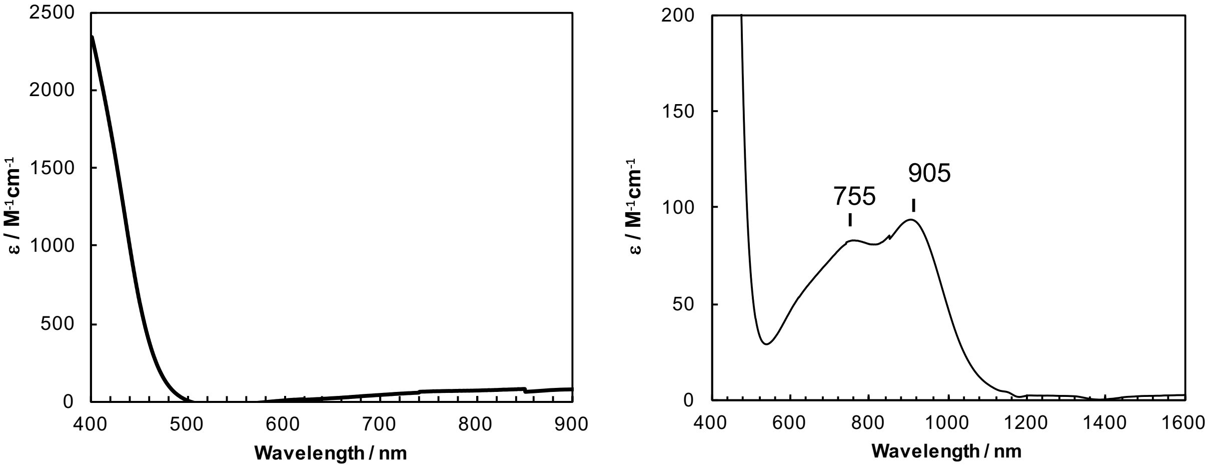

Figure A17. UV-vis/NIR spectrum of 5 mM [Cp_2VCl_2] in toluene.

Table A10. Summary of UV-vis/NIR spectra

Complex	Solvent	λ_{max}/ nm ($\varepsilon/M^{-1}cm^{-1}$)	Reference
$(Cp_2TiCl)_2$	Pyr_4FAP	449 (930), 697 (89), 817 (77), 1167 (28)	this work, 9
	0.2 M Pyr_4FAP/THF	452 (120), 751 (88), 817 (86), 1138 (46)	this work, 9
	THF	456 nm[a]	10
	Toluene	456 (1300), 690 (98), 813 (82), 1164 (23)	this work, 9
Cp^*_2TiCl	Toluene	558 (110), 640 (77)	this work, 9
Cp^*_2TiCl	Toluene	560 (144)	11
Cp_2VCl_2	Toluene	755 (82), 905 (93)	this work, 9

[a] ε values are noted in $M^{-1}\cdot cm^{-1}$ in the parentheses.

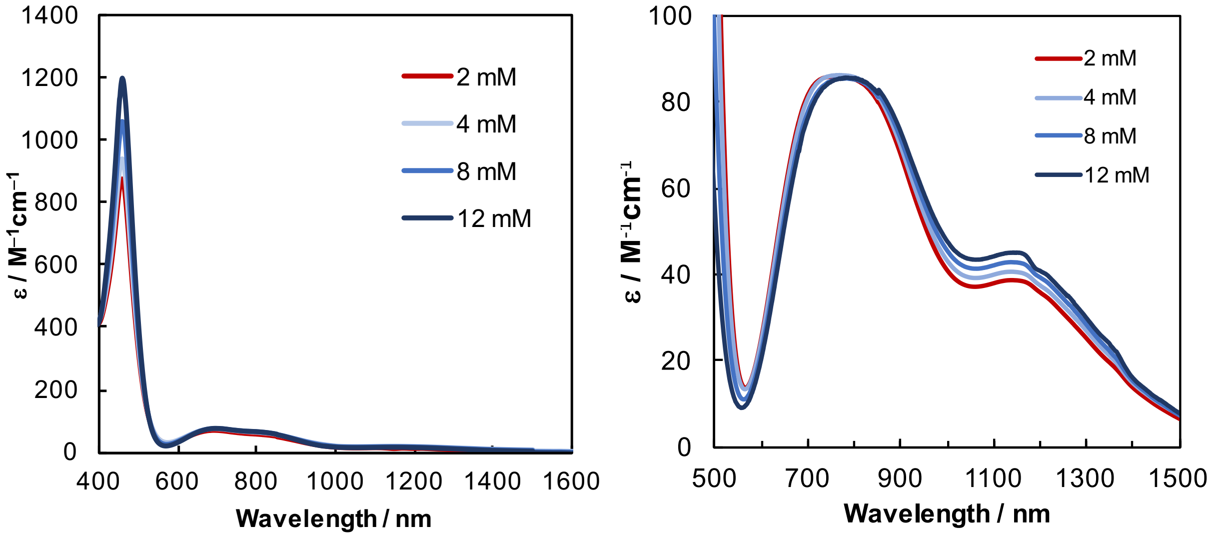

Figure A18. UV-vis/NIR spectra of 2, 4, 8, and 12 mM $[(Cp_2TiCl)_2]$ in Pyr_4FAP.

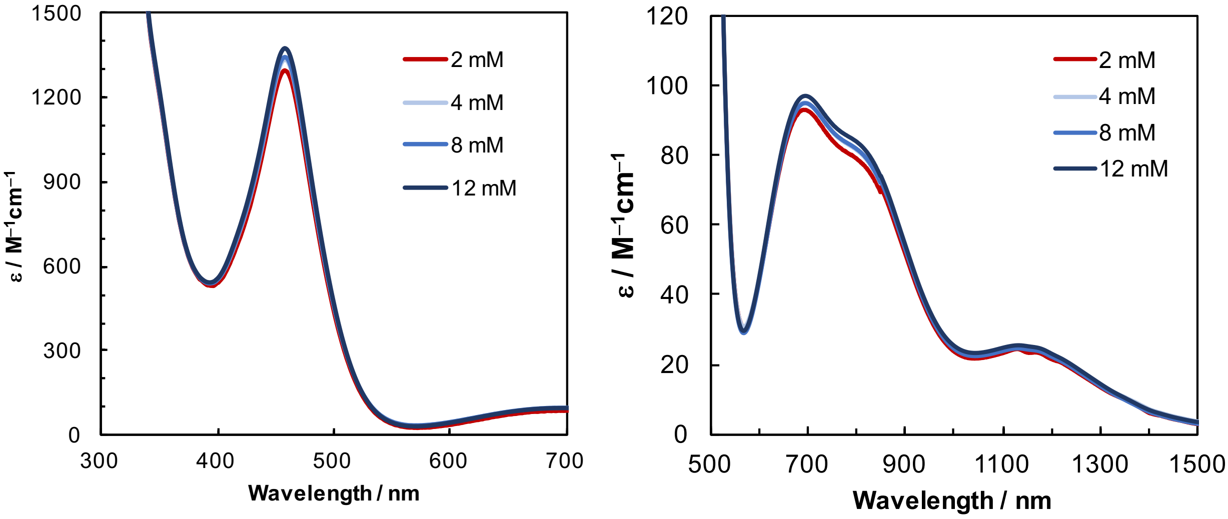

Figure A19. UV-vis/NIR spectra of 2, 4, 8, and 12 mM $[(Cp_2TiCl)_2]$ in toluene.

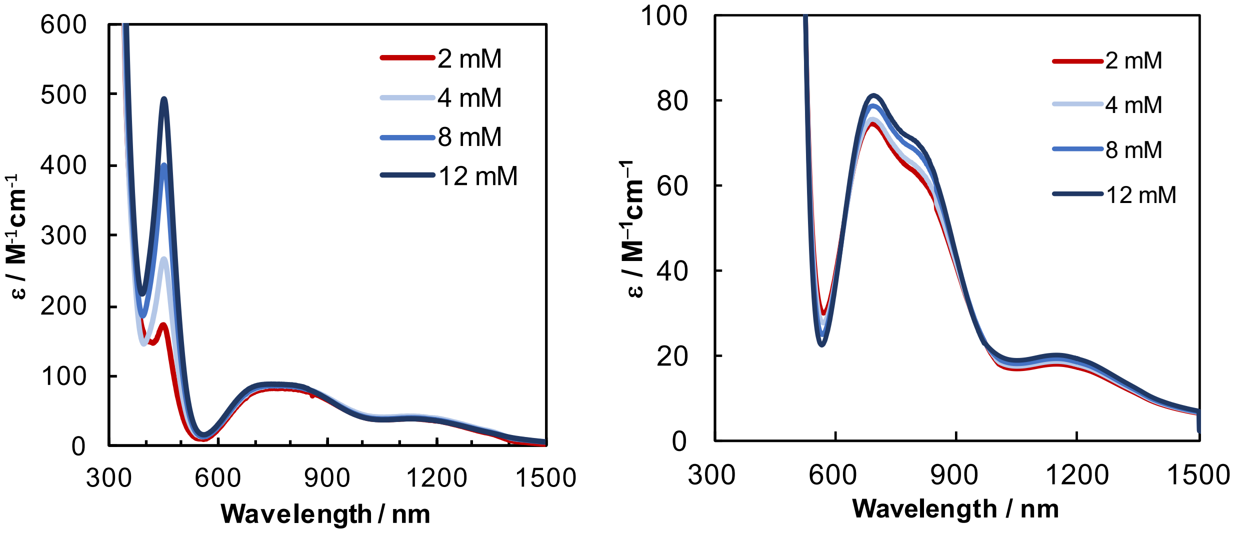

Figure A20. UV-vis/NIR spectra of 2, 4, 8, and 12 mM [$(Cp_2TiCl)_2$] in THF.

A.9 Cyclic voltammogram of [$(Cp_2TiCl)_2$] in ionic liquids

In Chapter 2, we described that dimeric [$(Cp_2TiCl)_2$] was generated after electrochemical reduction of [Cp_2TiCl_2]. To investigate the redox behaviors of the [$(Cp_2TiCl)_2$], CVs of [$(Cp_2TiCl)_2$] in Pyr_4FAP and Pyr_4OTf were measured, which are shown in Figures A21(A) and A21(B), respectively, where they were swept from the rest potential to negative potential region. The redox potential values are summarized in Table A11. In Figure A21(A), the redox waves observed as E_{red1}/E_{ox1} and E_{red2}/E_{ox2} in Pyr_4FAP are similar to those of [$(Cp_2TiCl)_2$] in 0.2 M Bu_4NPF_6/THF that was reported in previous literature.[12,13] Thus, the observed redox waves are characterized according to the following scheme (E_{red1}/E_{ox1}: Eq. (1), E_{red2}/E_{ox2}: Eqs. (2) and (3)) in the same way described in previous literature.[12,13]

In Figure A21(B), the redox couple observed at E_{red1}/E_{ox1} is also characterized according to Eq. (1), because the observed redox waves are similar to that in Figure A21(A). Interestingly, in the CV in Pyr_4OTf, as shown in Figure A21(B), the ratio of the current densities observed at E_{red2}/E_{ox2} against that at E_{red1}/E_{ox1} was quite larger than that in Pyr_4FAP, suggesting that [$(Cp_2TiCl)_2$] generated in Pyr_4OTf is coordinated with OTf anion. The shift is reasonable, because Daasbjerg and co-workers reported that the redox potential of [$(Cp_2TiCl)_2$] in 0.2 M Bu_4NPF_6/THF was shifted to negative potential region by addition of hexamethylphosphoramide (HMPA) that is a highly polar and aprotic solvent, through the coordination of O atom in HMPA to Ti nucleus.[14] Accordingly, for the CV measurement in Pyr_4OTf (Figure A21(B)), we estimated that the redox waves observed as E_{red2}/E_{ox2} has been derived from the redox of $[Cp_2TiCl(OTf)]^+$ in addition of Eqs. (2) and (3).

The irreversible reduction wave, E_{red3}, at −2.25 V showed in Figure A21(B) is characterized to the reduction of Ti(III) to Ti(II), which is similar to that (E_{red3} at −2.21 V) of $[(Cp_2TiCl)_2]$ in Pyr_4FAP, as shown in Figure A21(A), although the oxidation wave was not observed. This is because Ti(II) species is very unstable to occur the polymerization by forming Ti–C bond due to the reaction with cyclopentadienyl group in ILs like that in THF, as described in the previous literature.[15]

$$[Cp_2Ti]^+ - e^- \rightleftharpoons [Cp_2Ti]^{2+} \quad (1)$$

$$[Cp_2TiCl] - e^- \rightleftharpoons [Cp_2TiCl]^+ \quad (2)$$

$$[(Cp_2TiCl)_2] + e^- \rightleftharpoons [(Cp_2TiCl)_2]^- \quad (3)$$

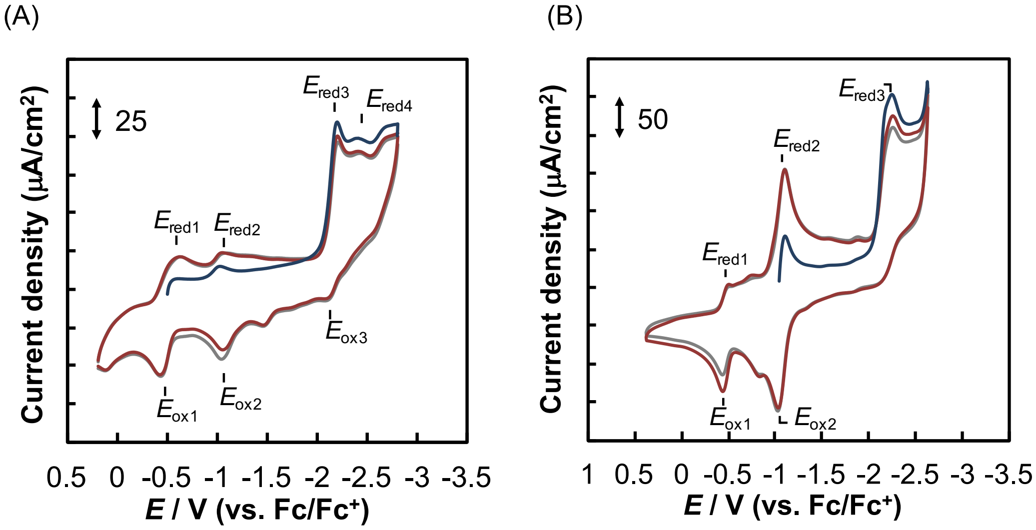

Figure A21. Cyclic voltammograms of 10 mM $[(Cp_2TiCl)_2]$ in (A) Pyr_4FAP and (B) Pyr_4OTf (WE: GCE (φ 1 mm), CE: Pt wire, RE:Ag/Ag^+ electrode, scan rate: 100 mV/s, 1st cycle: blue, 2nd cycle: red, and 3rd cycle: gray). The potentials were referred to the ferrocene/ferrocenium (Fc/Fc^+) couple in Pyr_4FAP and Pyr_4OTf, respectively.

Table A11. Summary of redox potentials for [Cp_2TiCl_2] and [$(Cp_2TiCl)_2$] shown in Figure A21

Complex	**Anion of IL**	**Redox potential (V vs. Fc/Fc$^+$)**							
		E_{red1}	E_{ox1}	E_{red2}	E_{ox2}	$E_{1/2}$	E_{red3}	E_{ox3}	E_{red4}
[$(Cp_2TiCl)_2$]	FAP	−0.63	−0.43	−1.05	−1.05	−1.05	−2.21	−2.12	−2.42
	OTf	−0.51	−0.44	−1.11	−1.04	−1.07	−2.25	–	–

A.10 Electrochemical synthesis of NH_3 by using [$(Cp_2TiCl)_2$] in SPE cell

The CPE of [$(Cp_2TiCl)_2$] was performed in the range of −1.0 to −1.4 V, but NH_3 was not detected. In contrast, when CPE was carried out at −1.5 V, NH_3 was generated. The yields of NH_3 per [$(Cp_2TiCl)_2$] (%) and current efficiency (%) against consumed electric charge are shown in Figures A22(A) and A22 (B), respectively. The maximum yield of NH_3 per [$(Cp_2TiCl)_2$] is 68% at 29.9 C, and thus the yield of NH_3 per Ti ion is 34%. The obtained yield is significantly higher than that reported previously for [Cp_2TiCl_2] (1.45% (in 0.3 M $LiClO_4$/MeOH).[16] The maximum current efficiency shown in Figure A22(B) is 1.44% at 5.28 C. When the CPE by using [Cp_2TiCl_2] in Pyr_4FAP, as described in previous report,[17] was carried out, the maximum current efficiency was found to be 1.24% at the early stage of electrolysis. The maximum current efficiency determined for [$(Cp_2TiCl)_2$] is slightly greater than the previous value (0.28% in 0.3 M LiClO4/MeOH),[16] although the current efficiency at the early stage (Figure A22(B)) is 0.80%. In the case of [Cp_2TiCl_2] in Pyr_4FAP reported previously, the maximum current efficiency was obtained at an early stage, and then gradually decreased. However, the current efficiency for [$(Cp_2TiCl)_2$] achieved its maximum value after consuming some of the electric charges at the early stage. This behavior has not yet been rationalized but it is possible that an induction period occurs during electrolysis. The current efficiency gradually decreases to 0.30%. This is similar to the previous result using [Cp_2TiCl_2] in Pyr_4FAP. H_2 quantification was also carried out, and the current efficiency was estimated to be 89% at 5.0 C under N_2 atmosphere. In the CPE for [$(Cp_2TiCl)_2$] at −1.5 V (vs. Ag/AgCl) under Ar, NH_3 was not generated, suggesting that the NH_3 obtained in the reaction was converted from N_2. Additionally, quantification of hydrazine was performed, but NH_3 was not detected, suggesting that coordinated N_2 was protonated according to the distal pathway[18] and/or that N_2 triple bond was cleaved immediately if a cluster structure was formed.[19,20] The results obtained for [($Cp_2TiCl)_2$] are similar to the results obtained for [Cp_2TiCl_2].[17]

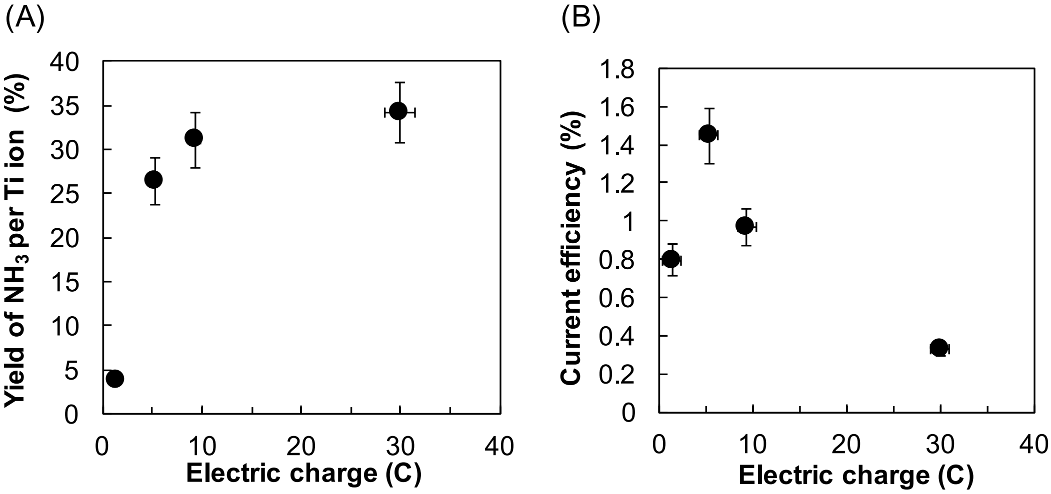

Figure A22. (A) Plots of NH_3 yields per Ti ion (%) against the consumed electric charge (C) and plots of current efficiency (%) (B) against the consumed electric charge (C), which are obtained from CPE by using [($Cp_2TiCl)_2$].

A.11 Linear sweep voltammograms of [($Cp_2TiCl)_2$] in Pyr$_4$FAP

To investigate the active species generated during electrolysis at −1.5 V (vs. Ag/AgCl) in a SPE cell,[17] we evaluated the electrochemical synthesis of NH_3 using [($Cp_2TiCl)_2$] in the equilibrium state with [Cp_2TiCl]. Because the key intermediate for NH_3 synthesis is monomeric [Cp_2TiCl] allowing the N_2 coordination, as described in Chapter 3.[9] The linear sweep voltammograms (LSVs) of [($Cp_2TiCl)_2$] in Pyr$_4$FAP measured before CPE are shown in Figure A23(A). The red line shows the result obtained with treatment under an N_2 atmosphere, and the blue line indicates the result obtained under an Ar atmosphere. The currents under N_2 and Ar were observed in the range of −0.6 V to −1.0 V (vs. Ag/AgCl), suggesting that protons react with [($Cp_2TiCl)_2$] and/or [Cp_2TiCl] and that H_2 evolution reaction occurs after the generated species is reduced. Therefore, hydride species such as [Cp_2TiHCl] is generated during electrochemical reduction. Moreover, the current measured under N_2 in the range of −1.0 to −1.5 V (vs. Ag/AgCl) is significantly greater than the current measured under Ar, suggesting that [($Cp_2TiCl)_2$] and/or [Cp_2TiCl] react with N_2.

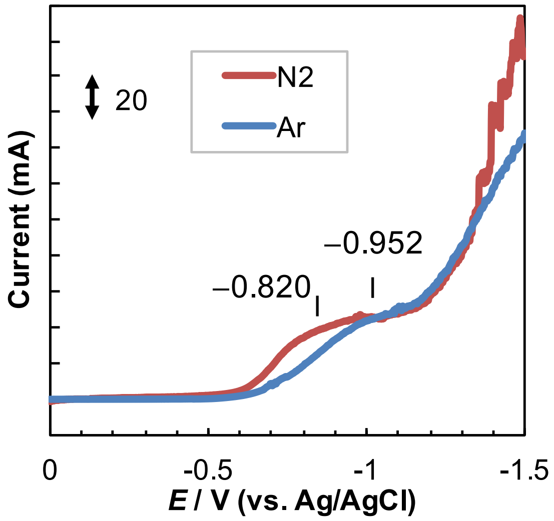

Figure A23. (A) LSVs of 10 mM [($Cp_2TiCl)_2$] in Pyr_4FAP in SPE under N_2 (red line) or Ar (blue line) (Scan rate: 5 mV/s).

A.12 DSC measurement

To understand the phase transition in Pyr_4FAP, the melting point of Pyr_4FAP was investigated by DSC measurement. The results are shown in Figure A24. The melting point of Pyr_4FAP is –21.6 °C. Although the DSC measurement of Pyr_4FAP containing [($Cp_2TiCl)_2$] was also performed, the results are similar to the result of Pyr_4FAP.

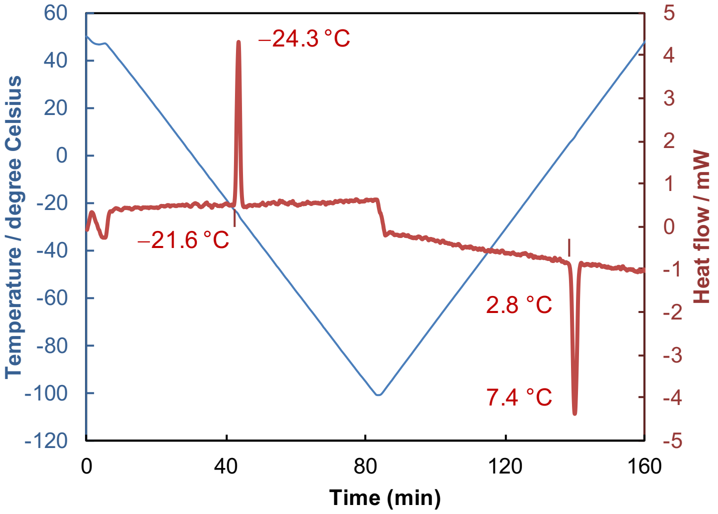

Figure A24. DSC measurement for Pyr_4FAP (Rate of temperature increase: 10 °C/min).

A.13 References

1. A. J. Bard, L. R. Faulkner, Electrochemical Methods: Fundamentals and Applications, 2nd ed.; Wiley: New York; pp 242.
2. R. J. Enemærke, J. Larsen, T. Skrydstrup and K. Daasbjerg, *Organometallics*, **2004**, *23*, 1866.
3. S. Tanimoto and A. Ichimura, *J. Chem. Educ.*, **2013**, *90*, 778.
4. C. L. Bentley, J. Li, A. M. Bond, and J. Zhang, *J. Phys. Chem. C.*, **2016**, *120*, 16516.
5. E. I. Rogers, D. S. Silvester, D. L. Poole, L. Aldous, C. Hardacre, and R. G. Compton, *J. Phys. Chem. C*, **2008**, *112*, 2729.
6. S. Stevanoic and M. F. Costa Gomes, *J. Chem. Thermodynamics*, **2013**, *59* 65.
7. M. Okuniewski and K. Paduszyński, U. Domańska, *J. Chem. Eng. Data*, **2016**, *61*, 1296.
8. D.H.S. Ramkumar and A.P. Kudchadker, *J. Chem. Eng. Data*, **1989**, *34*, 463.
9. A. Katayama, T. Inomata, T. Ozawa and H. Masuda, *Dalton Trans.*, **2017**, 46, 7668.
10. M. Paradas, A. G. Campaña, T. Jiménez, R. Robles, J. E. Oltra, E. Buñue, J. Justicia, D. J. Cárdenas and J. M. Cuerva, *J. Am. Chem. Soc.*, **2010**, *132*, 12748.
11. J. W. Pattiasina, H. J. Heeres, F. V. Bolhuis, A. Meetsma, J. H. Teuben and A. L. Spek, *Organometallics*, **1987**, *6*, 1004.
12. R. J. Enemærke, J. Larsen, T. Skrydstrup and K. Daasbjerg, *Organometallics*, **2004**, *23*, 1866.
13. R. J. Enemærke, J. Larsen, T. Skrydstrup and K. Daasbjerg, *J. Am. Chem. Soc*. **2004**, *126*, 7853.
14. J. Larsen, R. J. Enemærke, T. Skrydstrup and K. Daasbjerg, *Organometallics*, **2006**, *25*, 2031.
15. J. Langmaier, Z. Samec, V. Varga, M. Horáček and K. Mach, *J. Organomet. Chem.* **1999**, *579*, 348.
16. J. Y. Becker, S. Avraham (Tsarfaty) and B. Posin, *J. Electroanal. Chem*. **1987**, *230*, 143.
17. A. Katayama, T. Inomata, T. Ozawa and H. Masuda, *Electrochem. Commun*. **2016**, *67*.
18. Distal pathway: The N_2 molecule coordinated to monomeric metal complex in the end-on fashion is cleaved after three hydrogenations to the distal N atom to prepare nitride complex and release NH_3, and then, the nitride complex is protonated to generate NH_3. B. M. Hoffman, D. Lukoyanov, D. R. Dean, and L C. Seefeldt, *Acc. Chem. Res.*, **2013**, *46*, 587.
19. G. P. Pez, P Apgar, and R. K. Crissey, *J. Am. Chem. Soc*. **1982**, *104*, 482.
20. T. Shima, S. Hu, G. Luo, X. Kang, Y. Luo, and Z. Hou, *Science*, **2013**, *340*, 1549.

Appendix B: Supporting information in Chapter 3

B.1 Structural information of model complexes

Table B1. Selected bond lengths (Å) and angles (degree) optimized for the model complexes, **1** and **2,** and their comparison with crystal structure of [($Cp_2TiCl)_2$] reported in previous literature[1,2]

	singlet[2]	**triplet[2]**	**Crystal structure[1]**
Ti(1)-Cl(1)	2.57351	2.57499	2.536(1)
Ti(1)-Cl(2)	2.56749	2.57043	2.545(2)
Ti(2)-Cl(1)	2.56390	2.56611	2.545(2)
Ti(2)-Cl(2)	2.57424	2.57675	2.558(1)
Ti(1)-Cp (centroid)	2.090	2.089	2.058
Ti(1)-Cp' (centroid)	2.090	2.089	2.053
Ti(2)-Cp (centroid)	2.090	2.089	2.058
Ti(2)-Cp' (centroid)	2.093	2.092	2.057
Ti(1)-Ti(2)	3.91615	3.94936	3.943
Ti-Cl-Ti	99.3, 99.2	100.4, 100.2	101.8, 101.2
Cl-Ti-Cl	80.7, 80.7	79.7, 79.6	78.2, 78.6

Table B2. Selected bond lengths (Å) and angles (degree) for optimized model complexes with applying the dielectric permittivity of Pyr_4FAP (14.7)

	1	**2**	**3**	**4**	**4-TS**
Ti-Ti	4.0153	4.0657	-	-	-
Ti-Cl	2.5953	2.5987	2.3870	2.4849	2.4175
Ti-Cl-Ti	101.37	102.9325	-	-	-
Cl-Ti-Cl	78.6	77.0707	-	-	-
Cp-Ti	2.0758	2.0789	2.0568	2.0719	2.0592
Cp-Ti-Cp	132.32	132.8116	137.1751	134.6382	136.4527
Cp-Ti-Cl	108.3	107.7020	111.3522	107.6757	109.8719
N-N	-	-	-	1.1197	1.1069
Ti-N	-	-	-	2.1156	2.9406
Ti-N-N	-	-	-	178.3	158.6977
N-Ti-Cl	-	-	-	84.80	79.6063
Cp-Ti-N	-	-	-	105.1613	100.6478

Table B3. Selected bond lengths (Å) and angles (degree) for optimized model complexes with applying the dielectric permittivity of toluene (2.37471)

	1	**2**	**3**	**4**	**4-TS**
Ti-Ti	3.9964	4.0495	-	-	-
Ti-Cl	2.5882	2.5921	2.3584	2.4536	2.3801
Ti-Cl-Ti	101.07	102.7233	-	-	-
Cl-Ti-Cl	78.9254	77.2755	-	-	-
Cp-Ti	2.074	2.0767	2.0584	2.0745	2.0607
Cp-Ti-Cp	132.89	132.7489	137.2547	134.7650	137.8040
Cp-Ti-Cl	108.18	108.39	111.3930	107.5242	109.8588
N-N	-	-	-	1.12	1.1083
Ti-N	-	-	-	2.1154	3.0106
Ti-N-N	-	-	-	178.1404	148.1632
N-Ti-Cl	-	-	-	85.1547	99.8257

Table B4. Selected bond lengths (Å) and angles (degree) for optimized model complexes with applying the electric permittivity of THF (7.4257)

	1	**2**	**3**	**4**	**4-TS**	**5**
Ti-Ti	4.0118	4.0629	-	-	-	-
Ti-Cl	2.5938	2.5974	2.3797	2.4774	2.4105	2.5074
Ti-Cl-Ti	101.31	102.9047	-	-	-	-
Cl-Ti-Cl	78.6904	77.0974	-	-	-	-
Cp-Ti	2.0760	2.0753	2.0567	2.0724	2.0600	2.0879
Cp-Ti-Cp	132.38	132.7087	137.1842	134.7087	136.7105	133.6646
Cp-Ti-Cl	108.3509	108.4405	111.3514	107.6305	109.8740	107.8575
N-N	-	-	-	1.1198	1.1070	-
Ti-N	-	-	-	2.1155	2.9406	-
Ti-N-N	-	-	-	178.2641	158.9612	-
N-Ti-Cl	-	-	-	84.8848	79.5358	-
Cp-Ti-N	-	-	-	105.1268	100.69	-
Ti-O	-	-	-	-	-	2.2635
Cl-Ti-O	-	-	-	-	-	84.4415
Cp-Ti-O	-	-	-	-	-	106.0570
Cl-Ti-O	-	-	-	-	-	84.4415

Table B5. Selected bond lengths (Å) and angles (deg) for optimized model complexes by using BP86/TZVP with Empirical Dispersion=GD3BJ in Pyr$_4$FAP (14.7)

	3’	**4’**	**4’-TS**	**3’-FAP**	**4’-FAP**	**4’-FAP-TS**
Ti1-Cl1	2.3755	2.4690	2.3891	2.3810	2.4779	2.4000
Cp1-Ti1	2.0484	2.0553	2.0443	2.0805	2.0529	2.0423
Cp1-Ti-Cp2	132.6	134.7	137.25	132.6	134.6	137.1
Cp1-Ti-Cl1	108.5	108.0	110.57	108.3	107.8	110.3
N1-N2	-	1.1199	1.1077	-	1.1196	1.1072
Ti1-N1	-	2.0995	2.9845	-	2.0987	2.9487
Ti1-N1-N2	-	178.12	144.53	-	178.77	144.617
N1-Ti1-Cl1	-	85.2	79.9	-	84.9	76.85
F15-H1	-	-	-	3.8205	3.8974	3.5593
F15-H2	-	-	-	2.5147	2.4596	2.5480
F15-H6	-	-	-	2.5468	2.7927	2.9021
F15-H7	-	-	-	3.168	2.7080	2.6088
F5-H2	-	-	-	2.7660	2.6499	2.9469
F5-H1	-	-	-	2.8480	2.8546	2.7213
F10-H1	-	-	-	2.6159	2.7475	2.5827
F10-H6	-	-	-	2.6472	2.6748	2.6554
F10-N1	-	-	-	-	3.2935	3.2985
F10-N2	-	-	-	-	3.2999	3.2828
F9-H6	-	-	-	2.6520	2.5828	2.6547
P1-F16	-	-	-	1.6841	1.6922	1.6839
P1-F17	-	-	-	1.6924	1.6836	1.6924

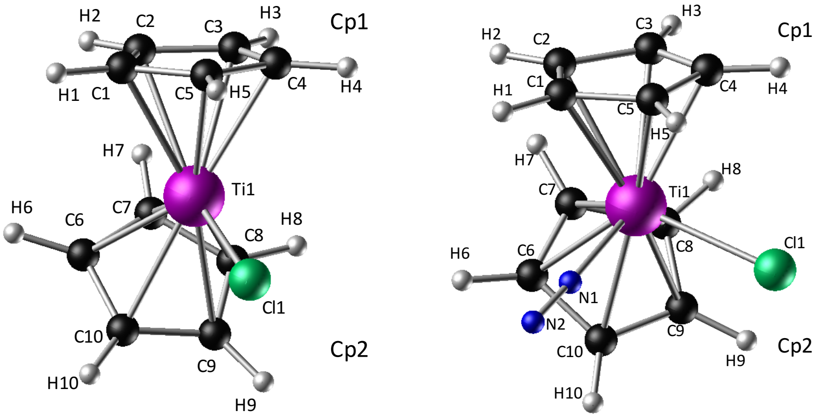

Figure B1. The optimized structures for **3’** (left) and **4’**(right).

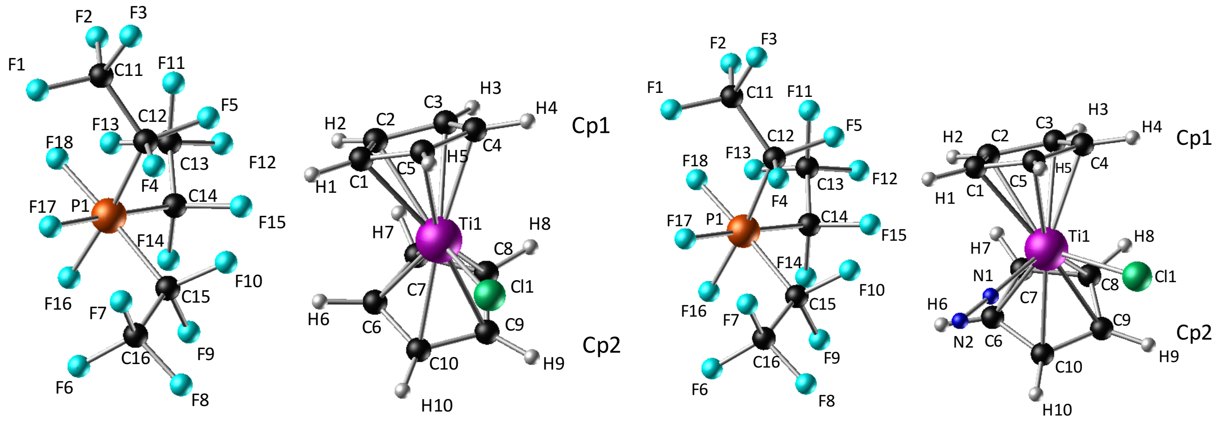

Figure B2. The optimized structure for **3’-FAP** (left) and **4’-FAP** (right).

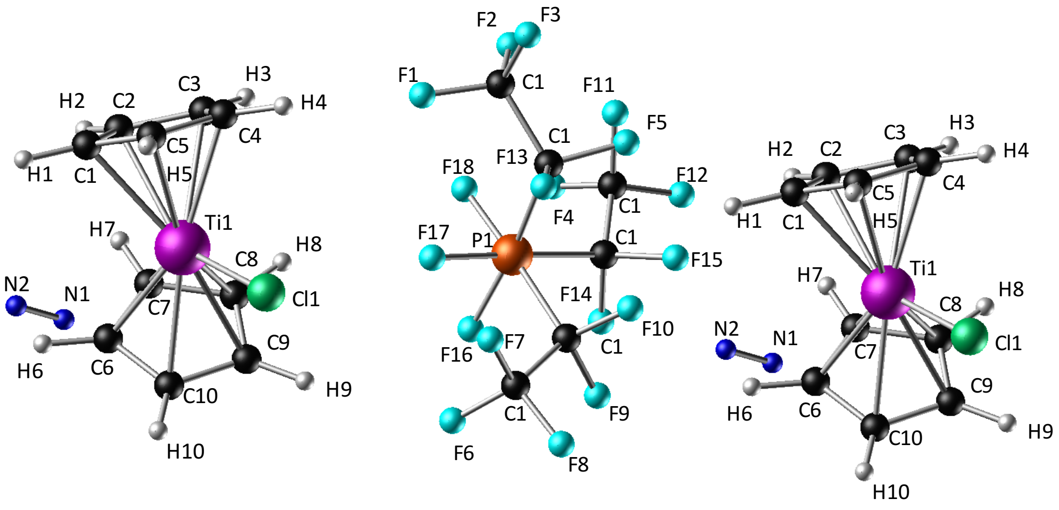

Figure B3. The optimized structure for **4’-TS** (left) and **4’-FAP-TS** (right).

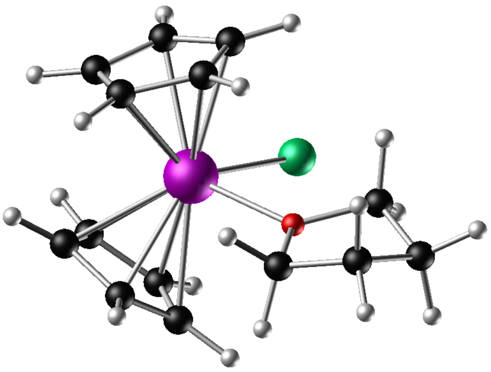

Figure B4. The optimized structure of [$Cp_2TiCl(THF)$] (**5**) with solvation model ε =7.4257 (purple: Ti atom, green: Cl atom, black: C atom, blue: N atom, red: O atom, and white: H atom).

B.2 TD-DFT calculations of model complexes in Pyr_4FAP ($\varepsilon = 14.7$)

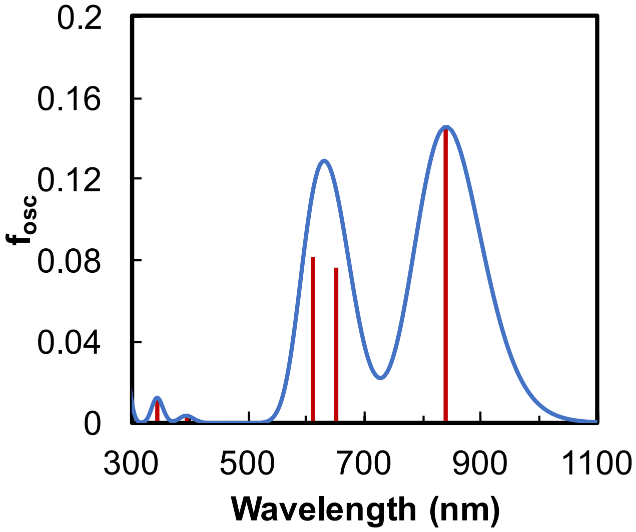

Figure B5. Absorption spectra of **1** in Pyr_4FAP ($\varepsilon = 14.7$) calculated by TD-DFT.

Table B6. Calculated transitions of **1** in Pyr_4FAP ($\varepsilon = 14.7$)

Excited State	Energy (eV)	Wavelength (nm)	f_{osc}	Transition	%
3	1.4771	839	0.1457	109 →110 109 →116	69.1 28.1
4	1.5138	819	0.0004	109 →111 109 →113	10.3 89.3
7	1.9028	652	0.076	109 →110 109 →116 109 →118	13.7 45.1 40.1
9	2.0287	611	0.0816	109 →110 109 →116 109 →118	12.7 26.5 58.8
11	3.1608	392	0.0036	107 →110	98.8
13	3.6202	342	0.0124	105 →110	99.0

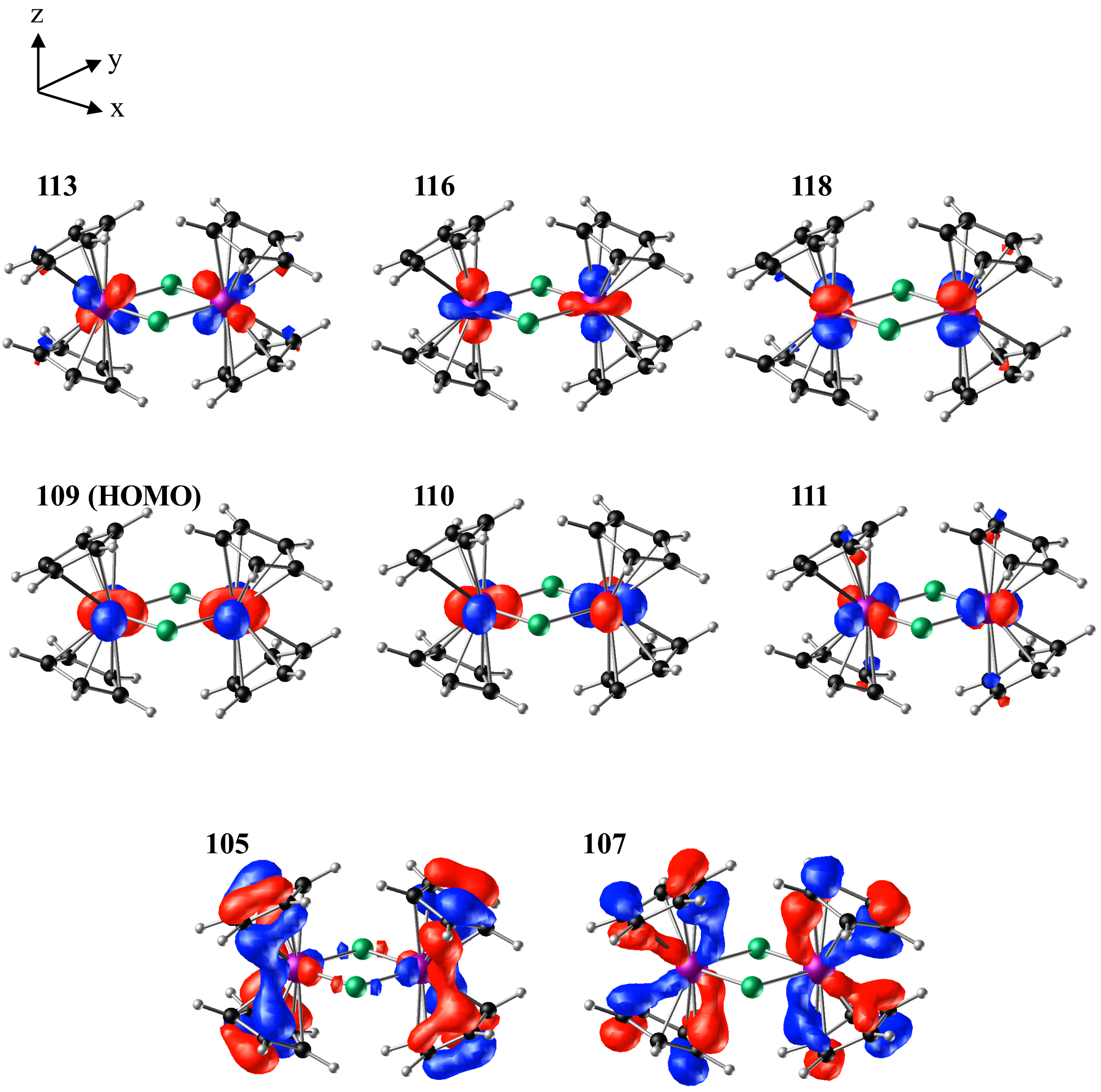

Figure B6. Molecular orbitals for model complex **1** in Pyr$_4$FAP (ε = 14.7) (isosurface values: ±0.07 (109, 110, 111, 113, 116 and 118), ±0.04 (105 and 107)).

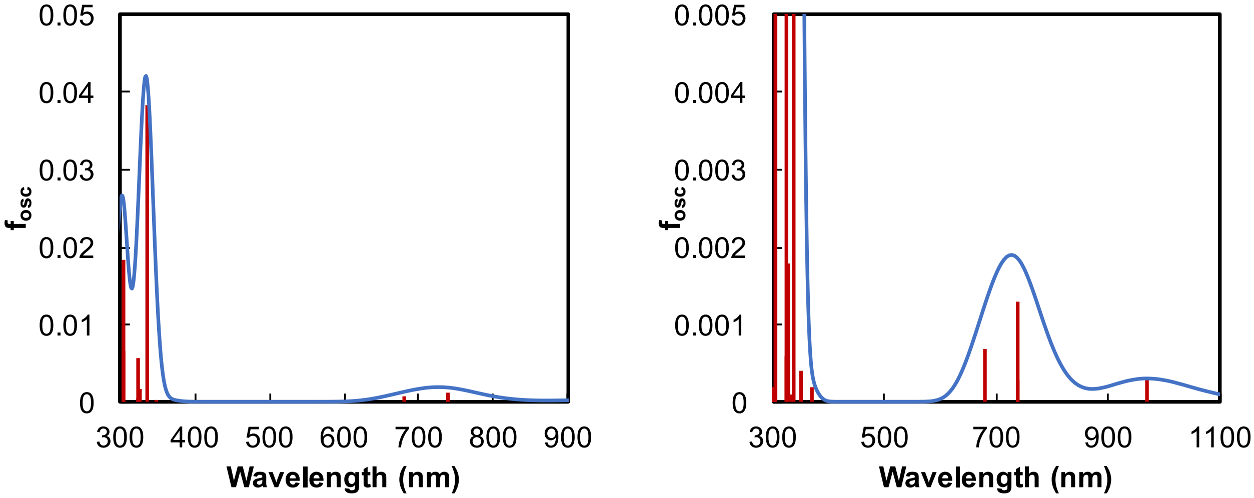

Figure B7. Absorption spectra of **2** in Pyr$_4$FAP (ε = 14.7) calculated by TD-DFT.

Table B7. Calculated transitions of **2** in Pyr$_4$FAP (ε = 14.7)

Excited State	Energy (eV)	Wavelength (nm)	f_{osc}	Transition	%
2	1.278	970	0.0003	109A →111A 110A →113A 110A →114A	51.9 10.6 31.9
3	1.6791	738	0.0013	109A →112A 109A →113A 109A →114A 110A →112A 110A →113A	9.7 25.2 8.8 43.7 7.4
5	1.8235	680	0.0007	109A →115A 110A →116A	44.1 52.1
14	3.6859	336	0.0384	109A →115A 110A →116A	53.6 44.3
16	3.8039	326	0.0018	107B →110B 108B →109B	16.2 61.6
18	3.8303	324	0.0058	107A →113A 108A →112A 108B →109B 108B →113B	14.5 33.9 11.0 10.2
21	4.0787	304	0.0184	107A →115A 108A →116A 108B →111B	16.6 37.7 13.7
22	4.0889	303	0.0067	108A →111A 108A →116A 108B →111B	11.0 14.7 40.3

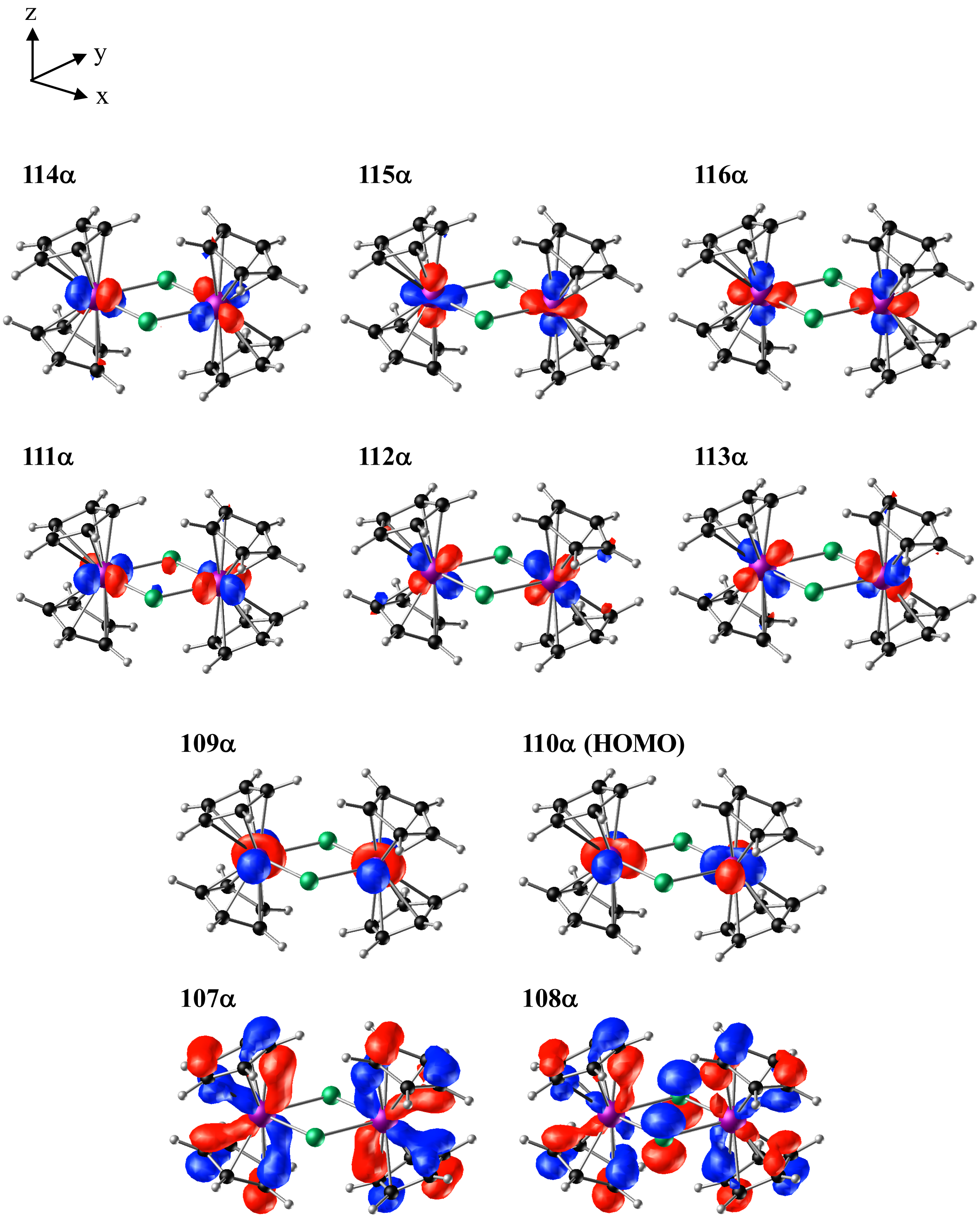

Figure B8. Molecular orbitals for model complex **2** in Pyr$_4$FAP (ε = 14.7) (isosurface values: ±0.07 (109α, 110α, 111α, 112α, 113α, 114α, 115α and 116α), ±0.04 (107α and 108α)).

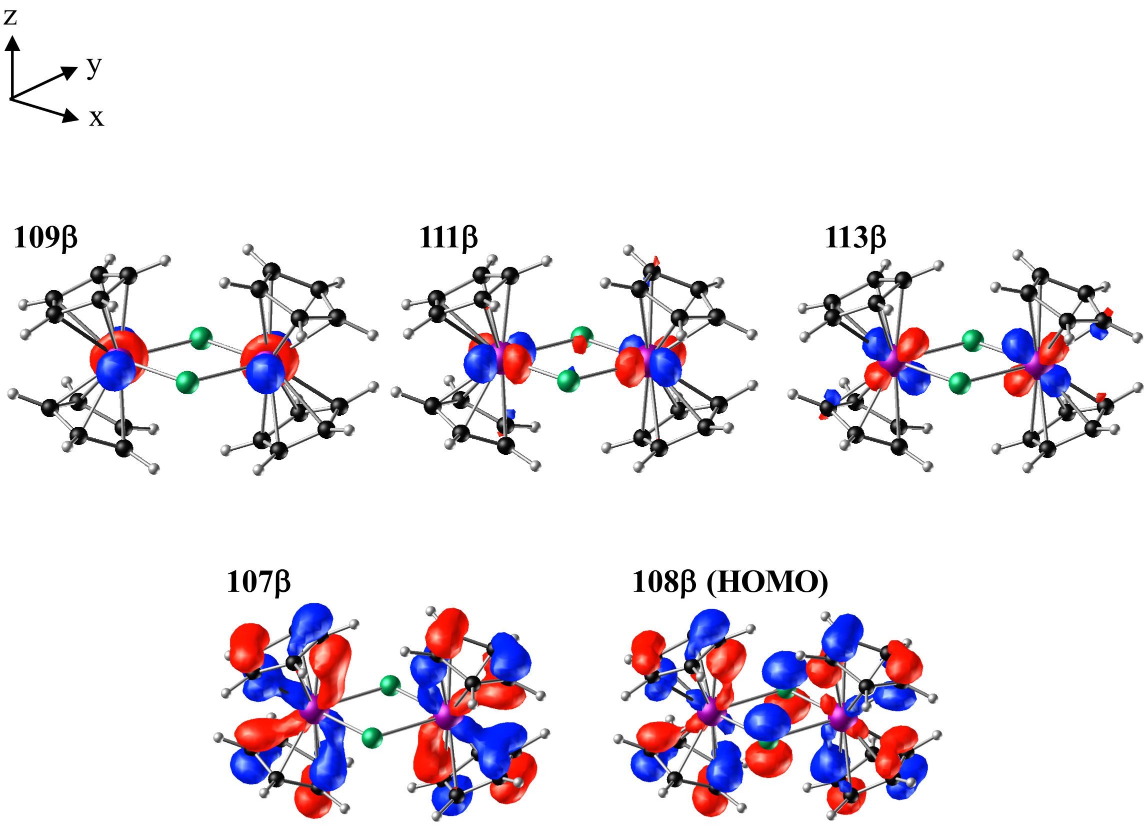

Figure B9. Molecular orbitals for model complex **2** in Pyr$_4$FAP (isosurface values: ±0.07 (109β, 111β, 113β), ±0.04 (107β and 108β)).

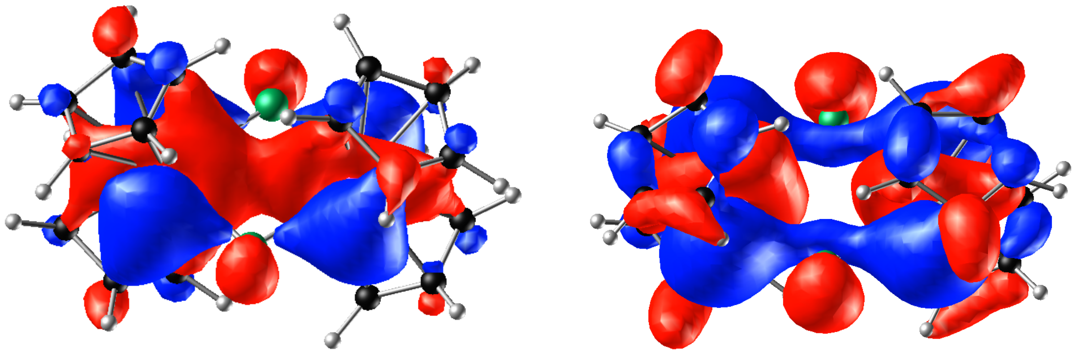

Figure B10. Molecular orbitals for model complex **1** (isosurface values: ±0.02 (109)) (left) and **2** (right) (Isosurface values: ±0.01 (109α) in Pyr$_4$FAP.

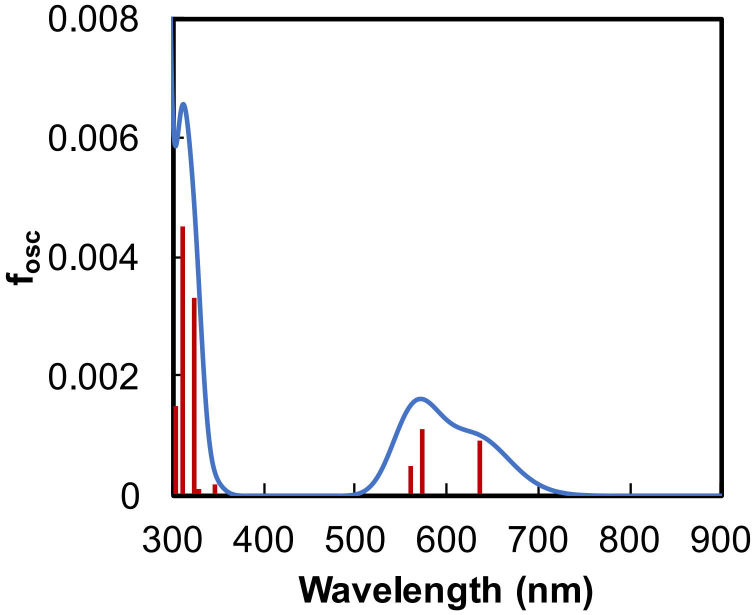

Figure B11. Absorption spectra of **3** in Pyr$_4$FAP calculated by TD-DFT.

Table B8. Calculated transitions of **3** in Pyr$_4$FAP (ε = 14.7)

Excited State	Energy (eV)	Wavelength (nm)	f_{osc}	Transition	%
2	1.9465	637	0.0009	55A → 57A	98.4
3	2.1666	572	0.0011	55A → 58A 55A → 59A	60.9 36.9
4	2.2145	560	0.0005	55A → 58A 55A → 59A	36.6 59.9
6	3.5868	346	0.0002	54A → 56A 54B → 55B	14.5 82.7
9	3.8204	325	0.0033	52A → 56A 52B → 55B	72.7 22.8
10	3.9819	311	0.0045	53A → 56A 54A → 57A 54B → 57B	6.6 64.2 22.1
11	4.0723	304	0.0015	51A → 56A 51B → 55B	72.5 17.7

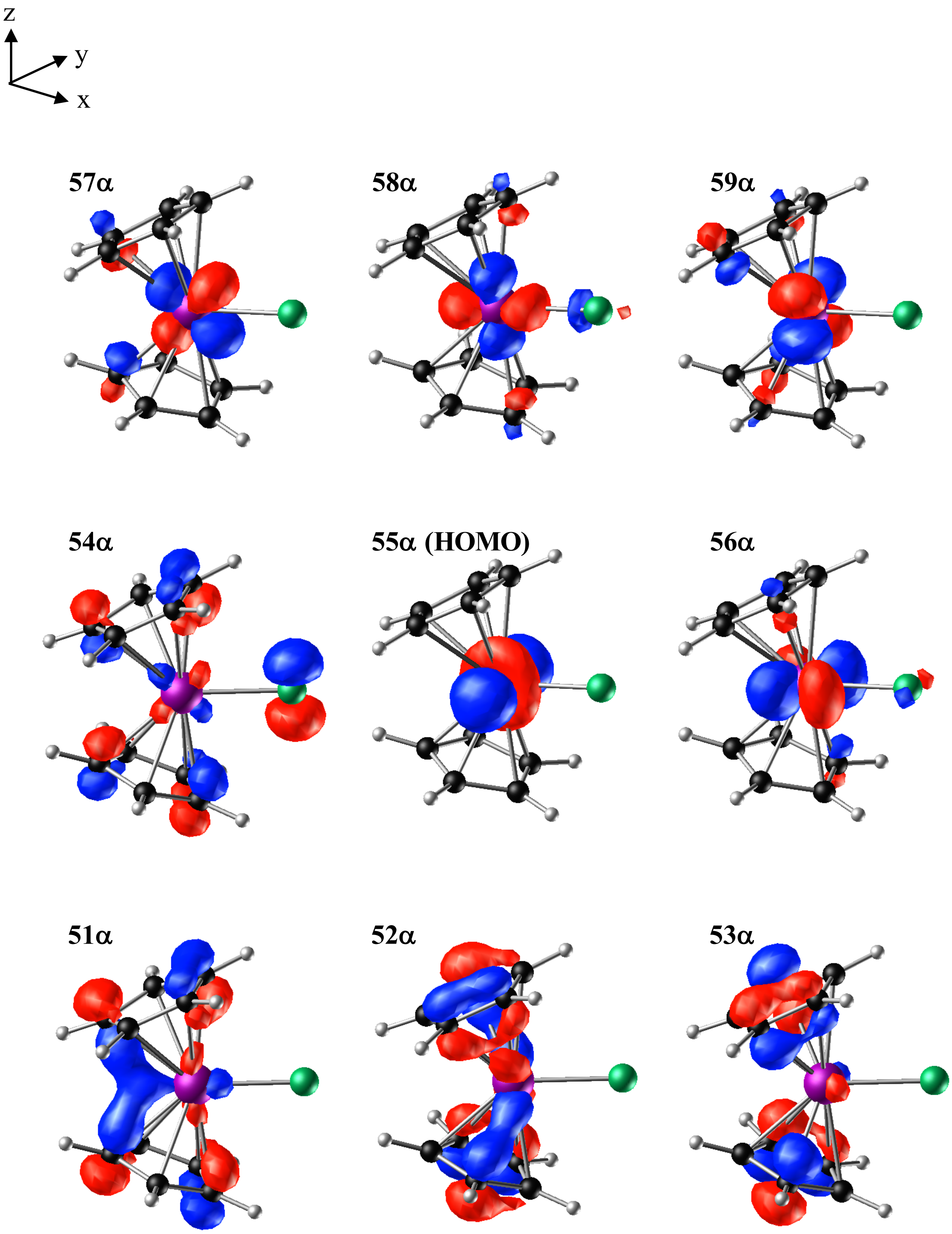

57α 58α 59α

54α 55α (HOMO) 56α

51α 52α 53α

Figure B12. Molecular orbitals for model complex **3** in Pyr$_4$FAP (ε = 14.7) (isosurface values: ±0.07 (51α, 52α, 53α, 54α, 55α, 56α, 57α, 58α and 59α).

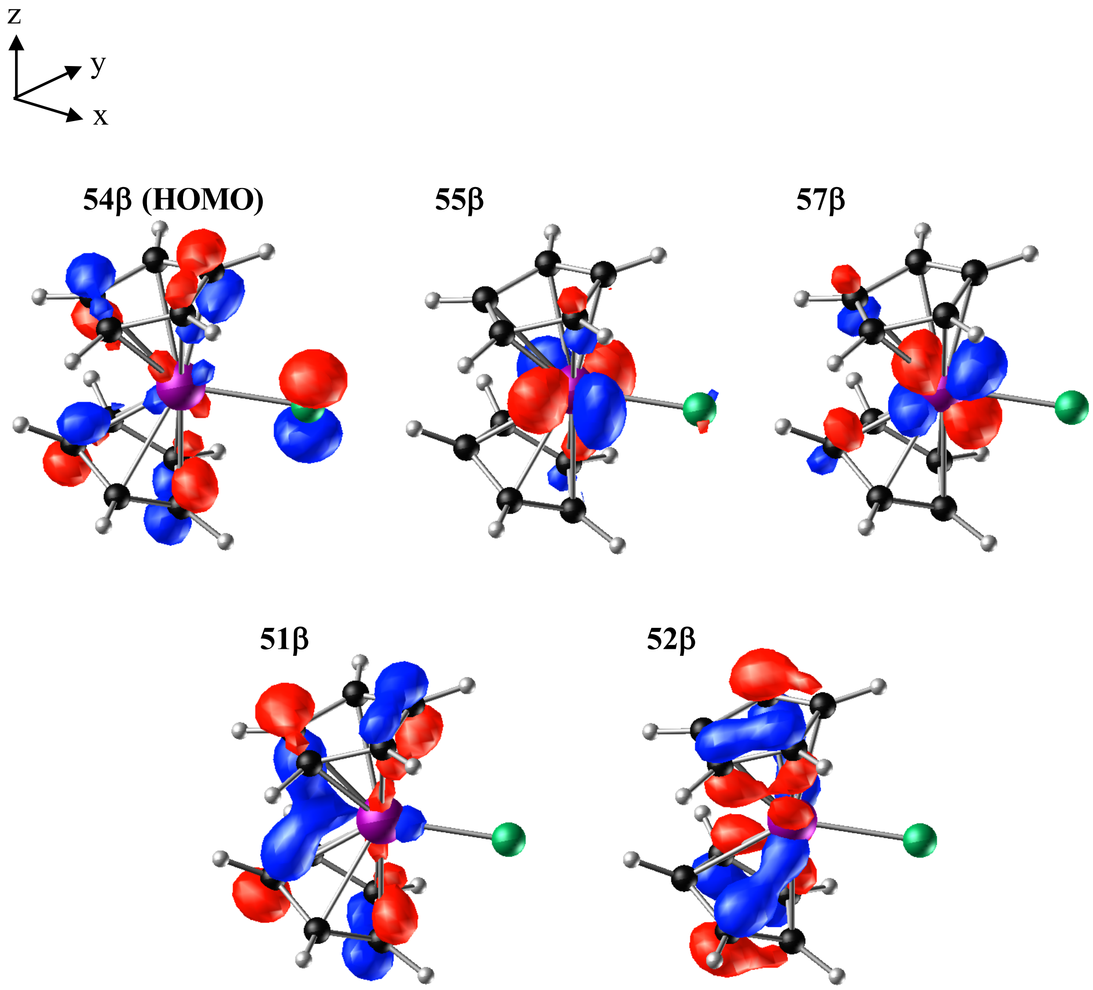

Figure B13. Molecular orbitals for model complex **3** in Pyr$_4$FAP (ε = 14.7) (isosurface values: ±0.07 (51β, 52β, 54β, 55β and 57β).

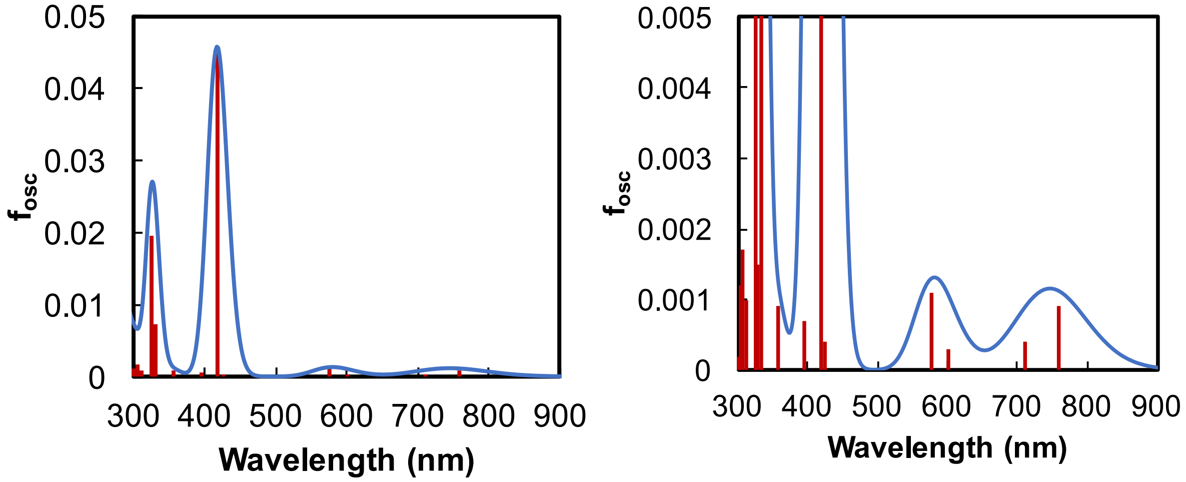

Figure B14. Absorption spectra of **4** in Pyr$_4$FAP (ε = 14.7) calculated by TD-DFT.

Table B9. Calculated transitions of **4** in Pyr$_4$FAP (ε = 14.7)

Excited State	Energy (eV)	Wavelength (nm)	f_{osc}	Transition	%
1	1.636	758	0.0009	62A → 63A 62A → 66A 62A → 68A	78.0 11.5 8.1
2	1.7448	711	0.0004	62A → 64A 62A → 65A 62A → 72A	9.4 82.2 4.7
3	2.0607	602	0.0003	62A → 66A 62A → 67A 62A → 68A	64.2 9.0 17.9
4	2.1521	576	0.0011	62A → 64A 62A → 66A 62A → 67A	8.3 7.0 76.9
6	2.9656	418	0.0452	62A → 64A 62A → 65A 62A → 67A	73.0 9.2 10.4
8	3.4671	358	0.0009	61A → 63A 61B → 63B	59.1 22.0
9	3.7317	332	0.0072	60B → 62B 61B → 63B	65.3 17.9
11	3.8106	325	0.0196	61A → 63A 59B → 62B 60B → 62B 61B → 63B	22.1 11.0 26.6 31.1

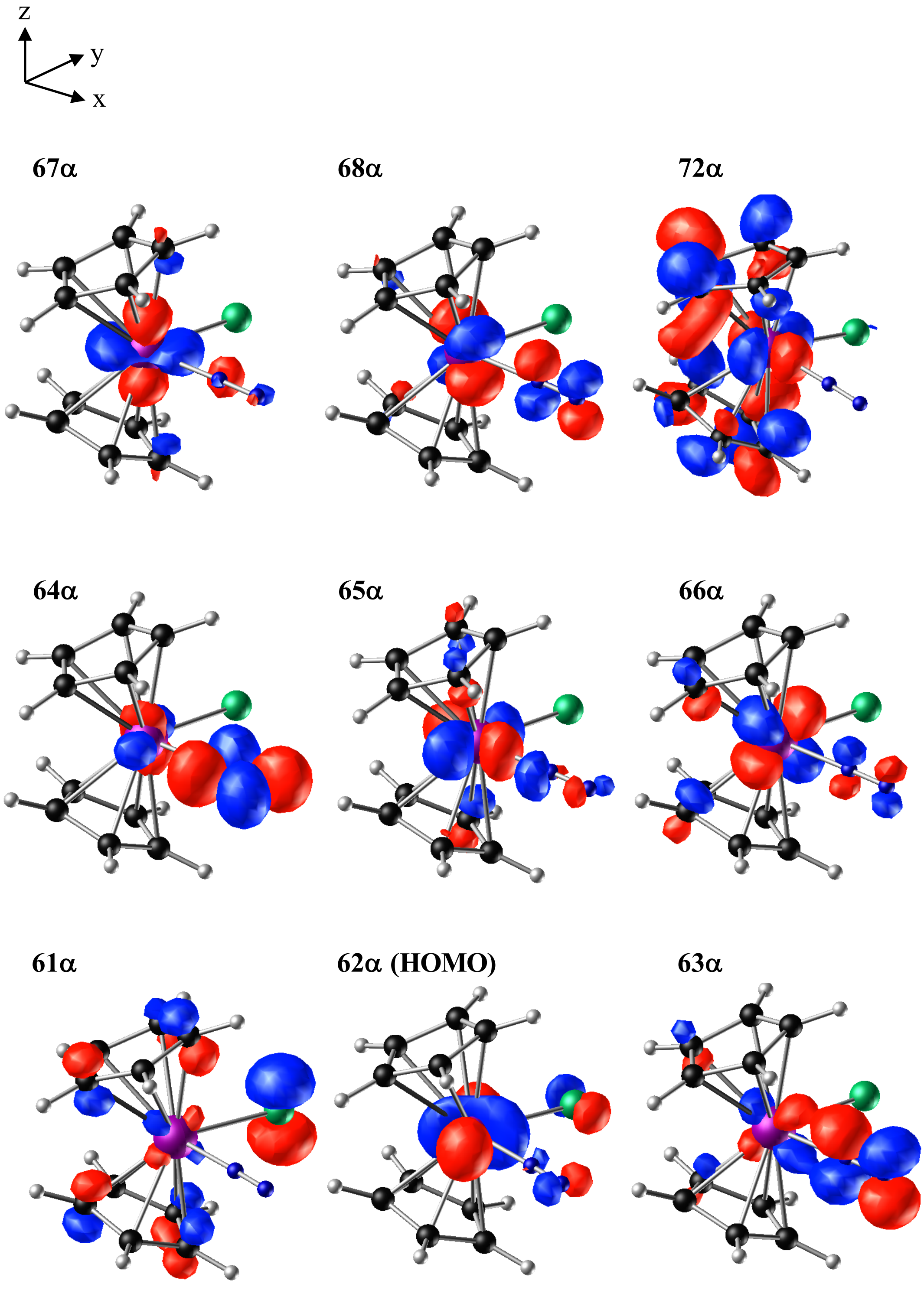

Figure B15. Molecular orbitals for model complex **4** in Pyr$_4$FAP (ε = 14.7) (isosurface values: ±0.07 (61α, 62α, 63α, 64α, 65α, 66α, 67α, 68α) and ±0.04 (72α).

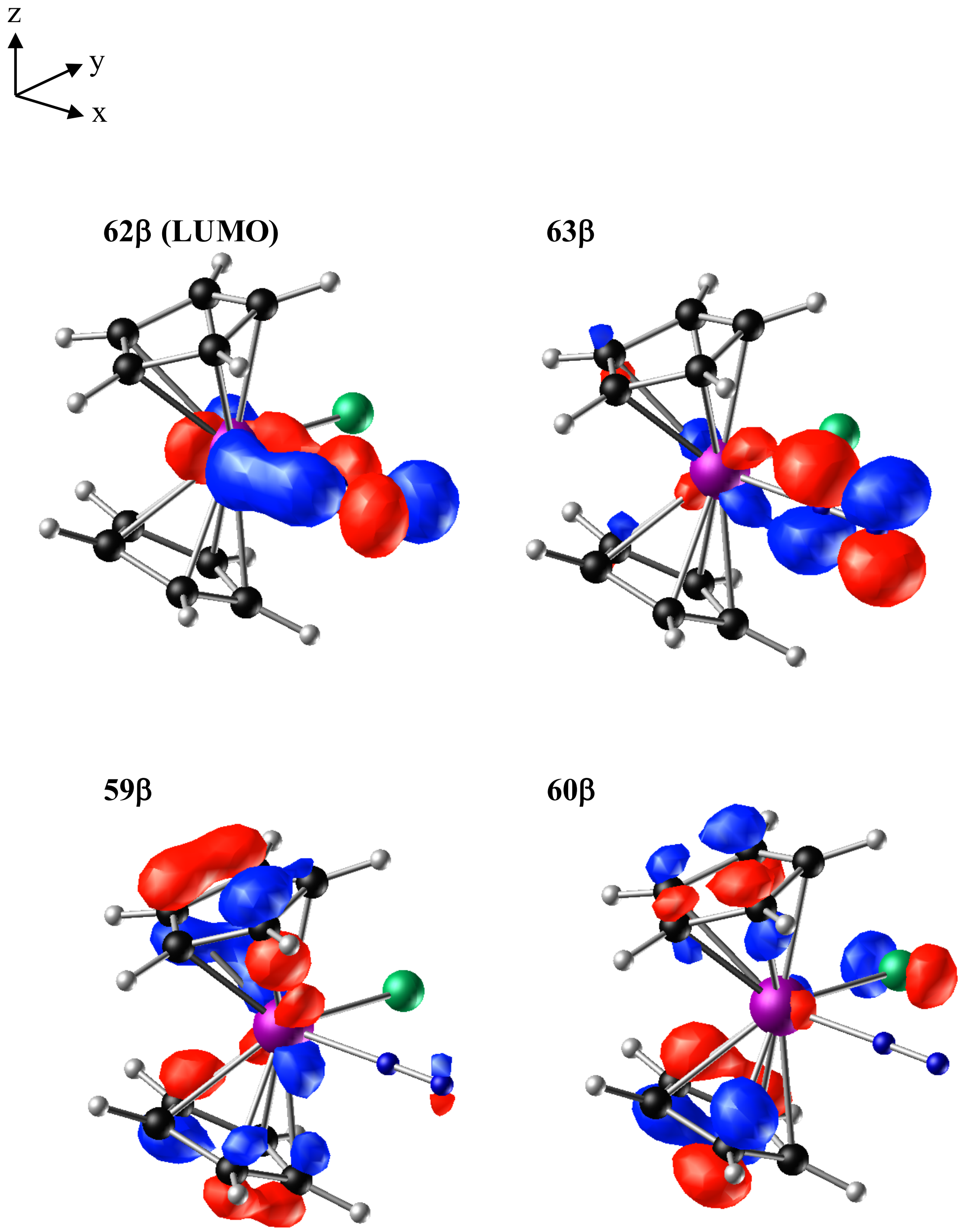

62β (LUMO) **63β**

59β **60β**

Figure B16. Molecular orbitals for model complex **4** in Pyr$_4$FAP (ε = 14.7) (isosurface values: ±0.07 (59β, 60β, 62β and 63β)).

B.3 TD-DFT calculations of model complexes in THF ($\varepsilon = 7.4257$)

UV-vis/NIR spectrum of [$(Cp_2TiCl)_2$] in 0.2 M Pyr_4FAP/THF, as shown in Figure 3.4, displays the absorption bands at 449, 751, 817 and 1138 nm, respectively. To characterize these absorption bands, TD-DFT calculations for **1**, **2**, **3**, **4** and **5** in the ionic liquid were carried out. The calculated absorption bands for **2**, **3**, and **5** are shown in Figure B17. In the range of 900 to 1100 nm, the absorption band of **5** in the excited state 2 at 933 nm is similar to the absorption band at 1138 nm shown in Figure A14 (see Figures B22 and B23 and Table B14). The absorption band of **5** in the excited state 2 consists of the d-d transition from molecular orbital 75α (HOMO) to 76α (LUMO). Moreover, the absorption band of **2** in the excited state 2 at 963 nm is composed of MMCT from the molecular orbital 109α to its 111α and d-d transition from its 110α to its 114α (see Figures B8, B9, B19 and Table B11). Accordingly, the absorption bands at 1138 nm are assigned to the d-d transition for **2** and **5** and MMCT for **2**, respectively. In the range of 500 to 900 nm, the absorption bands for **2** in the the excited state 3 (see Figures B8, B9, B19 and Table B11), **3** in the excited states 2 and 3 (see Figures B12, B13, B20 and Table B12), and **5** in the excited state 2 (see Figures B22, B23, Table B14) were observed. These absorption bands are characterized to the d-d transition on Ti atom. Therefore, the absorption band at 751 and 817 nm, as shown in Figure 3.4, are characterized to the d-d transitions of Ti atom. The calculated strong absorption bands at ca. 300 nm for **2**, **3** and **4** by TDDFT method are assigned to the LMCT. Thus, the absorption band at 449 nm can be characterized to the LMCT.

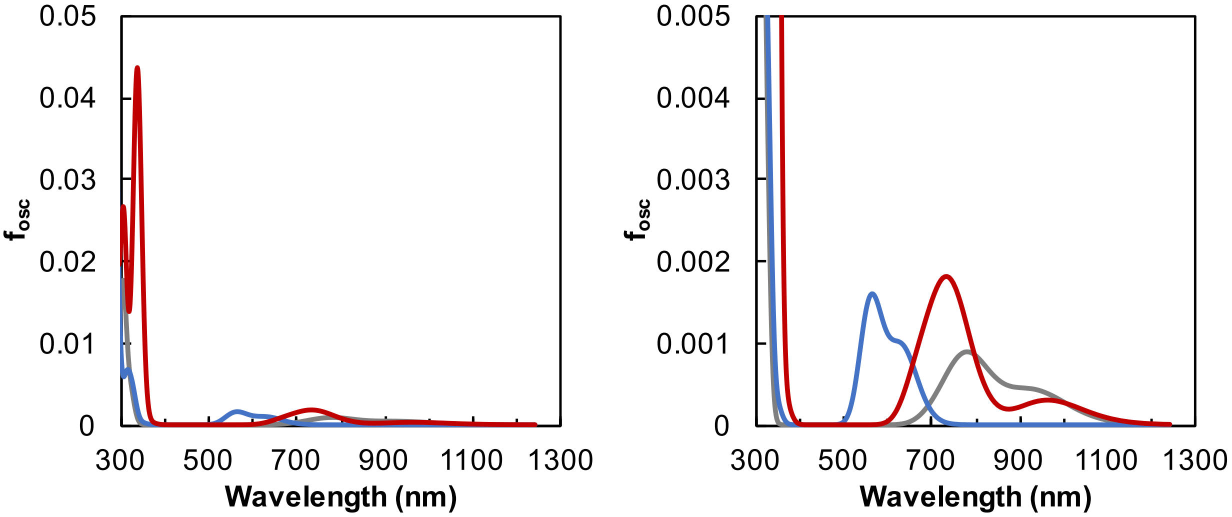

Figure B17. Absorption spectra of **2** (red), **3** (blue) and **5** (grey) in THF ($\varepsilon = 7.4257$) calculated by TD-DFT.

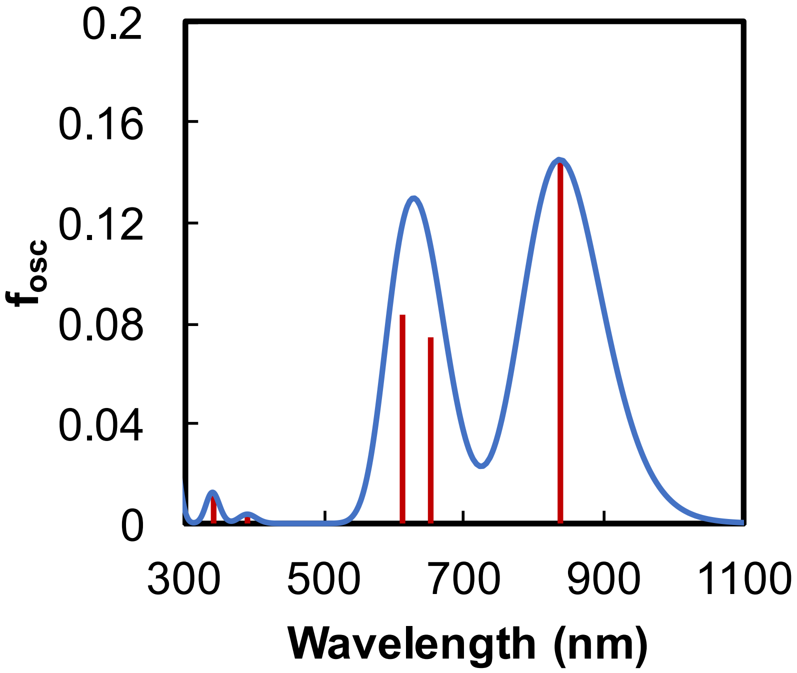

Figure B18. Absorption spectra of **1** in THF (ε = 7.4257) calculated by TD-DFT.

Table B10. Calculated transitions of **1** optimized in THF (ε = 7.4257)

Excited State	Energy (eV)	Wavelength (nm)	f_{osc}	Transition	%
3	1.4812	837	0.1449	109 →110 109 →116	68.7 28.4
4	1.5117	820	0.0006	109 →111 109 →112	11.2 88.3
7	1.9031	652	0.0749	109 →110 109 →116 109 →118	14.5 44.2 41.1
9	2.0294	611	0.0837	109 →110 109 →116 109 →118	13.1 27.0 57.8
11	3.1666	392	0.0037	107 →110	98.8
13	3.626	342	0.0124	105 →110	99.0

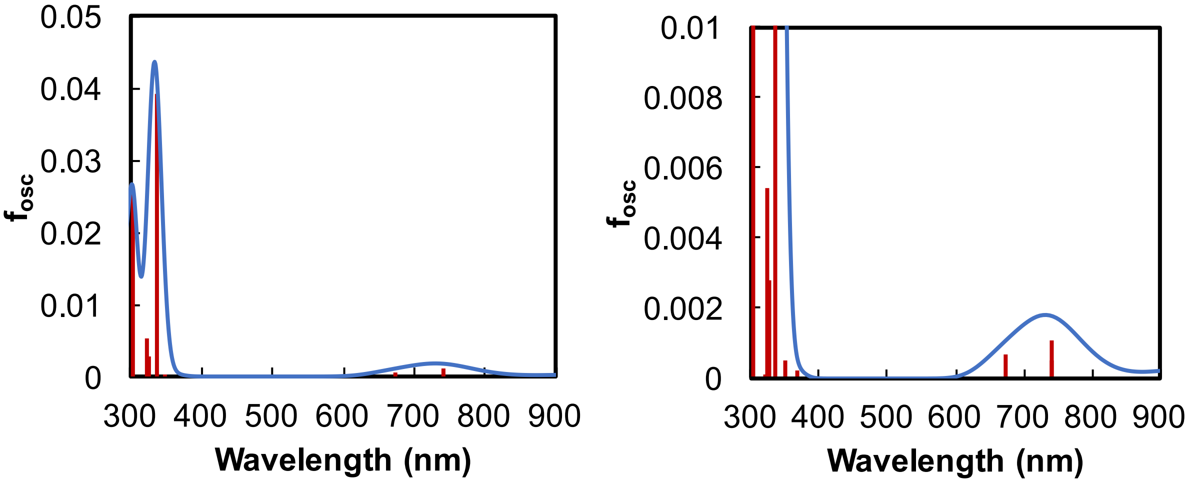

Figure B19. Absorption spectra of **2** in THF (ε = 7.4257) calculated by TD-DFT.

Table B11. Calculated transitions of **2** optimized in THF (ε = 7.4257)

Excited State	Energy (eV)	Wavelength (nm)	f_{osc}	Transition	%
2	1.288	963	0.0003	109A → 111A 110A → 114A	51.9 42.4
3	1.6732	741	0.0011	109A → 112A 109A → 113A 110A → 112A 110A → 113A	13.6 30.1 38.3 15.5
4	1.6738	741	0.0005	109A → 112A 109A → 113A 110A → 112A 110A → 113A	30.5 13.5 15.6 38.0
5	1.8395	674	0.0007	109A → 115A 110A → 116A	44.6 52.9
12	3.5459	350	0.0005	109A → 113A 110A → 112A	55.3 43.6
14	3.6948	336	0.0392	109A → 115A 110A → 116A	53.6 44.1
16	3.7983	326	0.0028	108A → 112A 107B → 110B 108B → 109B	12.6 13.8 54.6
18	3.8277	324	0.0054	107A → 113A 108A → 112A 108B → 109B 108B → 113B	17.0 33.0 19.9 9.8
22	4.092	303	0.0253	107A → 115A 108A → 116A	23.0 52.7

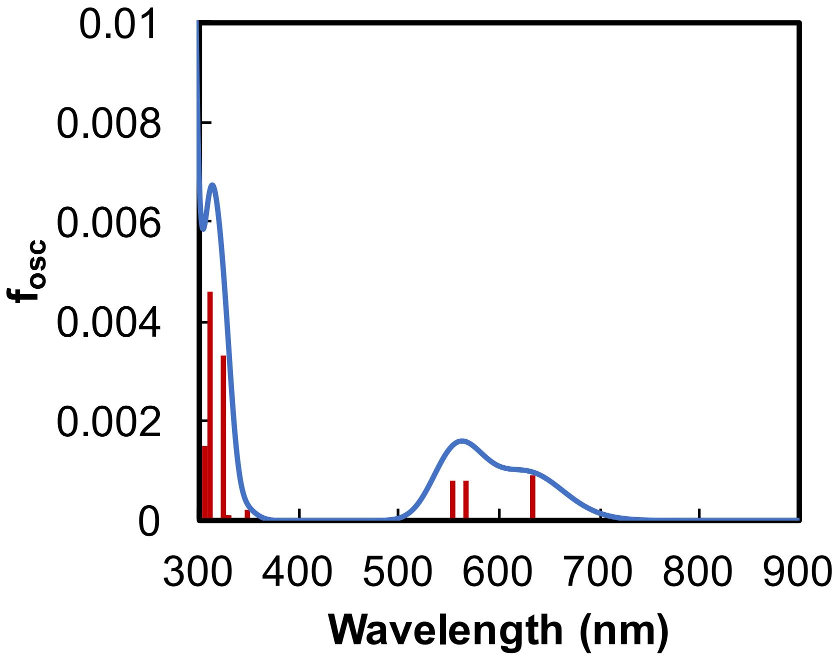

Figure B20. Absorption spectra of **3** in THF (ε = 7.4257) calculated by TD-DFT.

Table B12. Calculated transitions of **3** in the singlet state optimized in THF

Excited State	Energy (eV)	Wavelength (nm)	f_{osc}	Transition	%
2	1.9619	632	0.0009	55A → 57A	98.4
3	2.1893	566	0.0008	55A → 58A 55A → 59A	38.8 58.9
4	2.2365	554	0.0008	55A → 58A 55A → 59A	58.7 37.9
9	3.8265	324	0.0033	52A → 56A 52B → 55B	72.8 22.7
10	3.9793	312	0.0046	53A → 56A 54A → 57A 54B → 57B	6.8 64.4 21.8
11	4.0759	304	0.0015	51A → 56A 51B → 55B	72.5 17.8

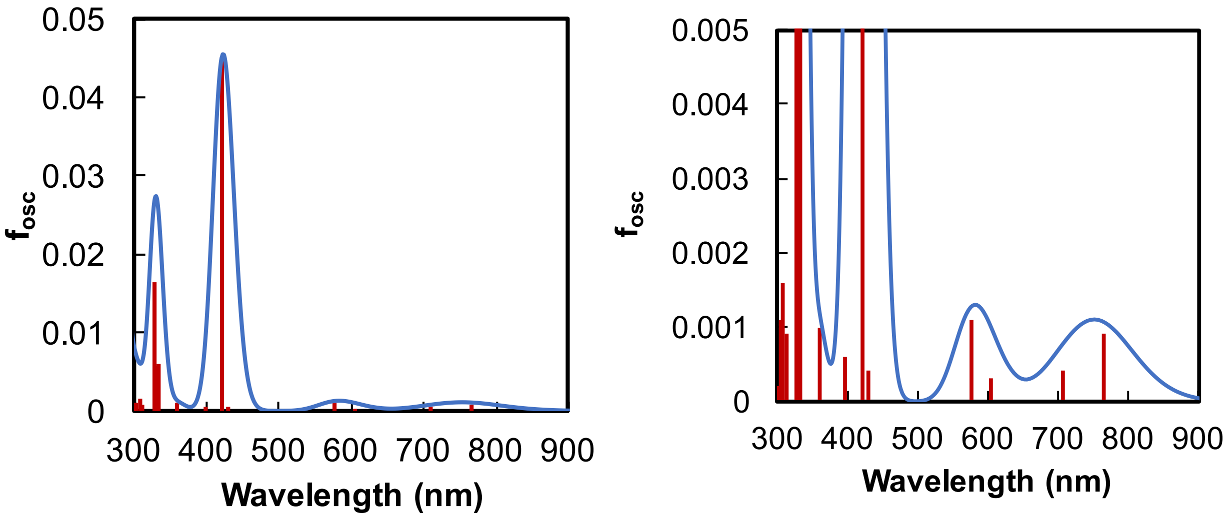

Figure B21. Absorption spectra of **4** in THF (ε = 7.4257) calculated by TD-DFT.

Table B13. Calculated transitions of **4** optimized in THF (ε = 7.4257)

Excited State	Energy (eV)	Wavelength (nm)	f_{osc}	Transition	%
1	1.6212	765	0.0009	62A → 63A	78.2
				62A → 66A	11.3
				62A → 68A	8.1
2	1.7502	708	0.0004	62A → 64A	7.4
				62A → 65A	83.9
3	2.0503	605	0.0003	62A → 66A	64.9
				62A → 67A	8.2
				62A → 68A	18.0
4	2.1466	578	0.0011	62A → 64A	8.4
				62A → 66A	6.3
				62A → 67A	77.6
6	2.9422	421	0.045	62A → 64A	75.0
				62A → 65A	7.4
				62A → 67A	10.4
9	3.7233	333	0.0061	61A → 63A	8.0
				60B → 62B	50.9
				61B → 63B	33.0
10	3.7647	329	0.0057	61A → 63A	12.1
				59B → 62B	53.9
				60B → 62B	8.1
				61B → 63B	17.9
11	3.7947	327	0.0165	61A → 63A	9.9
				59B → 62B	36.3
				60B → 62B	33.7
				61B → 63B	12.6

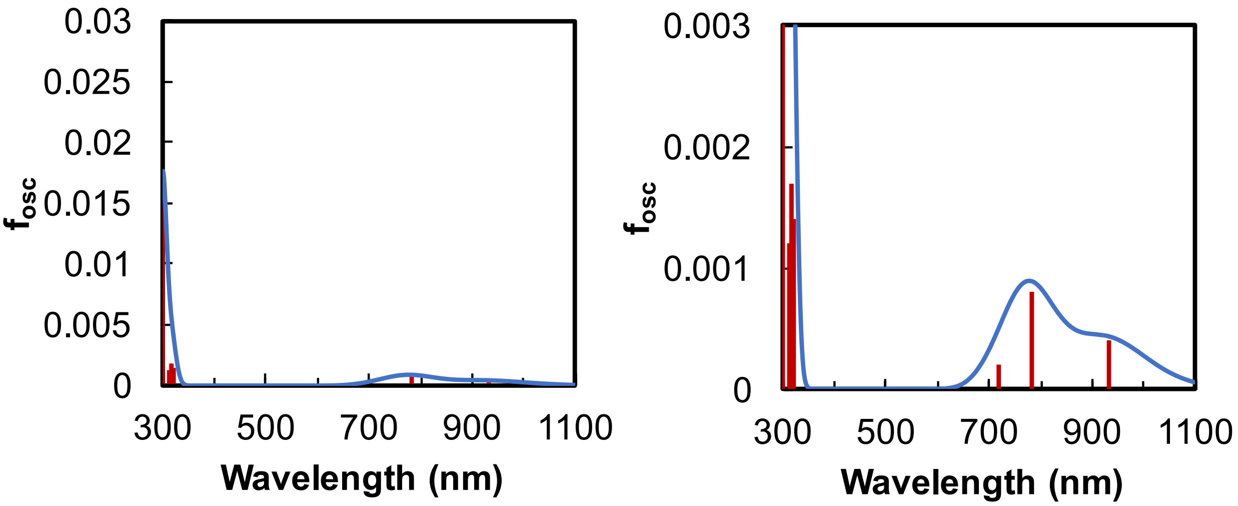

Figure B22. Absorption spectra of **5** in THF (ε = 7.4257) calculated by TD-DFT.

Table B14. Calculated transitions of **5** optimized in THF (ε = 7.4257)

Excited State	Energy (eV)	Wavelength (nm)	f_{osc}	Transition	%
1	1.3283	933	0.0004	75A → 76A 75A → 77A	73.5 17.5
2	1.5831	783	0.0008	75A → 76A 75A → 77A	18.8 78.3
5	3.8563	322	0.0014	74A → 76A 74A → 77A 74B → 75B 74B → 77B	19.4 11.4 52.1 7.3
6	3.887	319	0.0017	74A → 77A 74B → 75B 74B → 77B	36.5 34.2 13.0
7	3.9494	314	0.0012	74A → 76A 74A → 77A 74B → 76B	45.1 19.5 18.0
8	4.1083	302	0.0169	74A → 78A 74B → 78B	71.6 7.9

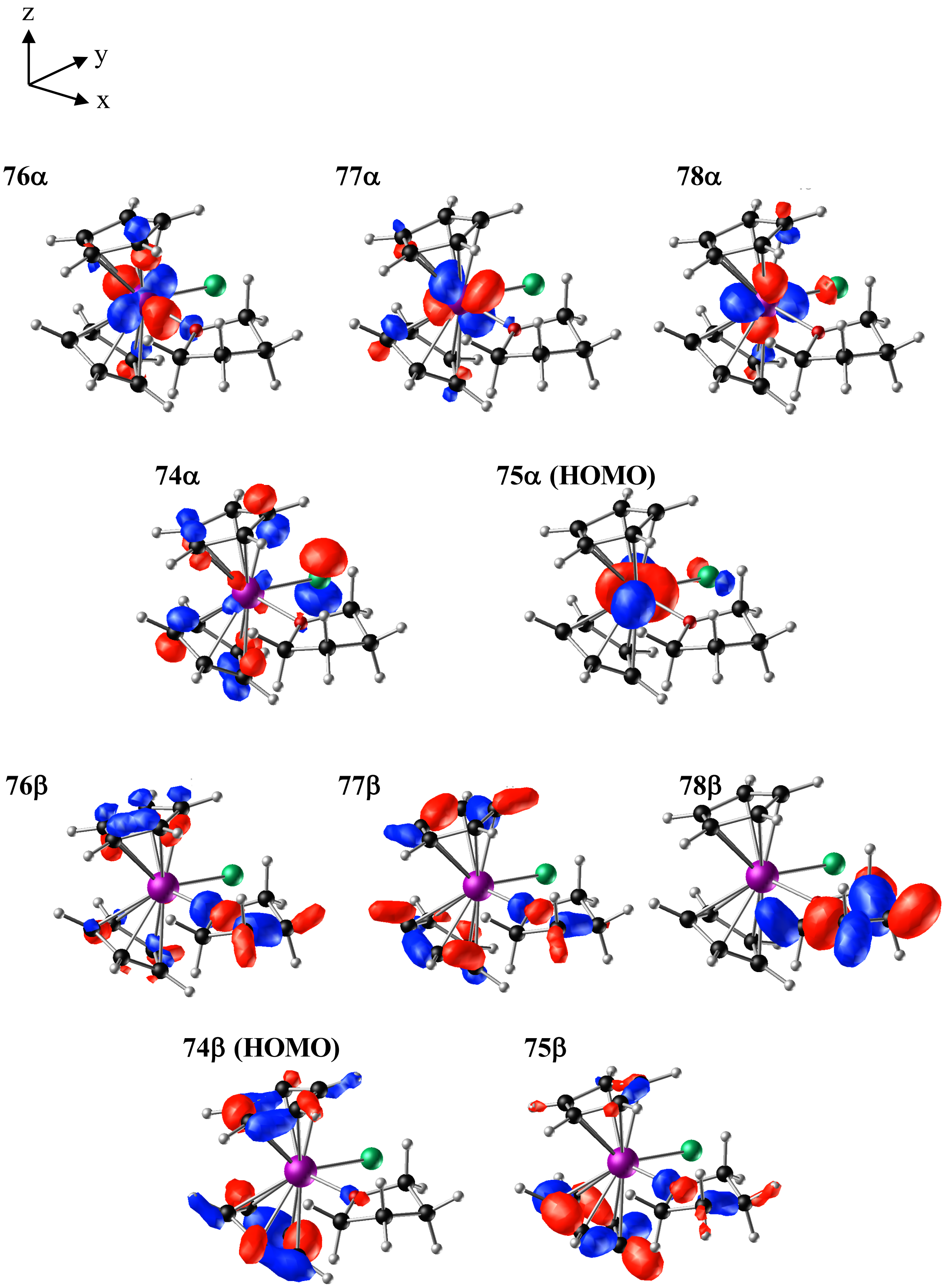

Figure B23. Molecular orbitals for model complex **5** in THF (ε = 7.4257) (isosurface values: ±0.07 (74α, 75α, 76α, 77α, 78α, 74β, 75β, 76β, 77β and 78β).

B.4 Computed profile of titanocene in toluene, THF, and Pyr$_4$FAP

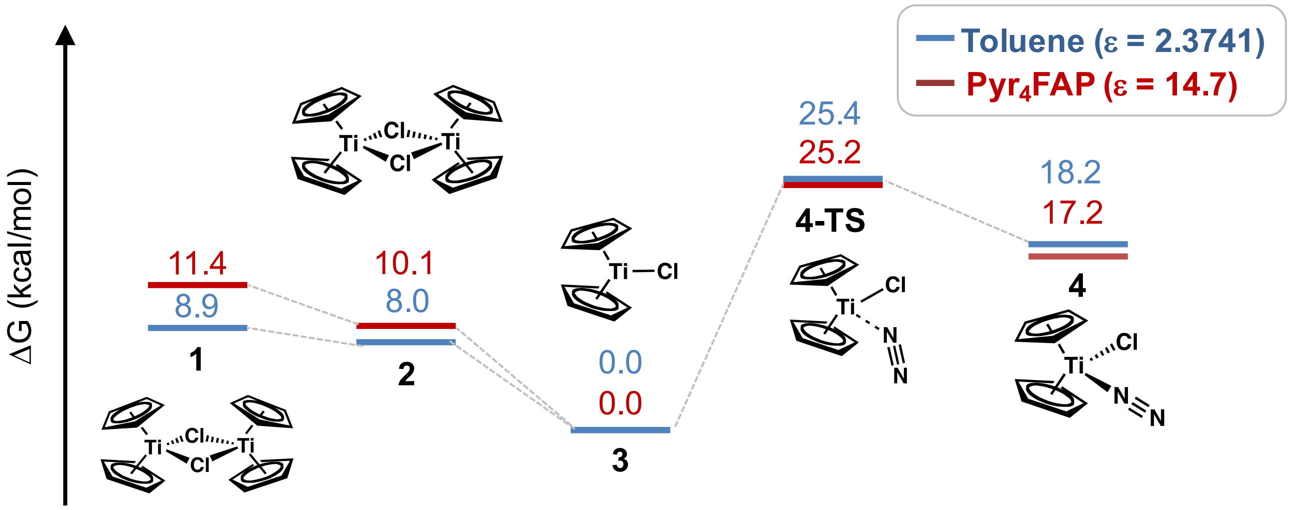

Figure B24. Computed profile of the equilibrium reactions among **1**, **2**, **3**, **4**, and **4-TS** in toluene (ε = 2.3741) (blue) and ionic liquid, Pyr$_4$FAP (ε = 14.7) (red), as estimated at 298.15 K.

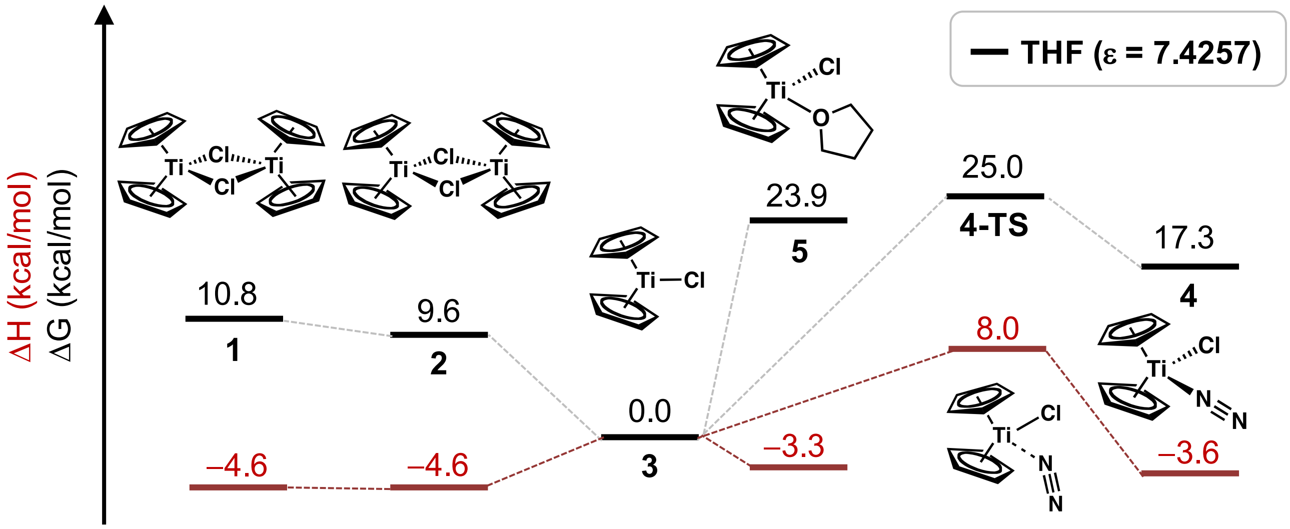

Figure B25. Computed profile of the equilibrium reactions among **1**, **2**, **3**, **4**, **4-TS,** and **5** in THF (ε = 7.4257), as estimated at 298.15 K.

B.5 Cartesian coordinates for optimized structure

Table B15. Cartesian coordinates for optimized structure of **1** in Pyr$_4$FAP (ε = 14.7)

Ti	-0.037336	0.001529	0.002383
Cl	1.972886	1.642132	0.002587
Cl	1.967705	-1.646331	0.003262
C	-0.539672	1.158501	2.042003
C	-1.783328	0.720170	1.526846
H	-2.589527	1.361351	1.178977
C	-1.786843	-0.709001	1.526617
H	-2.596202	-1.346130	1.178685
C	-0.545232	-1.153550	2.041402
H	-0.231676	-2.187849	2.154871
C	0.234535	0.000549	2.351208
H	1.243595	-0.002261	2.747963
H	-0.221229	2.191306	2.155460
C	-1.201917	-1.154985	-1.731339
C	-1.960426	0.001830	-1.384514
H	-2.950683	0.001855	-0.939424
C	-1.201863	1.158658	-1.731269
H	-1.503900	2.193805	-1.590774
C	0.005688	0.709777	-2.339038
H	0.805233	1.351761	-2.696836
C	0.005620	-0.706093	-2.339112
H	0.805427	-1.347950	-2.696600
H	-1.504019	-2.190121	-1.590876
Ti	3.977954	-0.005002	0.003444
C	5.140385	-1.164138	1.737070
C	5.901145	-0.008833	1.390188
H	6.891462	-0.010776	0.945210
C	5.144893	1.149498	1.737055
H	5.449059	2.184028	1.596609
C	3.936437	0.702979	2.344828
H	3.138134	1.346452	2.702725
C	3.933782	-0.712889	2.344926
H	3.132843	-1.353277	2.702519
H	5.440434	-2.199881	1.596701
C	4.487398	1.151258	-2.034285
C	5.728371	0.704229	-1.520078
H	6.538674	1.339764	-1.171422
C	5.722834	-0.724911	-1.521938
H	6.527935	-1.367797	-1.174681
C	4.478451	-1.160761	-2.037500
H	4.158562	-2.192994	-2.152064
C	3.705927	-0.001410	-2.345355
H	2.696789	0.003023	-2.741884
H	4.175507	2.186213	-2.146384

Table B16. Cartesian coordinates for optimized structure of **2** in Pyr$_4$FAP (ε = 14.7)

Ti	-0.062524	0.005048	0.002811
Cl	1.973205	1.620578	0.003230
Cl	1.967424	-1.617502	0.003028
C	-0.882421	1.250810	1.849586
C	-1.941468	0.402205	1.429328
H	-2.887113	0.730419	1.007202
C	-1.549233	-0.952896	1.654935
H	-2.135550	-1.838567	1.421455
C	-0.260187	-0.937218	2.245789
H	0.324655	-1.812780	2.514009
C	0.158605	0.414584	2.358126
H	1.112056	0.760314	2.743404
H	-0.872022	2.337166	1.808771
C	-0.892222	-1.238115	-1.841175
C	-1.943906	-0.379230	-1.422938
H	-2.892456	-0.698177	-1.000287
C	-1.539930	0.971837	-1.651786
H	-2.118522	1.863166	-1.420567
C	-0.251196	0.943346	-2.243078
H	0.341194	1.813151	-2.513442
C	0.155704	-0.412216	-2.352340
H	1.106132	-0.767230	-2.736697
H	-0.891334	-2.324429	-1.797866
Ti	4.003174	-0.002137	0.002995
C	4.828251	-1.248548	1.846902
C	5.883166	-0.393625	1.428692
H	6.830483	-0.716110	1.005949
C	5.484297	0.958945	1.657622
H	6.066272	1.848093	1.426503
C	4.195463	0.935295	2.248913
H	3.606372	1.807326	2.519314
C	3.783445	-0.418725	2.358092
H	2.831677	-0.770172	2.742400
H	4.823244	-2.334856	1.803544
C	4.827152	1.240841	-1.843736
C	5.883383	0.388670	-1.423597
H	6.830130	0.713698	-1.001480
C	5.486589	-0.965095	-1.649217
H	6.069910	-1.852744	-1.415732
C	4.197551	-0.945090	-2.239935
H	3.609727	-1.818671	-2.508103
C	3.783275	0.408121	-2.352206
H	2.830947	0.757040	-2.737388
H	4.820415	2.327210	-1.802864

Table B17. Cartesian coordinates for optimized structure of **3** in Pyr$_4$FAP (ε = 14.7)

Ti	3.236254	3.163636	1.327889
Cl	3.076989	2.328510	-0.902561
C	5.124223	4.526613	0.715558
C	5.048336	4.504430	2.133925
C	3.826937	5.137391	2.514076
C	3.136105	5.529032	1.330214
C	3.949295	5.156174	0.219656
H	3.694595	5.287326	-0.828225
H	5.919168	4.094064	0.111816
H	5.789231	4.082613	2.809370
C	1.366617	1.795992	1.989740
C	2.514422	0.960398	1.910512
C	3.457241	1.398445	2.886265
C	2.873449	2.499964	3.578270

C	1.588167	2.756162	3.013247
H	0.492597	1.741060	1.344395
H	2.665697	0.156671	1.195191
H	4.429020	0.954276	3.088731
H	3.332111	3.047579	4.396562
H	0.899952	3.542614	3.314714
H	3.479452	5.296436	3.530913
H	2.179239	6.043813	1.284643

Table B18. Cartesian coordinates for optimized structure of **4** in Pyr_4FAP (ε = 14.7)

Ti	-0.129215	0.008109	-0.001777
Cl	-0.229688	-2.474769	-0.012381
C	0.392089	1.365427	1.874660
C	-0.917550	1.722847	1.466071
H	-1.224376	2.689421	1.077942
C	-1.772908	0.592961	1.665747
H	-2.836763	0.548648	1.445178
C	-0.993328	-0.449843	2.224586
H	-1.344082	-1.448544	2.464459
C	0.345180	0.009350	2.340450
H	1.183891	-0.565517	2.724731
H	1.269241	2.007961	1.854350
C	-1.307234	-0.299041	-2.062934
C	-1.712711	0.958682	-1.548542
H	-2.715788	1.222894	-1.222479
C	-0.572728	1.821177	-1.534122
H	-0.554950	2.856194	-1.204817
C	0.532872	1.095237	-2.040427
H	1.542873	1.477816	-2.165455
C	0.085892	-0.226600	-2.353535
H	0.698810	-1.034708	-2.742957
H	-1.936012	-1.177367	-2.174654
N	1.968209	-0.268376	-0.004081
N	3.082099	-0.381846	-0.005931

Table B19. Cartesian coordinates for optimized structure of **4-TS** in Pyr_4FAP (ε = 14.7)

Ti	-0.193359	-0.071060	-0.006679
Cl	0.224618	-2.451786	-0.050794
C	0.337982	1.335131	1.822735
C	-1.026529	1.569328	1.485614
H	-1.441855	2.501931	1.116570
C	-1.765157	0.371393	1.735961
H	-2.831728	0.229749	1.578513
C	-0.860619	-0.587934	2.263863
H	-1.102317	-1.613745	2.526903
C	0.432661	-0.004215	2.307769
H	1.343213	-0.506557	2.626597
H	1.149825	2.055440	1.754384
C	-1.207555	-0.400023	-2.157318
C	-1.775564	0.777896	-1.609074
H	-2.819299	0.919522	-1.338059
C	-0.733861	1.745581	-1.472462
H	-0.848194	2.759475	-1.100469
C	0.481627	1.160279	-1.919160
H	1.450502	1.651455	-1.961249
C	0.186841	-0.173259	-2.339178
H	0.904508	-0.899958	-2.710716
H	-1.732435	-1.331251	-2.354345
N	2.747103	-0.093728	0.004222
N	3.781132	0.295044	0.073628

Table B20. Cartesian coordinates for optimized structure of $[Cp_2TiCl_2]^-$ in Pyr_4FAP (ε = 14.7)

Ti	-1.145365	0.009738	0.007495
Cl	0.618855	1.869171	0.063315
Cl	0.812708	-1.633689	-0.039754
C	-1.923937	1.104154	1.980633
C	-3.023827	0.353957	1.491741
H	-3.950227	0.765293	1.098957
C	-2.697848	-1.034756	1.588652
H	-3.327045	-1.864693	1.274690
C	-1.404912	-1.138890	2.155382
H	-0.854521	-2.060187	2.320394
C	-0.912601	0.175578	2.381832
H	0.073450	0.431654	2.758410
H	-1.852415	2.187409	2.023971
C	-1.959089	-1.183939	-1.884329
C	-3.020774	-0.352526	-1.432974
H	-3.960458	-0.695395	-1.008901
C	-2.639229	1.010778	-1.629869
H	-3.228256	1.887253	-1.368948
C	-1.357149	1.014843	-2.237558
H	-0.771245	1.897388	-2.475254
C	-0.927757	-0.327617	-2.382709
H	0.037671	-0.650749	-2.760691
H	-1.935059	-2.270476	-1.860405

Table B21. Cartesian coordinates for optimized structure of **1** in toluene (ε = 2.3741)

Ti	-0.026936	0.003026	0.003031
Cl	1.974594	1.644013	0.001573
Cl	1.967962	-1.646022	0.003225
C	-0.527246	1.160722	2.044283
C	-1.771589	0.723071	1.531328
H	-2.578094	1.365336	1.186159
C	-1.775959	-0.705854	1.531399
H	-2.586426	-1.343226	1.186471
C	-0.534277	-1.151153	2.044257
H	-0.219474	-2.185303	2.154305
C	0.245888	0.002446	2.352552
H	1.255956	-0.000614	2.746211
H	-0.206052	2.192927	2.154091
C	-1.193436	-1.152640	-1.731218
C	-1.950747	0.004749	-1.385128
H	-2.941770	0.005883	-0.941574
C	-1.191192	1.160502	-1.731833
H	-1.490731	2.196413	-1.592719
C	0.015521	0.710325	-2.339132
H	0.815924	1.352839	-2.693706
C	0.014198	-0.705059	-2.338718

H	0.813361	-1.349294	-2.692941
H	-1.494910	-2.187907	-1.591483
Ti	3.969487	-0.005028	0.001885
C	5.132563	-1.163260	1.736891
C	5.893159	-0.008208	1.390140
H	6.884196	-0.010229	0.946619
C	5.136864	1.149882	1.736151
H	5.439233	2.184875	1.596313
C	3.928822	0.703436	2.343624
H	3.130196	1.348384	2.697775
C	3.926215	-0.711947	2.344113
H	3.125271	-1.353738	2.698759
H	5.431161	-2.199450	1.597828
C	4.476691	1.149359	-2.039285
C	5.718404	0.704091	-1.526474
H	6.528851	1.341467	-1.181498
C	5.714112	-0.724838	-1.526542
H	6.520639	-1.367099	-1.181420
C	4.469790	-1.162516	-2.039512
H	4.148645	-2.194731	-2.149385
C	3.696591	-0.004248	-2.347666
H	2.686519	-0.001144	-2.741311
H	4.161838	2.183500	-2.149267

Table B22. Cartesian coordinates for optimized structure of **2** in toluene (ε = 2.3741)

Ti	-0.053576	0.001722	0.003280
Cl	1.973845	1.616856	0.002387
Cl	1.968498	-1.620184	0.003321
C	-0.545347	1.158225	2.046325
C	-1.792049	0.721599	1.537579
H	-2.599458	1.364406	1.195465
C	-1.797015	-0.707188	1.536720
H	-2.609028	-1.343970	1.194275
C	-0.553305	-1.153216	2.044756
H	-0.237931	-2.187572	2.151788
C	0.228621	-0.000334	2.351149
H	1.241118	-0.004105	2.738853
H	-0.222703	2.190232	2.154319
C	-1.214877	-1.153399	-1.733825
C	-1.972788	0.004002	-1.388760
H	-2.964605	0.005178	-0.946823
C	-1.212269	1.159672	-1.733857
H	-1.512042	2.195579	-1.595002
C	-0.003590	0.709450	-2.337695
H	0.798413	1.351442	-2.689620
C	-0.005170	-0.705911	-2.337639
H	0.795451	-1.349644	-2.689542
H	-1.517012	-2.188630	-1.595034
Ti	3.995895	-0.005101	0.002485
C	5.155192	-1.162461	1.739824
C	5.915228	-0.006534	1.394521
H	6.907042	-0.007377	0.952578
C	5.156846	1.150601	1.739434
H	5.458482	2.185925	1.600254
C	3.947312	0.702704	2.343331
H	3.146425	1.346160	2.695116
C	3.946354	-0.712663	2.343589
H	3.144552	-1.354886	2.695578
H	5.455423	-2.198278	1.601286
C	4.495375	1.150040	-2.038866
C	5.739212	0.704480	-1.530790
H	6.550938	1.341563	-1.188225
C	5.734772	-0.724309	-1.531597
H	6.542470	-1.366808	-1.189588
C	4.488244	-1.161415	-2.040427
H	4.165936	-2.193529	-2.148410
C	3.713871	-0.003123	-2.345300
H	2.701413	0.000251	-2.733109
H	4.179648	2.184282	-2.145939

Table B23. Cartesian coordinates for optimized structure of **3** in toluene (ε = 2.3741)

Ti	3.236286	3.163710	1.327241
Cl	3.078861	2.336981	-0.875889
C	5.123777	4.527000	0.713362
C	5.049347	4.507511	2.132097
C	3.829360	5.141319	2.512224
C	3.136754	5.529209	1.328139
C	3.949527	5.156055	0.217805
H	3.693216	5.280917	-0.830249
H	5.916352	4.093228	0.107761
H	5.793220	4.090333	2.807155
C	1.367216	1.795431	1.987509
C	2.513570	0.959347	1.909043
C	3.455526	1.395635	2.886036
C	2.871041	2.495399	3.580084
C	1.587649	2.753618	3.013486
H	0.495523	1.740970	1.339288
H	2.665779	0.160068	1.189297
H	4.425203	0.947886	3.090584
H	3.328330	3.040618	4.400875
H	0.897098	3.536884	3.317978
H	3.483538	5.303444	3.529273
H	2.181922	6.047633	1.281803

Table B24. Cartesian coordinates for optimized structure of **4** in toluene (ε = 2.3741)

Ti	-0.127607	0.008672	-0.002357
Cl	-0.234658	-2.442517	-0.021171
C	0.371005	1.375730	1.876550
C	-0.945302	1.707376	1.468094
H	-1.270671	2.667652	1.078882
C	-1.777937	0.560645	1.667877
H	-2.840721	0.493570	1.447814
C	-0.978708	-0.465433	2.229533
H	-1.306981	-1.472911	2.463415
C	0.349132	0.019991	2.345035
H	1.197850	-0.541315	2.727087
H	1.235014	2.036034	1.859983
C	-1.320949	-0.281041	-2.056150
C	-1.696908	0.987995	-1.546820
H	-2.692852	1.274142	-1.217202

C	-0.540304	1.827226	-1.544426
H	-0.498492	2.863433	-1.220188
C	0.545966	1.075746	-2.055575
H	1.562310	1.437355	-2.191865
C	0.070394	-0.237392	-2.358135
H	0.662959	-1.063898	-2.739771
H	-1.964397	-1.150130	-2.154354
N	1.970396	-0.261849	0.002928
N	3.085286	-0.368968	0.004899

Table B25. Cartesian coordinates for optimized structure of **4-TS** in toluene (ε = 2.3741)

Ti	-0.248377	-0.084483	0.001271
Cl	0.108510	-2.437544	-0.020612
C	0.444913	1.270070	1.822604
C	-0.897161	1.634730	1.513623
H	-1.226034	2.607621	1.162832
C	-1.740725	0.510437	1.769665
H	-2.819178	0.471263	1.635340
C	-0.921031	-0.534735	2.274977
H	-1.251305	-1.538189	2.528524
C	0.426632	-0.071905	2.301648
H	1.300638	-0.664576	2.594126
H	1.319715	1.911336	1.744450
C	-1.121772	-0.464870	-2.215984
C	-1.815753	0.640844	-1.659701
H	-2.880723	0.687824	-1.444489
C	-0.868104	1.690019	-1.460882
H	-1.090109	2.686043	-1.089473
C	0.414876	1.217210	-1.864071
H	1.342443	1.788909	-1.856425
C	0.251074	-0.118023	-2.332764
H	1.044037	-0.778392	-2.675645
H	-1.548742	-1.437459	-2.444556
N	2.760603	-0.143996	-0.076410
N	3.717118	0.396574	0.069211

Table B26. Cartesian coordinates for optimized structure of **1** in THF (ε = 7.4257)

Ti	-0.035634	0.001911	0.002377
Cl	1.973183	1.642840	0.002647
Cl	1.967331	-1.645990	0.003271
C	-0.535154	1.158339	2.043416
C	-1.779748	0.722418	1.528754
H	-2.585077	1.365347	1.182094
C	-1.785420	-0.706702	1.527342
H	-2.595932	-1.342588	1.179807
C	-0.544232	-1.153702	2.040912
H	-0.231852	-2.188540	2.152286
C	0.237313	-0.001038	2.351125
H	1.246919	-0.005462	2.746287
H	-0.214508	2.190449	2.156508
C	-1.201862	-1.152582	-1.731793
C	-1.957938	0.005902	-1.385313
H	-2.948516	0.008116	-0.940912
C	-1.196819	1.160984	-1.732048
H	-1.496299	2.196892	-1.592038
C	0.009837	0.709350	-2.339330
H	0.810886	1.350009	-2.696051
C	0.006732	-0.706394	-2.339104
H	0.805017	-1.350536	-2.695757
H	-1.505823	-2.187151	-1.591522
Ti	3.976110	-0.005466	0.003461
C	5.139194	-1.163234	1.737716
C	5.898584	-0.007006	1.390983
H	6.889139	-0.007829	0.946527
C	5.140853	1.150334	1.737612
H	5.443302	2.185350	1.597372
C	3.932901	0.702282	2.345011
H	3.133670	1.345253	2.701650
C	3.931966	-0.713466	2.345059
H	3.131886	-1.355290	2.701869
H	5.440152	-2.198700	1.597597
C	4.482812	1.149775	-2.036028
C	5.724749	0.705496	-1.522032
H	6.534090	1.343065	-1.174846
C	5.721606	-0.723633	-1.522243
H	6.528106	-1.364904	-1.175239
C	4.477759	-1.162285	-2.036518
H	4.158926	-2.195039	-2.148931
C	3.703286	-0.004527	-2.345267
H	2.693699	-0.002303	-2.740492
H	4.168621	2.183987	-2.148055

Table B27. Cartesian coordinates for optimized structure of **2** in THF (ε = 7.4257).

Ti	-0.060089	0.001964	0.003676
Cl	1.974011	1.617201	0.002492
Cl	1.968576	-1.620109	0.003247
C	-0.554457	1.159615	2.043928
C	-1.800240	0.719682	1.534812
H	-2.608538	1.360027	1.190224
C	-1.802186	-0.709335	1.535681
H	-2.612180	-1.347946	1.191875
C	-0.557612	-1.152070	2.045344
H	-0.241598	-2.185974	2.155711
C	0.222310	0.002892	2.350777
H	1.234229	0.001858	2.740360
H	-0.235565	2.192758	2.153122
C	-1.219204	-1.154725	-1.732349
C	-1.979363	0.001161	-1.386002
H	-2.970339	0.000093	-0.942341
C	-1.221403	1.158796	-1.731530
H	-1.524439	2.193675	-1.591372
C	-0.012009	0.711328	-2.336705
H	0.788127	1.354177	-2.691591
C	-0.010556	-0.704372	-2.337134
H	0.790813	-1.345365	-2.692549
H	-1.520250	-2.190310	-1.593107
Ti	4.002827	-0.004872	0.002126
C	5.159077	-1.164242	1.738446
C	5.921808	-0.010057	1.392041
H	6.912827	-0.013503	0.948481

C	5.166317	1.149259	1.737345
H	5.471508	2.183496	1.597101
C	3.955830	0.704464	2.342382
H	3.157029	1.349107	2.697013
C	3.951366	-0.711222	2.343031
H	3.148641	-1.350503	2.698475
H	5.457959	-2.200488	1.599472
C	4.504099	1.151523	-2.036670
C	5.747206	0.703118	-1.528337
H	6.559605	1.338005	-1.183328
C	5.740213	-0.725884	-1.530827
H	6.546138	-1.369928	-1.187559
C	4.492913	-1.160132	-2.041073
H	4.170316	-2.191896	-2.152379
C	3.720141	-0.000034	-2.344934
H	2.708174	0.005717	-2.734349
H	4.191781	2.186781	-2.144862

Table B28. Cartesian coordinates for optimized structure of **3** in THF (ε = 7.4257)

Ti	3.236426	3.163504	1.327748
Cl	3.076367	2.331452	-0.896046
C	5.124122	4.526354	0.715458
C	5.048238	4.504984	2.133878
C	3.826932	5.137971	2.513665
C	3.135891	5.528370	1.329513
C	3.949343	5.155508	0.219274
H	3.694858	5.285510	-0.828731
H	5.918906	4.094005	0.111480
H	5.789576	4.084337	2.809540
C	1.366995	1.796375	1.989154
C	2.514299	0.960506	1.909881
C	3.457138	1.397940	2.885882
C	2.873455	2.499075	3.578490
C	1.588542	2.755964	3.013263
H	0.493263	1.741411	1.343495
H	2.665306	0.157457	1.193884
H	4.428506	0.952949	3.088526
H	3.332027	3.046069	4.397266
H	0.900064	3.541941	3.315427
H	3.479509	5.297842	3.530459
H	2.179336	6.043674	1.283395

Table B29. Cartesian coordinates for optimized structure of **4** in THF (ε = 7.4257)

Ti	-0.128288	0.009060	-0.001814
Cl	-0.224142	-2.466467	-0.013801
C	0.388836	1.365327	1.877619
C	-0.921055	1.720416	1.467992
H	-1.229421	2.686766	1.080341
C	-1.774007	0.588299	1.665228
H	-2.837546	0.541552	1.443628
C	-0.992872	-0.453417	2.223757
H	-1.340912	-1.453811	2.460211
C	0.344240	0.008572	2.341585
H	1.183564	-0.565902	2.724994
H	1.264389	2.010164	1.860429
C	-1.310937	-0.296769	-2.059950
C	-1.709881	0.963963	-1.547643
H	-2.711262	1.232975	-1.220256
C	-0.566494	1.821755	-1.537804
H	-0.543432	2.857445	-1.210657
C	0.534603	1.089974	-2.045717
H	1.545727	1.468232	-2.174977
C	0.081492	-0.230430	-2.354606
H	0.689774	-1.043044	-2.741715
H	-1.942693	-1.173476	-2.167081
N	1.969864	-0.260933	-0.002501
N	3.084278	-0.370139	-0.003181

Table B30. Cartesian coordinates for optimized structure of **4-TS** in THF (ε = 7.4257)

Ti	-0.201294	-0.069405	-0.003129
Cl	0.192502	-2.447145	-0.045096
C	0.351237	1.333537	1.824571
C	-1.011682	1.582452	1.491765
H	-1.418285	2.520353	1.126641
C	-1.762404	0.392630	1.744307
H	-2.831075	0.262537	1.591215
C	-0.866714	-0.576343	2.269435
H	-1.118136	-1.599868	2.532028
C	0.433156	-0.006408	2.309372
H	1.339644	-0.519357	2.624523
H	1.170333	2.045514	1.755241
C	-1.183619	-0.411443	-2.170910
C	-1.781945	0.750585	-1.621069
H	-2.831870	0.869884	-1.363555
C	-0.761455	1.738564	-1.468126
H	-0.901339	2.749281	-1.096618
C	0.471429	1.179955	-1.903401
H	1.430843	1.691614	-1.933967
C	0.207134	-0.156075	-2.335252
H	0.942928	-0.867781	-2.700592
H	-1.685745	-1.353236	-2.376229
N	2.738771	-0.123880	-0.004404
N	3.779133	0.252743	0.030509

Table B31. Cartesian coordinates for optimized structure of **5** in THF (ε = 7.4257)

Ti	-0.962049	-0.924424	-0.030001
Cl	-0.808202	1.575294	-0.151516
C	-2.494661	-0.528298	1.741408
C	-2.683670	-1.877574	1.343749
H	-3.581009	-2.283311	0.884654
C	-1.494028	-2.607994	1.650598
H	-1.320573	-3.663499	1.453311
C	-0.583981	-1.711059	2.263193
H	0.420216	-1.955916	2.601582
C	-1.185567	-0.425095	2.306183
H	-0.727628	0.485309	2.681438
H	-3.210443	0.281931	1.633026
C	-0.606873	-2.521320	-1.762501

C	-1.999927	-2.512646	-1.472741
H	-2.563380	-3.340698	-1.052536
C	-2.528950	-1.238550	-1.844315
H	-3.561228	-0.913732	-1.736156
C	-1.465570	-0.476512	-2.394802
H	-1.531744	0.552640	-2.733282
C	-0.282292	-1.253056	-2.335968
H	0.707492	-0.921563	-2.640448
H	0.070418	-3.359045	-1.616641
O	1.290855	-0.833518	0.168412
C	2.124868	-2.039854	0.072822
H	2.267298	-2.262348	-0.996196
H	1.582018	-2.870626	0.544649
C	3.443986	-1.692783	0.763931
H	3.394167	-1.930341	1.837645
H	4.288861	-2.243457	0.328733
C	3.536450	-0.171608	0.555945
H	4.205681	0.320266	1.274997
H	3.886639	0.062651	-0.461170
C	2.088364	0.264384	0.737940
H	1.799530	1.177749	0.207703
H	1.823395	0.367554	1.803677

Table B32. Cartesian coordinates for optimized structure of **3’** in Pyr_4FAP ($\varepsilon = 14.7$)

Ti	-2.395846	0.628893	0.128457
Cl	-3.822993	-0.009409	-1.660102
C	-1.064084	-0.951212	1.296551
C	-1.671941	-0.087648	2.255757
H	-1.150790	0.599617	2.914961
C	-3.085184	-0.270909	2.194776
H	-3.826238	0.243513	2.801041
C	-3.342316	-1.276157	1.218382
H	-4.322788	-1.621687	0.903584
C	-2.101340	-1.692140	0.666822
H	-1.973171	-2.407750	-0.141723
H	0.000054	-1.031473	1.089218
C	-2.806703	2.967154	-0.130356
C	-2.026100	2.807664	1.044346
H	-2.344215	3.033655	2.059063
C	-0.760603	2.273340	0.662109
H	0.059126	2.031711	1.332515
C	-0.761877	2.083394	-0.747904
H	0.058533	1.691006	-1.343398
C	-2.029239	2.521643	-1.236862
H	-2.360815	2.482627	-2.269657
H	-3.832634	3.325237	-0.172303

Table B33. Cartesian coordinates for optimized structure of **4’** in Pyr_4FAP ($\varepsilon = 14.7$)

Ti	-2.276347	0.542388	0.005037
Cl	-4.454781	0.332485	-1.137838
C	-1.071977	-1.135111	1.140593
C	-1.452247	-0.171595	2.108757
H	-0.779969	0.461764	2.678416
C	-2.879706	-0.174202	2.207675
H	-3.478025	0.464065	2.852539
C	-3.373556	-1.168627	1.327133
H	-4.418752	-1.393796	1.144590
C	-2.271344	-1.753564	0.653822
H	-2.328961	-2.533591	-0.100282
H	-0.056735	-1.371156	0.832384
C	-2.832730	2.851002	-0.124272
C	-1.995456	2.696187	1.009226
H	-2.284360	2.859156	2.044113
C	-0.707286	2.274932	0.555979
H	0.156796	2.067461	1.179948
C	-0.751018	2.173420	-0.855166
H	0.074132	1.878363	-1.497742
C	-2.072659	2.512085	-1.281004
H	-2.438343	2.500696	-2.303387
H	-3.882074	3.128251	-0.111394
N	-1.488054	-0.403480	-1.695535
N	-1.033804	-0.902710	-2.589210

Table B34. Cartesian coordinates for optimized structure of **4’-TS** in Pyr_4FAP ($\varepsilon = 14.7$)

Ti	-2.454556	0.650868	0.168002
Cl	-4.465280	0.330340	-1.081791
C	-1.115238	-1.127818	0.951748
C	-1.331623	-0.239510	2.044398
H	-0.567521	0.325911	2.566499
C	-2.726394	-0.232251	2.350861
H	-3.209218	0.350866	3.130702
C	-3.362179	-1.150528	1.472257
H	-4.428783	-1.347691	1.420652
C	-2.377421	-1.694087	0.606532
H	-2.566162	-2.386542	-0.210053
H	-0.158709	-1.349822	0.485978
C	-2.869383	2.983137	-0.200060
C	-2.147762	2.856757	1.015448
H	-2.507283	3.122402	2.006315
C	-0.860416	2.323485	0.702286
H	-0.057871	2.139217	1.408409
C	-0.799856	2.089807	-0.699928
H	0.053126	1.698459	-1.247269
C	-2.047991	2.501839	-1.255473
H	-2.341415	2.416478	-2.298318
H	-3.897755	3.319303	-0.299186
N	-1.343094	-0.615749	-2.295278
N	-0.514474	-1.230449	-2.698346

Table B35. Cartesian coordinates for optimized structure of **3’-FAP** in Pyr_4FAP ($\varepsilon = 14.7$)

Ti	-2.357521	0.615502	0.112759
Cl	-3.768099	-0.038096	-1.690681
C	-1.068534	-0.991645	1.277411
C	-1.636061	-0.100751	2.235591
H	-1.083525	0.575018	2.880603
C	-3.056029	-0.241901	2.197327
H	-3.772697	0.302406	2.806976
C	-3.358374	-1.248645	1.237470
H	-4.354024	-1.564901	0.939184

C	-2.138965	-1.705627	0.671014
H	-2.044640	-2.430748	-0.133675
H	-0.011830	-1.103070	1.055557
C	-2.831399	2.937647	-0.136450
C	-2.061972	2.796647	1.047900
H	-2.401445	3.005733	2.059376
C	-0.775451	2.303017	0.681524
H	0.044292	2.081140	1.357052
C	-0.750086	2.123637	-0.728246
H	0.093429	1.759945	-1.307624
C	-2.023448	2.521937	-1.234003
H	-2.338040	2.478290	-2.271975
H	-3.866748	3.265535	-0.191814
P	4.244038	0.106932	0.252257
C	4.591050	3.012433	-0.721365
F	4.957695	-1.318352	0.795712
C	3.102651	-1.832962	-1.857121
C	3.572637	1.819337	-0.561848
F	5.508943	0.974141	0.963529
C	3.233252	0.214645	2.013757
C	2.780480	-1.019774	-0.553432
F	4.940474	3.560389	0.458821
F	5.709469	2.645746	-1.379740
F	3.990375	3.996070	-1.455551
F	2.494607	2.355498	0.103407
F	3.155640	1.565751	-1.851243
F	2.396093	-1.974532	0.366091
F	1.645701	-0.293760	-0.843235
F	4.174710	-2.636156	-1.692180
F	3.309546	-1.034768	-2.922689
F	2.035620	-2.632346	-2.153766
C	3.656626	1.276077	3.089939
F	1.887378	0.426204	1.790608
F	3.327680	-0.979583	2.691012
F	4.881365	1.008529	3.590846
F	3.644169	2.535396	2.611834
F	2.774446	1.229838	4.131070
F	5.160624	-0.047786	-1.162043

Table B36. Cartesian coordinates for optimized structure of **4'-FAP** in Pyr$_4$FAP (ε = 14.7)

Ti	-2.269084	0.540431	0.007720
Cl	-4.457544	0.319764	-1.133293
C	-1.070389	-1.158293	1.117181
C	-1.414673	-0.191074	2.094234
H	-0.717855	0.426083	2.651131
C	-2.839841	-0.168918	2.221950
H	-3.413798	0.476734	2.881518
C	-3.368916	-1.150032	1.347444
H	-4.421504	-1.354534	1.183711
C	-2.289718	-1.751287	0.649692
H	-2.375516	-2.525627	-0.107704
H	-0.065433	-1.403487	0.787370
C	-2.846686	2.843774	-0.155196
C	-2.040307	2.705323	1.002133
H	-2.358755	2.874686	2.027371
C	-0.736652	2.291317	0.588275
H	0.113798	2.096461	1.232115
C	-0.740045	2.174434	-0.821728
H	0.107657	1.878870	-1.432787
C	-2.052685	2.498940	-1.287194
H	-2.390522	2.476117	-2.319089
H	-3.898637	3.110365	-0.174251
N	-1.492959	-0.392831	-1.704389
N	-1.057194	-0.882794	-2.611830
P	4.249164	0.123857	0.295222
C	4.605036	3.032292	-0.666697
F	4.953036	-1.295347	0.865291
C	3.201257	-1.827007	-1.850729
C	3.593182	1.829230	-0.546309
F	5.479091	1.001959	1.052209
C	3.171751	0.224290	2.017021
C	2.825084	-1.014344	-0.561405
F	4.904483	3.582859	0.525875
F	5.750713	2.676078	-1.282332
F	4.023101	4.010408	-1.422948
F	2.483929	2.355381	0.075552
F	3.228943	1.571047	-1.850429
F	2.414761	-1.971957	0.344478
F	1.697281	-0.295842	-0.892012
F	4.276206	-2.616878	-1.645680
F	3.436004	-1.028766	-2.910329
F	2.155278	-2.640037	-2.181967
C	3.533260	1.297874	3.103651
F	1.831972	0.411101	1.739321
F	3.259841	-0.964581	2.703746
F	4.740958	1.054011	3.654862
F	3.518433	2.554576	2.618838
F	2.610453	1.240998	4.108477
F	5.217986	-0.023212	-1.084362

Table B37. Cartesian coordinates for optimized structure of **4'-FAP-TS** in Pyr$_4$FAP (ε = 14.7)

Ti	-2.404656	0.605220	0.177369
Cl	-4.335731	0.235215	-1.198850
C	-1.126231	-1.164531	1.053696
C	-1.366998	-0.247442	2.116770
H	-0.610754	0.319452	2.647650
C	-2.771209	-0.213458	2.374819
H	-3.271773	0.397331	3.121751
C	-3.391525	-1.141696	1.496552
H	-4.459044	-1.322950	1.411592
C	-2.385140	-1.719078	0.678079
H	-2.555774	-2.418741	-0.136059
H	-0.158637	-1.403205	0.622615
C	-2.856892	2.928588	-0.189405
C	-2.160503	2.817664	1.041145
H	-2.548934	3.073996	2.023576
C	-0.856937	2.306780	0.759441
H	-0.066690	2.131309	1.480442
C	-0.757698	2.075397	-0.639805
H	0.119615	1.702226	-1.158472
C	-2.000872	2.461860	-1.225354
H	-2.266750	2.378636	-2.275617

H	-3.888625	3.246219	-0.313006	F	2.484911	2.348008	0.022221
N	-1.280809	-0.693809	-2.219399	F	3.251939	1.539676	-1.885324
N	-0.708858	-0.526281	-3.152527	F	2.418215	-1.977525	0.344067
P	4.249463	0.121353	0.289707	F	1.710537	-0.318294	-0.920208
C	4.613894	3.017246	-0.705541	F	4.296246	-2.648057	-1.618114
F	4.947628	-1.289920	0.886596	F	3.475708	-1.071825	-2.909920
C	3.226339	-1.857281	-1.844359	F	2.181325	-2.670809	-2.179262
C	3.601133	1.815348	-0.580434	C	3.502641	1.330436	3.074219
F	5.470970	1.009915	1.048330	F	1.817115	0.429641	1.699429
C	3.151960	0.244267	1.996520	F	3.230287	-0.936146	2.699673
C	2.836653	-1.030501	-0.568086	F	4.702900	1.090352	3.643468
F	4.898998	3.585003	0.482589	F	3.497052	2.581258	2.574496
F	5.767164	2.653042	-1.302169	F	2.567340	1.287846	4.068264
F	4.040930	3.984323	-1.482515	F	5.234021	-0.043649	-1.076919

B.6 References

1. R. Jungst, D. Sekutowski, J. Davis, M. Luly and G. Stucky, *Inorg. Chem.*, **1977**, *16*, 1645.

2. C. Wolff, A. Gottschlich, J. England, K. Wieghardt, W. Saak, D. Haase, and R. Beckhaus, *Inorg. Chem.*, **2015**, *54*, 481.

Appendix C: Supporting information in Chapter 4

C.1 Design of apparatus

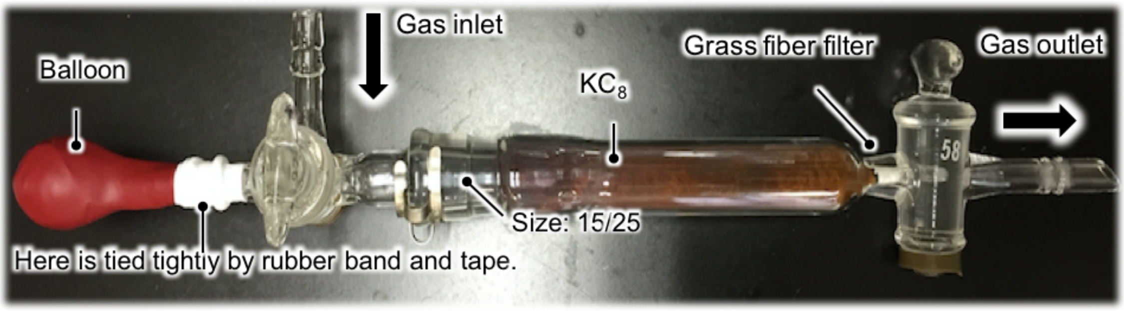

Figure C1. The picture of a gas purification column for $^{15}N_2$.

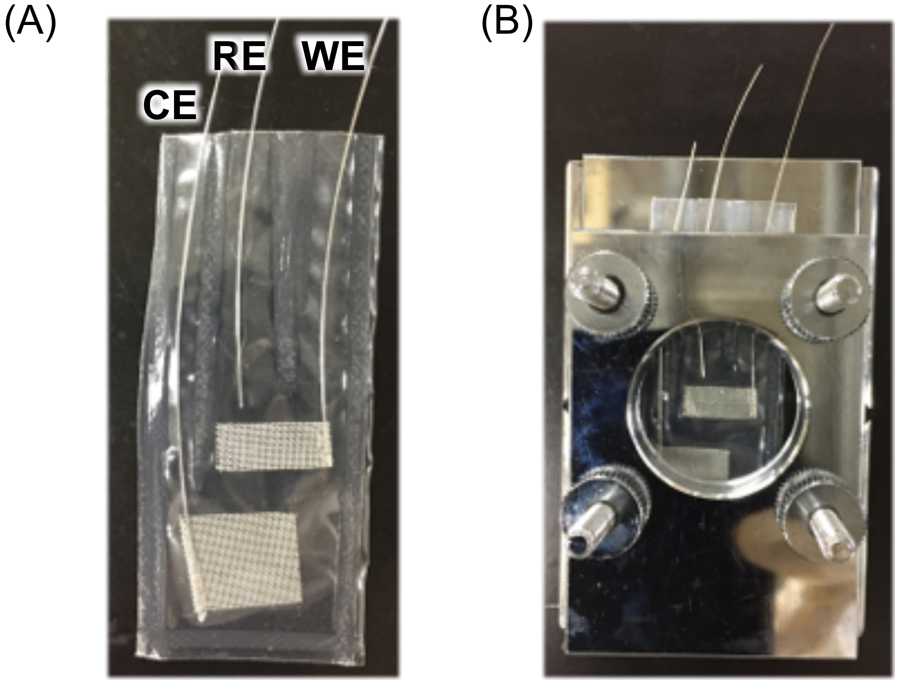

Figure C2. (A) Picture of a FT-IR film cell; WE and CE are Pt mesh (0.8 cm × 0.6 cm) connected to Pt wire and Cu wire and RE is Pt wire and Cu electrode. The film of FT-IR cell is made from nylon and PE (thickness: 75 μm), and the film is packed by laminating machine after setting electrodes and addition of sample solution. The thickness of FT-IR film cell is < 0.5 mm. The nylon film is transparent for the infrared light in the range of 1700 ~ 2200 cm^{-1}. (B) A picture of the FT-IR film cell and cell holder.

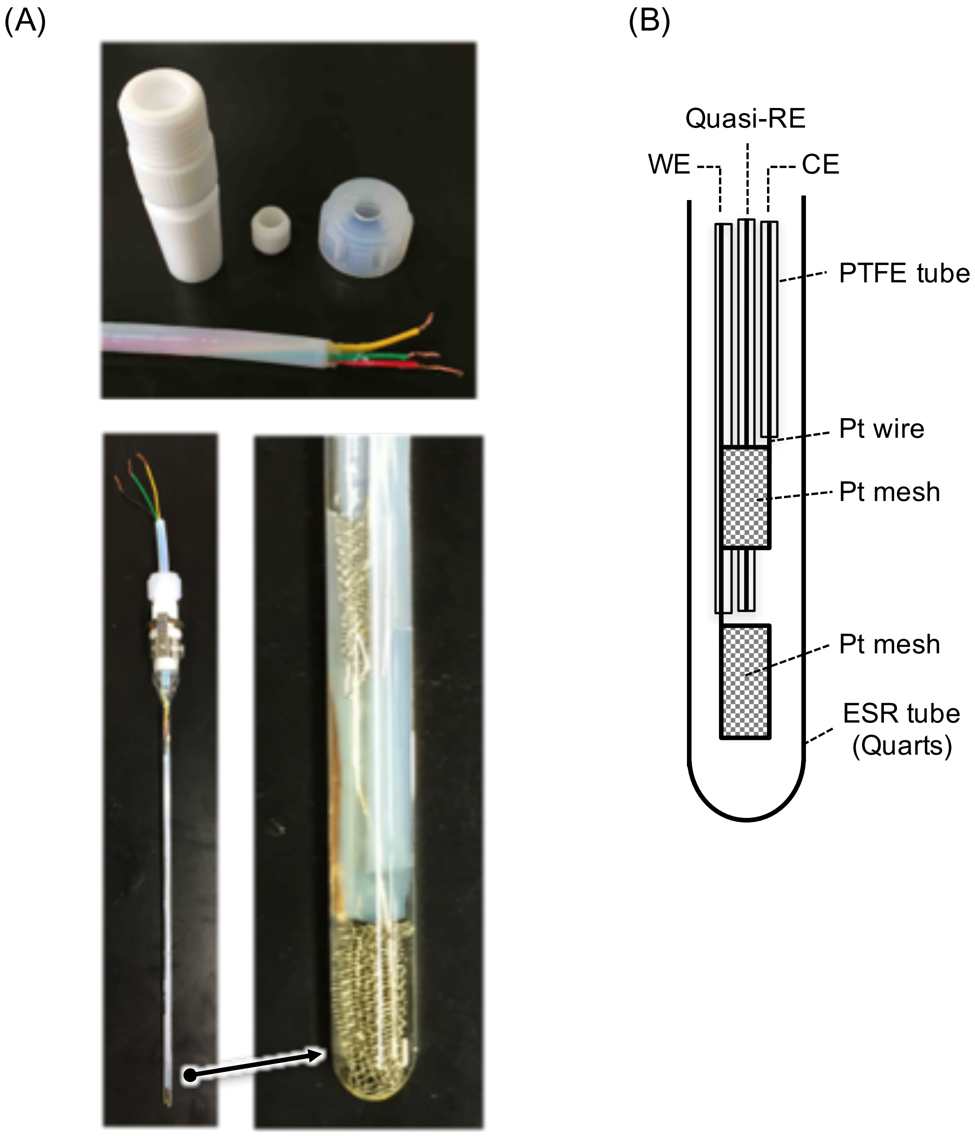

Figure C3. (A) Pictures and (B) drawing of resonance Raman cell made of quarts (diameter: 4 mm) (downside parts) and pyrex glass (upper parts). (WE: Pt mesh (0.2 cm × 0.4 cm) connected by Pt wire, CE: Pt mesh (0.2 cm × 0.4 cm) connected by Pt wire and quasi-RE: Pt wire. Each Pt wire is covered with PTFE tube for preventing to contact each other.

C.2. Cyclic voltammogram of *trans*–[Mo(depe)$_2$(^{15}N$_2$)$_2$]

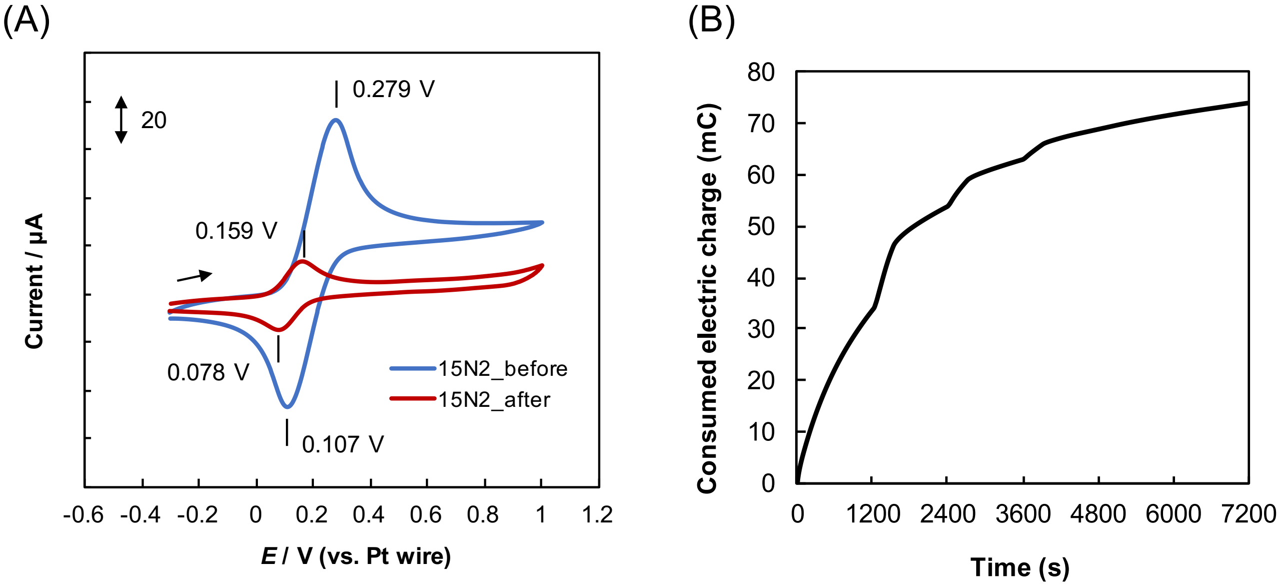

Figure C4. (A) Cyclic voltammogram of 2 mM *trans*–[Mo(depe)$_2$(^{15}N$_2$)$_2$] in 0.2 M Pyr$_4$FAP/THF before (blue) and after (red) CPE at 0.5 V (vs. Pt wire) (WE: Pt mesh, CE: Pt coil, quasi-RE: Pt wire, cell: handmade Raman cell (diameter: 4 mm), scan rate: 10 mV/s), as shown in Figure S3, and (B) the plots of consumed electric charge (mC) against time (s) in CPE at +0.5 V (vs. Pt wire). The resonance Raman spectroscopy was performed under ^{14}N$_2$ by an excitation wavelength at 355 nm. The excitation laser was irradiated at 0, 20, 40, 60, and 120 min when the CPE started (exposure times: 30 (s) and accumulation times: 10). Amount of solution: 0.5 mL.

C.3 Evaluation of the appropriate functional for DFT calculation

To determine the appropriate functional for the calculations, we performed geometry optimization and frequency calculations using the B3LYP and B3LYP* functionals for complex **1**. The obtained $\nu(N_2)$ (cm^{-1}) and N–N and Mo–N and Mo–P bond distances (Å) for *trans*-[Mo(depe)$_2$(N$_2$)$_2$] (**1**) are summarized in Table C1. The reported $\nu(N_2)$ (cm^{-1}) and N–N and Mo–N and Mo–P bond distances (Å) are 1928 cm^{-1} in KBr,[1] N-N = 1.117 Å, Mo-N = 2.030 Å and Mo-P = 2.453, 2.444 Å, respectively.[2] We decided to adopt B3LYP* as hybrid functional and as the basis set, SDD on the Mo atom, 6-311G(d) on N and P atoms, and 6-31G(d) on C and H atoms, because they are the closest to the reported values.[1,2]

Table C1. Comparison of functionals and basis sets against $\nu(N_2)$, N–N and Mo–N bond distances for *trans*-[Mo(depe)$_2$(N$_2$)$_2$] (**1**) under vacuum condition for DFT calculations

Hybrid Functional	**Basis Set**	**$\nu(N_2)$ /cm^{-1}**	**N-N /Å**	**Mo-N /Å**	**Mo-P /Å**
B3LYP	Mo: LanL2DZ N, P, C, H: 6-31G(d)	2118	1.1230 1.1230	2.0193 2.0193	2.4431 2.4354 2.4431 2.4354
B3LYP*	Mo: LanL2DZ N, P, C, H: 6-31G(d)	2089	1.1392 1.1392	2.0349 2.0349	2.4864 2.4955 2.4864 2.4955
B3LYP	Mo: LanL2DZ N: 6-311G(d) P, C, H: 6-31G(d)	2103	1.1263 1.1264	2.0439 2.0439	2.4914 2.4994 2.4914 2.4994
B3LYP	Mo: LanL2DZ N, P: 6-311G(d) C, H: 6-31G(d)	2104	1.1262 1.1262	2.0428 2.0428	2.4932 2.5024 2.4931 2.5024
B3LYP	Mo: SDD N, P, C, H: 6-31G(d)	2099	1.1370 1.1370	2.0278 2.0278	2.4868 2.4947 2.4868 2.4947
B3LYP*	Mo: SDD N, P: 6-311G(d) C, H: 6-31G(d)	2060	1.1321 1.1321	2.0285 2.0285	2.4830 2.4913 2.4830 2.4913

C.4 DFT and TD-DFT calculations of Mo complexes in THF

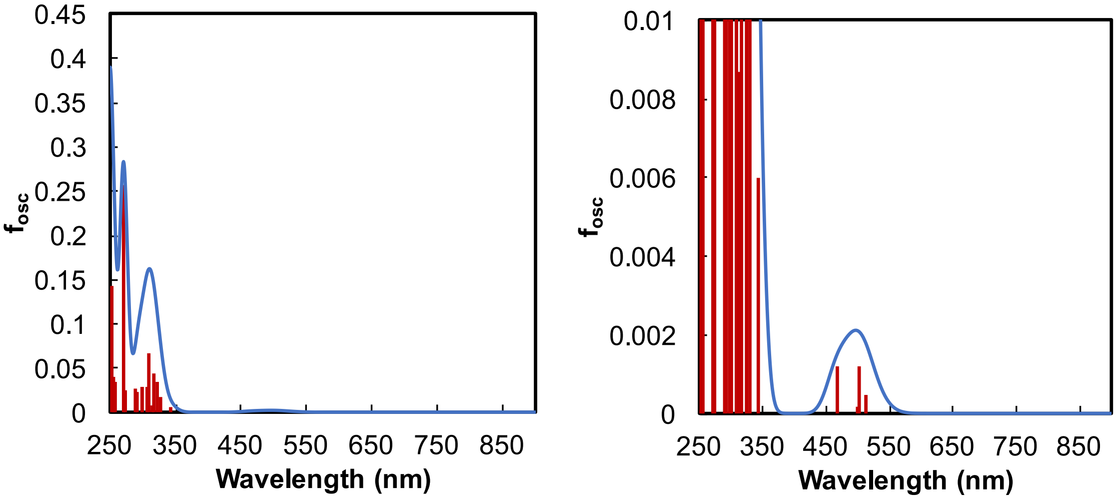

Figure C5. Absorption spectra of complex **1** calculated by TD-DFT.

Table C2. Calculated transitions of complex **1**

Excited State	Energy (eV)	Wavelength (nm)	f_{osc}	Transition	%
2	2.4760	500.75	0.0012	134 →136 135 →136 135 →137	47.4 43.1 7.8
4	2.6481	468.2	0.0012	133 →136 134 →137	46.8 52.1
11	3.8409	322.8	0.034	135→140	83.0
13	3.9185	316.41	0.0439	134→140 135→141	13.6 54.9
16	4.0115	309.08	0.0664	133→136 133→139 133→140 133→141 134→137 134→140 134→141 135→141	7.7 8.4 3.2 2.8 6.2 13.1 48.8 6.6
28	4.5878	270.25	0.2564	133→136 134→137	21.1 19.7

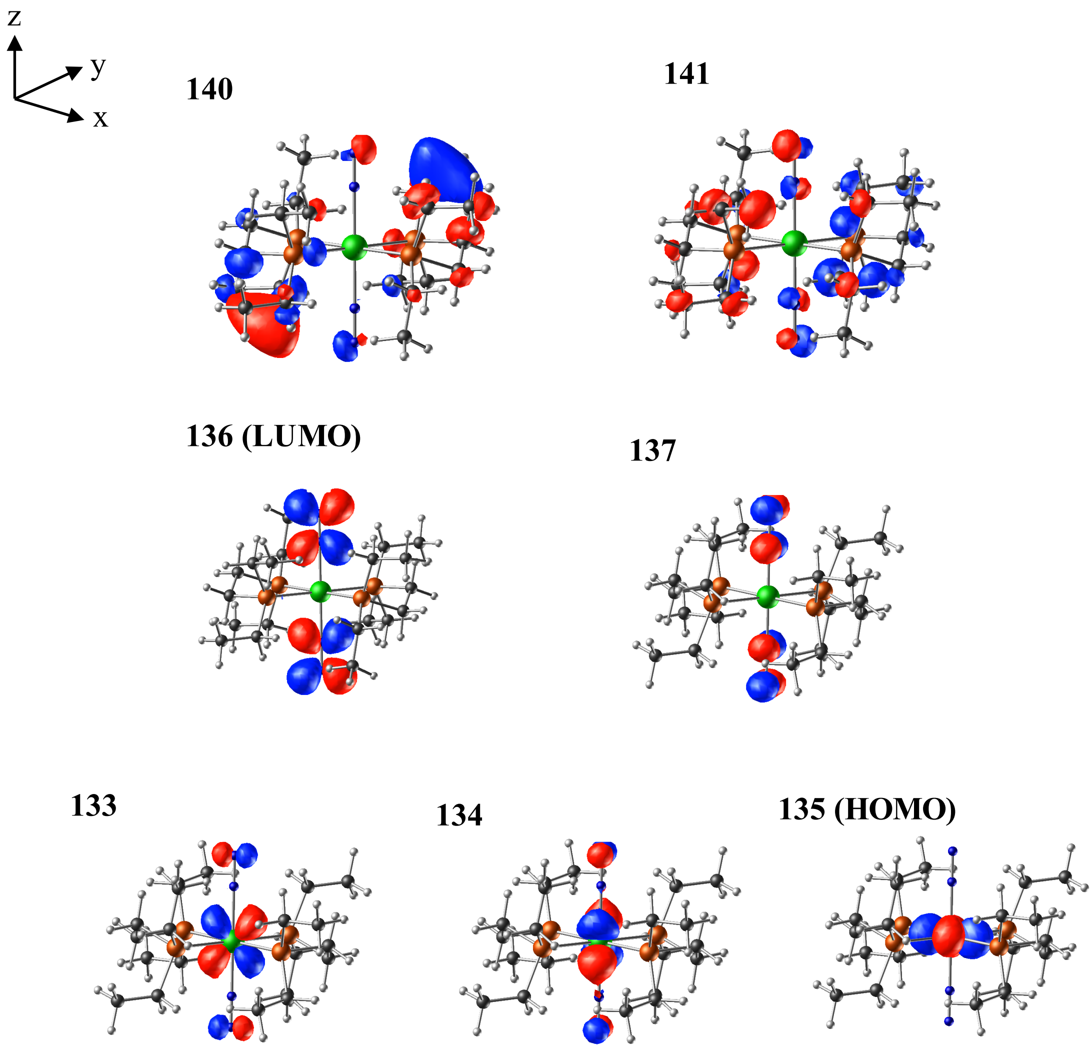

Figure C6. Molecular orbitals for model complex **1** (Isosurface values: ±0.07 (133, 134, 135, 136, and 137), ±0.04 (140 and 141)).

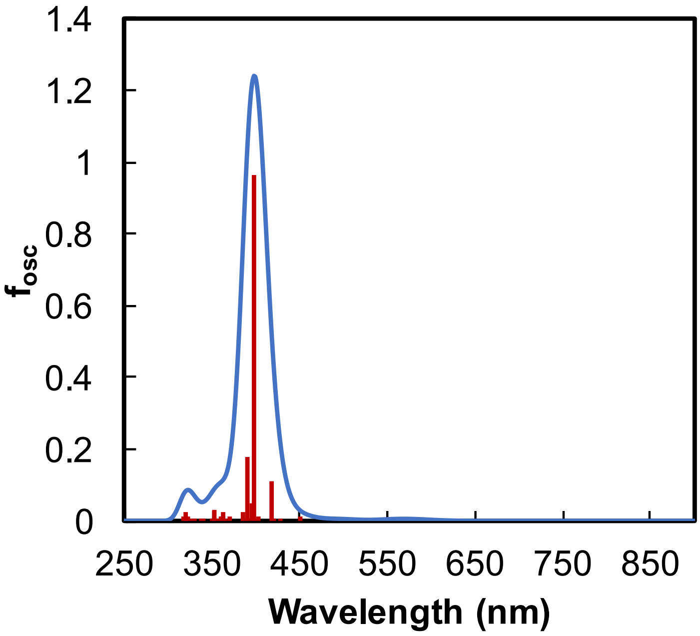

Figure C7. Absorption spectra of complex **2** calculated by TD-DFT.

Table C3. Calculated transitions of complex **2**

Excited State	Energy (eV)	Wavelength (nm)	fosc	Transition	%
12	2.9768	416.51	0.113	258→265	73.6
14	3.1139	398.17	0.9651	262→264 263→265	35.2 28.7
16	3.1763	390.35	0.1784	259→264 263→269 263→270	15.6 52.1 11.6

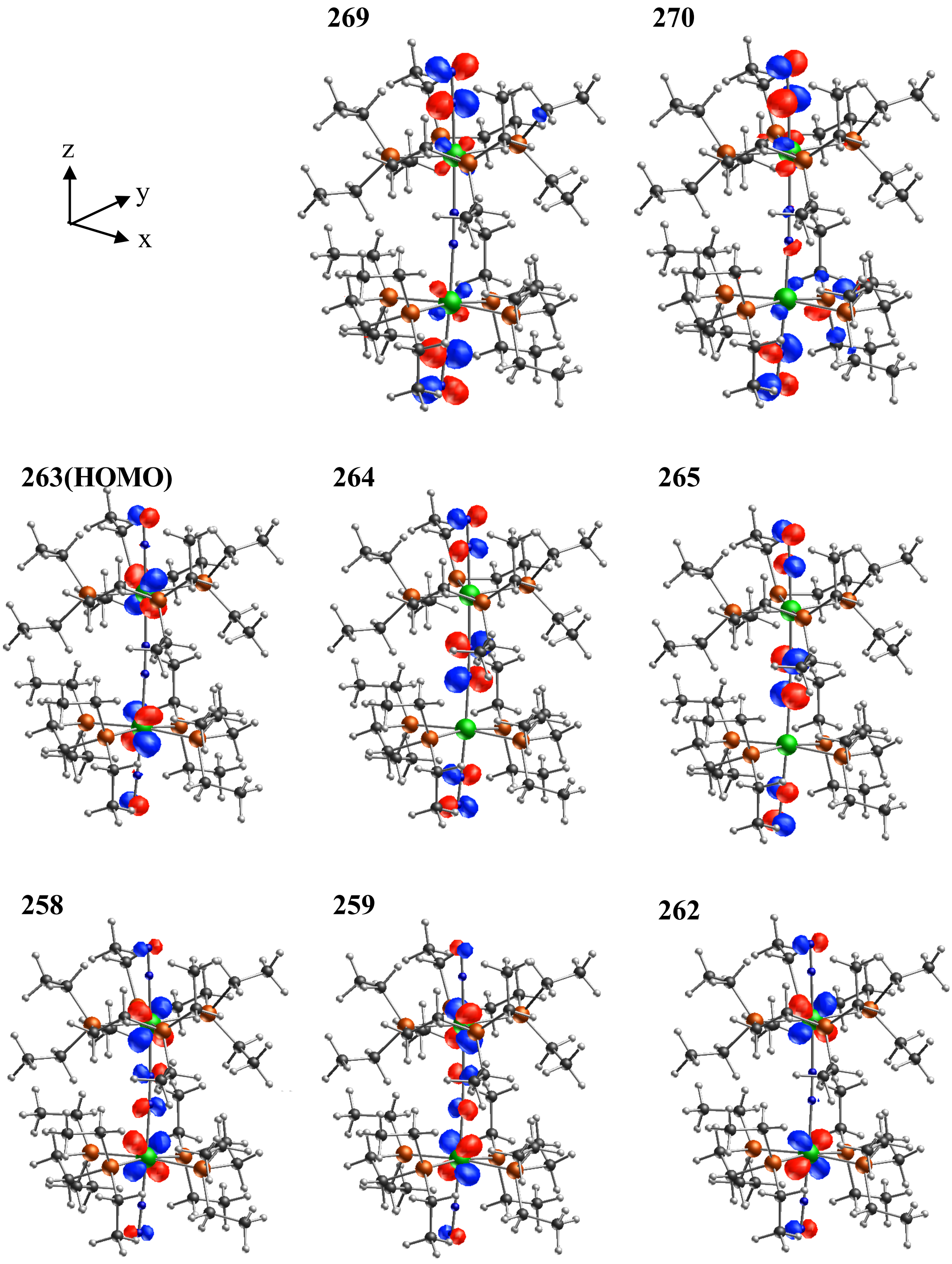

Figure C8. Molecular orbitals for model complex **2** (Isosurface values: ±0.07 (258, 259, 262, 263, 264 and 265), ±0.04 (269 and 270)).

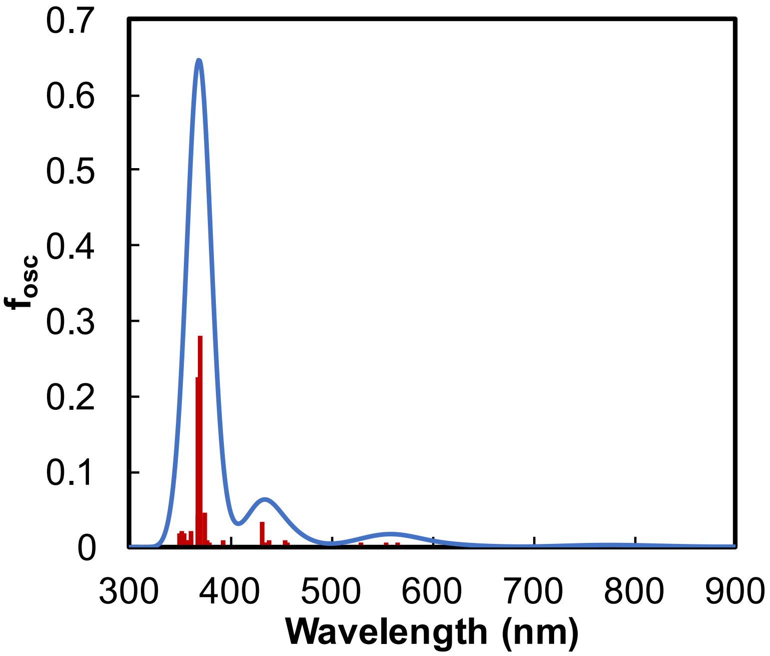

Figure C9. Absorption spectra of complex **3** calculated by TD-DFT.

Table C4. Calculated transitions of complex **3**

Excited State	Energy (eV)	Wavelength (nm)	fosc	Transition	%
27	2.8757	431.14	0.0343	248 → 256 248 → 257 249 → 258 249 → 260	11.0 16.2 57.5 2.5
39	3.3406	371.15	0.2805	245 → 253 248 → 259 248 → 260 249 → 261	16.9 6.3 15.8 20.9
41	3.3746	367.4	0.2264	244 → 252 245 → 253 248 → 259 248 → 260 249 → 261	11.6 4.3 5.4 9.9 15.4

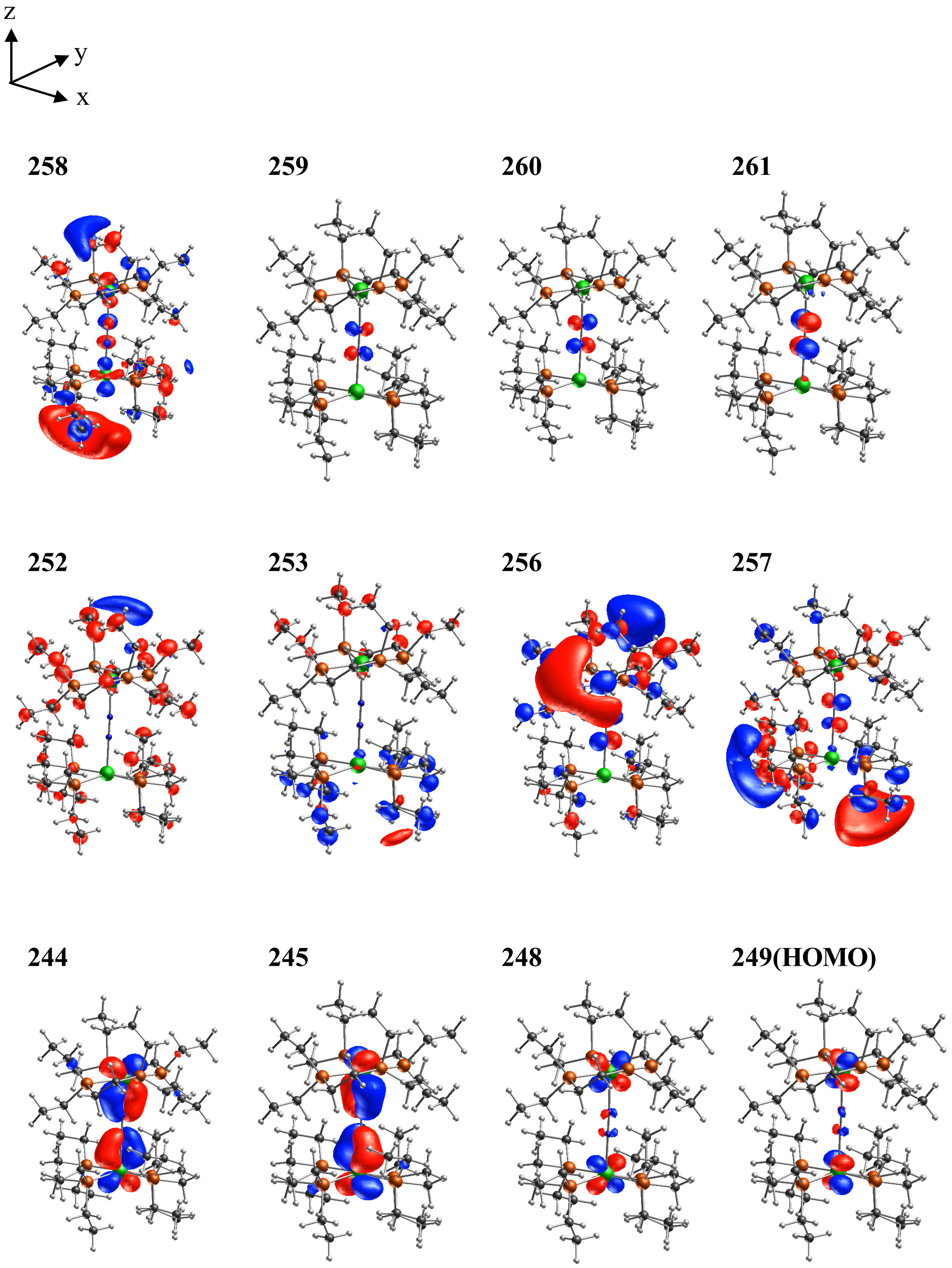

Figure C10. Molecular orbitals for model complex **3** (Isosurface values: ±0.07 (248, 249, 259, 260 and 261), ±0.04 (244 and 245)), ±0.02(252, 253, 256, 257 and 258).

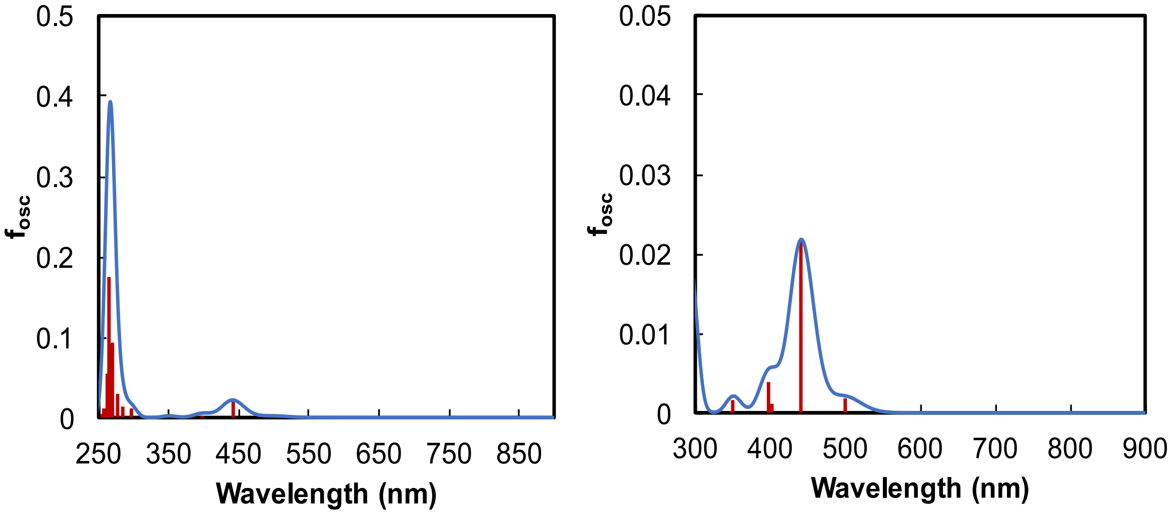

Figure C11. Absorption spectra of complex **4** calculated by TD-DFT.

Table C5. Calculated transitions of complex **4**

Excited State	Energy (eV)	Wavelength (nm)	f_{osc}	Transition	%
7	2.8099	441.24	0.0216	132B →135B	98.7
9	3.0829	402.16	0.0013	134A → 136A 135A → 137A	44.5 40.7
10	3.1149	398.03	0.0039	131B → 135B	98.7
36	4.5787	270.78	0.0938	134B →142B	67.8
37	4.6334	267.59	0.0916	134A →140A 133B →139B	71.0 8.4
39	4.6660	265.72	0.1748	134A →136A 134A →140A 135A →137A 133B →136B 134B →137B 134B →142B 134B →144B	8.9 13.1 8.4 8.1 7.0 24.3 14.7

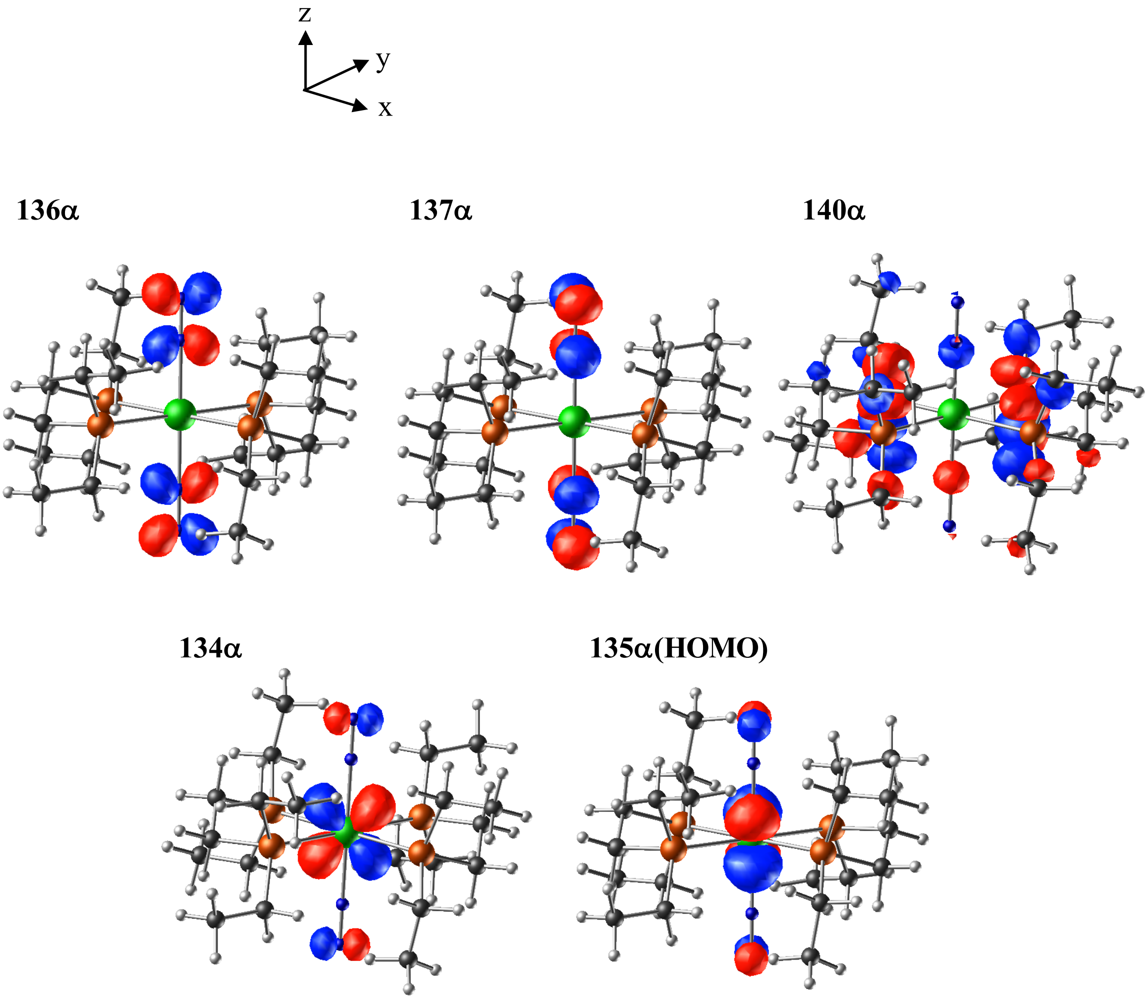

Figure C12. (A) Molecular orbitals for model complex **4** (Isosurface values: ±0.07 (134α, 135α, 136α, 137α and 140α), ±0.04 (140α)).

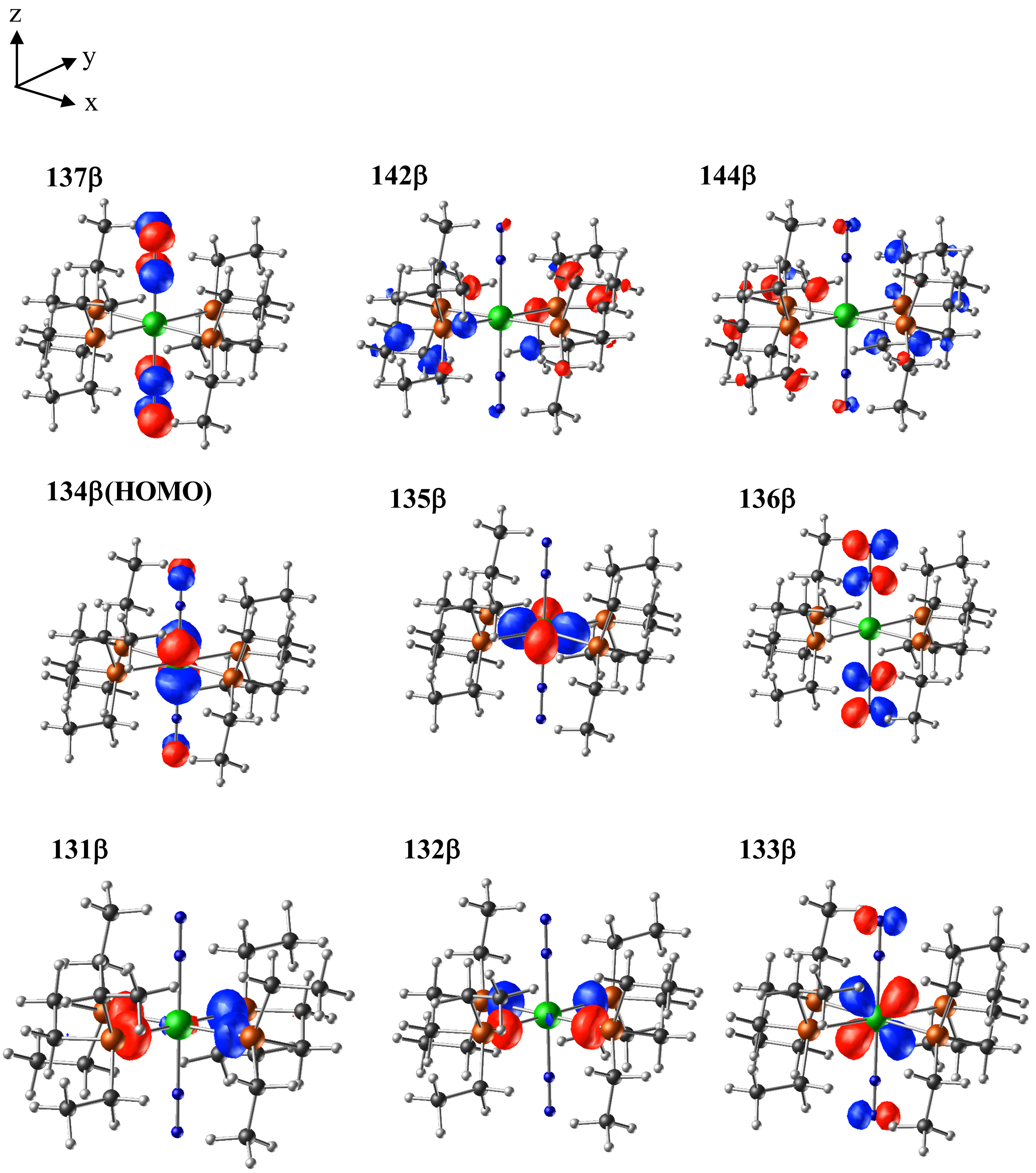

Figure C12. (B) Molecular orbitals for model complex **4** (Isosurface values: ±0.07 (1322, 133β, 134β, 135β, 136β, and 137β), ±0.03 (142β and 144β)).

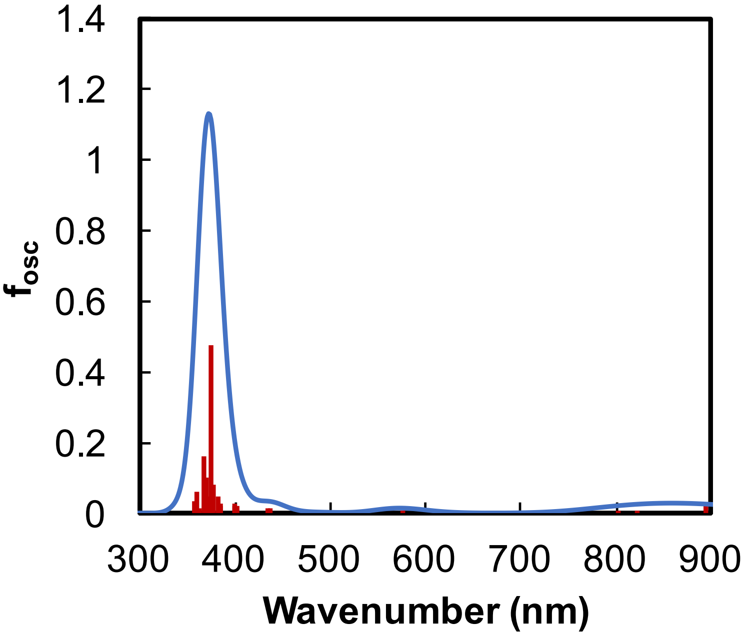

Figure C13. Absorption spectra of complex **5** in the triplet state calculated by TD-DFT.

Table C6. Calculated transitions of complex **5** in the triplet state

Excited State	Energy (eV)	Wavelength (nm)	f_{osc}	Transition	%
32	3.3126	374.28	0.4779	258A → 264A	6.7
				260A → 264A	13.4
				261A → 264A	7.3
				262A → 264A	7.3
				263A → 265A	6.5
				256B → 262B	3.5
				256B → 263B	11.7
				260B → 264B	6.2
				261B → 265B	4.9

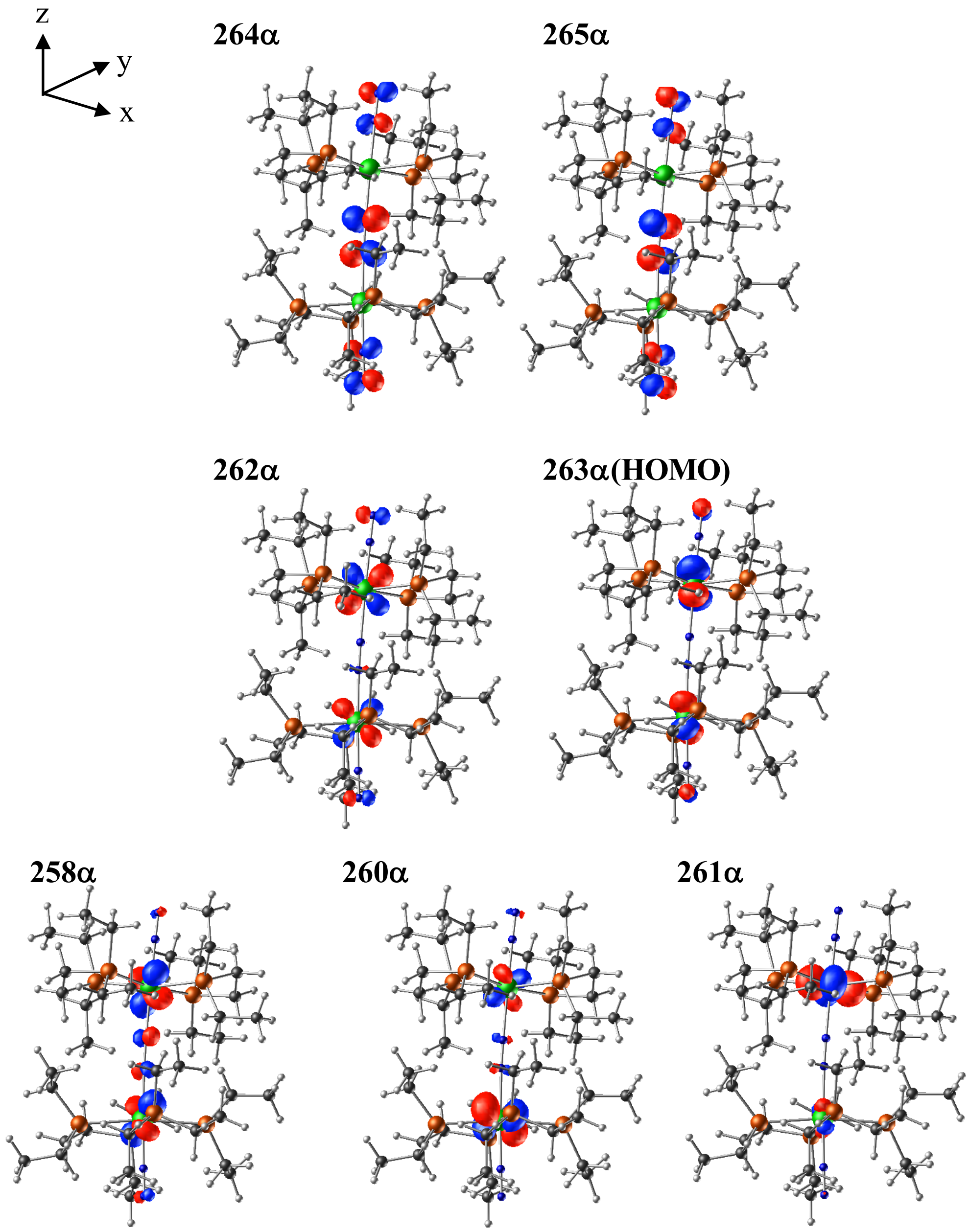

Figure C14. (A) Molecular orbitals for model complex **5** in the triplet state (Isosurface values: ±0.07 (258α, 260α, 261α, 262α, 263α, 264α and 265α).

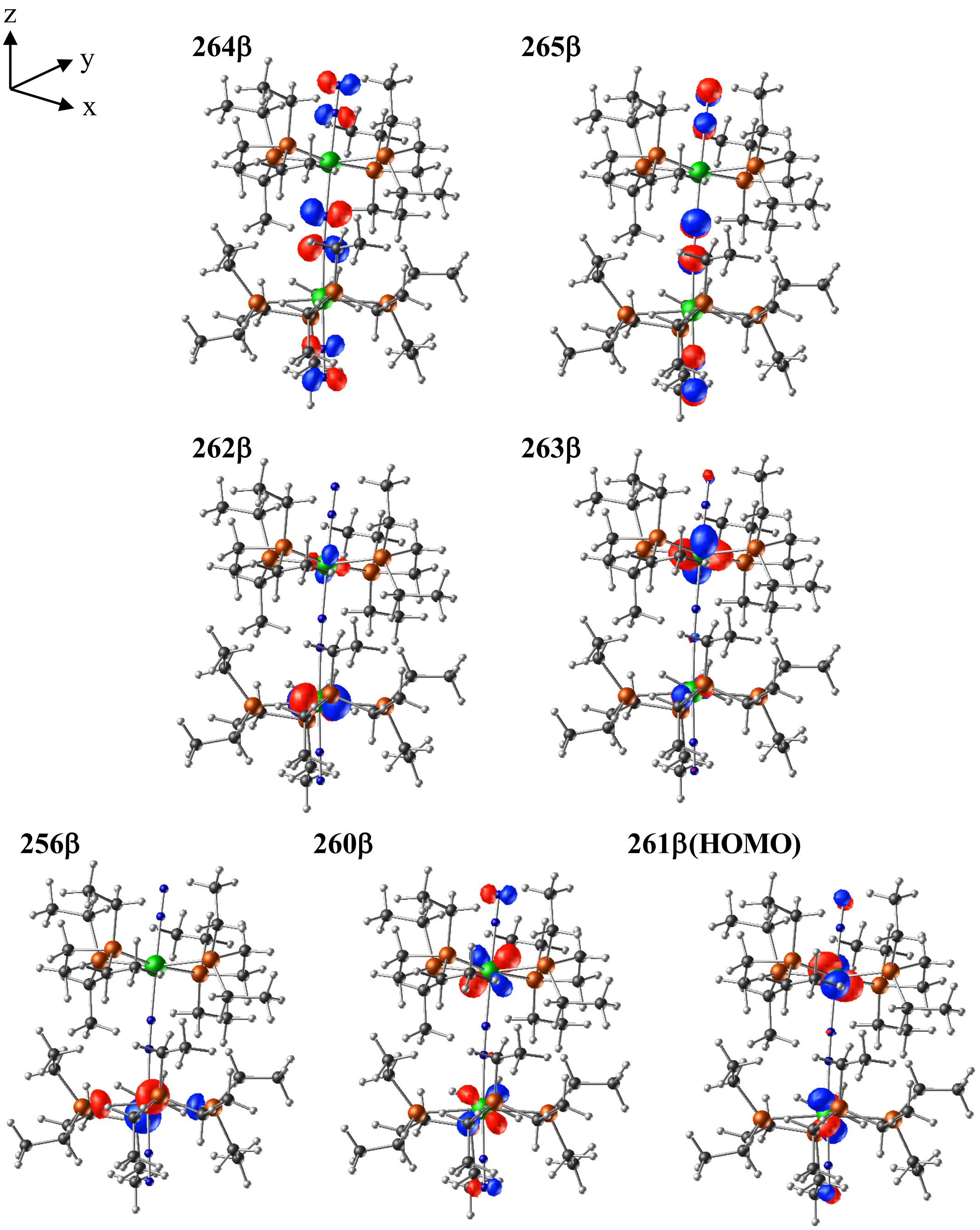

Figure C14. (B) Molecular orbitals for model complex **5** in the triplet state (Isosurface values: ±0.07 (256β, 260β, 261β, 262β, 263β, 264β and 265β).

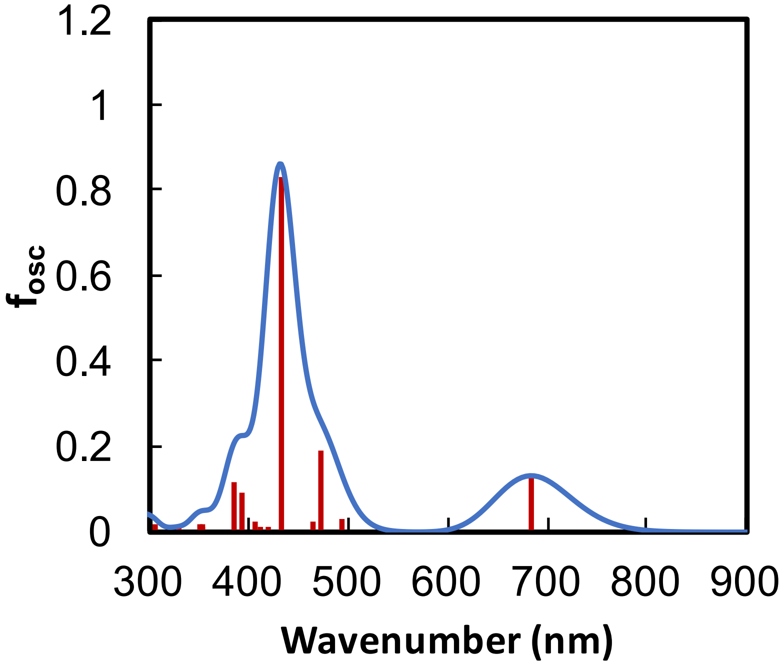

Figure C15. Absorption spectra of complex **5** in the singlet state calculated by TD-DFT.

Table C7. Calculated transitions of complex **5** in the singlet state

Excited State	Energy (eV)	Wavelength (nm)	fosc	Transition	%
5	1.8105	684.79	0.1316	259 → 263 262 → 264	79.7 18.8
11	2.6194	473.33	0.1878	256 → 263 257 → 263 259 → 263 260 → 265 262 → 264	48.4 29.0 3.1 2.5 15.6
13	2.8659	432.62	0.8324	254 → 263 255 → 263 256 → 263 257 → 263 259 → 263 262 → 264	8.6 4.1 5.5 15.0 12.7 48.8
18	3.2082	386.45	0.1171	254 → 263 258 → 264 259 → 265 262 → 264 262 → 266	32.1 9.8 35.6 4.4 9.9

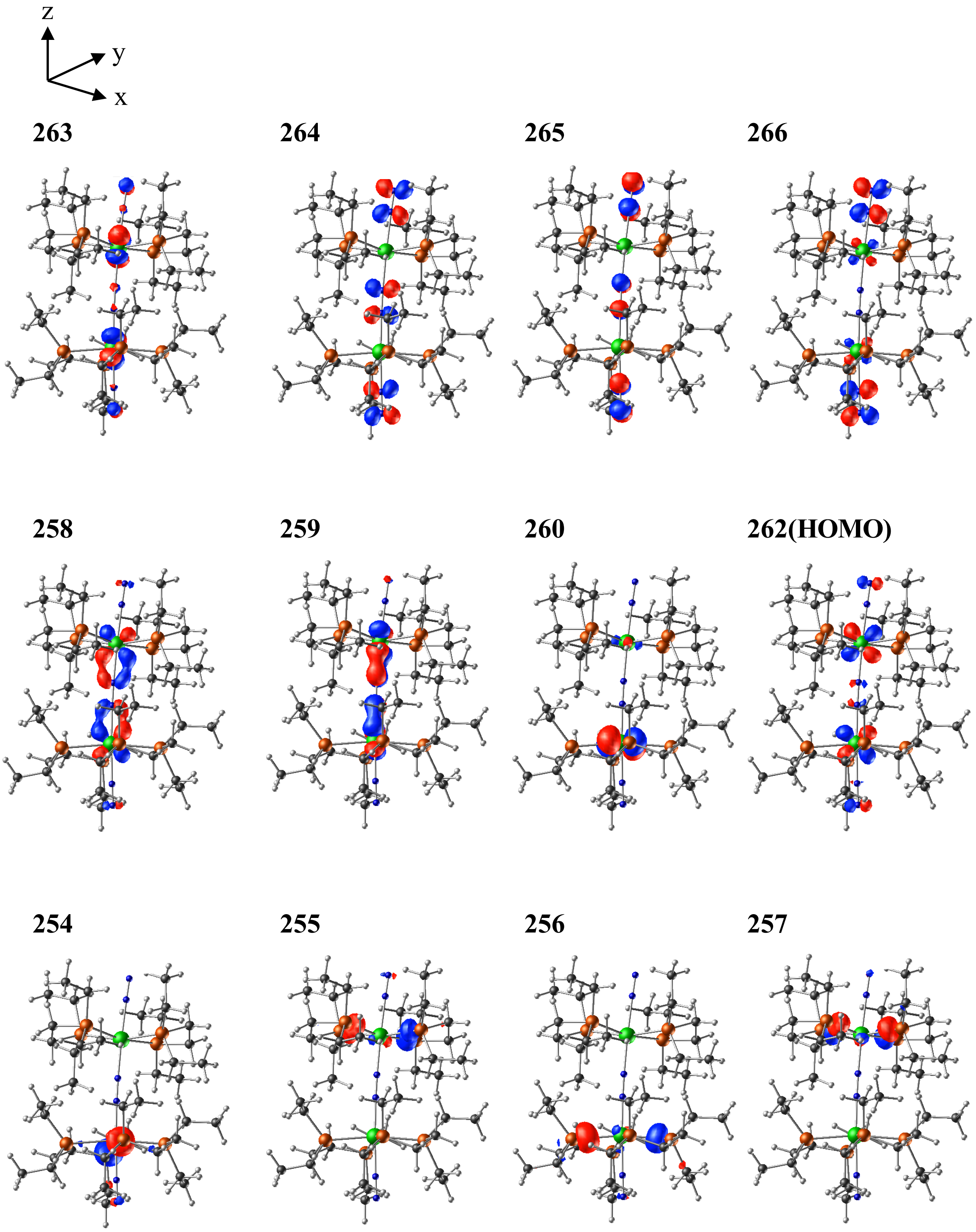

Figure C16. Molecular orbitals for model complex **5** in the singlet state (Isosurface values: ±0.07 (254, 255, 256, 257, 258, 259, 260, 262, 263, 264, 265 and 266).

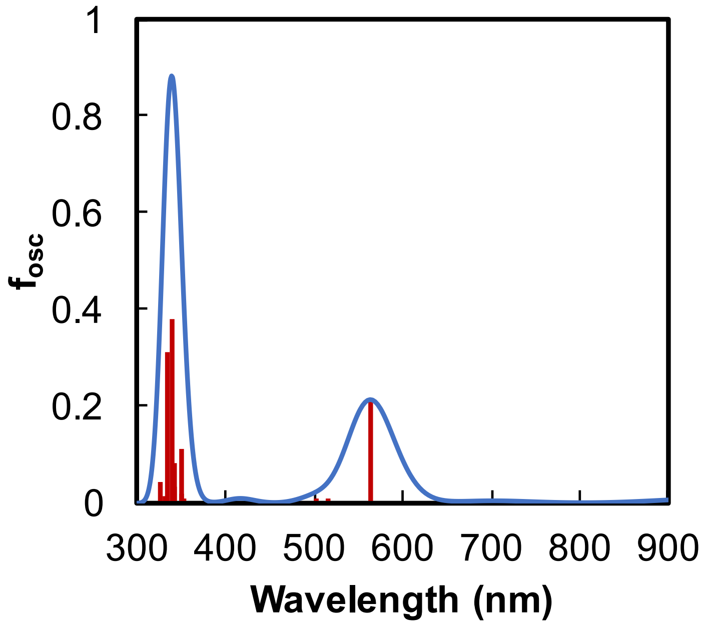

Figure C17. Absorption spectra of complex **6** in the triplet state calculated by TD-DFT.

Table C8. Calculated transitions of complex **6** in the triplet state

Excited State	Energy (eV)	Wavelength (nm)	fosc	Transition	%
16	2.1959	564.61	0.2120	248A → 254A 249A → 255A 244B → 248B 245B → 249B	5.6 8.7 33.5 47.3
38	3.5523	349.02	0.1101	248A → 252A 248A → 253A 248A → 254A 248A → 256A 248A → 257A 248A → 258A 248A → 259A 249A → 255A 249A → 259A	5.5 8.2 4.1 12.3 5.7 26.4 9.1 4.6 6.8
42	3.6379	340.81	0.3810	248A → 253A 248A → 254A 248A → 258A 249A → 255A 242B → 248B 243B → 248B	3.8 19.5 3.2 13.2 29.1 13.9
44	3.6945	335.59	0.3112	248A → 254A 248A → 259A 249A → 255A 242B → 248B 243B → 249B	8.2 4.3 11.9 50.6 4.6

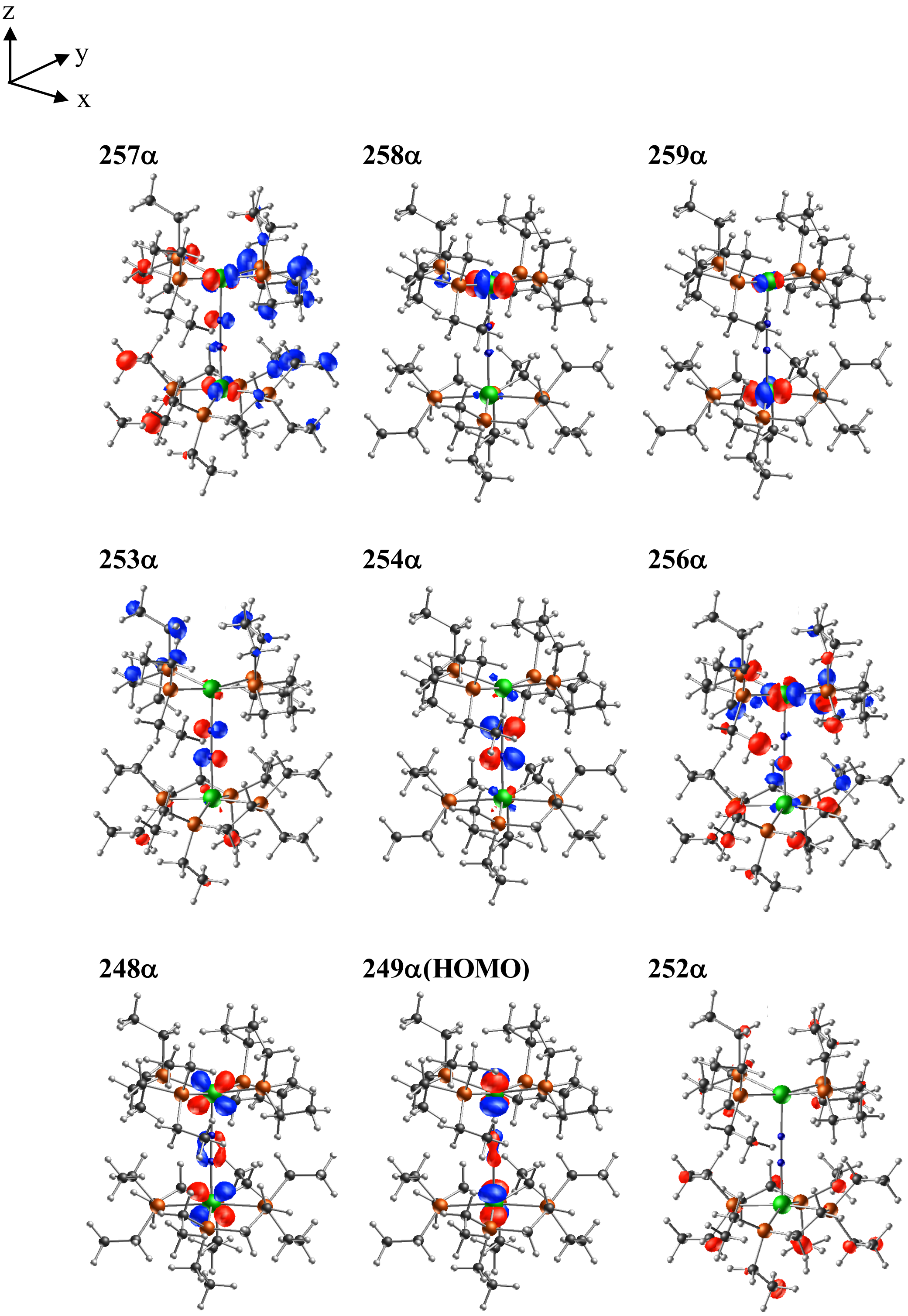

257α **258α** **259α**

253α **254α** **256α**

248α **249α(HOMO)** **252α**

[

Figure C18. (A) Molecular orbitals for model complex **6** in the triplet state (Isosurface values: ±0.07 (248α, 249α, 254α, 255α, 258α and 259α), 0.03 (252α, 253α, 256α, and 257α).

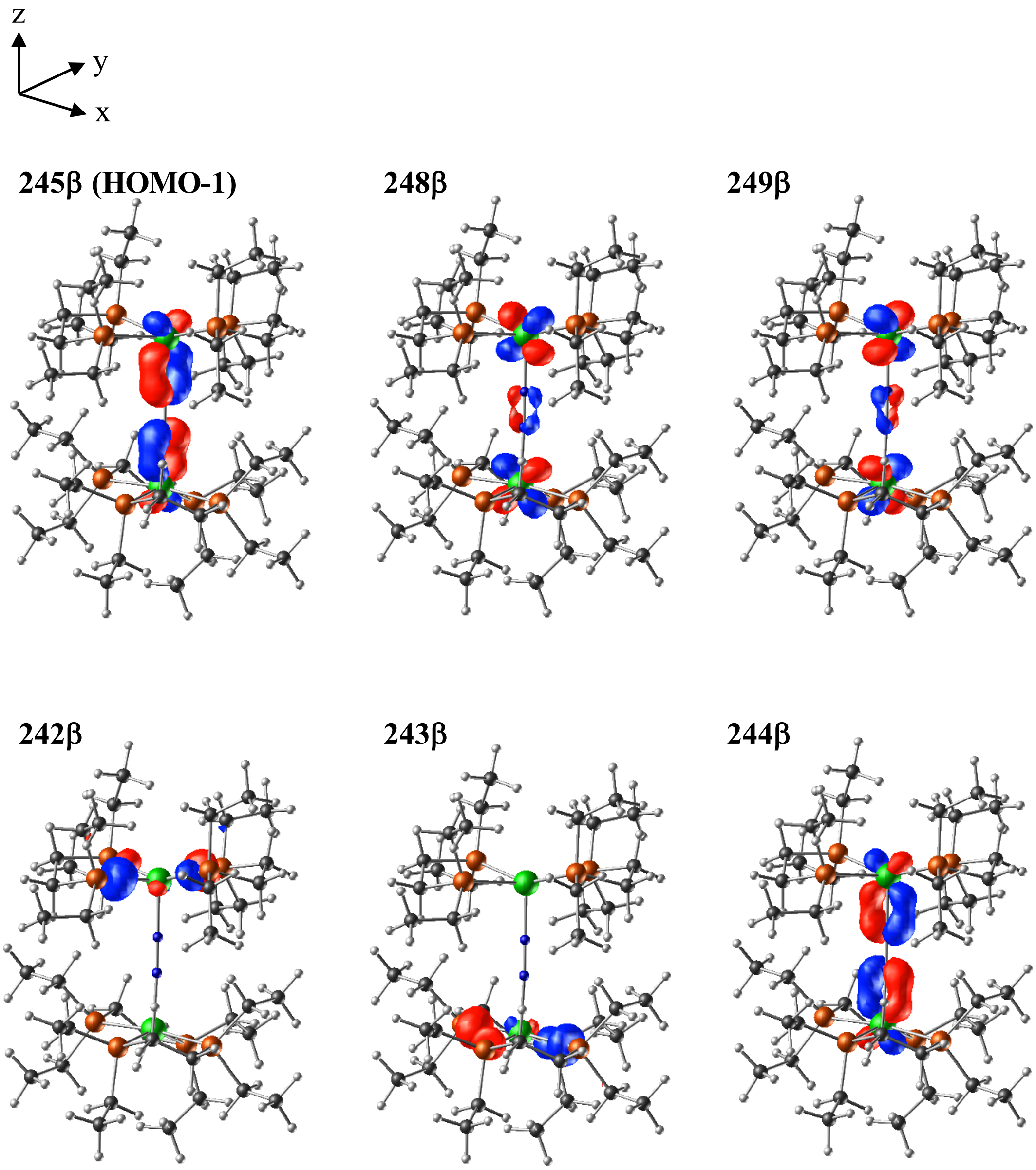

245β (HOMO-1)

248β

249β

242β

243β

244β

Figure C18. (B) Molecular orbitals for model complex **6** in the triplet state (Isosurface values: ±0.07 (242β, 243β, 244β, 245β, 248β and 249β).

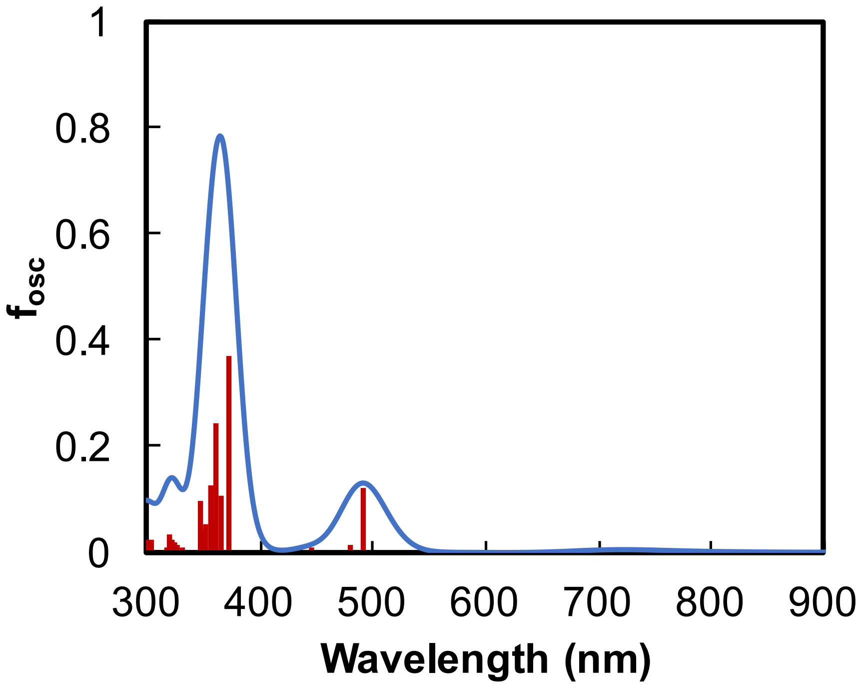

Figure C19. Absorption spectra of complex **6** in the singlet state calculated by TD-DFT.

Table C9. Calculated transitions of complex **6** in the singlet state

Excited State	Energy (eV)	Wavelength (nm)	fosc	Transition	%
11	2.5208	491.84	0.1205	245 → 249 248 → 254	73.1 19.8
19	3.3329	372.00	0.3709	243 → 249 245 → 249 248 → 254 248 → 255 248 → 259	12.2 7.6 34.2 29.2 5.8
20	3.3843	366.35	0.1058	243 → 249 248 → 254 248 → 255	39.4 5.3 48.0
21	3.4367	360.77	0.2431	243 → 249 248 → 254 248 → 255 248 → 257	42.6 15.5 16.7 7.6
22	3.4778	356.51	0.1283	242 → 249 248 → 257 248 → 258 248 → 259 248 → 261 248 → 263	5.8 34.2 7.6 22.2 8.1 5.8

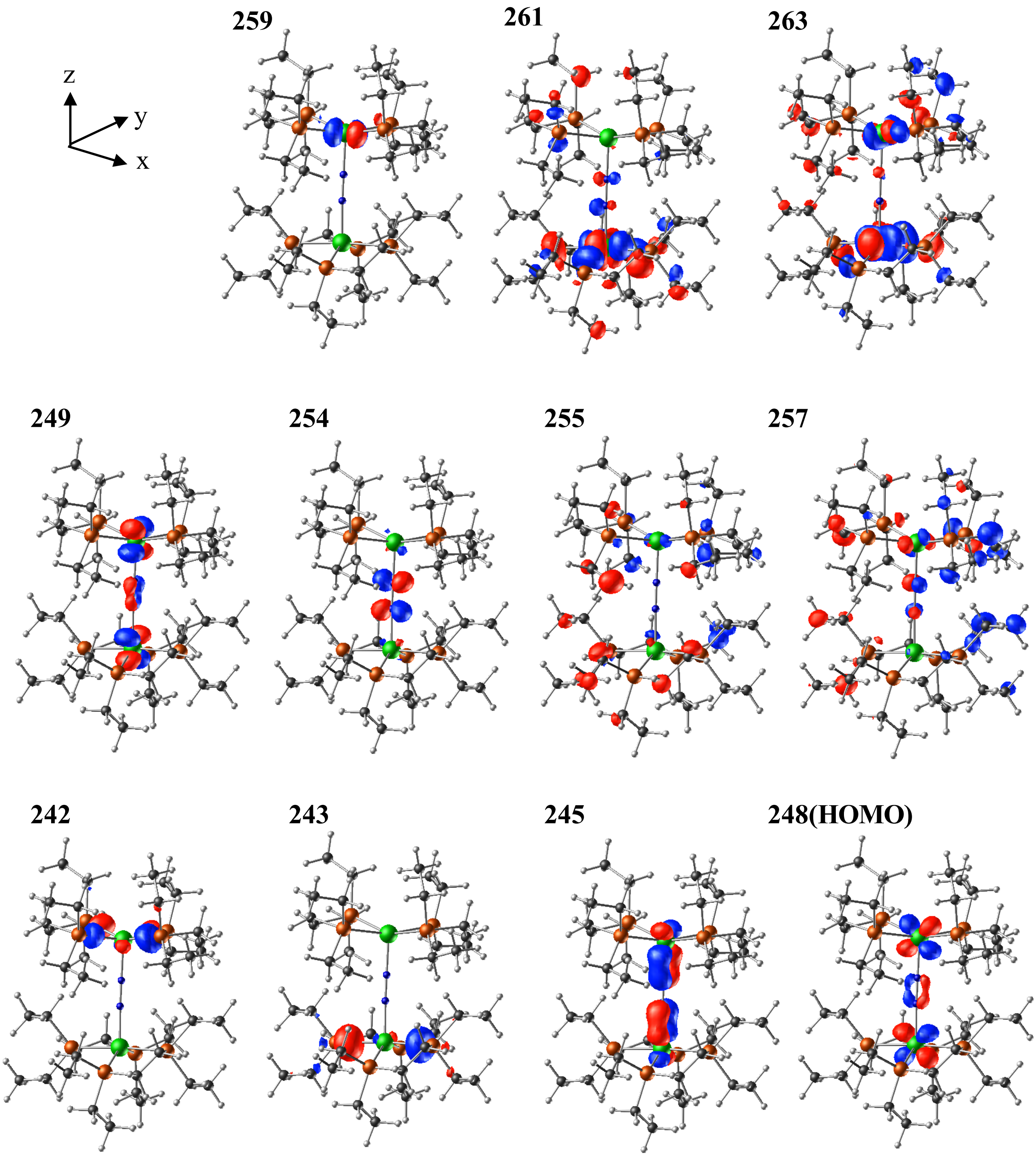

Figure C20. Molecular orbitals for model complex **6** in the singlet state (Isosurface values: ±0.07 (242, 243, 245, 248, 249, 254, 258 and 259), ±0.03 (255, 257, 261 and 263)).

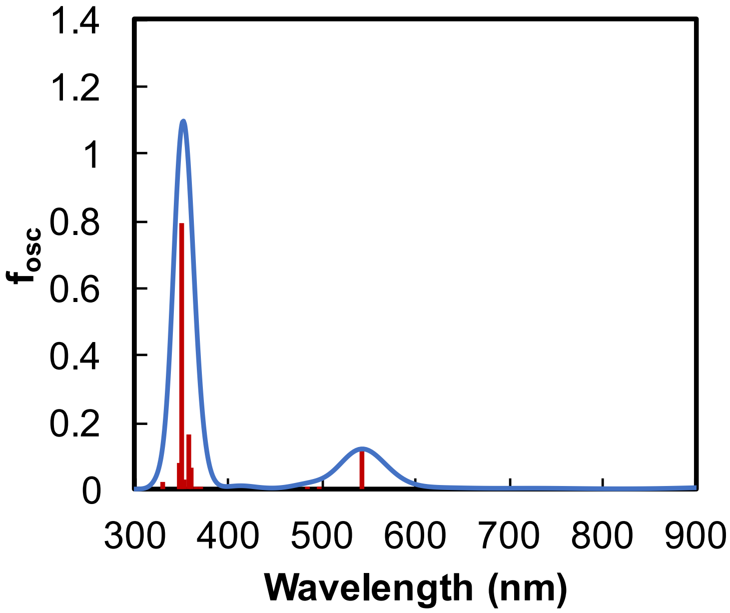

Figure C21. Absorption spectra of complex **7** in the triplet state calculated by TD-DFT.

Table C10. Calculated transitions of complex **7** in the triplet state

Excited State	Energy (eV)	Wavelength (nm)	fosc	Transition	%
17	2.2796	543.88	0.1168	248A → 252A 249A → 255A 244B → 248B 245B → 249B	8.3 12.2 27.3 44.7
37	3.4579	358.55	0.1641	248A → 252A 248A → 256A 248A → 258A 248A → 259A 249A → 259A	8.2 12.3 21.1 8.6 10.7
40	3.5327	350.97	0.7940	248A → 252A 248A → 254A 248A → 258A 249A → 255A 244B → 248B 245B → 249B	17.2 16.2 8.5 20.5 5.8 6.4

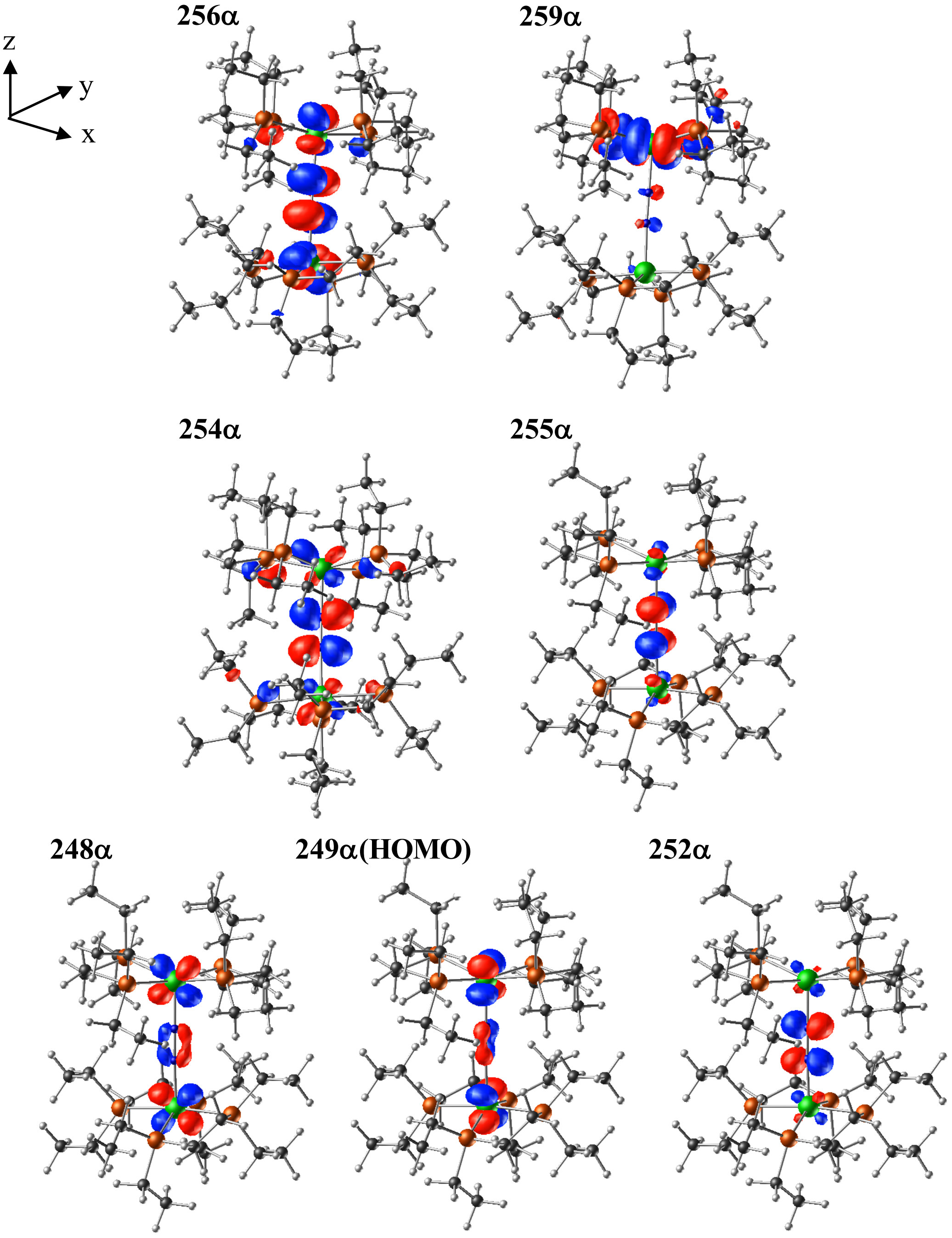

Figure C22. (A) Molecular orbitals for model complex **7** in the triplet state (Isosurface values: ±0.07 (248α, 249α, 252α, 254α, 255α, 256α and 259α), ±0.04 (254α and 256α).

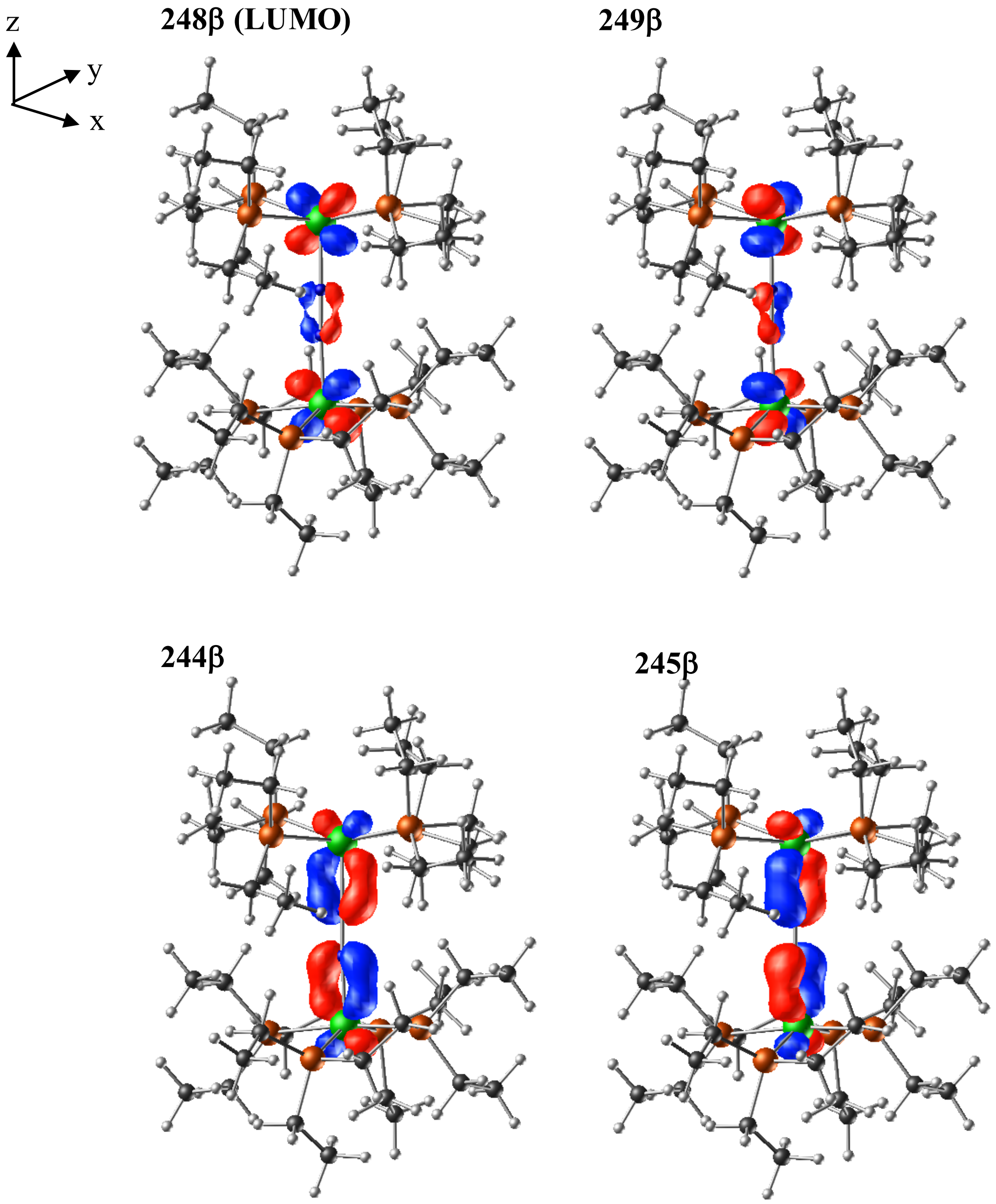

Figure C22. (B) Molecular orbitals for model complex **7** in the triplet state (Isosurface values: ±0.07 (244β, 245β, 248β and 249β).

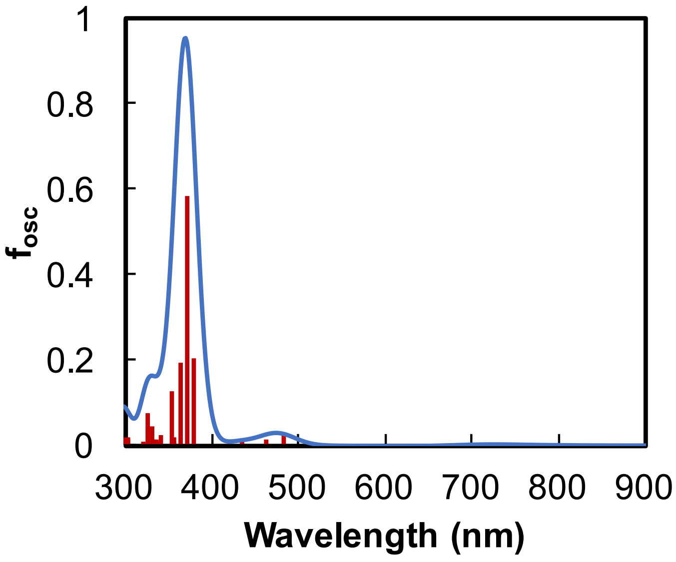

Figure C23. Absorption spectra of complex **7** in the singlet state calculated by TD-DFT.

Table C11. Calculated transitions of complex **7** in the singlet state

Excited State	Energy (eV)	Wavelength (nm)	fosc	Transition	%
19	3.2693	379.24	0.2057	245 → 249 248 → 252 248 → 256 248 → 259	6.9 12.4 58.8 9.1
20	3.3410	371.10	0.5823	245 → 249 248 → 252 248 → 256 248 → 257	17.0 28.1 33.8 5.8
21	3.3943	365.28	0.1932	248 → 252 248 → 257 248 → 258 248 → 259 248 → 261	6.5 33.6 10.0 21.6 8.6
24	3.5104	353.19	0.1241	243 → 249	81.2

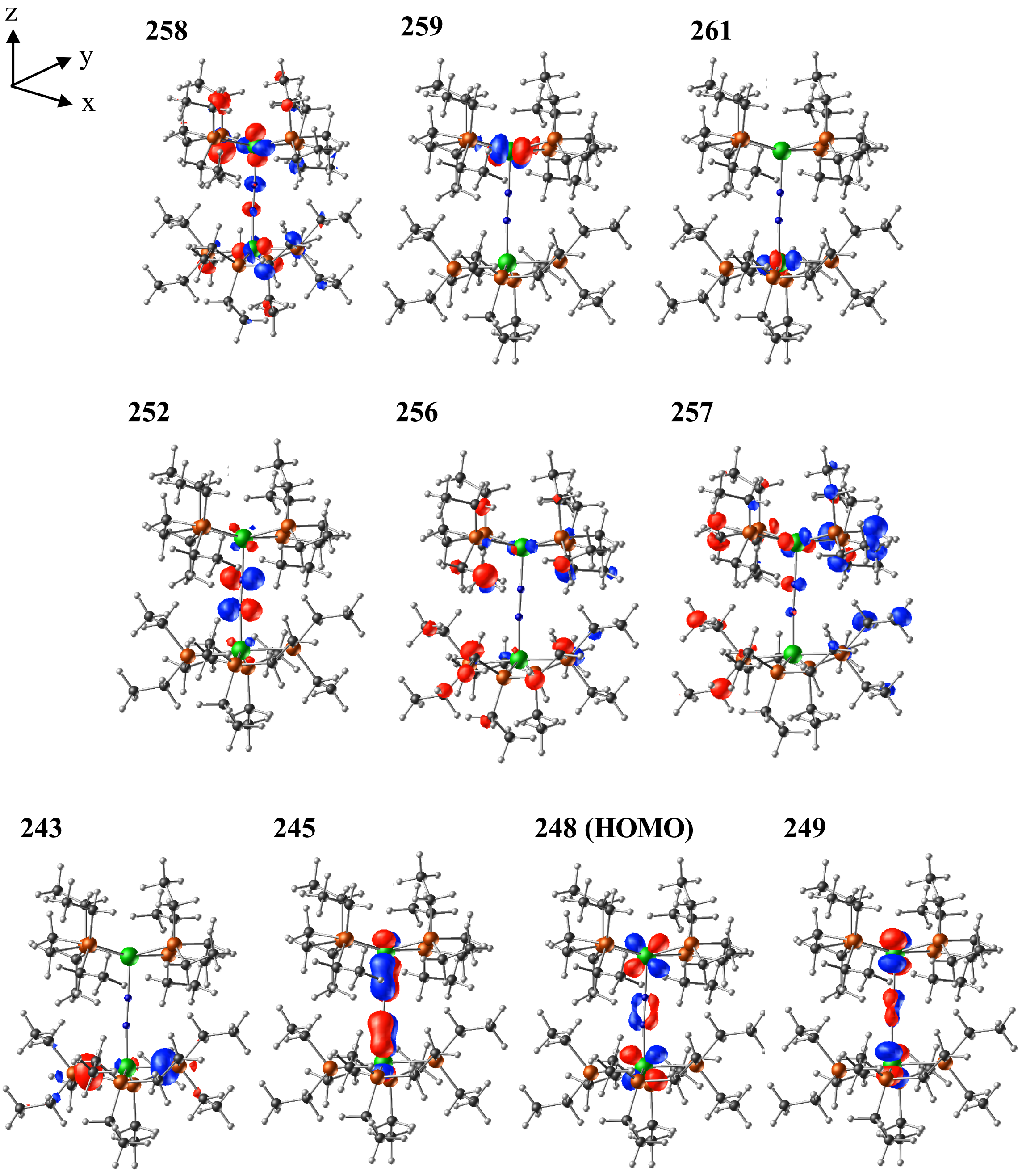

Figure C24. Molecular orbitals for model complex **7** in the singlet state (Isosurface values: ±0.07 (243, 245, 248, 249, 252, 259 and 261), ±0.03 (256, 257 and 258)).

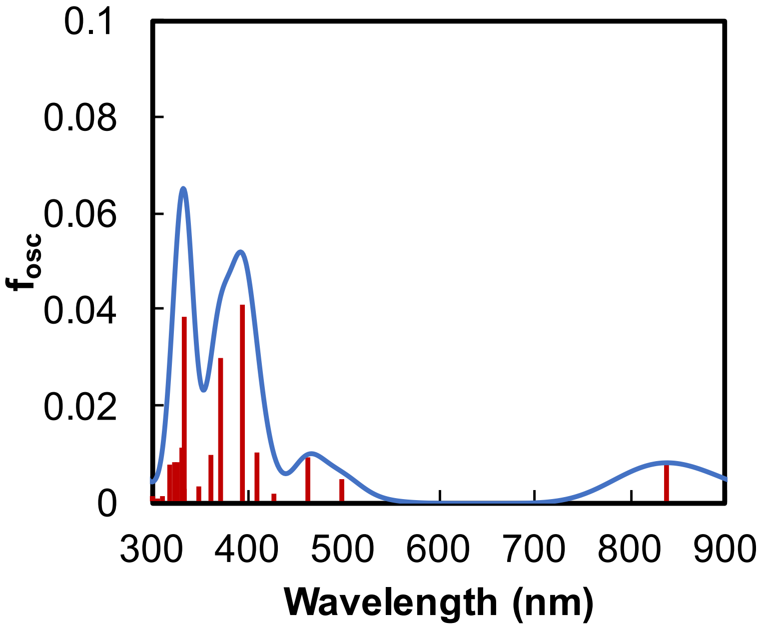

Figure C25. Absorption spectra of complex **8** in the triplet state calculated by TD-DFT.

Table C12. Calculated transitions of complex **8** in the triplet state

Excited State	Energy (eV)	Wavelength (nm)	fosc	Transition	%
1	1.4804	837.5	0.0084	125A → 126A	98.2
3	2.4859	498.76	0.0049	125A → 127A 125A → 129A 125A → 130A	22.2 57.9 13.6
4	2.6799	462.65	0.0093	123B → 124B	94.7
6	3.0205	410.48	0.0102	125A → 128A	88.0
8	3.1463	394.07	0.0411	124A → 126A 125A → 129A 125A → 130A	8.5 10.9 71.2
9	3.3305	372.27	0.0301	124A → 126A 121B → 124B	61.9 16.3
10	3.4303	361.44	0.0097	125A → 131A	86.4
11	3.5436	349.88	0.0032	125A → 132A	81.2

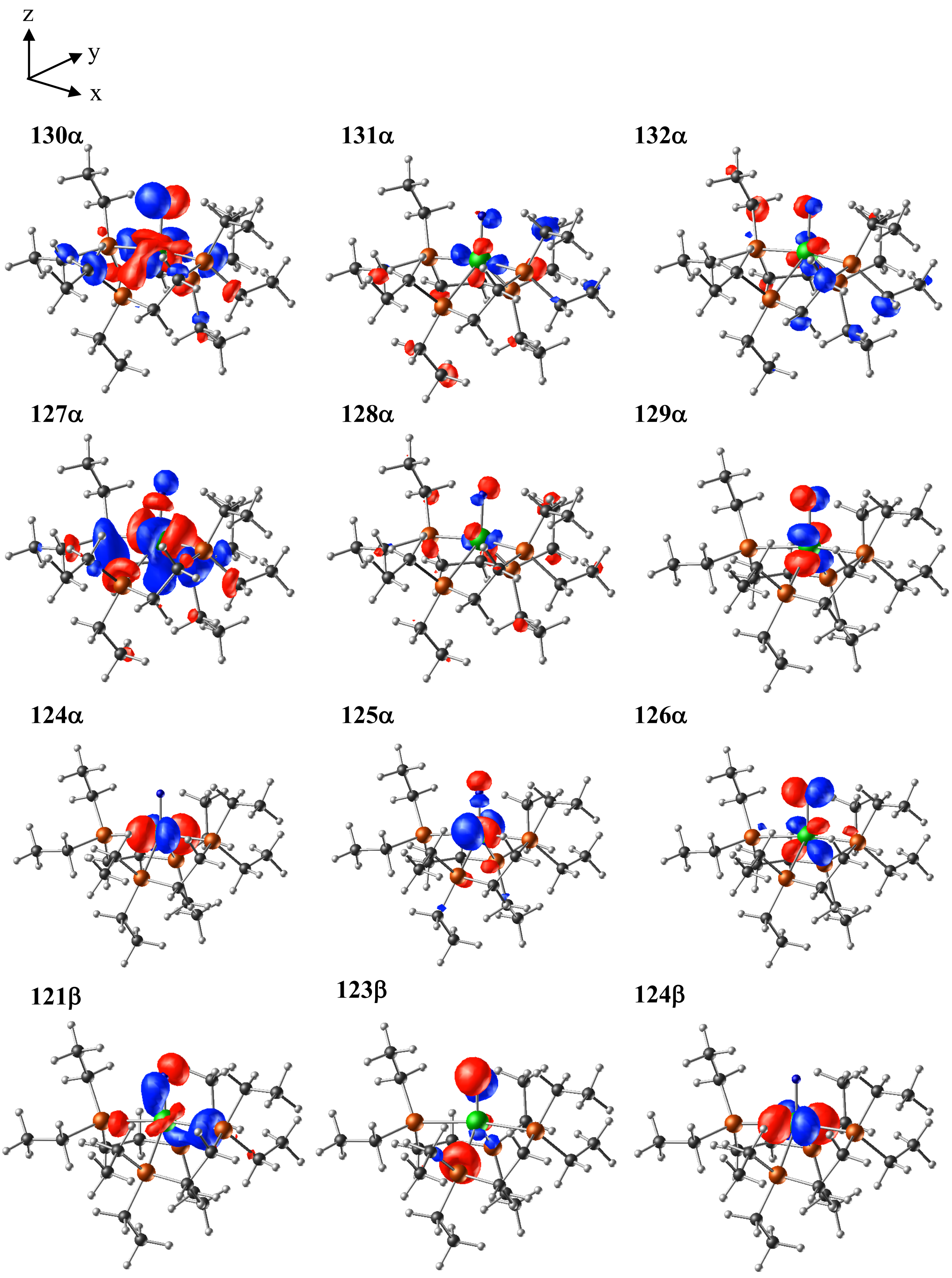

130α 131α 132α

127α 128α 129α

124α 125α 126α

121β 123β 124β

Figure C26. Molecular orbitals for model complex **8** in the triplet state (Isosurface values: ±0.07 (124α, 125α, 126α, 129α, 121β, 123β and 124β), 0.04 (127α, 128α, 130α, 131α and 132α)).

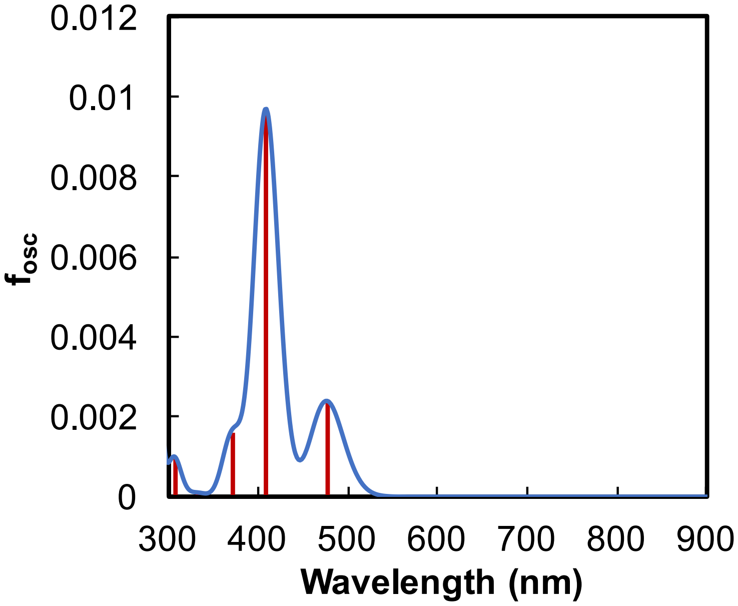

Figure C27. Absorption spectra of complex **8** in the singlet state calculated by TD-DFT.

Table C13. Calculated transitions of complex **8** in the singlet state

Excited State	Energy (eV)	Wavelength (nm)	f_{osc}	Transition	%
1	2.6001	476.84	0.0024	124→125	99.2
2	3.0283	409.42	0.0097	124→126	98.2
3	3.3294	372.39	0.0016	124→127	96.9

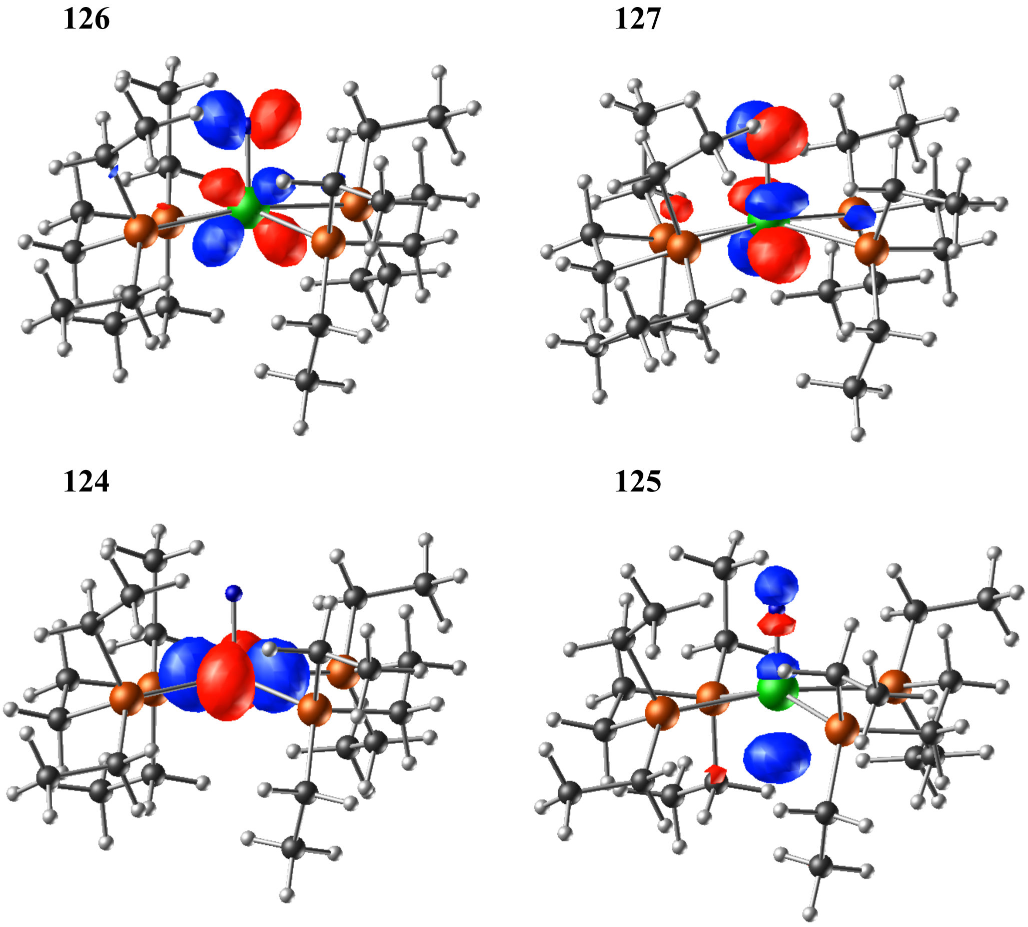

126 **127**

124 **125**

Figure C28. Molecular orbitals for model complex **8** in the singlet state (Isosurface values: ±0.07 (124, 125, 126 and 127).

Table C14. Summary for ν(N_2) in Mo-N_2 complexes

Complex	Media	Wavenumber / cm^{-1}	Reference
trans-[Mo(depe)$_2$(N_2)$_2$]	in THF	2008 (vw), 1939	3
	in toluene	2008 (vw), 1940	
	KBr	2002 (vw), 1928	
[Mo(depe)$_2$(N_2)]	in Pyr$_4$FAP	1919	this study
[Mo(depe)$_2$(N_2)]$^+$	in Pyr$_4$FAP	1955	
trans-[Mo(N_2)$_2$(dppe)$_2$]	in Nujol	2020 (vw), 1975	4
trans-[Mo(N_2)$_2$(dppe)$_2$]I_3	in Nujol	2047	

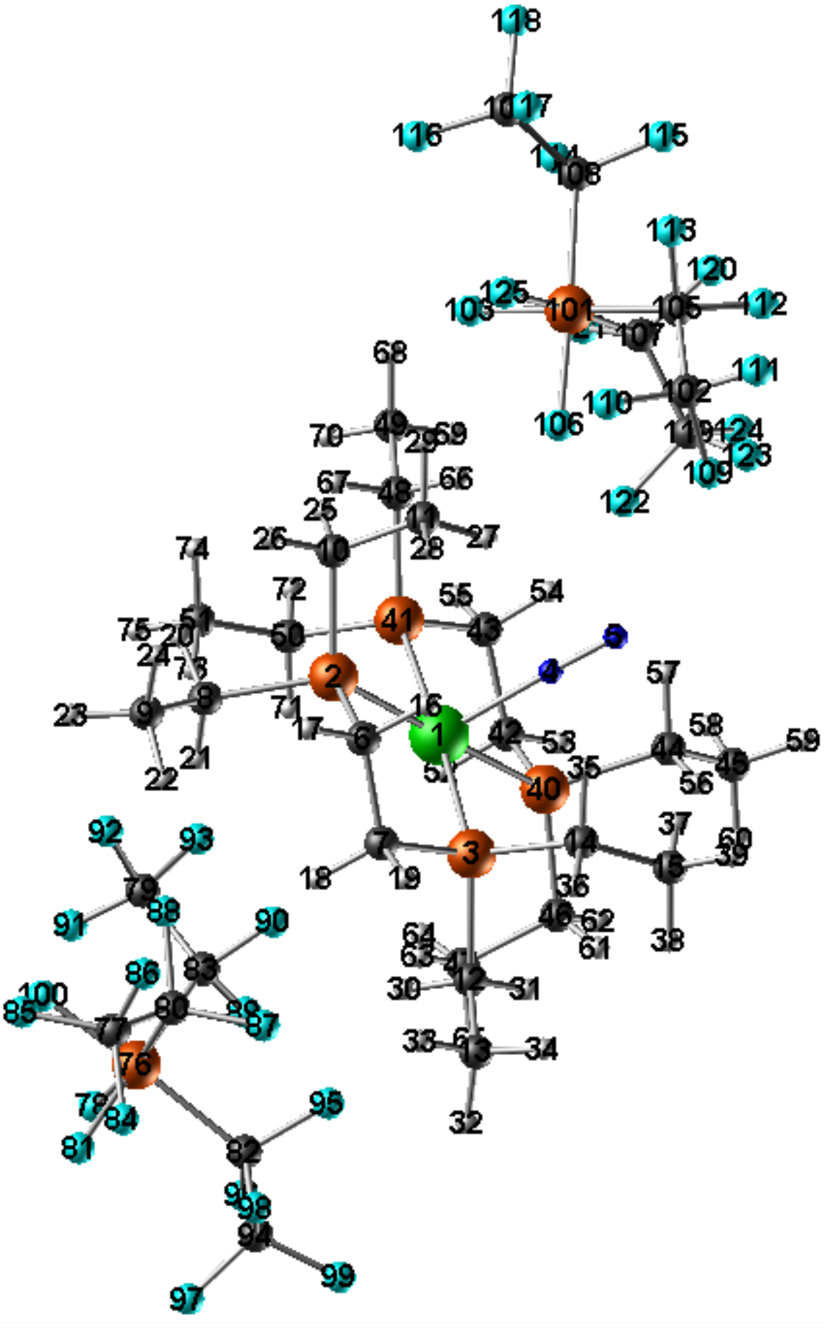

Figure C29. The optimized structure of **12**’. Selected bond lengths for the complex; F93···H73 2.8278, F93···H71 2.3380, F89···H64 2.9302, F89···H63 2.6904, F90···H63 2.3938, F90···H21 2.9037, F90···H30, Mo1···F90 3.5837, F92···H73 2.6136, F88···H21 2.2994, F88···H22 2.6106, F86···H22 2.8267, F106···H27 2.4178, F106···H66 2.4039, F106···H29 2.8833, F103···H66 2.4849, F125···H29 2.5953, F110···H29 2.7437, F110···H27 2.8770, F122···H66 2.4211, F121···H68 2.7540, F122···H54 2.3705.

C.5 Electrochemical NH_3 synthesis by *trans*-[Mo(depe)$_2$(N_2)$_2$] in Pyr$_4$FAP by using SPE cell

In order to characterize the electrochemical conversion of N_2 to NH_3 by *trans*-[Mo(depe)$_2$(N_2)$_2$] in Pyr$_4$FAP in the SPE cell as shown in Figure A2 in appendix A, the reduction potential was evaluated and the linear sweep voltammograms in SPE cell were measured (Figure C30). Surprisingly, the electric current was found to dramatically increase at −0.24 V (vs. Ag/AgCl). At this potential, *trans*-[Mo(depe)$_2$(N_2)$_2$] in the Mo(0) state cannot receive any more electrons from the electrode. In fact, H_2 evolution is not observed through the reduction of proton transferred from proton exchange membrane. Therefore, it appears that the observed current is derived from protonation of the terminal N_2 of *trans*-[Mo(depe)$_2$(N_2)$_2$] and successive electron transfer to generate NH_3, as shown in Scheme C1. In general, chemical protonation of *trans*-[Mo(depe)$_2$(N_2)$_2$] proceeds by addition of a strong acid such as H_2SO_4 without a reducing agent, and the coordinated N_2 is converted to NH_3.[5] In our system, protons are generated electrochemically when oxidation of H_2O occurs at the counter electrode. These protons are transferred to the WE across the proton exchange membrane. On the basis of these results, we decided to carry out the CPE analysis at −0.3, −0.5 and −1.0 V (vs. Ag/AgCl). The results obtained in the CPE analysis are summarized in Table C15.

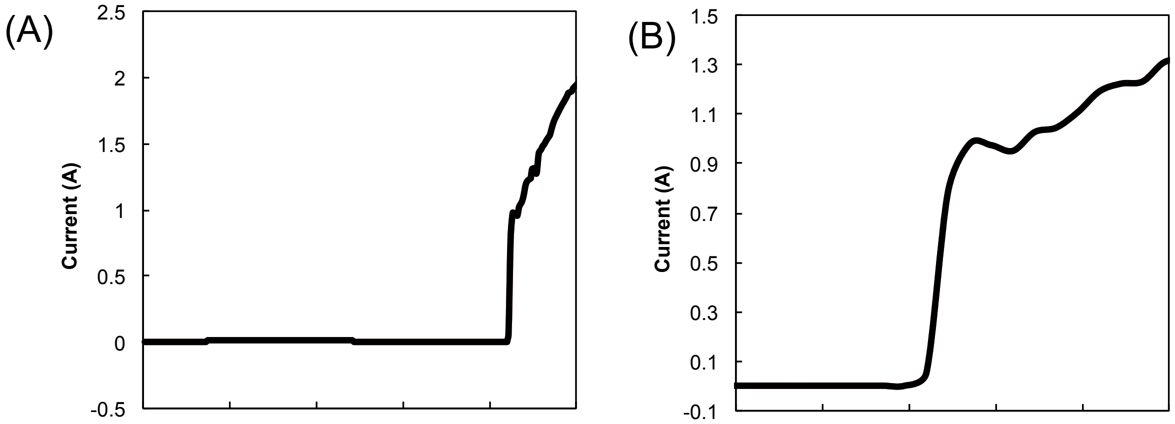

Figure C30. (A) Linear sweep voltammogram of 10 mM *trans*-[Mo(depe)$_2$(N_2)$_2$] in Pyr$_4$FAP in SPE cell, where WE is carbon paper (1 cm × 3 cm) coated with 50 μL of the Pyr$_4$FAP, CE is Pt mesh, RE is Ag/AgCl (3 M NaCl), CE chamber was flowed with 0.2 M H_2SO_4 aq, and WE and CE were separated by Nafion membrane (scan rate is 5 mV/s). The rest potential was 0.59 V. (B) Plots of the consumed electricity (C) against time (s) in controlled-potential electrolysis at −0.3V.

In the case of CPE analysis at –0.3 V (vs. Ag/AgCl), the yield of NH_3 per *trans*-[Mo(depe)$_2$(N_2)$_2$] is 77% and the current efficiency is 0.013%. In this analysis, H_2 evolution is not observed and hydrazine is not generated.[6] Ammonia is generated under an Ar atmosphere. Therefore, it is clear that the ammonia is derived from N_2 coordinated to the molybdenum ion. These findings indicate that 25% of the two coordinated N_2 molecules are protonated to generate NH_3. Unfortunately, the current efficiency is quite low. This indicates that most of the electric charges are consumed for other reactions after the protonation reaction. We cannot yet rationalize these reactions in detail.

In the case of CPE analysis at –0.5 V (vs. Ag/AgCl), the yield of NH_3 per *trans*-[Mo(depe)$_2$(N_2)$_2$] is 76% and the current efficiency is 0.015%. Likewise, the CPE analysis at −1.0 V (vs. Ag/AgCl) provides 71% yield of NH_3 per *trans*-[Mo(depe)$_2$(N_2)$_2$] and current efficiency is 0.015%. Therefore, the reactivity is not improved at negative potential below –0.3 V.

It is well known that a Mo(0)-N_2 complex supported by a phosphine ligand can convert the coordinated N_2 to ammonia by protonation of the terminal nitrogen in the presence of a strong acid.[7] Therefore, the result obtained in the present work as shown in Figure C30 demonstrates that the reaction proceeds electrochemically through the proton exchange membrane, as shown in Scheme C1. Many reactions involving protonation of a dinitrogen complex using a protonation agent have been reported, but such a direct protonation of the metal-N_2 complex through the proton exchange membrane has not been reported hitherto, to the best of our knowledge.

Scheme C1. Proposed reaction scheme for NH_3 generation from *trans*-[Mo(depe)$_2$(N_2)$_2$]

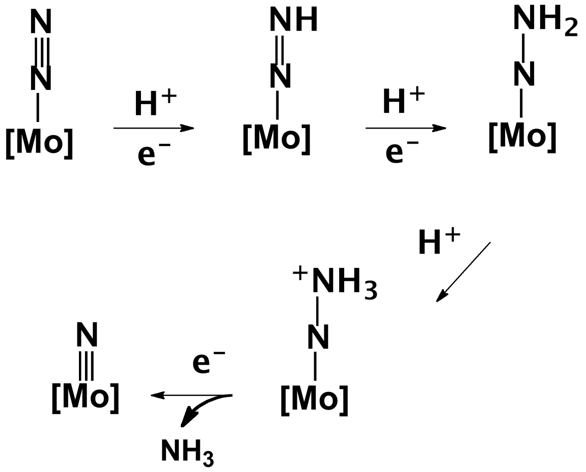

Table C15. Results of controlled-potential electrolysis

Reduction potential (V) (vs. Ag/AgCl)	**Amount of NH_3 generated (nmol)**	**Consumed electric charge (C)[a]**	**Yield of NH_3 per Mo ion (%)[b,c]**	**Current efficiency (%)[b,c,d]**
−0.3	386	95.2	77.2	0.013
−0.5	378	83.3	75.6	0.015
−1.0	353	76.4	70.6	0.015

[a] CPE was carried out for 180 (s).

[b] Experimental error within ±5%

[c] Total amount of *trans*-[Mo(depe)$_2$(N$_2$)$_2$] used is 500 nmol.

[d] The amount of NH_3 was estimated by indophenol method.

C.6 Cartesian coordinates for optimized structures

Table C16. Cartesian coordinates for optimized structure of **1**

Mo	-2.435421	-0.000034	0.000016
P	0.059795	0.021679	-0.003753
P	-1.985153	-2.453301	-0.018102
N	-2.451956	-0.018849	-2.020593
N	-2.480535	-0.043437	-3.154801
C	0.646431	-1.645908	-0.631356
C	-0.124395	-2.762769	0.083415
C	0.886655	0.108255	1.679844
C	2.356020	-0.316886	1.806719
C	1.155045	1.190367	-0.973550
C	0.853675	1.262592	-2.476025
C	-2.607522	-3.536768	1.374022
C	-2.116313	-4.989997	1.428867
C	-2.379972	-3.480236	-1.536618
C	-3.865200	-3.795332	-1.747263
H	0.440581	-1.673964	-1.710745
H	1.731089	-1.766385	-0.506702
H	0.145945	-2.783303	1.149899
H	0.130866	-3.747144	-0.331525
H	0.771015	1.148120	2.015097
H	0.266890	-0.488548	2.361008
H	2.495958	-1.379781	1.572990
H	2.704364	-0.161429	2.837146
H	3.016258	0.261075	1.148035
H	1.020913	2.182297	-0.517929
H	2.206404	0.909869	-0.818251
H	-0.184934	1.556902	-2.662596
H	1.020203	0.296497	-2.969797
H	1.508642	1.997801	-2.963251
H	-2.337350	-3.009155	2.299890
H	-3.704492	-3.509023	1.323264
H	-2.545164	-5.505887	2.298942
H	-1.024234	-5.047578	1.516860
H	-2.409957	-5.554488	0.534654
H	-1.994244	-2.916597	-2.397266
H	-1.804273	-4.415010	-1.487675
H	-4.463716	-2.879831	-1.815085
H	-4.272128	-4.402127	-0.927664
H	-4.010913	-4.358594	-2.679019
P	-4.930635	-0.021760	0.003772
P	-2.885700	2.453231	0.018131
N	-2.418920	0.018811	2.020624
N	-2.390094	0.043262	3.154829
C	-5.517292	1.645838	0.631326
C	-4.746454	2.762692	-0.083443
C	-5.757468	-0.108380	-1.679834
C	-7.226888	0.316563	-1.806718
C	-6.025885	-1.190427	0.973594
C	-5.724496	-1.262639	2.476067
C	-2.263284	3.536714	-1.373959
C	-2.754495	4.989942	-1.428809
C	-2.490946	3.480155	1.536670
C	-1.005723	3.795214	1.747407
H	-5.311469	1.673914	1.710721
H	-6.601948	1.766310	0.506646
H	-5.016766	2.783209	-1.149934
H	-5.001730	3.747071	0.331476
H	-5.641678	-1.148213	-2.015137
H	-5.137771	0.488538	-2.360961
H	-7.366999	1.379406	-1.572854
H	-7.575163	0.161192	-2.837182
H	-7.887068	-0.261587	-1.148141
H	-5.891773	-2.182364	0.517984
H	-7.077242	-0.909917	0.818307
H	-4.685889	-1.556960	2.662628
H	-5.891005	-0.296536	2.969829

H	-6.379467	-1.997834	2.963309
H	-2.533419	3.009108	-2.299842
H	-1.166315	3.508971	-1.323160
H	-2.325615	5.505839	-2.298866
H	-3.846570	5.047521	-1.516839
H	-2.460881	5.554426	-0.534583
H	-2.876742	2.916528	2.397295
H	-3.066618	4.414943	1.487689
H	-0.407239	2.879698	1.815290
H	-0.598725	4.401981	0.927821
H	-0.860058	4.358493	2.679160

Table C17. Cartesian coordinates for optimized structure of **2**

Mo	0.050897	0.145078	-3.292999
P	2.540258	0.004755	-3.558805
P	0.586411	2.561540	-3.584843
N	0.046050	0.166490	-1.126702
N	-0.011146	0.143093	0.019396
C	3.293964	1.718980	-3.408669
C	2.393977	2.748732	-4.100052
C	3.073420	-0.423674	-5.308829
C	4.558824	-0.622261	-5.636533
C	3.654613	-1.045883	-2.472826
C	5.127737	-0.659169	-2.265043
C	-0.236649	3.490893	-4.989532
C	0.285757	4.893359	-5.331860
C	0.502797	3.829703	-2.208513
C	-0.923033	4.197083	-1.784734
H	3.377158	1.948642	-2.340425
H	4.310161	1.747565	-3.825678
H	2.425575	2.604597	-5.190168
H	2.748720	3.770014	-3.904845
H	2.510665	-1.318861	-5.596700
H	2.663432	0.380018	-5.934705
H	5.169272	0.245753	-5.356274
H	4.685651	-0.774857	-6.717816
H	4.973638	-1.503618	-5.132206
H	3.149807	-1.070900	-1.500917
H	3.581240	-2.069481	-2.870461
H	5.223334	0.345108	-1.836027
H	5.704279	-0.679344	-3.194874
H	5.603133	-1.360605	-1.564591
H	-0.152215	2.832772	-5.865004
H	-1.306991	3.537804	-4.751697
H	-0.273265	5.311433	-6.180616
H	1.346083	4.877844	-5.612923
H	0.173300	5.589989	-4.491142
H	1.046946	3.392297	-1.362041
H	1.054546	4.732095	-2.507639
H	-1.502655	3.300294	-1.534367
H	-1.456962	4.727319	-2.584428
H	-0.915820	4.851335	-0.902326
P	-2.437783	0.269132	-3.396020
P	-0.473632	-2.301407	-3.332377
N	-0.025302	0.057753	-5.271858
N	-0.070268	-0.009464	-6.412400
C	-3.033259	-1.377665	-4.075038
C	-2.349248	-2.533256	-3.336241
C	-3.428750	0.455407	-1.812476
C	-4.842368	-0.141235	-1.768629
C	-3.439204	1.462082	-4.450706
C	-3.253688	1.375624	-5.970516
C	0.031480	-3.496088	-1.982561
C	-0.591995	-4.899230	-1.992934
C	-0.033015	-3.289312	-4.872182
C	1.375475	-3.900344	-4.884688
H	-2.756005	-1.395635	-5.138361
H	-4.127098	-1.463816	-4.025738
H	-2.677036	-2.552977	-2.287020
H	-2.622590	-3.501514	-3.777692
H	-3.475286	1.539396	-1.633115
H	-2.814873	0.045314	-1.003664
H	-4.822910	-1.236713	-1.831083
H	-5.342544	0.124858	-0.827848
H	-5.474826	0.226110	-2.587229
H	-3.171357	2.467807	-4.096436
H	-4.502162	1.320941	-4.206832
H	-2.207382	1.505565	-6.264018
H	-3.590758	0.407827	-6.363202
H	-3.846729	2.154848	-6.469609
H	-0.191879	-2.986749	-1.036448
H	1.126860	-3.565687	-2.030245
H	-0.191038	-5.505337	-1.168366
H	-1.681306	-4.859992	-1.873206
H	-0.379922	-5.434512	-2.927030
H	-0.148971	-2.605804	-5.722845
H	-0.776529	-4.087906	-5.003682
H	2.146985	-3.158667	-4.647624
H	1.470554	-4.717647	-4.159109
H	1.606090	-4.311841	-5.876837
Mo	-0.079503	0.038126	2.184020
P	-1.875289	-1.696452	2.271136
P	1.337923	-2.014126	2.201153
N	-0.043950	-0.121814	4.159419
N	0.014284	-0.224801	5.296045
C	-1.078609	-3.278979	2.894719
C	0.232889	-3.545176	2.147195
C	-2.730648	-2.264153	0.696009
C	-3.319055	-3.680699	0.639956
C	-3.399925	-1.617846	3.371549
C	-3.165556	-1.579397	4.887062
C	2.574647	-2.412649	0.858420
C	3.260190	-3.785676	0.881271
C	2.312740	-2.424963	3.750439
C	3.575830	-1.586747	3.975903
H	-0.873499	-3.125928	3.963364
H	-1.764504	-4.133410	2.819058
H	0.029184	-3.768974	1.089913
H	0.753695	-4.417340	2.566326
H	-3.526487	-1.526741	0.522291
H	-2.010463	-2.122490	-0.117693
H	-2.537088	-4.448578	0.686889
H	-3.866894	-3.828705	-0.301388
H	-4.024648	-3.871773	1.458668

H	-3.947679	-0.718436	3.058652
H	-4.042826	-2.475452	3.126356
H	-2.530408	-0.738523	5.183132
H	-2.686308	-2.498783	5.246745
H	-4.125045	-1.483993	5.414541
H	2.027130	-2.279874	-0.082935
H	3.326537	-1.611877	0.885229
H	3.940972	-3.888268	0.024635
H	2.532096	-4.604570	0.823484
H	3.855194	-3.931541	1.791697
H	1.625862	-2.289147	4.595954
H	2.574356	-3.491836	3.721837
H	3.340775	-0.518153	4.034199
H	4.307620	-1.725631	3.168780
H	4.064815	-1.872274	4.917466
P	1.657751	1.813310	2.449222
P	-1.503879	2.083722	2.451682
C	0.935295	3.409866	1.789080
C	-0.435113	3.659057	2.429331
C	2.022611	2.278903	4.234274
C	2.688050	3.631826	4.522212
C	3.401981	1.867054	1.770784
C	3.483972	1.837886	0.244874
C	-2.346055	2.279852	4.116101
C	-3.055561	3.607907	4.414683
C	-2.885829	2.625427	1.301337
C	-4.173114	1.802021	1.407848
H	0.823320	3.274481	0.706809
H	1.609059	4.264210	1.946830
H	-0.302738	3.981911	3.471573
H	-0.967714	4.469096	1.913490
H	2.641512	1.466216	4.639490
H	1.073006	2.214135	4.778133
H	2.062360	4.473367	4.198398
H	2.852890	3.745258	5.602789
H	3.664311	3.734446	4.032481
H	3.919718	0.994172	2.192597
H	3.916411	2.759971	2.151406
H	2.943182	0.978280	-0.168825
H	3.053520	2.747561	-0.193074
H	4.529081	1.776216	-0.087010
H	-1.568076	2.090394	4.867803
H	-3.054253	1.446082	4.209111
H	-3.467027	3.598906	5.433622
H	-2.371886	4.463512	4.345097
H	-3.889573	3.792971	3.726114
H	-2.481699	2.558460	0.284243
H	-3.106018	3.686149	1.486687
H	-3.982424	0.737893	1.226497
H	-4.635693	1.895913	2.398831
H	-4.911025	2.139252	0.667463

Table C18. Cartesian coordinates for optimized structure of **3**

Mo	-0.106016	0.112441	-3.201108
P	2.239594	-0.438177	-3.619922
P	0.848790	2.379114	-3.320369
N	-0.067478	0.112097	-1.136464
N	-0.023052	0.069234	0.016536
C	3.350219	0.998432	-3.124344
C	2.732910	2.316985	-3.604532
C	2.493457	-0.470045	-5.496350
C	3.912395	-0.524781	-6.080849
C	3.233963	-1.955616	-3.089702
C	4.751057	-1.826654	-2.884567
C	0.379406	3.527101	-4.741506
C	1.125802	4.861492	-4.883701
C	0.778318	3.582057	-1.875413
C	-0.588161	4.234590	-1.642674
H	3.409155	0.977116	-2.027424
H	4.373287	0.886553	-3.507917
H	2.894968	2.421910	-4.687584
H	3.222866	3.176936	-3.127894
H	1.916477	-1.332539	-5.858458
H	1.972642	0.418892	-5.881413
H	4.535966	0.307529	-5.729713
H	3.874983	-0.466613	-7.178117
H	4.421716	-1.460441	-5.820986
H	2.770025	-2.303347	-2.158019
H	3.015378	-2.730296	-3.840178
H	4.987022	-1.110165	-2.087974
H	5.269649	-1.495178	-3.791077
H	5.180024	-2.795788	-2.592521
H	0.506048	2.927927	-5.655956
H	-0.700916	3.707419	-4.651062
H	0.771100	5.412032	-5.766631
H	2.206826	4.713021	-5.001138
H	0.972923	5.508623	-4.010630
H	1.059245	2.991430	-0.995229
H	1.548416	4.355955	-2.007900
H	-1.360761	3.477063	-1.470596
H	-0.901074	4.847131	-2.498874
H	-0.561885	4.892459	-0.762456
P	-2.435013	0.682557	-3.732316
P	-1.107863	-2.120694	-3.108912
C	-3.571939	-0.838125	-3.605235
C	-2.945941	-1.930121	-2.726677
C	-3.516684	2.043022	-2.995376
C	-4.923405	2.282755	-3.562998
C	-2.671473	1.130013	-5.551046
C	-1.817186	0.315067	-6.529065
C	-0.576110	-3.340008	-1.788644
C	-1.364750	-4.644910	-1.613384
C	-1.247886	-3.268278	-4.600798
C	0.069642	-3.904620	-5.057982
H	-3.733007	-1.222010	-4.623224
H	-4.559140	-0.548457	-3.220849
H	-3.011216	-1.645999	-1.666613
H	-3.485300	-2.881325	-2.846263
H	-2.920701	2.961995	-3.081871
H	-3.576091	1.822547	-1.923324
H	-5.546702	1.379927	-3.520532
H	-5.440905	3.062925	-2.986268
H	-4.891522	2.615737	-4.607698
H	-2.420926	2.196454	-5.643378

H	-3.733936	1.029906	-5.815355
H	-0.743066	0.422071	-6.319233
H	-2.060451	-0.754472	-6.487413
H	-1.982089	0.647401	-7.564097
H	-0.579945	-2.755318	-0.859621
H	0.480995	-3.561960	-1.992732
H	-0.957362	-5.233077	-0.778399
H	-2.424193	-4.457938	-1.396319
H	-1.316500	-5.275264	-2.510705
H	-1.670734	-2.669693	-5.419239
H	-1.984186	-4.054080	-4.377438
H	0.816873	-3.140694	-5.306546
H	0.500684	-4.547586	-4.278934
H	-0.083852	-4.525918	-5.951409
Mo	0.021595	-0.000116	2.087365
P	-1.277918	-2.045766	2.495560
P	1.843010	-1.635892	2.065048
C	-0.158148	-3.584264	2.488754
C	1.133185	-3.345944	1.697237
C	-2.794723	-2.660509	1.554094
C	-3.503939	-3.942529	2.013641
C	-1.968708	-2.175590	4.245022
C	-1.028089	-1.633973	5.328006
C	3.260151	-1.567162	0.837987
C	4.209500	-2.770548	0.749948
C	2.787176	-2.071239	3.646337
C	3.885112	-1.085015	4.061671
H	0.084489	-3.814471	3.536500
H	-0.700970	-4.455107	2.096989
H	0.928299	-3.369406	0.618892
H	1.867703	-4.136472	1.908433
H	-3.501961	-1.820775	1.573224
H	-2.476622	-2.759605	0.507715
H	-2.830098	-4.808897	2.025591
H	-4.333402	-4.184994	1.333807
H	-3.926767	-3.835857	3.020308
H	-2.911025	-1.610063	4.256798
H	-2.223203	-3.222781	4.462680
H	-0.775559	-0.578733	5.148759
H	-0.088057	-2.200142	5.369853
H	-1.492728	-1.697586	6.322274
H	2.783866	-1.377865	-0.132778
H	3.823828	-0.654199	1.075295
H	5.002327	-2.586680	0.012221
H	3.681110	-3.682264	0.443781
H	4.698184	-2.977704	1.710818
H	2.036726	-2.143337	4.445905
H	3.219568	-3.076350	3.534578
H	3.489570	-0.069798	4.183551
H	4.691669	-1.038780	3.318336
H	4.335972	-1.383083	5.018640
P	1.290756	2.009853	2.619550
P	-1.813120	1.642333	2.284522
C	0.322479	3.558206	2.173078
C	-1.137904	3.399961	2.612506
C	1.358013	2.148896	4.510472
C	1.613745	3.524319	5.144183
C	3.058142	2.536380	2.245113
C	3.415618	2.581619	0.756034
C	-3.001922	1.519832	3.746839
C	-4.033023	2.638709	3.953548
C	-3.036066	2.024521	0.907958
C	-4.028662	0.893487	0.618086
H	0.385920	3.659245	1.082527
H	0.771806	4.461126	2.611510
H	-1.212601	3.570680	3.696515
H	-1.779872	4.149463	2.130023
H	2.136090	1.444363	4.834623
H	0.408766	1.739937	4.886899
H	0.811186	4.236449	4.914245
H	1.670786	3.436749	6.238437
H	2.558728	3.964411	4.801352
H	3.697269	1.801505	2.755222
H	3.261432	3.512314	2.709784
H	3.163021	1.635193	0.259875
H	2.879308	3.384456	0.236234
H	4.491209	2.761391	0.617927
H	-2.360936	1.432673	4.636829
H	-3.514336	0.552659	3.653353
H	-4.612296	2.465301	4.871621
H	-3.556111	3.622804	4.046619
H	-4.746845	2.692829	3.121859
H	-2.433058	2.228105	0.014171
H	-3.575167	2.951324	1.150941
H	-3.505741	-0.003370	0.266494
H	-4.608021	0.619655	1.510370
H	-4.749532	1.189556	-0.156478

Table C19. Cartesian coordinates for optimized structure of **4**

Mo	-2.435424	-0.000051	0.000018
P	0.137416	-0.003317	0.001899
P	-1.995033	-2.535693	-0.039462
N	-2.508147	-0.028207	-2.029167
N	-2.560006	-0.056391	-3.153822
C	0.648298	-1.693705	-0.590419
C	-0.149077	-2.785646	0.138384
C	0.940144	0.118797	1.681186
C	2.459582	-0.080066	1.770525
C	1.160617	1.156695	-1.032668
C	0.812776	1.185751	-2.526642
C	-2.695646	-3.571362	1.337622
C	-2.256357	-5.041646	1.389669
C	-2.348703	-3.519031	-1.582327
C	-3.832359	-3.782436	-1.864721
H	0.459736	-1.735309	-1.671305
H	1.726608	-1.842814	-0.448803
H	0.081389	-2.776727	1.212546
H	0.128676	-3.778095	-0.239039
H	0.667518	1.103919	2.081159
H	0.425150	-0.609679	2.320904
H	2.771951	-1.062062	1.394635
H	2.776881	-0.015845	2.819342
H	3.009353	0.687944	1.214136
H	1.034713	2.156245	-0.593042

H	2.216142	0.885208	-0.899706
H	-0.223261	1.496014	-2.698558
H	0.954002	0.205016	-2.997498
H	1.468214	1.896378	-3.046100
H	-2.421343	-3.056273	2.268662
H	-3.788998	-3.502939	1.262943
H	-2.719300	-5.537344	2.252493
H	-1.169164	-5.139438	1.495751
H	-2.559925	-5.591733	0.490759
H	-1.899930	-2.964514	-2.417216
H	-1.804925	-4.470337	-1.507308
H	-4.390959	-2.848246	-1.989959
H	-4.307016	-4.356431	-1.058935
H	-3.941411	-4.359920	-2.791396
P	-5.008264	0.003217	-0.001865
P	-2.875814	2.535591	0.039501
N	-2.362717	0.028108	2.029203
N	-2.310754	0.056278	3.153854
C	-5.519144	1.693603	0.590458
C	-4.721770	2.785546	-0.138343
C	-5.810992	-0.118887	-1.681153
C	-7.330430	0.079977	-1.770490
C	-6.031468	-1.156799	1.032694
C	-5.683627	-1.185870	2.526667
C	-2.175200	3.571263	-1.337582
C	-2.614490	5.041547	-1.389625
C	-2.522142	3.518925	1.582369
C	-1.038485	3.782322	1.864766
H	-5.330581	1.735204	1.671344
H	-6.597455	1.842713	0.448844
H	-4.952237	2.776629	-1.212505
H	-4.999522	3.777994	0.239082
H	-5.538367	-1.104008	-2.081131
H	-5.295998	0.609592	-2.320867
H	-7.642798	1.061970	-1.394594
H	-7.647729	0.015762	-2.819307
H	-7.880201	-0.688037	-1.214104
H	-5.905569	-2.156346	0.593059
H	-7.086992	-0.885306	0.899734
H	-4.647592	-1.496142	2.698580
H	-5.824845	-0.205138	2.997532
H	-6.339070	-1.896497	3.046120
H	-2.449504	3.056176	-2.268622
H	-1.081848	3.502839	-1.262902
H	-2.151547	5.537246	-2.252449
H	-3.701682	5.139339	-1.495707
H	-2.310921	5.591632	-0.490715
H	-2.970919	2.964409	2.417255
H	-3.065915	4.470234	1.507350
H	-0.479890	2.848129	1.990004
H	-0.563823	4.356315	1.058982
H	-0.929432	4.359805	2.791441

Table C20. Cartesian coordinates for optimized structure of **5** in the triplet state

Mo	0.022457	-3.269223	-0.303773
P	2.585743	-3.602659	-0.358327
P	0.415872	-3.414032	-2.848454
N	0.010563	-1.137572	-0.231552
N	-0.036072	0.004293	-0.147814
C	3.164329	-3.245397	-2.090544
C	2.214056	-3.866588	-3.122991
C	3.114286	-5.378685	-0.132447
C	4.613212	-5.700671	-0.067086
C	3.680942	-2.588881	0.756049
C	5.133014	-2.315709	0.332816
C	-0.455692	-4.800144	-3.737171
C	-0.053828	-5.038492	-5.199929
C	0.183333	-1.959975	-3.984623
C	-1.284333	-1.599708	-4.240287
H	3.205705	-2.158645	-2.209971
H	4.183798	-3.624544	-2.238331
H	2.272385	-4.962644	-3.079247
H	2.514156	-3.576082	-4.137947
H	2.615977	-5.750275	0.770178
H	2.653273	-5.928133	-0.963753
H	5.161163	-5.325530	-0.940098
H	4.749204	-6.789566	-0.037940
H	5.079427	-5.288030	0.834848
H	3.152824	-1.637333	0.878272
H	3.650781	-3.079205	1.739818
H	5.182720	-1.800278	-0.633113
H	5.728811	-3.229609	0.257142
H	5.611258	-1.666692	1.078265
H	-0.270421	-5.703753	-3.141735
H	-1.532769	-4.604012	-3.668145
H	-0.615779	-5.890912	-5.602444
H	1.013331	-5.270255	-5.299071
H	-0.273119	-4.170825	-5.833703
H	0.707004	-1.119233	-3.513508
H	0.698174	-2.164281	-4.933008
H	-1.829254	-1.453294	-3.299837
H	-1.800101	-2.384249	-4.807515
H	-1.357802	-0.671596	-4.820722
P	-2.560259	-3.381315	-0.263501
P	-0.349279	-3.472599	2.250317
N	-0.023095	-5.276998	-0.304346
N	-0.056946	-6.405756	-0.288598
C	-2.954953	-4.149010	1.387133
C	-2.200329	-3.441364	2.521869
C	-3.550036	-1.801816	-0.295367
C	-4.921469	-1.817489	0.395374
C	-3.567068	-4.401360	-1.461275
C	-3.349792	-5.919260	-1.458088
C	0.292176	-2.172030	3.412689
C	-0.204368	-2.229881	4.864688
C	0.126289	-5.067442	3.099017
C	1.596105	-5.168481	3.529909
H	-2.662133	-5.205228	1.332183
H	-4.036860	-4.128502	1.568971
H	-2.506079	-2.389087	2.581502
H	-2.442355	-3.901796	3.488403
H	-3.668966	-1.564641	-1.361593
H	-2.916345	-1.011784	0.120722
H	-4.831188	-1.938635	1.481700
H	-5.443089	-0.869746	0.212455

H	-5.567994	-2.620489	0.020912
H	-3.364538	-3.985216	-2.457667
H	-4.622199	-4.183497	-1.247481
H	-2.318566	-6.193901	-1.700062
H	-3.599534	-6.363918	-0.487280
H	-4.003835	-6.382798	-2.207668
H	0.035334	-1.209296	2.953896
H	1.388032	-2.239343	3.379226
H	0.254224	-1.422945	5.450839
H	-1.292078	-2.109131	4.928871
H	0.058993	-3.177336	5.349599
H	-0.121921	-5.885733	2.411955
H	-0.523929	-5.186150	3.976019
H	2.286007	-4.987993	2.697700
H	1.837514	-4.452425	4.324328
H	1.802447	-6.173960	3.917166
Mo	-0.026171	2.159192	0.062536
P	-1.757221	2.180965	1.980316
P	1.530116	2.107273	2.086801
N	0.120667	4.148177	0.312816
N	0.211644	5.262567	0.469296
C	-0.817284	2.688830	3.510304
C	0.499216	1.910958	3.635340
C	-2.595626	0.589207	2.482507
C	-3.166411	0.481324	3.903586
C	-3.223431	3.342296	2.014812
C	-2.926652	4.847188	1.989855
C	2.786979	0.746426	2.219965
C	3.638005	0.687105	3.495875
C	2.500880	3.639561	2.517081
C	3.637101	3.987749	1.549184
H	-0.614339	3.764020	3.422584
H	-1.439084	2.557574	4.404699
H	0.301963	0.840133	3.776480
H	1.066281	2.251803	4.511216
H	-3.399746	0.446897	1.747998
H	-1.873016	-0.214948	2.300872
H	-2.378412	0.506888	4.665253
H	-3.702304	-0.470486	4.016890
H	-3.880581	1.282688	4.127437
H	-3.859397	3.066155	1.163220
H	-3.797914	3.101580	2.919229
H	-2.379363	5.150219	1.091922
H	-2.341848	5.162696	2.862208
H	-3.871117	5.405956	2.010745
H	2.214652	-0.181610	2.100213
H	3.432113	0.825766	1.334652
H	4.302099	-0.186484	3.458362
H	3.019557	0.596627	4.397181
H	4.270695	1.575328	3.607869
H	1.786521	4.470965	2.568316
H	2.896588	3.504889	3.532531
H	3.260327	4.175422	0.537416
H	4.385198	3.186792	1.490252
H	4.151892	4.896893	1.884472
P	1.559879	2.590845	-1.894467
P	-1.666652	2.543523	-1.907527
C	0.697108	2.001634	-3.432255
C	-0.692956	2.644293	-3.521913
C	1.865223	4.397917	-2.264175
C	2.536925	4.747846	-3.599739
C	3.283284	1.907457	-2.025902
C	3.371616	0.383200	-1.968087
C	-2.518302	4.204942	-1.877733
C	-3.335124	4.590806	-3.119388
C	-3.056777	1.392532	-2.380046
C	-4.276899	1.443238	-1.454467
H	0.607315	0.912526	-3.354528
H	1.285549	2.219582	-4.333202
H	-0.595304	3.707331	-3.777083
H	-1.279798	2.182830	-4.325682
H	2.466160	4.785240	-1.430748
H	0.899356	4.911917	-2.191096
H	1.946227	4.412539	-4.460963
H	2.641349	5.837541	-3.679709
H	3.540831	4.317067	-3.688398
H	3.854579	2.357924	-1.203194
H	3.729604	2.270104	-2.960502
H	2.913504	-0.014175	-1.054070
H	2.869732	-0.072677	-2.830570
H	4.421336	0.064153	-1.991364
H	-1.730989	4.948830	-1.697865
H	-3.157429	4.223383	-0.985969
H	-3.753494	5.597013	-2.988391
H	-2.720803	4.605666	-4.027758
H	-4.173451	3.905351	-3.291769
H	-2.631712	0.382161	-2.399635
H	-3.359481	1.627984	-3.409130
H	-4.008826	1.211487	-0.417193
H	-4.757541	2.428758	-1.466769
H	-5.027539	0.710357	-1.776162

Table C21. Cartesian coordinates for optimized structure of **5** in the singlet state

Mo	0.009537	-3.102357	-0.281521
P	2.525367	-3.579110	-0.338838
P	0.394046	-3.272383	-2.778486
N	0.022457	-1.089441	-0.208118
N	-0.008491	0.086974	-0.134179
C	3.152371	-3.187791	-2.048122
C	2.191220	-3.735128	-3.106858
C	3.027617	-5.368659	-0.148194
C	4.523341	-5.701474	-0.060526
C	3.600128	-2.596032	0.823502
C	5.071053	-2.350917	0.450302
C	-0.460883	-4.653509	-3.701656
C	-0.016363	-4.903768	-5.150488
C	0.136387	-1.814545	-3.912981
C	-1.322005	-1.584529	-4.329675
H	3.228326	-2.099675	-2.127801
H	4.161120	-3.596667	-2.190982
H	2.235946	-4.833134	-3.122628
H	2.490306	-3.395097	-4.106415
H	2.513196	-5.763141	0.735119
H	2.586955	-5.889288	-1.008415

H	5.094049	-5.298820	-0.905870
H	4.649711	-6.791761	-0.068930
H	4.969374	-5.326560	0.867304
H	3.087613	-1.634300	0.933940
H	3.525353	-3.089961	1.802007
H	5.166639	-1.839264	-0.513799
H	5.652579	-3.275427	0.399580
H	5.532531	-1.708714	1.212169
H	-0.306417	-5.562407	-3.104880
H	-1.537204	-4.445223	-3.667833
H	-0.599426	-5.728107	-5.581246
H	1.042149	-5.182630	-5.211116
H	-0.169169	-4.024208	-5.787629
H	0.519021	-0.942877	-3.370100
H	0.765874	-1.938102	-4.804446
H	-1.994784	-1.558790	-3.463928
H	-1.677766	-2.373373	-5.002698
H	-1.421628	-0.628854	-4.859483
P	-2.522915	-3.477638	-0.281658
P	-0.402515	-3.335721	2.214456
N	-0.044638	-5.188472	-0.275054
N	-0.066665	-6.308149	-0.249825
C	-2.984277	-4.136668	1.400490
C	-2.259120	-3.361129	2.507445
C	-3.472691	-1.881392	-0.448886
C	-4.888211	-1.850886	0.146306
C	-3.517991	-4.557796	-1.435513
C	-3.241630	-6.066296	-1.434590
C	0.193862	-2.068755	3.441022
C	-0.314673	-2.180794	4.885513
C	0.066994	-4.940099	3.064089
C	1.531030	-5.063974	3.506058
H	-2.700870	-5.197405	1.427537
H	-4.072267	-4.099166	1.538190
H	-2.607206	-2.320453	2.526283
H	-2.486344	-3.794590	3.489871
H	-3.511879	-1.688561	-1.529560
H	-2.852391	-1.088391	-0.019109
H	-4.877851	-1.946114	1.238640
H	-5.370564	-0.895768	-0.096093
H	-5.527343	-2.646121	-0.255061
H	-3.372582	-4.142047	-2.441276
H	-4.572257	-4.385811	-1.179465
H	-2.234323	-6.305651	-1.788726
H	-3.367732	-6.506465	-0.437851
H	-3.953293	-6.565865	-2.104021
H	-0.072868	-1.093873	3.016172
H	1.290667	-2.117363	3.419597
H	0.121827	-1.382848	5.500733
H	-1.404976	-2.084598	4.944799
H	-0.035239	-3.136455	5.344858
H	-0.189864	-5.762317	2.384965
H	-0.587072	-5.050769	3.939185
H	2.230323	-4.931647	2.673104
H	1.787912	-4.326989	4.276418
H	1.709745	-6.060164	3.930301
Mo	-0.059771	2.084038	0.057853
P	-1.845149	2.166453	1.881464
P	1.390239	2.113481	2.143880
N	-0.023185	4.155830	0.348194
N	0.020748	5.259483	0.528170
C	-1.009712	2.708758	3.462802
C	0.309985	1.956281	3.667108
C	-2.657964	0.548728	2.339356
C	-3.267254	0.416577	3.742396
C	-3.361910	3.265912	1.848782
C	-3.149666	4.785389	1.871994
C	2.628609	0.742524	2.321285
C	3.376237	0.632782	3.656867
C	2.370996	3.637459	2.600992
C	3.620772	3.916026	1.758382
H	-0.821483	3.787352	3.380140
H	-1.680590	2.572849	4.320164
H	0.119420	0.888420	3.835001
H	0.838688	2.331687	4.552715
H	-3.436559	0.395458	1.580437
H	-1.910944	-0.234996	2.172305
H	-2.501802	0.450627	4.526724
H	-3.786839	-0.546668	3.832712
H	-4.003621	1.201178	3.953125
H	-3.928820	2.980025	0.952701
H	-3.979135	2.979163	2.710704
H	-2.611057	5.146306	0.990018
H	-2.598349	5.110518	2.762460
H	-4.124419	5.289516	1.890404
H	2.068768	-0.178311	2.120449
H	3.335819	0.858055	1.488974
H	4.062514	-0.223902	3.627917
H	2.687549	0.478490	4.496517
H	3.974445	1.526892	3.868902
H	1.686484	4.494078	2.555406
H	2.654076	3.528239	3.656273
H	3.381562	4.048998	0.697751
H	4.356421	3.106152	1.839452
H	4.105971	4.837246	2.104798
P	1.664052	2.580654	-1.736927
P	-1.512733	2.559722	-1.984840
C	0.937147	2.076915	-3.376968
C	-0.455907	2.692325	-3.546626
C	1.980212	4.408400	-2.001048
C	2.842042	4.822444	-3.202239
C	3.393222	1.900376	-1.789308
C	3.454937	0.375749	-1.861544
C	-2.415145	4.193466	-2.018784
C	-3.170985	4.536194	-3.310865
C	-2.835588	1.352288	-2.502370
C	-4.125173	1.397854	-1.675943
H	0.872610	0.983916	-3.374034
H	1.593912	2.361188	-4.209748
H	-0.364381	3.759771	-3.786386
H	-0.986879	2.227239	-4.386472
H	2.428319	4.791640	-1.075392
H	0.998073	4.891659	-2.074533
H	2.427750	4.468139	-4.153921
H	2.889488	5.917845	-3.254387
H	3.871571	4.455712	-3.121957

H	3.897008	2.259801	-0.882261
H	3.921575	2.336345	-2.646313
H	2.894025	-0.083144	-1.038121
H	3.038937	0.006862	-2.807262
H	4.495771	0.033652	-1.802491
H	-1.665354	4.968011	-1.810037
H	-3.102739	4.198183	-1.163790
H	-3.641433	5.522955	-3.213417
H	-2.502897	4.574147	-4.179582
H	-3.964841	3.811934	-3.528375
H	-2.380131	0.357556	-2.442533
H	-3.064367	1.534557	-3.560850
H	-3.935959	1.197936	-0.615134
H	-4.627435	2.369583	-1.751843
H	-4.829052	0.637870	-2.038338

Table C22. Cartesian coordinates for optimized structure of **6** in the triplet state

Mo	0.003807	0.035915	1.956113
P	2.394000	0.620521	2.288031
P	1.020929	-2.268461	2.228417
N	-0.024470	-0.018570	0.026235
N	0.000194	-0.014309	-1.182152
C	3.457018	-0.836843	1.801474
C	2.895513	-2.126686	2.415986
C	2.655185	0.729504	4.142654
C	4.089149	0.724186	4.693504
C	3.281046	2.126592	1.620815
C	4.799217	2.036050	1.403152
C	0.588160	-3.316969	3.713282
C	1.357183	-4.634390	3.888724
C	0.871543	-3.473018	0.813594
C	-0.510248	-4.115092	0.651402
H	3.436841	-0.889259	0.704825
H	4.502780	-0.692694	2.099705
H	3.112595	-2.148585	3.493031
H	3.384493	-3.006835	1.979612
H	2.139985	1.643090	4.468035
H	2.089943	-0.103150	4.585997
H	4.652165	-0.162343	4.376691
H	4.061918	0.722045	5.791044
H	4.647552	1.613111	4.380318
H	2.783046	2.385789	0.677765
H	3.042052	2.942596	2.317478
H	5.056398	1.273415	0.658131
H	5.338355	1.795934	2.325563
H	5.179403	2.998354	1.036869
H	0.730862	-2.676319	4.595116
H	-0.490142	-3.514674	3.654368
H	1.025239	-5.142910	4.803182
H	2.437941	-4.469663	3.975819
H	1.187254	-5.320674	3.050149
H	1.135514	-2.908697	-0.087989
H	1.637304	-4.249939	0.942520
H	-1.283389	-3.359345	0.475732
H	-0.798696	-4.696035	1.536381
H	-0.512119	-4.803431	-0.204102
P	-2.363001	-0.508036	2.714294
P	-1.008675	2.325002	1.965395
C	-3.406854	1.062521	2.707832
C	-2.855624	2.114444	1.733576
C	-3.465096	-1.783570	1.919059
C	-4.849206	-2.023865	2.538105
C	-2.424367	-1.020851	4.510633
C	-1.487172	-0.236296	5.440137
C	-0.517778	3.505895	0.617668
C	-1.313360	4.811234	0.482589
C	-0.980037	3.405538	3.495737
C	0.346145	4.125112	3.770757
H	-3.410826	1.460806	3.731480
H	-4.448867	0.821894	2.463870
H	-3.011965	1.787896	0.696152
H	-3.382838	3.069399	1.861789
H	-2.887537	-2.716662	1.917285
H	-3.562970	-1.478666	0.870748
H	-5.458240	-1.111953	2.564687
H	-5.396935	-2.765560	1.941903
H	-4.776629	-2.411638	3.560909
H	-2.167067	-2.088189	4.536367
H	-3.459914	-0.934720	4.866004
H	-0.436913	-0.302263	5.118558
H	-1.758133	0.825981	5.492743
H	-1.541576	-0.636038	6.460824
H	-0.566075	2.920290	-0.308257
H	0.547175	3.720444	0.779597
H	-0.912978	5.412122	-0.344720
H	-2.374146	4.626377	0.274104
H	-1.252335	5.422029	1.391441
H	-1.239807	2.766894	4.349791
H	-1.791236	4.140714	3.401493
H	1.179420	3.419748	3.866951
H	0.599345	4.834550	2.973436
H	0.280733	4.691232	4.708585
Mo	0.019937	0.003796	-3.111015
P	-1.306313	2.108364	-3.570277
P	1.885344	1.679400	-3.292628
C	-0.151669	3.604143	-3.606597
C	1.172442	3.357069	-2.869297
C	-2.763599	2.641765	-2.531947
C	-3.436583	3.980797	-2.863675
C	-2.050918	2.176968	-5.282879
C	-1.137483	1.651461	-6.397565
C	3.401785	1.574167	-2.220877
C	4.318436	2.805755	-2.192871
C	2.598715	2.018032	-4.997160
C	3.790292	1.145626	-5.415583
H	0.047544	3.828179	-4.663614
H	-0.661135	4.484187	-3.195685
H	1.017873	3.363318	-1.782746
H	1.889955	4.155220	-3.102005
H	-3.489041	1.823635	-2.627323
H	-2.429335	2.630007	-1.487696
H	-2.752014	4.829851	-2.750599
H	-4.280320	4.148953	-2.181470
H	-3.831814	3.998067	-3.886109

H	-2.973961	1.584391	-5.244804
H	-2.346821	3.212358	-5.498670
H	-0.784802	0.630738	-6.187586
H	-0.256144	2.290055	-6.536725
H	-1.674399	1.625722	-7.354320
H	3.041154	1.333955	-1.213168
H	3.953771	0.687389	-2.560286
H	5.220787	2.593862	-1.605922
H	3.820899	3.669465	-1.735522
H	4.641807	3.100413	-3.198757
H	1.780170	1.887860	-5.716599
H	2.885509	3.077970	-5.038432
H	3.554281	0.075916	-5.373810
H	4.667846	1.318596	-4.781807
H	4.078315	1.378645	-6.448643
P	1.300423	-2.057751	-3.737017
P	-1.854102	-1.683339	-3.403411
C	0.304566	-3.570614	-3.291138
C	-1.146883	-3.403870	-3.760194
C	1.271570	-2.062670	-5.614675
C	1.505413	-3.401488	-6.329895
C	3.065665	-2.555805	-3.407720
C	3.428636	-2.747062	-1.932028
C	-3.012999	-1.478455	-4.858535
C	-4.020217	-2.607041	-5.122456
C	-3.038151	-2.053774	-2.010875
C	-4.066922	-0.951852	-1.733126
H	0.347177	-3.669344	-2.199614
H	0.751073	-4.478703	-3.718490
H	-1.201722	-3.549605	-4.847339
H	-1.789663	-4.169487	-3.307916
H	2.034134	-1.336978	-5.926778
H	0.308869	-1.632624	-5.927398
H	0.730524	-4.139347	-6.090126
H	1.489653	-3.247858	-7.416594
H	2.478277	-3.837373	-6.073351
H	3.688211	-1.764241	-3.845944
H	3.278032	-3.476093	-3.968647
H	3.201765	-1.847791	-1.345744
H	2.888470	-3.591285	-1.487918
H	4.501901	-2.952877	-1.830243
H	-2.377306	-1.327999	-5.742714
H	-3.543167	-0.529947	-4.703548
H	-4.616342	-2.374174	-6.014378
H	-3.522996	-3.568364	-5.299447
H	-4.717070	-2.737113	-4.285664
H	-2.423973	-2.239964	-1.121096
H	-3.549549	-2.996164	-2.248347
H	-3.584957	-0.034729	-1.376565
H	-4.652026	-0.702483	-2.627227
H	-4.780200	-1.280128	-0.966314

Table C23. Cartesian coordinates for optimized structure of **6** in the singlet state

Mo	0.034809	0.015534	1.925583
P	2.445290	0.393356	2.458000
P	0.816773	-2.353131	2.139805
N	0.003579	-0.023941	0.001210
N	-0.009066	0.001717	-1.207097
C	3.400492	-1.132499	1.972920
C	2.680730	-2.391895	2.467376
C	2.638808	0.487051	4.314808
C	4.065457	0.490738	4.883487
C	3.444440	1.824250	1.788608
C	4.944680	1.601697	1.541629
C	0.222079	-3.402854	3.573382
C	0.894318	-4.768294	3.778445
C	0.647840	-3.537133	0.701242
C	-0.743517	-4.166038	0.555525
H	3.462380	-1.127132	0.877410
H	4.428416	-1.094706	2.354742
H	2.810792	-2.487901	3.554273
H	3.126599	-3.288227	2.018125
H	2.108740	1.394467	4.632237
H	2.071394	-0.355178	4.734234
H	4.630805	-0.401326	4.587991
H	4.022435	0.506247	5.980131
H	4.627074	1.375363	4.562718
H	2.955328	2.123287	0.853596
H	3.289832	2.656570	2.488335
H	5.119905	0.825288	0.787595
H	5.480322	1.313188	2.452583
H	5.396137	2.531026	1.170779
H	0.347636	-2.785606	4.474356
H	-0.860767	-3.531520	3.442601
H	0.457771	-5.276236	4.648480
H	1.971336	-4.670287	3.960194
H	0.760102	-5.426150	2.911166
H	0.892968	-2.949444	-0.191069
H	1.409002	-4.324150	0.791004
H	-1.531122	-3.403897	0.538750
H	-0.965090	-4.857348	1.377442
H	-0.813011	-4.736765	-0.379982
P	-2.323661	-0.306916	2.828601
P	-0.783208	2.355779	1.893585
C	-3.236724	1.333753	2.811980
C	-2.654458	2.283135	1.755207
C	-3.499832	-1.500718	2.021229
C	-4.887221	-1.655344	2.660443
C	-2.363906	-0.805431	4.622296
C	-1.284930	-0.132415	5.482614
C	-0.314320	3.476684	0.483609
C	-1.022443	4.832759	0.359723
C	-0.628448	3.489208	3.382119
C	0.748964	4.128740	3.594870
H	-3.140740	1.774244	3.813807
H	-4.308452	1.169535	2.644530
H	-2.887693	1.914550	0.745815
H	-3.100557	3.281789	1.853004
H	-2.981938	-2.467900	2.002329
H	-3.590297	-1.177370	0.976771
H	-5.440956	-0.709067	2.686359
H	-5.484037	-2.368452	2.077121
H	-4.822850	-2.038756	3.685559
H	-2.240040	-1.895641	4.649813

H	-3.362658	-0.585558	5.022274
H	-0.274310	-0.359222	5.112503
H	-1.400526	0.958649	5.507265
H	-1.344839	-0.491374	6.517890
H	-0.474444	2.868803	-0.415617
H	0.772546	3.620505	0.557567
H	-0.635586	5.385246	-0.507320
H	-2.104676	4.719939	0.221439
H	-0.861673	5.460512	1.244549
H	-0.898645	2.898111	4.267351
H	-1.391659	4.274374	3.288378
H	1.529670	3.373329	3.738699
H	1.044385	4.758420	2.746405
H	0.736769	4.764392	4.489562
Mo	-0.032492	0.040566	-3.115043
P	-1.489506	2.037027	-3.533889
P	1.695948	1.844904	-3.385006
C	-0.466377	3.620280	-3.695870
C	0.914855	3.507516	-3.041710
C	-2.940420	2.552702	-2.468667
C	-3.781042	3.757945	-2.913500
C	-2.283515	1.987744	-5.229473
C	-1.337347	1.572770	-6.366128
C	3.191940	1.844554	-2.278746
C	4.038001	3.125757	-2.250184
C	2.406370	2.122539	-5.101665
C	3.689538	1.351030	-5.441385
H	-0.356537	3.826337	-4.768854
H	-1.021667	4.466831	-3.273873
H	0.833595	3.593951	-1.952097
H	1.572956	4.317044	-3.384392
H	-3.578495	1.663451	-2.388351
H	-2.531638	2.725629	-1.464457
H	-3.180979	4.670626	-3.014097
H	-4.562509	3.961288	-2.169316
H	-4.280303	3.575062	-3.872242
H	-3.128826	1.291039	-5.167192
H	-2.705990	2.977452	-5.448803
H	-0.845415	0.606404	-6.177886
H	-0.548982	2.319050	-6.526594
H	-1.891381	1.479830	-7.309163
H	2.817602	1.608325	-1.274222
H	3.802198	0.984577	-2.583384
H	4.917306	2.980844	-1.609224
H	3.472839	3.976354	-1.851211
H	4.398582	3.402943	-3.248419
H	1.616756	1.866582	-5.820692
H	2.588293	3.200191	-5.213399
H	3.574526	0.269061	-5.310743
H	4.534869	1.672128	-4.822049
H	3.962009	1.528059	-6.489658
P	1.405333	-1.919685	-3.721774
P	-1.757239	-1.806026	-3.462013
C	0.527892	-3.521782	-3.330721
C	-0.924041	-3.464347	-3.818511
C	1.457153	-1.936119	-5.601415
C	2.016840	-3.191477	-6.287987
C	3.181521	-2.295279	-3.294134
C	3.485895	-2.276906	-1.792676
C	-2.933763	-1.691067	-4.910444
C	-3.853922	-2.895592	-5.157412
C	-2.896587	-2.232734	-2.049760
C	-4.006127	-1.211816	-1.774320
H	0.565085	-3.647154	-2.241944
H	1.053505	-4.378517	-3.773662
H	-0.953036	-3.606383	-4.907303
H	-1.517417	-4.276086	-3.379028
H	2.039166	-1.056424	-5.904745
H	0.431440	-1.752878	-5.950804
H	1.435454	-4.088371	-6.041510
H	1.981796	-3.066209	-7.378021
H	3.060997	-3.377693	-6.010768
H	3.791339	-1.539874	-3.808314
H	3.452146	-3.268696	-3.724999
H	3.186569	-1.321287	-1.344446
H	2.961270	-3.079904	-1.261115
H	4.561022	-2.413321	-1.618096
H	-2.316354	-1.500030	-5.799398
H	-3.534673	-0.786163	-4.759048
H	-4.475220	-2.712397	-6.043578
H	-3.287236	-3.817084	-5.336331
H	-4.530258	-3.073144	-4.312551
H	-2.260567	-2.349786	-1.165288
H	-3.333272	-3.217819	-2.261851
H	-3.595280	-0.256092	-1.430132
H	-4.620108	-1.018032	-2.662700
H	-4.679584	-1.590907	-0.994706

Table C24. Cartesian coordinates for optimized structure of **7** in the triplet state

Mo	-0.000555	0.028637	1.941214
P	2.390217	0.612636	2.270974
P	1.015355	-2.277734	2.217280
N	-0.031205	-0.023969	0.025748
N	0.003786	-0.009737	-1.232331
C	3.451218	-0.847438	1.788722
C	2.889055	-2.134610	2.408468
C	2.654241	0.728947	4.124479
C	4.089343	0.723827	4.672234
C	3.274696	2.115823	1.594834
C	4.791622	2.022587	1.369931
C	0.580074	-3.329146	3.698961
C	1.347339	-4.648016	3.871216
C	0.868297	-3.476170	0.797585
C	-0.513741	-4.116657	0.631202
H	3.430050	-0.904004	0.692375
H	4.497328	-0.703117	2.085641
H	3.103599	-2.151455	3.486158
H	3.379514	-3.016460	1.977177
H	2.140902	1.644736	4.446560
H	2.088253	-0.100771	4.572394
H	4.649554	-0.166005	4.359716
H	4.064647	0.728707	5.769816
H	4.649099	1.609424	4.352039
H	2.772012	2.372178	0.653445

H	3.040029	2.934225	2.290179
H	5.043825	1.257430	0.625781
H	5.334962	1.784319	2.290395
H	5.171380	2.983301	0.999071
H	0.723433	-2.690860	4.582425
H	-0.498482	-3.525212	3.639107
H	1.014631	-5.158428	4.784335
H	2.428295	-4.484834	3.958773
H	1.176566	-5.331860	3.030829
H	1.133324	-2.907324	-0.100802
H	1.633551	-4.253920	0.924641
H	-1.286276	-3.359271	0.460232
H	-0.802470	-4.702987	1.512534
H	-0.515760	-4.799597	-0.228630
P	-2.368599	-0.512953	2.704735
P	-1.011098	2.319517	1.947761
C	-3.410062	1.058766	2.692986
C	-2.857419	2.106389	1.714668
C	-3.468051	-1.789946	1.908902
C	-4.854533	-2.027003	2.523824
C	-2.429694	-1.021656	4.501765
C	-1.487890	-0.237552	5.427061
C	-0.518298	3.491386	0.593516
C	-1.311757	4.797313	0.451907
C	-0.983552	3.406760	3.472912
C	0.343522	4.125375	3.746285
H	-3.413212	1.460596	3.715269
H	-4.452509	0.818906	2.450088
H	-3.011329	1.774713	0.678511
H	-3.385614	3.061508	1.837443
H	-2.890907	-2.723315	1.912418
H	-3.561480	-1.488626	0.859122
H	-5.463770	-1.115038	2.542570
H	-5.399748	-2.772275	1.929800
H	-4.785947	-2.408707	3.549208
H	-2.175632	-2.089747	4.529749
H	-3.464376	-0.931246	4.858600
H	-0.438343	-0.310441	5.104580
H	-1.753461	0.826314	5.475225
H	-1.543292	-0.632534	6.449539
H	-0.567588	2.899088	-0.328156
H	0.547000	3.705100	0.754015
H	-0.911769	5.392896	-0.379455
H	-2.373242	4.613324	0.246180
H	-1.248230	5.413301	1.357101
H	-1.245828	2.772840	4.329772
H	-1.793323	4.142870	3.373721
H	1.175332	3.418978	3.847559
H	0.599244	4.829979	2.945490
H	0.277657	4.696673	4.680925
Mo	0.023692	0.010037	-3.146392
P	-1.304165	2.114619	-3.608581
P	1.890506	1.687966	-3.330800
C	-0.148868	3.609679	-3.645205
C	1.173659	3.362842	-2.904736
C	-2.759248	2.647190	-2.567380
C	-3.434105	3.985134	-2.899678
C	-2.049940	2.181829	-5.320386
C	-1.136965	1.655358	-6.435072
C	3.406762	1.581695	-2.259497
C	4.322689	2.813755	-2.229156
C	2.601068	2.027832	-5.035697
C	3.792815	1.156098	-5.455172
H	0.052434	3.832517	-4.702088
H	-0.658637	4.490355	-3.236109
H	1.015761	3.364881	-1.818615
H	1.890296	4.163110	-3.132872
H	-3.484105	1.828246	-2.659865
H	-2.422367	2.637124	-1.523988
H	-2.749949	4.834924	-2.789648
H	-4.276248	4.153680	-2.215614
H	-3.831895	4.000426	-3.921156
H	-2.972680	1.588804	-5.280956
H	-2.346439	3.216863	-5.537071
H	-0.784116	0.634892	-6.224099
H	-0.255798	2.293960	-6.575378
H	-1.674410	1.628538	-7.391484
H	3.046103	1.339238	-1.252463
H	3.959220	0.695956	-2.600771
H	5.225011	2.600980	-1.642432
H	3.824736	3.676247	-1.769998
H	4.646141	3.110588	-3.234394
H	1.781794	1.896875	-5.754190
H	2.886913	3.088018	-5.077267
H	3.557505	0.086235	-5.412751
H	4.670876	1.329894	-4.822336
H	4.079538	1.389026	-6.488595
P	1.305463	-2.051670	-3.770227
P	-1.850233	-1.677579	-3.435254
C	0.309097	-3.562655	-3.319726
C	-1.142109	-3.397608	-3.790302
C	1.277787	-2.061264	-5.647414
C	1.511893	-3.401944	-6.358978
C	3.070116	-2.547415	-3.435907
C	3.429953	-2.730693	-1.958353
C	-3.017369	-1.477991	-4.883763
C	-4.024958	-2.608494	-5.137859
C	-3.021335	-2.042579	-2.030882
C	-4.052941	-0.943134	-1.753532
H	0.350779	-3.657023	-2.227746
H	0.755829	-4.472403	-3.743295
H	-1.196118	-3.544405	-4.877368
H	-1.784492	-4.163280	-3.337520
H	2.040620	-1.336338	-5.960799
H	0.315333	-1.631520	-5.961221
H	0.736628	-4.138973	-6.117875
H	1.497146	-3.251215	-7.446084
H	2.484432	-3.837320	-6.100293
H	3.693273	-1.758056	-3.877260
H	3.283486	-3.470636	-3.991657
H	3.203573	-1.827596	-1.377836
H	2.887084	-3.571157	-1.510387
H	4.502592	-2.938189	-1.853418
H	-2.386535	-1.330104	-5.771889
H	-3.547228	-0.529246	-4.729010
H	-4.627822	-2.378578	-6.025996

H	-3.527527	-3.569459	-5.316153
H	-4.715487	-2.737537	-4.295671
H	-2.398291	-2.217661	-1.144951
H	-3.530140	-2.989186	-2.257017
H	-3.572379	-0.022596	-1.404260
H	-4.644132	-0.700780	-2.645576
H	-4.760676	-1.270155	-0.981079

Table C25. Cartesian coordinates for optimized structure of **7** in the singlet state

Mo	0.039132	0.001584	1.912392
P	2.453550	0.368580	2.443708
P	0.807501	-2.373105	2.136555
N	0.007165	-0.044999	0.001349
N	-0.014853	0.013886	-1.255726
C	3.399127	-1.170873	1.982729
C	2.666266	-2.419295	2.485716
C	2.644798	0.493296	4.298291
C	4.069575	0.488829	4.871548
C	3.459743	1.780498	1.747585
C	4.960400	1.549762	1.511251
C	0.195400	-3.426756	3.559421
C	0.858205	-4.797341	3.761271
C	0.648144	-3.545757	0.688572
C	-0.745180	-4.166339	0.526858
H	3.468325	-1.178493	0.887495
H	4.424808	-1.136739	2.370936
H	2.781497	-2.502500	3.575468
H	3.111790	-3.324154	2.053557
H	2.125418	1.413124	4.597104
H	2.064821	-0.333323	4.731332
H	4.624477	-0.415427	4.593879
H	4.023387	0.524490	5.967586
H	4.643377	1.360326	4.536826
H	2.975648	2.057811	0.803526
H	3.303508	2.629376	2.426763
H	5.137061	0.753435	0.778665
H	5.493223	1.285037	2.431036
H	5.413768	2.468537	1.117042
H	0.320356	-2.815308	4.464396
H	-0.887456	-3.547992	3.421604
H	0.411657	-5.308091	4.624558
H	1.934203	-4.706526	3.952523
H	0.727309	-5.449011	2.888851
H	0.902869	-2.951668	-0.196757
H	1.405124	-4.336702	0.779335
H	-1.527787	-3.399093	0.506669
H	-0.978340	-4.860621	1.343084
H	-0.809293	-4.731819	-0.412210
P	-2.320382	-0.306060	2.816550
P	-0.768056	2.345370	1.867717
C	-3.224158	1.339114	2.797951
C	-2.640152	2.280764	1.735431
C	-3.498431	-1.494974	2.005033
C	-4.889496	-1.641961	2.637942
C	-2.365748	-0.803467	4.610238
C	-1.280535	-0.139043	5.469553
C	-0.300842	3.448880	0.444122
C	-1.002655	4.807667	0.313552
C	-0.601487	3.489069	3.347015
C	0.776967	4.132199	3.542543
H	-3.120852	1.782390	3.797878
H	-4.297635	1.180919	2.635860
H	-2.878000	1.908856	0.728280
H	-3.081115	3.282010	1.829812
H	-2.984714	-2.464499	1.989982
H	-3.582229	-1.172953	0.959556
H	-5.439893	-0.693568	2.656619
H	-5.485973	-2.355563	2.054898
H	-4.831762	-2.020841	3.665167
H	-2.251632	-1.894679	4.638898
H	-3.362520	-0.574308	5.009960
H	-0.272152	-0.376401	5.099796
H	-1.385491	0.953199	5.491774
H	-1.343956	-0.495279	6.505549
H	-0.470811	2.831806	-0.447214
H	0.787419	3.586427	0.509044
H	-0.619462	5.351853	-0.560388
H	-2.086403	4.699289	0.184034
H	-0.832582	5.441751	1.192106
H	-0.862699	2.902906	4.238397
H	-1.366528	4.272744	3.255499
H	1.560836	3.379390	3.682821
H	1.062566	4.757650	2.687634
H	0.772393	4.772860	4.433727
Mo	-0.039534	0.054470	-3.149040
P	-1.507647	2.045492	-3.573646
P	1.681082	1.868422	-3.421993
C	-0.491422	3.631884	-3.741076
C	0.889953	3.527788	-3.086245
C	-2.959050	2.550662	-2.505538
C	-3.796399	3.763013	-2.936553
C	-2.301506	1.987600	-5.268444
C	-1.350469	1.579742	-6.403753
C	3.165565	1.879153	-2.301677
C	4.012860	3.159524	-2.276470
C	2.399616	2.143865	-5.135002
C	3.686995	1.375538	-5.466056
H	-0.382257	3.833779	-4.814896
H	-1.050579	4.477825	-3.323278
H	0.807832	3.617774	-1.997042
H	1.544218	4.339350	-3.431464
H	-3.598570	1.661184	-2.439939
H	-2.553041	2.708228	-1.497696
H	-3.196417	4.678021	-3.013101
H	-4.585737	3.951217	-2.196729
H	-4.285507	3.597939	-3.903752
H	-3.140300	1.283123	-5.205749
H	-2.732678	2.973304	-5.489042
H	-0.850524	0.617866	-6.213849
H	-0.568262	2.332492	-6.564221
H	-1.902643	1.480999	-7.347247
H	2.775998	1.655991	-1.299972
H	3.778208	1.014555	-2.587728
H	4.881924	3.021123	-1.620140

H	3.443142	4.015816	-1.896684
H	4.389404	3.423724	-3.272285
H	1.614316	1.883800	-5.857438
H	2.578804	3.221790	-5.248301
H	3.573611	0.293146	-5.337941
H	4.526958	1.697589	-4.839960
H	3.966789	1.554714	-6.512020
P	1.413297	-1.897641	-3.747946
P	-1.751798	-1.802072	-3.496805
C	0.543095	-3.502033	-3.351630
C	-0.906689	-3.455072	-3.847519
C	1.470677	-1.921001	-5.627470
C	2.031850	-3.179150	-6.307477
C	3.189882	-2.257008	-3.310146
C	3.482596	-2.250601	-1.806108
C	-2.930337	-1.698624	-4.943819
C	-3.841880	-2.910520	-5.186646
C	-2.884458	-2.229745	-2.079779
C	-4.000127	-1.215054	-1.806283
H	0.574877	-3.620180	-2.261842
H	1.075473	-4.358831	-3.786331
H	-0.929157	-3.598819	-4.936274
H	-1.496869	-4.270074	-3.409784
H	2.053570	-1.042393	-5.932076
H	0.445760	-1.738290	-5.979886
H	1.449251	-4.074776	-6.059336
H	2.000305	-3.058094	-7.398077
H	3.075048	-3.365008	-6.026401
H	3.794605	-1.489345	-3.811950
H	3.475122	-3.222952	-3.748388
H	3.171507	-1.302607	-1.349717
H	2.961399	-3.064025	-1.287127
H	4.557638	-2.379442	-1.625298
H	-2.315602	-1.505004	-5.834048
H	-3.537355	-0.797677	-4.793034
H	-4.466137	-2.733899	-6.072049
H	-3.268422	-3.827996	-5.364730
H	-4.515266	-3.091446	-4.340144
H	-2.244965	-2.336554	-1.196594
H	-3.314552	-3.219108	-2.285369
H	-3.594061	-0.254229	-1.471074
H	-4.620137	-1.032311	-2.692837
H	-4.666625	-1.593362	-1.020308

Table C26. Cartesian coordinates for optimized structure of **8** in the triplet state

Mo	0.297310	-0.895680	-0.703983
P	1.841328	-0.545781	-2.857175
P	-1.390817	0.229457	-2.383030
N	0.194411	0.372755	0.417155
C	0.861356	0.491344	-4.064892
C	-0.634790	0.139291	-4.082981
C	2.470977	-1.978138	-3.880536
C	3.413813	-1.660115	-5.049944
C	3.364936	0.490204	-2.590935
C	3.158356	1.716812	-1.693405
C	-3.112806	-0.422863	-2.638841
C	-3.971301	0.292512	-3.692113
C	-1.615804	2.050918	-2.096937
C	-2.394739	2.377670	-0.815746
H	0.998627	1.540204	-3.771496
H	1.288529	0.390900	-5.070965
H	-0.787874	-0.887096	-4.445982
H	-1.169969	0.807234	-4.770578
H	2.961370	-2.660999	-3.172864
H	1.577669	-2.506016	-4.240971
H	2.959133	-0.970699	-5.772200
H	3.658596	-2.584528	-5.589006
H	4.355842	-1.218485	-4.705157
H	4.125559	-0.172455	-2.156964
H	3.741252	0.798538	-3.575574
H	2.767857	1.435008	-0.708313
H	2.454495	2.432249	-2.137996
H	4.112583	2.240400	-1.552505
H	-3.002651	-1.483952	-2.899751
H	-3.609031	-0.393325	-1.660027
H	-4.956307	-0.187624	-3.752558
H	-3.518363	0.245821	-4.689598
H	-4.133750	1.347063	-3.440017
H	-0.608666	2.483046	-2.038985
H	-2.105935	2.488285	-2.977657
H	-1.900853	1.942649	0.061376
H	-3.425589	2.003112	-0.857909
H	-2.443504	3.464999	-0.676123
P	-1.128493	-3.250121	-0.722006
P	1.675803	-2.409702	0.934664
C	-0.139431	-4.474496	0.281864
C	0.581350	-3.818009	1.468377
C	-2.651198	-2.972576	0.323462
C	-3.523282	-4.189472	0.661004
C	-1.765347	-4.330197	-2.109966
C	-0.719106	-4.649897	-3.184162
C	2.166023	-1.586902	2.521656
C	2.784204	-2.484494	3.602080
C	3.205886	-3.291887	0.344661
C	4.434552	-2.388488	0.177573
H	0.588068	-4.938846	-0.397403
H	-0.794191	-5.281056	0.637317
H	-0.145349	-3.405954	2.181620
H	1.175487	-4.565785	2.010190
H	-3.247426	-2.215481	-0.203189
H	-2.298492	-2.483597	1.241710
H	-2.962190	-4.965525	1.196481
H	-4.353330	-3.880462	1.309409
H	-3.958045	-4.643519	-0.237215
H	-2.617507	-3.801641	-2.559499
H	-2.162338	-5.258760	-1.677668
H	-0.339454	-3.735106	-3.656644
H	0.138417	-5.196408	-2.770768
H	-1.160484	-5.276412	-3.969608
H	1.254163	-1.098857	2.889902
H	2.851677	-0.773170	2.250175
H	3.035246	-1.882022	4.484336
H	2.090939	-3.270665	3.924993
H	3.707681	-2.967088	3.258727

H	2.948053	-3.763845	-0.613072
H	3.426871	-4.105161	1.049537
H	4.232043	-1.548980	-0.497882
H	4.765481	-1.972960	1.137010
H	5.269888	-2.962933	-0.241606

Table C27. Cartesian coordinates for optimized structure of **8** in the singlet state

Mo	0.025931	-0.022029	-1.589648
P	-0.200686	2.468317	-2.059918
P	-2.514069	0.235005	-1.686795
N	0.148757	-0.047531	0.074099
C	-1.941115	2.993560	-1.634456
C	-2.959993	1.986736	-2.188756
C	-0.077551	2.880679	-3.876681
C	-0.360276	4.330190	-4.297102
C	0.859725	3.740247	-1.221018
C	0.908786	3.602669	0.307134
C	-3.620091	-0.805740	-2.765975
C	-5.105839	-0.423635	-2.827216
C	-3.296946	0.143310	-0.000333
C	-3.236816	-1.229870	0.676203
H	-2.003782	3.036047	-0.538899
H	-2.147577	4.005499	-2.006123
H	-2.980076	2.025322	-3.287052
H	-3.972227	2.232127	-1.842819
H	0.932144	2.589273	-4.191861
H	-0.763589	2.197850	-4.397737
H	-1.377214	4.645528	-4.034402
H	-0.257853	4.425356	-5.385688
H	0.344088	5.032863	-3.836595
H	1.867439	3.632458	-1.645393
H	0.496724	4.738207	-1.501592
H	1.243956	2.603265	0.608062
H	-0.074933	3.778323	0.760671
H	1.602182	4.342159	0.727412
H	-3.182446	-0.782170	-3.773971
H	-3.506853	-1.838544	-2.408875
H	-5.642530	-1.118899	-3.485563
H	-5.250285	0.587477	-3.226333
H	-5.582274	-0.470577	-1.840521
H	-2.773058	0.884491	0.616217
H	-4.338052	0.480497	-0.097364
H	-2.198661	-1.537043	0.842607
H	-3.739856	-2.003111	0.080579
H	-3.739124	-1.187775	1.651351
P	0.145317	-2.511724	-2.098584
P	2.543713	-0.306268	-1.908177
C	1.927895	-3.007220	-2.404729
C	2.898031	-2.120726	-1.613173
C	-0.420325	-3.625869	-0.722015
C	-0.322313	-5.139454	-0.953494
C	-0.710774	-3.172505	-3.611054
C	-0.500951	-2.301921	-4.858420
C	3.597213	0.537076	-0.631350
C	5.073125	0.121927	-0.559487
C	3.430988	-0.008534	-3.525762
C	3.788278	1.454786	-3.818206
H	2.114226	-2.904891	-3.482979
H	2.077415	-4.066586	-2.160836
H	2.779670	-2.291333	-0.533605
H	3.937633	-2.362017	-1.870528
H	-1.459768	-3.338333	-0.520130
H	0.154793	-3.327465	0.164739
H	0.708620	-5.467156	-1.134583
H	-0.682155	-5.671311	-0.063309
H	-0.936072	-5.463630	-1.802547
H	-1.780326	-3.237019	-3.371241
H	-0.361966	-4.196635	-3.799771
H	-0.859909	-1.276049	-4.696779
H	0.557034	-2.248320	-5.147112
H	-1.051962	-2.717084	-5.711668
H	3.092332	0.347268	0.324929
H	3.506854	1.616459	-0.812346
H	5.585995	0.704027	0.217087
H	5.184474	-0.938630	-0.304221
H	5.599184	0.298811	-1.505951
H	2.791643	-0.405726	-4.325701
H	4.344432	-0.618912	-3.524618
H	2.904756	2.103258	-3.815786
H	4.497837	1.854113	-3.083859
H	4.255448	1.535469	-4.807813

Table C28. Cartesian coordinates for optimized structure of **7-TS** in the triplet state

Mo	-0.372216	0.340550	-3.252479
P	-2.221443	-1.066720	-4.276431
P	1.017212	-1.401953	-4.619010
N	0.194439	-0.066607	-1.625866
N	-0.206266	-0.060561	0.081463
C	-1.483414	-2.719109	-4.726199
C	-0.183077	-2.525025	-5.512818
C	-3.122240	-0.571283	-5.842224
C	-4.295408	-1.431458	-6.332335
C	-3.572604	-1.490185	-3.048270
C	-4.182395	-2.899639	-3.104098
C	2.161670	-0.909233	-6.005968
C	2.833374	-2.050656	-6.783675
C	2.039572	-2.600985	-3.624684
C	3.328534	-2.000272	-3.052346
H	-1.287508	-3.252193	-3.786957
H	-2.193749	-3.326837	-5.301203
H	-0.392531	-2.062555	-6.487488
H	0.295996	-3.491902	-5.714067
H	-3.454176	0.462969	-5.682310
H	-2.341003	-0.515302	-6.614204
H	-4.001819	-2.474271	-6.504860
H	-4.673571	-1.035591	-7.284269
H	-5.128368	-1.424381	-5.619416
H	-3.139375	-1.316580	-2.055365
H	-4.358296	-0.733834	-3.176150
H	-3.435515	-3.671736	-2.884944
H	-4.627671	-3.125668	-4.078692
H	-4.974916	-2.984891	-2.348750

H	1.554703	-0.298081	-6.686823
H	2.923104	-0.240564	-5.584126
H	3.451827	-1.634674	-7.589303
H	2.097225	-2.719921	-7.244429
H	3.488205	-2.654738	-6.144642
H	1.391572	-2.955003	-2.814168
H	2.268263	-3.468395	-4.258588
H	3.116735	-1.124522	-2.428311
H	4.021639	-1.693716	-3.845920
H	3.848236	-2.741175	-2.431107
P	0.817000	2.308088	-4.512592
P	-1.834566	2.345942	-2.636568
C	0.041470	3.922121	-3.964388
C	-0.675515	3.801907	-2.613794
C	2.565576	2.441160	-3.866113
C	3.448160	3.563164	-4.430323
C	1.031328	2.626493	-6.345273
C	-0.243487	2.417690	-7.170332
C	-2.599616	2.328839	-0.948176
C	-3.121214	3.670854	-0.414821
C	-3.189261	3.002638	-3.751671
C	-4.577175	2.373672	-3.576733
H	-0.668958	4.224123	-4.745057
H	0.813207	4.701587	-3.926917
H	0.042909	3.629654	-1.801246
H	-1.220028	4.728403	-2.388233
H	3.039611	1.466234	-4.037788
H	2.464064	2.537547	-2.777825
H	3.007163	4.556429	-4.279093
H	4.421920	3.557249	-3.923475
H	3.633740	3.435938	-5.503207
H	1.827528	1.959913	-6.700512
H	1.401117	3.653558	-6.469489
H	-0.615307	1.388532	-7.082876
H	-1.050592	3.091048	-6.852829
H	-0.046031	2.619428	-8.230917
H	-1.832969	1.900888	-0.289866
H	-3.409343	1.586782	-0.984901
H	-3.597230	3.527526	0.564524
H	-2.311252	4.398738	-0.284503
H	-3.870266	4.118708	-1.079200
H	-2.844388	2.861303	-4.784098
H	-3.254459	4.087443	-3.586944
H	-4.562735	1.289958	-3.736666
H	-4.987953	2.559347	-2.577252
H	-5.274337	2.804811	-4.306185
Mo	0.164434	-0.430516	1.730093
P	-0.220032	1.717918	3.116139
P	-2.254795	-0.762289	2.511825
C	-1.983450	1.740072	3.760983
C	-2.936918	0.945072	2.860478
C	-0.000859	3.338113	2.225761
C	-0.404528	4.619203	2.968117
C	0.752376	1.954072	4.686379
C	0.883379	0.675047	5.524930
C	-3.431435	-1.442949	1.245219
C	-4.931059	-1.342439	1.557784
C	-2.704673	-1.649100	4.095740
C	-2.755719	-3.180129	4.014758
H	-1.961470	1.302584	4.768419
H	-2.329122	2.773969	3.881254
H	-3.054477	1.444858	1.889190
H	-3.932529	0.880733	3.318965
H	1.064333	3.373457	1.964571
H	-0.543730	3.253188	1.275858
H	-1.477408	4.649555	3.192359
H	-0.177143	5.492449	2.343037
H	0.143457	4.737202	3.910523
H	1.746357	2.320389	4.398839
H	0.277088	2.748502	5.277445
H	1.378334	-0.123844	4.956534
H	-0.094440	0.299057	5.854294
H	1.480246	0.867653	6.425232
H	-3.190247	-0.912496	0.314642
H	-3.141435	-2.488894	1.080069
H	-5.512030	-1.799535	0.746089
H	-5.259424	-0.300607	1.653531
H	-5.194963	-1.865433	2.485256
H	-1.974953	-1.340829	4.856059
H	-3.679142	-1.262726	4.424706
H	-1.795620	-3.608770	3.706020
H	-3.520686	-3.526442	3.309449
H	-3.001029	-3.596571	4.999818
P	0.840645	-2.828588	1.595020
P	2.668085	-0.207333	1.491639
C	2.441131	-2.915277	0.647854
C	3.444957	-1.905462	1.218858
C	1.294580	-3.491837	3.285311
C	2.058238	-4.823113	3.342086
C	-0.187720	-4.201173	0.876626
C	-0.656928	-3.960202	-0.563171
C	3.742766	0.475480	2.855087
C	5.260540	0.434319	2.625709
C	3.241943	0.729759	-0.013819
C	3.146943	2.255826	0.097077
H	2.202294	-2.671168	-0.394417
H	2.854880	-3.932475	0.660500
H	3.813706	-2.255020	2.193298
H	4.319382	-1.815514	0.562151
H	0.353045	-3.574697	3.843793
H	1.871169	-2.703968	3.789448
H	3.030552	-4.760855	2.838476
H	2.246402	-5.096635	4.388245
H	1.490710	-5.642004	2.884575
H	-1.053103	-4.316652	1.542683
H	0.386746	-5.135666	0.935471
H	-1.175514	-2.999456	-0.664007
H	0.187551	-3.961165	-1.262830
H	-1.343586	-4.758100	-0.874714
H	3.482103	-0.082046	3.765270
H	3.413696	1.508972	3.024815
H	5.781642	0.851139	3.497263
H	5.624858	-0.589956	2.481476
H	5.557305	1.024416	1.750154
H	2.614731	0.380035	-0.842890
H	4.277629	0.428584	-0.221800

H	2.105321	2.584251	0.183796
H	3.704834	2.647977	0.956921
H	3.570100	2.723152	-0.801608

Table C29. Cartesian coordinates for optimized structure of **7-TS** in the singlet state

Mo	-0.417610	0.379457	-3.317992
P	-2.217033	-1.193849	-4.110237
P	0.920912	-1.293804	-4.769422
N	0.010371	0.008412	-1.656577
N	-0.061248	-0.003365	-0.114391
C	-1.441160	-2.833071	-4.555393
C	-0.220050	-2.616668	-5.456216
C	-3.013825	-0.671190	-5.717768
C	-4.090467	-1.571828	-6.339576
C	-3.598396	-1.646392	-2.939601
C	-4.255659	-3.027516	-3.086199
C	1.963443	-0.886151	-6.260968
C	2.614369	-2.069876	-6.991723
C	2.076742	-2.298259	-3.701684
C	3.385691	-1.591066	-3.331046
H	-1.142623	-3.309993	-3.612279
H	-2.165574	-3.499361	-5.040196
H	-0.537762	-2.292430	-6.456738
H	0.334139	-3.554557	-5.589244
H	-3.416914	0.333843	-5.546577
H	-2.179402	-0.534771	-6.420443
H	-3.729516	-2.592539	-6.515276
H	-4.398679	-1.160421	-7.309680
H	-4.983971	-1.628285	-5.707127
H	-3.169679	-1.547425	-1.934790
H	-4.351042	-0.851451	-3.028632
H	-3.535707	-3.837343	-2.919586
H	-4.707121	-3.174719	-4.072756
H	-5.051360	-3.134475	-2.337283
H	1.312441	-0.331823	-6.950144
H	2.733113	-0.178777	-5.926382
H	3.200335	-1.702349	-7.843921
H	1.866536	-2.769851	-7.382721
H	3.296007	-2.630363	-6.340540
H	1.513798	-2.554103	-2.796632
H	2.290234	-3.238449	-4.228285
H	3.198365	-0.639985	-2.819987
H	4.003501	-1.387184	-4.214389
H	3.976649	-2.224507	-2.656678
P	0.813026	2.397364	-4.228353
P	-2.004134	2.227933	-2.747644
C	-0.075903	3.981405	-3.754075
C	-0.964856	3.766781	-2.525154
C	2.522364	2.629616	-3.517472
C	3.357268	3.805031	-4.044796
C	1.075769	2.650030	-6.056967
C	-0.176033	2.410387	-6.910155
C	-2.881513	2.080555	-1.116222
C	-3.498549	3.361728	-0.535523
C	-3.328075	2.875348	-3.913738
C	-4.715034	2.226020	-3.806796
H	-0.685871	4.288379	-4.614222
H	0.651940	4.784273	-3.580871
H	-0.351686	3.609221	-1.626530
H	-1.597464	4.645680	-2.344809
H	3.054196	1.683478	-3.682250
H	2.380388	2.713976	-2.432658
H	2.848947	4.768736	-3.916480
H	4.306390	3.860686	-3.495757
H	3.597687	3.688618	-5.108060
H	1.882635	1.974579	-6.366937
H	1.443821	3.674140	-6.205373
H	-0.567633	1.393518	-6.774793
H	-0.981395	3.112059	-6.656992
H	0.056887	2.547948	-7.973852
H	-2.137584	1.654597	-0.429552
H	-3.652296	1.309358	-1.247208
H	-4.043824	3.133684	0.390300
H	-2.732655	4.107857	-0.292623
H	-4.211105	3.828691	-1.226433
H	-2.936995	2.759096	-4.932978
H	-3.421013	3.955940	-3.736946
H	-4.684485	1.141230	-3.958749
H	-5.177606	2.411376	-2.830577
H	-5.380410	2.644905	-4.572498
Mo	0.244638	-0.374832	1.563821
P	-0.032858	1.716469	3.056037
P	-2.156335	-0.659867	2.441764
C	-1.769917	1.776536	3.761963
C	-2.774418	1.053325	2.858571
C	0.115827	3.286370	2.058783
C	-0.217064	4.612426	2.755840
C	0.984259	2.075811	4.575217
C	1.075278	0.907346	5.566277
C	-3.390416	-1.282623	1.200611
C	-4.875701	-1.094233	1.541076
C	-2.579981	-1.574964	4.021604
C	-2.809127	-3.086707	3.889821
H	-1.737268	1.298629	4.750046
H	-2.071774	2.817747	3.930402
H	-2.897193	1.593202	1.910058
H	-3.760581	1.004904	3.338607
H	1.152015	3.301313	1.698411
H	-0.512924	3.148071	1.169502
H	-1.258681	4.654767	3.095799
H	-0.069767	5.442193	2.052331
H	0.431270	4.795814	3.620645
H	1.985465	2.365053	4.232055
H	0.553514	2.954999	5.073105
H	1.473131	0.000620	5.092343
H	0.095693	0.660293	5.994415
H	1.738442	1.171343	6.399673
H	-3.142668	-0.774576	0.260585
H	-3.160873	-2.344422	1.041341
H	-5.497349	-1.549063	0.758892
H	-5.146276	-0.033597	1.603662
H	-5.145381	-1.567439	2.493155
H	-1.766395	-1.380104	4.732209
H	-3.480026	-1.103411	4.439759

H	-1.940409	-3.606213	3.470420
H	-3.674228	-3.315419	3.256485
H	-3.001913	-3.517847	4.880260
P	0.806192	-2.798502	1.575749
P	2.773864	-0.302903	1.544399
C	2.451632	-3.000998	0.723649
C	3.474978	-2.040542	1.338262
C	1.118536	-3.516070	3.275609
C	1.676913	-4.944628	3.354795
C	-0.261565	-4.082265	0.757202
C	-0.588154	-3.773678	-0.709119
C	3.818303	0.334648	2.953768
C	5.340672	0.206290	2.794423
C	3.494652	0.578613	0.067166
C	3.478434	2.108963	0.151200
H	2.291562	-2.767224	-0.336741
H	2.801958	-4.040204	0.780063
H	3.769113	-2.393937	2.336161
H	4.389582	-2.002990	0.733310
H	0.165855	-3.453298	3.816546
H	1.794304	-2.814693	3.783469
H	2.645540	-5.037296	2.848569
H	1.827416	-5.223962	4.405586
H	0.990966	-5.677651	2.914247
H	-1.185739	-4.146642	1.346435
H	0.235614	-5.058125	0.838506
H	-0.978965	-2.755780	-0.828575
H	0.303029	-3.867656	-1.341940
H	-1.336642	-4.482242	-1.087308
H	3.485727	-0.202146	3.852309
H	3.544169	1.385774	3.106245
H	5.841520	0.598884	3.688758
H	5.653899	-0.837405	2.672273
H	5.712337	0.773956	1.932853
H	2.915216	0.245030	-0.801656
H	4.523770	0.219682	-0.067186
H	2.453980	2.497372	0.179956
H	4.010569	2.481184	1.035650
H	3.974878	2.536882	-0.729017

Table C30. Cartesian coordinates for optimized structure of **9’**

Mo	0.590699	0.403157	-1.650679
P	-0.753677	-1.673594	-1.920424
P	2.375777	-1.243914	-2.207349
N	1.111575	0.211638	0.213930
N	1.388350	0.107896	1.311542
C	0.376770	-3.150572	-1.919740
C	1.604728	-2.844454	-2.783872
C	-1.608657	-1.787355	-3.570040
C	-1.987134	-3.188336	-4.061543
C	-2.085469	-2.160189	-0.731377
C	-1.617385	-2.132286	0.727638
C	3.581194	-0.840573	-3.557079
C	4.571637	-1.945260	-3.939369
C	3.436538	-1.867839	-0.819916
C	4.421067	-0.839389	-0.260139
H	0.677441	-3.328440	-0.879031
H	-0.146529	-4.050158	-2.264072
H	1.313113	-2.713676	-3.835817
H	2.332030	-3.664410	-2.742716
H	-2.505539	-1.163912	-3.473761
H	-0.963500	-1.285409	-4.304219
H	-1.100314	-3.794186	-4.281024
H	-2.575337	-3.115826	-4.985053
H	-2.592876	-3.727801	-3.323088
H	-2.913236	-1.454472	-0.882859
H	-2.459812	-3.157316	-0.999566
H	-1.257067	-1.136895	1.009700
H	-0.800973	-2.843937	0.902170
H	-2.441631	-2.400032	1.400125
H	2.972294	-0.548705	-4.423983
H	4.115792	0.064504	-3.240918
H	5.224220	-1.604334	-4.752942
H	4.054469	-2.849115	-4.282345
H	5.211977	-2.222178	-3.093453
H	2.749248	-2.195645	-0.029329
H	3.968180	-2.761650	-1.171312
H	3.893383	0.011576	0.179594
H	5.097880	-0.460270	-1.036526
H	5.038658	-1.293913	0.524760
P	1.908333	2.510494	-1.743077
P	-1.182485	2.050858	-1.119422
C	0.792136	3.977519	-1.433902
C	-0.358383	3.598847	-0.494579
C	3.315235	2.757195	-0.564234
C	4.061548	4.093170	-0.636109
C	2.648663	2.906834	-3.395546
C	1.699629	2.543021	-4.543403
C	-2.353563	1.597012	0.243368
C	-3.313270	2.691845	0.720071
C	-2.267727	2.735046	-2.459408
C	-3.069356	1.661920	-3.198970
H	0.397819	4.293446	-2.408677
H	1.365966	4.822735	-1.037146
H	0.021530	3.377602	0.512339
H	-1.078047	4.422189	-0.405246
H	4.005776	1.928620	-0.759835
H	2.912348	2.587301	0.443591
H	3.407692	4.944063	-0.411448
H	4.879205	4.105508	0.095785
H	4.500096	4.256327	-1.627823
H	3.582804	2.336201	-3.477779
H	2.914983	3.971097	-3.433600
H	1.473510	1.468060	-4.543604
H	0.747431	3.083789	-4.467003
H	2.146531	2.791880	-5.513828
H	-1.719100	1.252805	1.071338
H	-2.911754	0.717167	-0.100651
H	-3.936149	2.314803	1.540994
H	-2.771819	3.570875	1.088871
H	-3.985455	3.018772	-0.082128
H	-1.608295	3.261274	-3.162295
H	-2.931106	3.492755	-2.022431
H	-2.399819	0.971435	-3.723505

H	-3.689974	1.072417	-2.511610
H	-3.735141	2.118295	-3.941957

Table C31. Cartesian coordinates for optimized structure of **10’**

Mo	0.732671	-1.571047	-0.291253
P	-0.415340	-1.730498	1.910264
P	2.498388	-2.698095	1.043919
N	1.677731	0.068256	0.184087
N	2.259436	0.993539	0.487925
C	0.908643	-1.906585	3.203231
C	1.874266	-3.018736	2.778957
C	-1.514981	-3.199569	2.214423
C	-1.831321	-3.536825	3.675051
C	-1.440447	-0.319013	2.529413
C	-0.723116	1.031445	2.445713
C	3.021999	-4.386670	0.478340
C	4.001672	-5.127969	1.394426
C	4.102982	-1.830320	1.369924
C	4.982572	-1.718724	0.122495
H	1.433838	-0.943838	3.254704
H	0.481981	-2.100246	4.194766
H	1.356589	-3.988637	2.770011
H	2.715373	-3.104647	3.477641
H	-2.439100	-2.990412	1.660791
H	-1.049774	-4.059147	1.714782
H	-0.933792	-3.852848	4.219826
H	-2.555000	-4.360409	3.723783
H	-2.265730	-2.681464	4.206436
H	-2.350551	-0.302776	1.915096
H	-1.749957	-0.533664	3.561225
H	-0.456131	1.275977	1.415352
H	0.195294	1.037593	3.046446
H	-1.369578	1.835527	2.812365
H	2.094821	-4.964116	0.356497
H	3.444971	-4.272142	-0.527529
H	4.221988	-6.123625	0.989148
H	3.589536	-5.260394	2.401912
H	4.951947	-4.588799	1.487070
H	3.846723	-0.830658	1.743257
H	4.635257	-2.349174	2.177349
H	4.436134	-1.246452	-0.700646
H	5.320382	-2.704448	-0.221371
H	5.873434	-1.112565	0.327962
P	1.793144	-1.271213	-2.518847
P	-1.229552	-1.020700	-1.726090
C	0.534418	-0.957021	-3.873945
C	-0.721640	-0.252805	-3.344703
C	2.934044	0.177915	-2.722951
C	3.763828	0.210378	-4.009823
C	2.730749	-2.717877	-3.203619
C	1.914822	-4.012863	-3.102252
C	-2.711466	-0.070640	-1.155114
C	-3.737765	0.289994	-2.233752
C	-1.946546	-2.622324	-2.355347
C	-2.259393	-3.655052	-1.269618
H	0.269295	-1.931163	-4.301739
H	0.995789	-0.375857	-4.681602
H	-0.532393	0.809255	-3.170532
H	-1.540776	-0.325608	-4.071157
H	3.591045	0.208265	-1.846968
H	2.296529	1.067422	-2.649202
H	3.136209	0.148122	-4.907669
H	4.330664	1.148300	-4.068649
H	4.482704	-0.616776	-4.044626
H	3.655416	-2.802112	-2.617149
H	3.021033	-2.526699	-4.244761
H	1.564820	-4.186309	-2.076033
H	1.030736	-3.982707	-3.751402
H	2.516669	-4.878900	-3.404578
H	-2.348538	0.839516	-0.666759
H	-3.169297	-0.689765	-0.370222
H	-4.596045	0.792752	-1.773892
H	-3.308734	0.985738	-2.961334
H	-4.107000	-0.594883	-2.766837
H	-1.215452	-3.038740	-3.058759
H	-2.846822	-2.391310	-2.940199
H	-1.346197	-4.002765	-0.767877
H	-2.930621	-3.248164	-0.504442
H	-2.749180	-4.534719	-1.706974
P	-2.577883	4.235326	-0.516711
C	-0.955534	4.992424	1.901169
F	-3.591739	3.167477	-1.266755
C	-4.793534	6.122944	-1.270521
C	-1.508243	5.490095	0.539071
F	-1.951952	2.971679	0.364385
C	-1.204158	3.874745	-1.910625
C	-3.367593	5.642843	-1.625204
F	0.007638	4.067511	1.762268
F	-1.924888	4.486164	2.682653
F	-0.410460	6.043362	2.555536
F	-0.425163	5.991212	-0.131143
F	-2.294255	6.563647	0.875979
F	-3.466957	5.182437	-2.915361
F	-2.605729	6.780194	-1.673503
F	-5.664773	5.101393	-1.221786
F	-4.828946	6.781150	-0.102686
F	-5.218685	6.977101	-2.230308
C	0.120050	3.156481	-1.546470
F	-0.812195	5.029441	-2.535077
F	-1.730590	3.060218	-2.886861
F	-0.102957	1.916412	-1.072699
F	0.870442	3.822528	-0.666183
F	0.855045	3.013589	-2.681613
F	-3.744339	4.439137	0.649185

Table C32. Cartesian coordinates for optimized structure of **11’**

Mo	0.597034	0.375766	-1.877855
P	-0.821134	-1.681827	-1.915566
P	2.325509	-1.342206	-2.401466
N	1.116496	0.161874	-0.021422
N	1.401300	0.031220	1.072257
C	0.304540	-3.167538	-1.897823

C	1.491904	-2.948675	-2.842011
C	-1.916072	-1.947964	-3.397418
C	-2.145584	-3.392531	-3.852428
C	-2.010392	-2.078572	-0.546421
C	-1.413099	-2.025391	0.861493
C	3.481310	-1.006071	-3.800075
C	4.375337	-2.162815	-4.255411
C	3.435042	-1.881628	-1.019012
C	4.425958	-0.802439	-0.577160
H	0.658663	-3.283276	-0.865045
H	-0.248643	-4.078439	-2.153464
H	1.156424	-2.880473	-3.883246
H	2.203005	-3.782009	-2.777239
H	-2.872501	-1.480359	-3.131552
H	-1.500849	-1.359802	-4.216361
H	-1.230859	-3.837387	-4.258755
H	-2.898005	-3.411614	-4.651477
H	-2.510854	-4.029545	-3.036930
H	-2.835850	-1.359660	-0.636241
H	-2.434820	-3.071938	-0.749569
H	-1.049536	-1.021924	1.102918
H	-0.570689	-2.718951	0.972492
H	-2.170453	-2.301787	1.606061
H	2.850541	-0.675844	-4.625478
H	4.085359	-0.139014	-3.503176
H	4.954380	-1.857051	-5.136540
H	3.780457	-3.036818	-4.543071
H	5.080513	-2.469551	-3.473281
H	2.785097	-2.159833	-0.179606
H	3.964562	-2.791057	-1.332660
H	3.899306	0.099290	-0.249748
H	5.107197	-0.522043	-1.390177
H	5.036579	-1.160750	0.261206
P	1.956652	2.474790	-1.842909
P	-1.166222	2.066762	-1.352932
C	0.798683	3.917305	-2.041446
C	-0.372580	3.735153	-1.068520
C	2.784401	2.847378	-0.220674
C	3.241036	4.290988	0.011662
C	3.312657	2.826277	-3.054040
C	2.871021	2.665285	-4.509186
C	-2.048657	1.731423	0.243462
C	-2.987172	2.830046	0.751712
C	-2.525186	2.553760	-2.520279
C	-3.424497	1.396897	-2.956268
H	0.439634	3.911904	-3.079388
H	1.313432	4.871801	-1.878913
H	-0.016020	3.765567	-0.029641
H	-1.114713	4.534502	-1.183861
H	3.641105	2.163916	-0.162847
H	2.098968	2.535333	0.575401
H	2.389850	4.979398	0.073094
H	3.788943	4.360905	0.960172
H	3.907739	4.647718	-0.782483
H	4.122917	2.122573	-2.817484
H	3.701448	3.837086	-2.873799
H	2.484838	1.662415	-4.700765
H	2.082392	3.380554	-4.772658
H	3.713317	2.834506	-5.191771
H	-1.257236	1.528060	0.977323
H	-2.594682	0.788846	0.112773
H	-3.410692	2.544880	1.723183
H	-2.459575	3.782411	0.883788
H	-3.823322	2.998596	0.063020
H	-2.042763	3.003838	-3.395921
H	-3.113210	3.346841	-2.040222
H	-2.864901	0.667177	-3.546982
H	-3.863798	0.876188	-2.095222
H	-4.250590	1.766642	-3.576904
P	0.652224	-0.622828	-8.051159
C	0.524542	-3.587990	-7.459286
F	0.395471	0.630552	-9.091279
C	-1.192544	1.100818	-6.385944
C	0.738379	-2.175638	-6.858272
F	0.967240	-1.614416	-9.339095
C	2.573737	-0.146799	-7.988081
C	0.267980	0.637088	-6.582218
F	1.530450	-3.973517	-8.253991
F	-0.625220	-3.669086	-8.143199
F	0.457683	-4.472988	-6.432942
F	1.904735	-2.266301	-6.142842
F	-0.276894	-2.073507	-5.935731
F	0.962489	1.796562	-6.804425
F	0.661883	0.182066	-5.335841
F	-1.694211	1.650316	-7.496894
F	-2.000927	0.107013	-5.985113
F	-1.212638	2.048717	-5.409640
C	3.621991	-1.092791	-8.622523
F	2.993868	0.039231	-6.691977
F	2.787553	1.040684	-8.632587
F	3.494010	-1.129932	-9.957818
F	3.555305	-2.344790	-8.146321
F	4.857352	-0.619330	-8.341421
F	-0.963091	-0.985375	-8.173910

Table C33. Cartesian coordinates for optimized structure of **12’**

Mo	0.595839	0.405037	-1.791210
P	-0.783234	-1.672532	-1.823548
P	2.329351	-1.274033	-2.410581
N	1.235128	0.128893	0.032542
N	1.637609	-0.061064	1.074234
C	0.354434	-3.146742	-1.899292
C	1.503418	-2.879833	-2.876694
C	-1.927925	-1.889267	-3.276122
C	-2.205123	-3.323595	-3.736844
C	-1.913011	-2.100212	-0.413294
C	-1.195686	-2.471106	0.887896
C	3.448214	-0.890228	-3.827338
C	4.371463	-2.009331	-4.317387
C	3.490024	-1.858179	-1.086419
C	4.529803	-0.812312	-0.679493
H	0.748976	-3.288105	-0.885339
H	-0.195103	-4.058157	-2.162289
H	1.129758	-2.784814	-3.901059

H	2.228596	-3.703737	-2.864031
H	-2.862339	-1.400010	-2.970410
H	-1.527676	-1.303025	-4.106347
H	-1.315895	-3.777325	-4.187971
H	-2.994235	-3.323603	-4.500055
H	-2.541252	-3.964264	-2.911436
H	-2.545049	-1.216823	-0.258731
H	-2.575877	-2.915276	-0.736831
H	-0.444228	-1.726910	1.162771
H	-0.703703	-3.447963	0.804147
H	-1.906700	-2.517889	1.719043
H	2.789778	-0.570842	-4.634604
H	4.029410	-0.006817	-3.532565
H	4.900134	-1.682316	-5.222335
H	3.804274	-2.909171	-4.579545
H	5.119578	-2.283325	-3.563437
H	2.877319	-2.133798	-0.219033
H	3.981020	-2.774587	-1.439770
H	4.044414	0.103509	-0.328727
H	5.186836	-0.548084	-1.517474
H	5.161051	-1.191503	0.134151
P	1.922484	2.519724	-1.728094
P	-1.191748	2.079094	-1.293442
C	0.766957	3.978385	-1.799943
C	-0.416650	3.722149	-0.860058
C	2.827447	2.821908	-0.133693
C	3.461760	4.202073	0.062078
C	3.192594	2.926693	-3.013305
C	2.661172	2.726600	-4.434409
C	-2.371556	1.740281	0.087170
C	-3.250457	2.915224	0.523920
C	-2.314638	2.645492	-2.665171
C	-3.278140	1.576750	-3.181078
H	0.419346	4.071413	-2.837602
H	1.286356	4.911117	-1.549352
H	-0.081689	3.675409	0.182691
H	-1.161243	4.524329	-0.933068
H	3.595505	2.041570	-0.069701
H	2.118058	2.610647	0.674349
H	2.707991	4.998019	0.083481
H	3.997617	4.233906	1.019710
H	4.183085	4.440002	-0.728810
H	4.047645	2.262200	-2.826005
H	3.545314	3.956215	-2.868805
H	2.296824	1.707412	-4.580748
H	1.831161	3.409744	-4.654255
H	3.447189	2.910880	-5.177599
H	-1.786810	1.368049	0.930893
H	-2.995055	0.899495	-0.244277
H	-3.887905	2.600217	1.355922
H	-2.643076	3.755379	0.878768
H	-3.891772	3.273569	-0.290735
H	-1.671059	2.994024	-3.480475
H	-2.870155	3.520952	-2.303262
H	-2.738138	0.722488	-3.595978
H	-3.936312	1.208477	-2.383779
H	-3.913819	1.985362	-3.976853
P	0.635243	-0.711233	-8.058473
C	0.506459	-3.650452	-7.353374
F	0.383423	0.500654	-9.147839
C	-1.232077	1.065587	-6.495916
C	0.712144	-2.214518	-6.808116
F	0.965297	-1.750098	-9.306198
C	2.554817	-0.226850	-8.000452
C	0.235278	0.604617	-6.642344
F	1.522756	-4.065306	-8.120019
F	-0.634423	-3.762966	-8.047589
F	0.429384	-4.493495	-6.293004
F	1.877025	-2.270905	-6.087752
F	-0.307130	-2.078292	-5.894158
F	0.933122	1.754685	-6.899396
F	0.607752	0.205644	-5.369388
F	-1.731966	1.523610	-7.649289
F	-2.027655	0.089539	-6.030177
F	-1.276452	2.083928	-5.597554
C	3.613805	-1.196610	-8.579869
F	2.960510	0.025363	-6.711933
F	2.770258	0.929156	-8.700539
F	3.507803	-1.283892	-9.914935
F	3.541833	-2.430410	-8.059750
F	4.844696	-0.711692	-8.295834
F	-0.977813	-1.085127	-8.182449
P	-2.026426	0.307788	4.012363
C	0.293383	-1.512112	4.653496
F	-3.165269	0.822281	2.925098
C	-4.517761	-0.222779	5.619434
C	-0.745373	-0.519893	5.242420
F	-0.989299	0.013704	2.749858
C	-1.296983	2.149567	4.092186
C	-3.313834	0.728546	5.430714
F	1.216727	-0.909164	3.894942
F	-0.286834	-2.486356	3.933260
F	0.945188	-2.103899	5.684462
F	-0.008962	0.381024	5.964563
F	-1.437954	-1.284143	6.150242
F	-3.880390	1.950894	5.161144
F	-2.738876	0.836019	6.669615
F	-5.210790	-0.378281	4.478784
F	-4.147013	-1.430334	6.070116
F	-5.357680	0.310844	6.537335
C	0.093556	2.458766	3.478858
F	-1.222209	2.594661	5.387187
F	-2.124736	3.021041	3.429287
F	0.078078	2.337274	2.132845
F	1.071177	1.685498	3.961857
F	0.413746	3.743955	3.751778
F	-2.652558	-1.224643	3.841937

Table C34. Cartesian coordinates for optimized structure of **1** with empirical corrections

Mo	-2.435473	-0.000056	-0.000035
P	0.014586	0.055207	0.026292
P	-1.965565	-2.402597	0.029675
N	-2.426323	-0.073120	-2.008662
N	-2.441077	-0.135654	-3.141536

C	0.613787	-1.580140	-0.651461
C	-0.110568	-2.708493	0.091292
C	0.826605	0.070460	1.707653
C	2.278009	-0.410527	1.800855
C	1.070947	1.272684	-0.900233
C	0.750162	1.328309	-2.397391
C	-2.576688	-3.454795	1.433723
C	-2.099859	-4.909697	1.475025
C	-2.385193	-3.424987	-1.467376
C	-3.887720	-3.599350	-1.687654
H	0.350131	-1.600467	-1.717672
H	1.704322	-1.680281	-0.580233
H	0.190851	-2.720851	1.148605
H	0.138720	-3.690706	-0.329996
H	0.748698	1.101021	2.076845
H	0.186389	-0.528824	2.366602
H	2.366850	-1.475030	1.552252
H	2.658141	-0.278615	2.822690
H	2.941054	0.146793	1.127578
H	0.885838	2.251841	-0.437160
H	2.133393	1.038182	-0.747145
H	-0.309878	1.543454	-2.565306
H	0.977095	0.374549	-2.890218
H	1.342499	2.108371	-2.893508
H	-2.280324	-2.922525	2.348434
H	-3.672748	-3.409573	1.400580
H	-2.498913	-5.423013	2.359985
H	-1.005682	-4.974043	1.517822
H	-2.433370	-5.467124	0.590920
H	-1.938139	-2.905406	-2.325487
H	-1.889106	-4.401624	-1.389983
H	-4.375305	-2.624524	-1.781696
H	-4.358976	-4.131595	-0.850877
H	-4.089075	-4.171346	-2.602908
P	-4.885550	-0.055214	-0.026352
P	-2.905301	2.402480	-0.029639
N	-2.444589	0.073026	2.008592
N	-2.429862	0.135569	3.141466
C	-5.484633	1.580078	0.651632
C	-4.760289	2.708474	-0.091068
C	-5.697626	-0.070098	-1.707690
C	-7.148942	0.411173	-1.800779
C	-5.941965	-1.272764	0.900020
C	-5.620937	-1.328873	2.397108
C	-2.294228	3.454734	-1.433667
C	-2.771020	4.909651	-1.474861
C	-2.485432	3.424723	1.467442
C	-0.982851	3.598476	1.687863
H	-5.220893	1.600279	1.717824
H	-6.575171	1.680271	0.580498
H	-5.061799	2.720948	-1.148354
H	-5.009497	3.690658	0.330337
H	-5.619923	-1.100615	-2.077035
H	-5.057324	0.529167	-2.366574
H	-7.237578	1.475653	-1.552002
H	-7.529124	0.279498	-2.822627
H	-7.812075	-0.146131	-1.127577
H	-5.757099	-2.251824	0.436647
H	-7.004396	-1.038043	0.747171
H	-4.560915	-1.544296	2.564785
H	-5.847584	-0.375203	2.890241
H	-6.213357	-2.108946	2.893107
H	-2.590660	2.922522	-2.348390
H	-1.198169	3.409483	-1.400587
H	-2.371996	5.423009	-2.359811
H	-3.865198	4.974028	-1.517601
H	-2.437452	5.467017	-0.590739
H	-2.932758	2.905304	2.325511
H	-2.981140	4.401550	1.390010
H	-0.495654	2.623450	1.781933
H	-0.511305	4.130549	0.851141
H	-0.781351	4.170373	2.603146

C.7 References

1. A. C. Filippou, G. Schnakenburg, A. I. Philippopoulos, and N. Weidemann, *Angew. Chem. Int. Ed.*, **2005**, *44*, 5979.
2. Johan Cugny, Helmut W. Schmalle, Thomas Fox, Olivier Blacque, Montserrat Alfonso, Heinz Berke *Eur. J. Inorg.*, **2006**, *3*, 540. (CCDC Number: 280785)
3. A. C. Filippou, G. Schnakenburg, A. I. Philippopoulos and N. Weidemann, *Angew. Chem. Int. Ed.*, **2005**, *44*, 5979.
4. T. A. Geoge and C. D. Sebold, *Inorg. Chem.*, **1973**, *12*, 2544.
5. M. Hidai, *Coord. Chem. Rev.*, **1999**, *185–186*, 99.
6. See Section 2.4.5 in Chapter 2
7. J. Chatt, J. R. Dilworth, R. L. Richards, *Chem. Rev*., **1978**, *78*, 589.